Microstructure and mechanical properties of titanium-containing steel weld metal with varying molybdenum and nickel levels before and after thermal cycling

Prepared by

Sinéa Monique van Wijngaarden

Submitted in partial fulfilment of the requirements for the degree

of Doctorate of Philosophy

University of Pretoria

Faculty of Engineering, Built Environment and Information Technology

Department of Materials Science and Metallurgical Engineering

Supervisor: Prof. PGH Pistorius

December 2021

Acknowledgements

Throughout the writing of this dissertation I have received a great deal of support and assistance.

I would like to offer my sincere gratitude to my supervisor, Prof. Pistorius, whose support, patient guidance, and insight was invaluable to the completion of this work.

I would also like to thank Corney van Rooyen, from the CSIR, for his assistance in developing my experimental technique, Josef Henning from Linconl Electric for his assistance with my welding, and Dr Japheth Obiko and Dr Michael Bodundrin from the University of Witwatersrand for their assistance with the Gleeble simulation section of my experiments.

I am deeply grateful to my mom and dad; whose unwavering backing and technical input helped me a tremendous amount throughout, but especially towards the end, of this project.

I would like to thank my dearest friend AJ, for the laughter and intellectual sustenance he with which he supplied me throughout the final months of completing this project. I would also like to thank my husband, C-J de Beer, who patiently stood by me and provided me the much-needed comfort that I required for the duration of my candidateship.

Lastly and most importantly I would like to thank our Lord Jesus Christ for all that he has done for me leading up to and throughout the work on this thesis.

Abstract

The purpose of this research was to investigate the effects of Ni and Mo on the mechanical properties of Ti-containing weld metal. Alloyed weld metals of varying chemical compositions were produced with a unique weld-alloying technique developed for the purposes of this research. The weld-alloying technique was used to make controlled changes to the chemical composition of commercially available high-strength low-alloy (HSLA) steel weld metal. The technique involves the deposition of beads of alloying elements on steel plates by means of laser metal deposition (LMD), followed by the deposition of commercially available welding wire.

This technique was used to produce nine Ti-containing welds with varying weld metal compositions with regard to Ni and Mo. The responses of Ni and Mo in the presence of Ti have not previously been investigated. These welds were produced by depositing LMD beads of pure Ni, Mo, and Ti on low-carbon steel plates. Submerged arc welds (SAWs) were deposited over the LMD beads to produce alloyed welds. Ti was added because it is increasingly being used in HSLA-steel weld wires to promote acicular ferrite formation. Ti was maintained at 0.019 mass%–0.030 mass%; the Ni content was varied between 0.01 mass%–2.44 mass% whilst the Mo content was varied between 0.01 mass%–0.03 %.

When welds with the same intended alloy content were produced using this procedure, the alloy content of those welds, in the best case, varied within a range of 12 mass% (expressed as a percentage of the intended alloy content). This is comparable with ranges of alloy content measured in welds made with conventionally alloyed welding wire. However, this range increased to as high as 50 mass% when the intended alloying content decreased. This indicates that there is a lower limit of alloying element content below which this technique becomes unstable. The weld-alloying technique requires refinement, but shows promise as a method for altering submerged arc weld metals composition for research purposes.

Results from the literature indicated that multi-pass welds may have different mechanical properties to comparable single-pass welds. This indicated that it may be necessary to investigate the response of the nine welds to thermal cycling with regard to both mechanical properties and microstructure. To do this, the as-welded samples were exposed to thermal cycling, which was intended to simulate the intercritically reheated (IR) heat-affected zone (HAZ), the fine-grained (FG) HAZ and the coarse-grained (CG) HAZ in the weld metal of each weld.

The peak temperature required for the thermal cycling of each weld was determined by measuring the individual A_{C1} (as the lowest temperature at which austenite can form upon heating) and A_{C3} (the temperature at which all metal has transformed to austenite upon heating) temperatures of each weld metal and accordingly calculating the requisite peak temperature. This is an improvement on conventional thermal cycling, which usually uses the same peak temperature for all weld compositions studied.

Simulation of the HAZ was carried out by exposing the welds to thermal cycles using a Gleeble dynamic thermomechanical testing instrument. Mechanical testing and microscopy were performed on welds in the as-welded condition and on each of the simulated HAZ regions. Impact testing was done using half-size Charpy impact test coupons at a testing temperature of −40°C. Hardness testing was done by done by using a Vickers hardness tester and a mass of 10 kg. Microscopy included optical and scanning electron microscopy on mounted samples and fractography of Charpy impact test fracture surfaces using a low-voltage high-resolution scanning

electron microscope (SEM). Such equipment has not been previously used to study the microstructure of HSLA-steel weld metal.

Hardness results indicated that the addition of both Ni and Mo increased the hardness of welds and that there was an interaction between the two elements. Multivariant linear regression analysis on the effects of Ni content, Mo content, and the product of the Ni and Mo contents was used to predict the hardness of individual welds with an accuracy of 82 mass%. The average hardness of the welds was 240 HV10 with a range of 208 HV10 to 271 HV10.

The impact toughness of welds in the as-welded condition showed that, individually, neither Ni nor Mo had a strong effect on impact energy. Of the nine weld metal compositions tested, two had a significantly lower impact energy than the rest. The impact energies of the two outliers were 29 J and 31 J. These welds contained 0.12 mass% Mo, 2.34 mass% Ni and 0.23 mass% Mo, 2.44 mass% Ni, respectively. The average impact energy of the remaining seven welds was 43 J, with a range of 39–49 J.

Quantitative microscopy showed that increases in both Ni and Mo led to a reduction in the fraction of grain-boundary products. The equation derived to predict grain boundary product content of welds was 86 % accurate when the Mo content, Ni content, and product of the Mo and Ni contents were used as independent variables. No other trends with regard to the influence of chemical composition on microstructure were detected. An etch effect was observed during optical microscopy, which indicated that alloying elements segregated to the prior austenite grain boundaries of the two Mo- containing high-Ni welds. SEM and energy-dispersive X-ray spectroscopy confirmed that the etch effect was a result of segregation of Ni to prior austenite grain boundaries.

SEM revealed that regions of coalesced bainite had formed on and directly adjacent to the PAGBs of the Mo-containing high-Ni welds in which Ni and Mn segregation had been confirmed. Fractography of these samples revealed that fracture occurred along the regions of coalesced bainite. The low impact energy values of the Mo-containing high-Ni welds were attributed to these networks of coalesced bainite. Segregation of these elements is believed to have contributed to the formation of coalesced bainite. Segregation is attributed to the fact that a significant amount of the weld metal solidified as austenite.

The results of thermal cycling indicated that reheating of the weld metal did not have a strong effect on hardness; however, the impact energies of welds that contained Mo appeared to be sensitive to thermal cycling. With the exception of one weld, the largest decrease in impact energy seen across the three thermally cycled samples from each weld exceeded 10 J. The exception was a low-Mo high-Ni weld that did not experience any significant reduction in impact energy after thermal cycling.

The results of this study clearly show that thermal cycling associated with multi-pass submerged arc welding may significantly affect the impact energy as measured in single-pass welds of Ti-containing HSLA steel. Hence, single-pass welds should preferably not be used in isolation to evaluate the influence of chemical composition on impact energy of SAWs. It is recommended that future studies on the influence of chemical composition on HSLA-steel welds include an evaluation of both as-welded and thermally cycled weld metal. Thermal cycling by means of Gleeble simulation increases the likelihood of detecting brittle zones that may be more difficult to detect in actual multi-pass SAWs. Although the impact energy of thermally cycled weld metal may prove useful in detecting brittle HAZ regions, it cannot be used to estimate the impact behaviour of multi-pass

welds and should be used in tandem with actual multi-pass welding to accurately evaluate the influence of varying chemical composition on the impact energy of such welds.

Lastly, the results indicate that the presence of Ti in the weld metal did not affect the way in which the weld metal reacted to changes in Ni and Mo levels. In the as-welded state, both Ni and Mo increase the strength without significantly affecting impact energy. An interaction between Ni and Mo was noted, but its nature could not be identified. When weld metal was thermally cycled, the presence of Mo made it susceptible to mechanisms that reduced the impact energy of the welds.

Contents

List of Tables

List of Figures

List of definitions

Acicular ferrite (AF): an intergranularly nucleated lath-like ferrite. The extent to which this phase is present in welds is often considered the most important factor for HLSA-steel weld metal toughness.

Allotriomorphic ferrite: A type of ferrite that grows epitaxially via a reconstructive mechanism from either an austenite crystal or a non-metallic inclusion into an adjacent austenite crystal.

Alpha ferrite (α): A lower-temperature form of body-centred cubic ferrite.

Austenite (γ): A face-centred cubic form of iron. It forms either directly from the liquid phase or from delta ferrite, depending on metal composition.

Bainite: A type of ferrite that nucleates directly on a non-ferritic interface and grows via a shear mechanism. There is no carbon diffusion during growth, but carbon is diffused out directly following transformation.

Brittle fracture: Fracture occurring with minimal plastic deformation.

Crack initiation: The process whereby a crack forms in a metal.

Crack propagation: The process whereby a crack grows in a metal.

Crystallographic matching: Refers to a case where the crystalline structure and orientation of two adjacent grains are similar and reduce lattice interface energy.

Delta ferrite (δ): A high-temperature form of body-centred cubic iron. It forms when low-carbon low-alloy steel cools from the liquid phase.

Ductile fracture: Fracture that occurs following significant plastic strain.

Ferrite with second phase aligned (FS(A)): Lath-like ferrite that nucleates at γ/γ grain boundaries and grows in parallel sheaths.

Geometric effect: The ability of an inclusion to aid nucleation merely by acting as an inert substance with a specific shape, size, and interface energy.

Grain boundary ferrite (GBF): A type of allotriomorphic ferrite that forms on prior austenite grain boundaries.

High-strength low-alloy (HSLA) steels: A type of thermo-mechanically controlled steel with a minimum yield strength of 275 Mpa; a carbon content of between 0.05 % C and 0.25 % C; up to 2% Mn, and that may contain small amounts of Cr, Ni, Mo, Cu, N, V, Nb, Ti, and Zr.

HSLA-80 steel: HSLA steel with a minimum yield strength of 550 Mpa.

Interferritic regions (IfRs): Regions occurring between AF laths. These regions consist of varying amounts of allotriomorphic ferrite, upper and lower bainite, and islands of martensite with retained austenite.

Lower bainite: A type of lower-temperature bainite where carbon is precipitated within laths.

Martensite with retained austenite (M/A) islands: Small regions of martensite with retained austenite that form within interferritic regions.

Non-metallic inclusions: Chemical compounds and non-metals that form during the cooling of metal and, instead of rising to the slag, become embedded in the metal during solidification. These inclusions act as nucleation sites during the formation of the metal matrix.

Parent metal (PM): Metal of the base metal that has not been affected by the welding process

Primary AF: A type of AF that nucleates directly on intergranular inclusions.

Secondary AF: A type of AF that nucleates on primary AF.

Upper bainite: A type of higher-temperature bainite where carbon is precipitated between laths.

Widmanstätten ferrite: A type of ferrite that nucleates epitaxially from allotriomorphic ferrite and grows via a shear mechanism. To avoid excessive shear of the surrounding austenite matrix, the ferrite grows in distinct lath pairs. Each individual lath cancels out the shear of the lath with which it is paired. There is no carbon diffusion during growth, but carbon is diffused out directly following transformation.

A_{c1}: the lowest temperature at which austenite begin to form upon heating

A_{r3}: when the first ferrite forms from austenite on cooling from a high temperature

List of Abbreviations

AF: Acicular Ferrite

B_s: Bainite start temperature

C: Carbon

CG HAZ: Coarse grained heat affected zone

EBS-D: Electron backscatter diffraction

FG HAZ: Fine grained heat affected zone

FS(A): Ferrite with aligned second phase

GBF: Grain boundary ferrite

HAZ: Heat affected zone

HSLA: High-strength low-alloy

IfR: Interferritic regions

IR HAZ: Intercritically reheated heat affected zone

M/A: Martensite with retained austenite

MDZ: Manganese depleted zone

Mn: Manganese

Mo: Molybdenum

M_s: Martensite start temperature

N: Nitrogen

Ni: Nickel

O: Oxygen

OES: Optical emission spectroscopy

P: Phosphorous

PAGB: Prior austenite grain boundary

PM: Parent metal

S: Sulphur

SEM: Scanning electron microscopy

Si: Silicon

TEM: Transmission electron microscope

Ti: Titanium

α: Alpha-ferrite

γ: Austenite

δ: Delta-ferrite

1. Introduction

1.1. Background

High-strength low-alloy (HSLA) steels are thermomechanically controlled steels, also referred to as microalloyed steels. These steels are not considered to be alloy steels owing to the fact that they are designed to meet mechanical properties rather than specific chemical composition limits. HSLA steels are defined as thermomechanically processed steels with a minimum yield strength of 275 Mpa (Vervynckt et al., 2012). They have a carbon content of between 0.05 mass% C and 0.25 mass% C that produces good formability and weldability. Mn content can be as high as 2 mass% and they may contain small amounts of chromium, copper, molybdenum (Mo), nitrogen (N), nickel (Ni), niobium, vanadium, titanium (Ti), and zirconium (Skobir, 2001).

The yield strength of more recently developed HSLA steels is much higher than the minimum requirement of 275 MPa, and the term now usually refers to steels with a yield strength above 550 MPa. HSLA steels that have a minimum yield strength of 550 MPa are referred to as HSLA-80 steels. They usually have a carbon (C) content of below 0.05 mass% C, with good weldability, formability, and toughness (Skobir, 2001).

Welding these steels can be problematic because, in order to meet yield strength requirements, the alloy content of the weld metal usually needs to be considerably higher than that of the base metal (Mathers, 2018). Higher alloying content, whilst beneficial for yield strength, often reduces the impact energy of the welds. This specific problem has led to a focus in research on the simultaneous increase in impact energy and strength of HSLA-steel weld metal. This line of research has become largely focused on increasing the amount of a microstructural component known as acicular ferrite (AF) (Dolby, 1980) AF is an intergranularly nucleated lath-like ferrite and the extent to which this phase is present in welds is often considered the most important factor for HLSA-steel weld metal toughness (Koseki and Thewlis, 2005; Babu, 2004).

A significant amount of research has been done to evaluate the influence of chemical composition on the impact energy of HSLA-80 steel's weld metal, mostly on single-pass welds (Beidokhti et al., 2009a, 2009b; Bhole et al., 2006; Ebden and Weatherly, 1983). This is problematic because industrial welding of HSLA-steel welds usually involves multi-pass welding. Kang *et al.* (2015) showed that reheating of weld metal during multi-pass welding of HSLA-steel welds may negatively affect the impact energy of the weld metal. Gubeljak (2003) showed that reheating associated with multi-pass welds can also lead to a hardness mismatch that negatively influences fracture toughness. Mohseni *et al.* (2012) showed how reheating associated with multi-pass welding can cause local brittle zones to form in parent metal. This mechanism may also become active in reheated weld metal.

It is imperative to study the effects of the chemical composition of weld metal on the mechanical properties of welds within a framework that takes the effects of reheating into account. Because multi-pass welding results in multiple thermal cycles – each of which produces a different microstructure that might have a different impact energy and hardness – it may be necessary to evaluate different weld heat-affected zone (HAZ) regions in isolation so that possible problematic microstructures may be detected.

The aim of this research was to investigate how (i) changes in chemical composition might affect the mechanical properties of HSLA-80-steel weld metal and (ii) how thermal cycling associated with multi-pass welding might further affect these properties.

1.1.1. As-deposited weld metal microstructure

Microstructural formation of weld metal begins with the precipitation of non-metallic inclusions as the result of a reaction between oxygen and deoxidizing elements such as manganese (Mn) sulfur (S), Ti, and Si. Examples of such inclusions include $MnSiO_3$, MnS, $MnTi_2O_4$ Mn-silicate, (Mn, Ti)-spinel oxide, MnS (Mn,Ti)-spinel oxide, and Mn-silicate (Seo et al., 2015). Inclusions can be of an amorphous of crystalline structure, but are usually coated in at least a thin layer of crystalline solid (Kang et al., 2016; Thewlis et al., 1997) These inclusions have diameters in the range of 0.1 to 1 μm at temperatures well above the liquidus temperature (Babu, 2004). These inclusions act as nucleation sites during solidification

In C steel weld metal, the first metallic phase that forms can be either delta ferrite (δ) or austenite (γ). This will depend on the chemical composition of the steel (Babu, 2004; Kadoi *et al.*, 2020). The addition of Ni to weld metal has also been shown to lead to a shift in solidification mode. Kadoi *et al.* (2020), for instance, showed that steels containing 0.015 mass % C, 0.05 mass % Si, and 0.05 mass % Mn, switched from pure δ-solidification to hypo-peritectic solidification with the addition of 4 mass % Ni; to hyper-peritectic solidification with the addition of 4.8 mass % Ni; and solidified completely as austenite with the addition of 10 mass % Ni. The Fe-Ni phase diagram shows that a shift to pure austenite solidification occurs at 4.6 mass% Ni. Given that the hyper-peritectic region is very small (Chen et al., 2007), it is likely that the shift to pure austenite for this composition would have occurred at levels of Ni much lower than 10 mass%, had these been tested. An increase in C ahs also been shown to promote a shift from δ-solidification to γ-solidification (Zhang, 2021). It is therefore reasonable to assume that the shift in solidification mode would occur at lower levels of Ni in steels that contain higher amounts of C.

Kadoi *et al.* (2020) also showed that a shift from pure δ-solidification to hypo-peritectic, then hyper-peritectic, and finally pure γ solidification was associated with an increase in the segregation of Ni, S, and phosphorus (P) in the quenched weld metal (see Figure 1). This effectively means that an increase in Ni content led to an increase in Ni segregation.

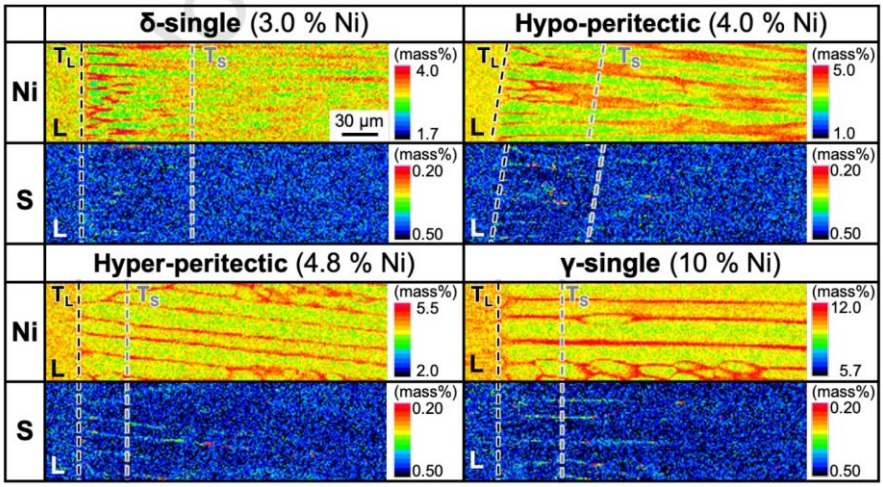

Figure 1: Solidification structure of welds at different quenching temperatures for varying Ni contents. The average C content was 0.015 mass%. Welds were quenched using liquid tin and thermocouples were inserted into the rear of the molten pool during welding. This created a temperature distribution in the quenched specimen (Kadoi et al., 2020). The figure shows that a shift away from δ-solidification towards γ-solidification increases the extent of segregation, with the largest difference occurring when the solidification became peritectic.

Mo additions have also been associated with an increase the segregation of both Mo and interstitial alloying elements. When Mo segregation occurs as a result of an increase in Mo concentration the Mo atoms segregate to austenite grain boundaries. Once here the presence of the Mo changes the free energy potential of the grain boundaries. This change in free energy affects diffusion of other elements to these grain boundaries (Hua et al., 2018; Takahashi et al., 2017). Mo segregation can occur during both solidification and solid-state transformation (Takahashi *et al.*, 2017).

Segregation associated with increases in both Ni and Mo concentrations at prior austenite grain boundaries (PAGBs) was reported by Yang *et al.* (2015) and Ebden and Weatherly (1983).

Whether initial solidification occurs as δ-ferrite or γ, all C-steel weld metals will eventually transform to γ. Nucleation of new grains and growth of stable γ grains will continue until the Ar_3 temperature is reached. The Ar_3 temperature is the temperature at which the austenite metal begins to revert back to ferrite upon cooling. Once the Ar_3 temperature is reached on cooling, allotriomorphic alpha (α) ferrite will nucleate at and grow from the austenite grain boundaries. Allotriomorphic ferrite is a type of ferrite that grows epitaxially from an austenite crystal into an adjacent austenite crystal. Allotriomorphic ferrite grows via a reconstructive mechanism and when it grows from austenite grain boundaries it is referred to as grain-boundary ferrite (GBF).

Owing to its epitaxial growth, GBF can form at higher temperatures where undercooling and therefore driving force is low. The high transformation temperatures also make the diffusion required for the reconstructive growth mechanism possible (Babu, 2004; Okaguchi et al., 1991; Rees and Bhadeshia, 1994; Ricks et al., 1982; Thewlis et al., 1997). A micrograph of GBF is shown in Figure 2.

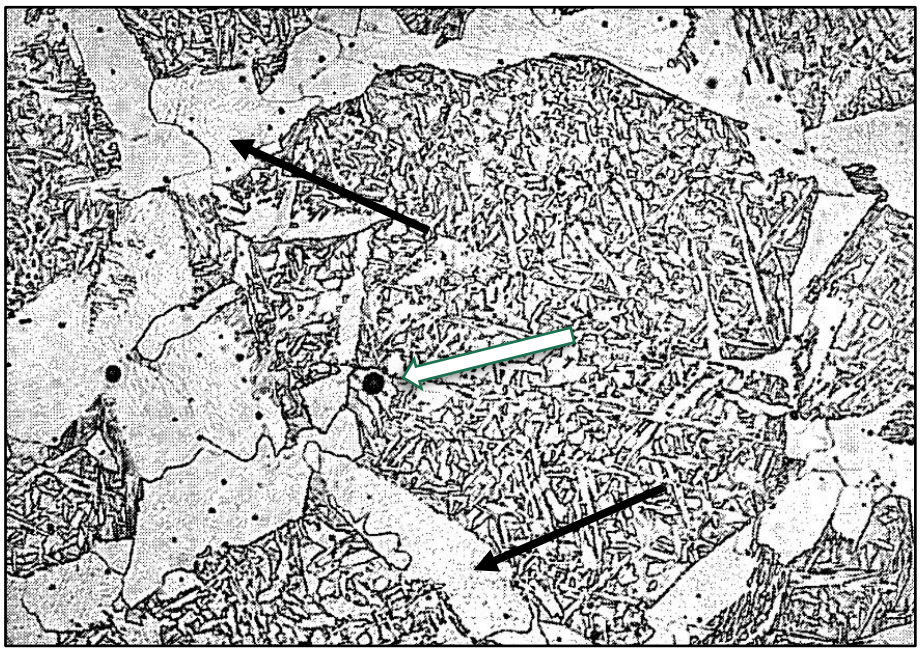

Figure 2: Micrograph of γ/γ-GBF (indicated by black arrows) and an inclusion nucleating ferrite (indicated by a white arrow). The micrograph was captured at 530× magnification (Thewlis et al., 1997).

At lower transformation temperatures, a second type of allotriomorphic ferrite begins to nucleate at and grow from inclusions. This type of ferrite nucleates and grows through the same mechanisms as conventional GBF (Thewlis et al., 1997). Figure 3 shows a micrograph of an inclusion nucleating such allotriomorphic ferrite.

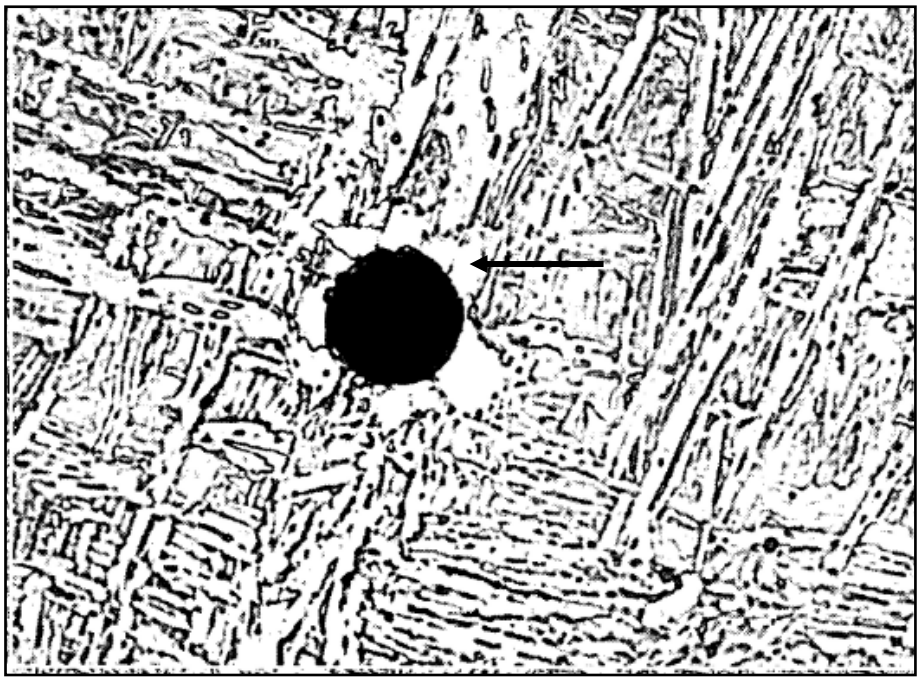

Figure 3: Inclusion surrounded by rosettes of ferrite (indicated by the black arrow). The low aspect ratio and non-uniform shape of the grains indicate growth by a reconstructive mechanism. The micrograph was taken at 1130× magnification (Thewlis et al., 1997).

When the temperature drops below the bainite start temperature (B_s), the displacive transformation mechanism becomes possible and the first lath-like structures begin to form. These structures are referred to as Widmanstätten ferrite. Widmanstätten ferrite is a type of ferrite that nucleates epitaxially from allotriomorphic ferrite, but grows via a shear mechanism (Thewlis et al., 1997). This type of ferrite forms at a temperature where undercooling should not be sufficiently low to allow for the activation energy required for a shear transformation. This problem is overcome via growth by a unique lath-pair mechanism. During growth, two laths grow next to each other and shear in opposite directions, thereby cancelling out the lattice strain that would have made shear growth impossible in the absence of such pairing (Bhadeshia, 1981). A schematic of the Widmanstätten ferrite growth is shown in Figure 4.

Owing to the high temperature of formation, Widmanstätten ferrite is relatively free to grow and undergo shape change through diffusional processes. Widmanstätten ferrite resultantly often loses its distinctive lath-like shape. Figure 5 presents a micrograph of Widmanstätten ferrite that nucleated and grew from GBF.

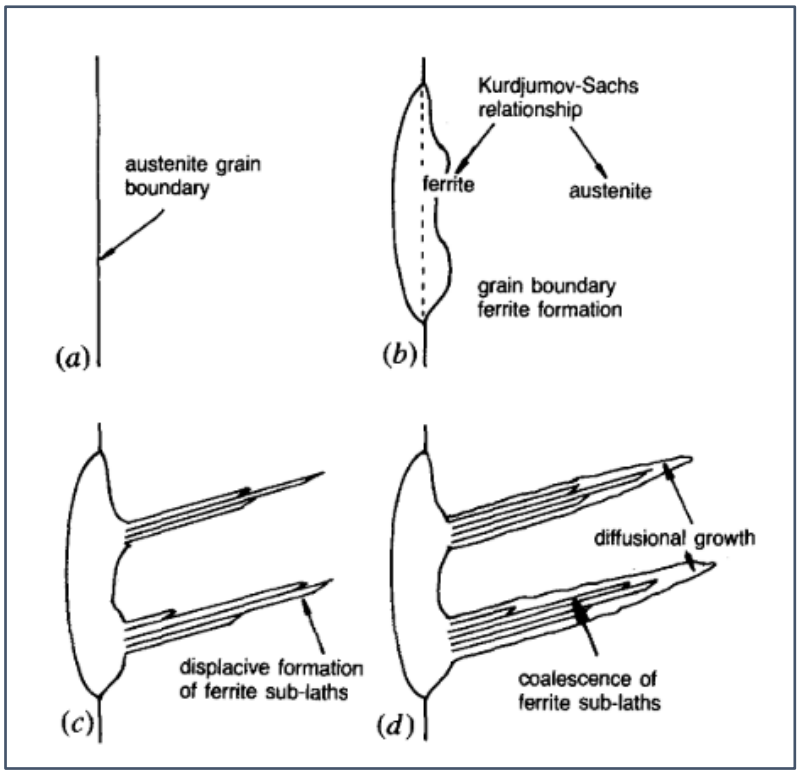

Figure 4: Schematic showing the nucleation and growth of Widmanstätten ferrite, showing a) austenite grain boundary, b) diffusion-controlled formation of GBF maintaining a Kurdjumov–Sachs relationship with the austenite, c) displacive growth of ferrite sub-laths that then coalesce in a diffusion-controlled manner (Ohmori et al., 1994).

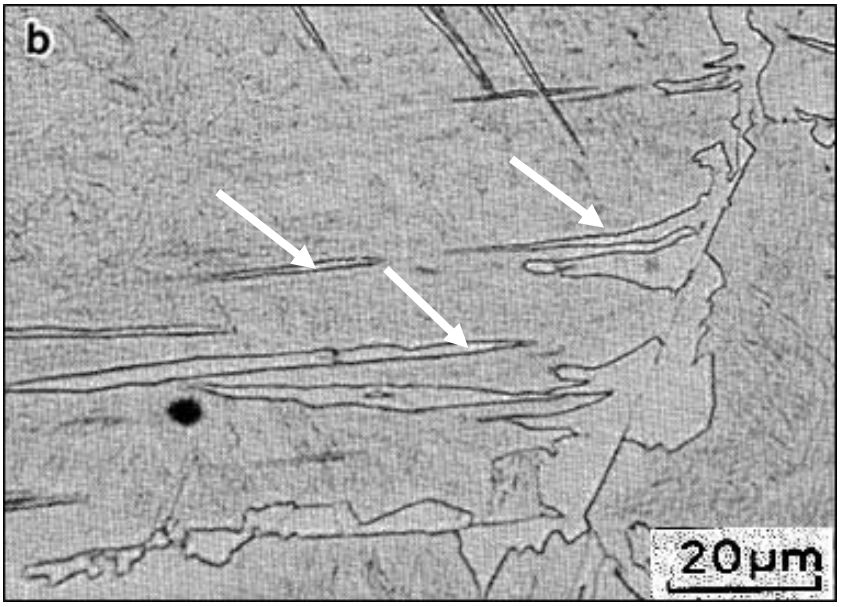

Figure 5: Widmanstätten ferrite (arrowed) that nucleated from allotriomorphic ferrite at prior austenite grain boundary (Okaguchi et al., 1991).

Widmanstätten ferrite usually nucleates and grows from GBF, but it can also nucleate from inclusion-nucleated allotriomorphic ferrite. The shear growth mechanism through which Widmanstätten ferrite grows requires a certain orientation relationship to the austenite into which it grows. When Widmanstätten ferrite grows from GBF, this orientation relationship is ensured because the GBF

would have needed to form from an austenite grain with which it had a specific orientation relationship. However, such a relationship is not ensured when Widmanstätten ferrite grows from inclusion-nucleated allotriomorphic ferrite. Nucleation of this phase from GBF is therefore more likely than from inclusion-nucleated allotriomorphic ferrite (Bhadeshia, 2001). Figure 6 shows Widmanstätten ferrite growing from inclusion-nucleated allotriomorphic ferrite. When Widmanstätten ferrite grows in this way it is referred to as acicular ferrite (AF).

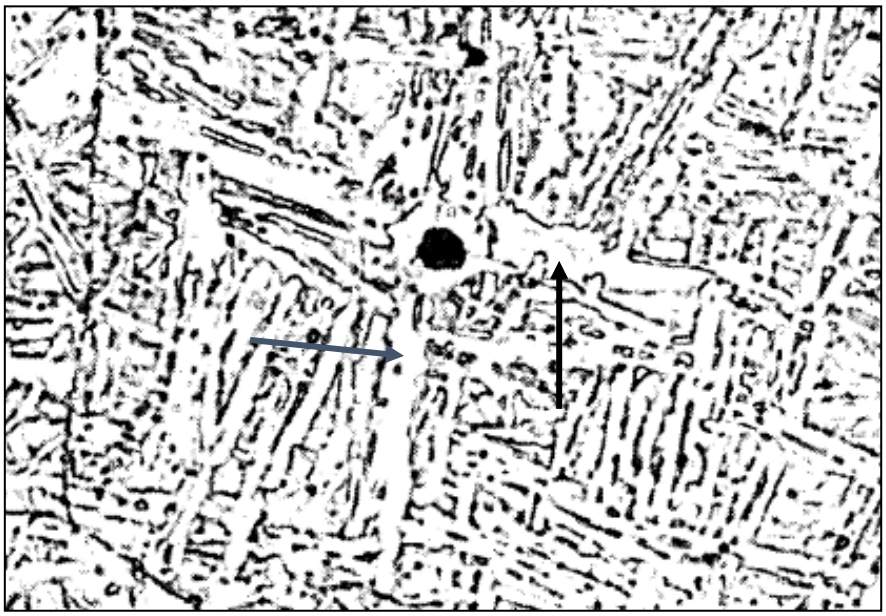

Figure 6: Inclusion surrounded by ferrite rosettes, with ferrite growing in a displacive manner from rosettes. The micrograph was taken at 1130× magnification (Thewlis et al., 1997).

The next lath-like structure which begins to form is bainite. Bainite is a type of ferrite that nucleates directly on a non-ferritic interface and grows via a shear mechanism. Owing to the free energy required for nucleation at non-ferrite interfaces, it forms at temperatures that can accommodate the activation energy required for the shear transformation. It is therefore not necessary for bainite laths to grow in pairs as Widmanstätten ferrite does. This means that the sheaths are generally thinner than those associated with Widmanstätten ferrite (Thewlis et al., 1997).

Both Widmanstätten ferrite and bainite are known to grow without C diffusion, but, in both cases, C diffuses out of the lath directly following the transformation. When Widmanstätten ferrite or upper bainite forms (at higher temperatures), C diffuses all the way to the edge of the lath, where it enriches and eventually saturates the surrounding austenite. Eventually this C precipitates out as carbides or is captured with martensite during the final part of transformation. This is discussed in more detail in Section 1.1.2. The extent to which this diffusion occurs is dependent on temperature. Lower bainite nucleates and grows at lower temperatures. In lower bainite, the C cannot diffuse all the way to the edges of laths, but precipitates inside the laths as carbides (Bhadeshia, 2001). Bainite can nucleate either at γ/γ-grain boundaries or at boundaries between inclusions and an γ grain. Bainite that nucleates at inclusion/γ grain boundaries is also referred to as acicular ferrite (Bhadeshia, 2001).

Factors affecting the balance of both Widmanstätten ferrite and bainite nucleation on inclusions are discussed in more detail in Section 1.1.3, but in general it is accepted that the extent of bainite nucleation on γ/γ grain boundaries, as opposed to inclusions, depends on the number of γ/γ grain boundaries available for this transformation. The number of available γ/γ grain boundaries depends on the total number of austenite grain boundaries and the number of grain boundaries that have not

been populated by allotriomorphic ferrite. The total number of grain boundaries is a function of austenite grain size (Babu and Bhadeshia, 1990).

A micrograph of weld metal that contains both bainite and AF is shown in Figure 7. It is noted that the bainite laths are much longer, but also thinner than the AF laths. The increased thickness and irregular shape of the AF indicates that the grains formed at higher temperatures than the bainite, and likely means that they formed via the Widmanstätten mechanism on inclusion-nucleated allotriomorphic ferrite.

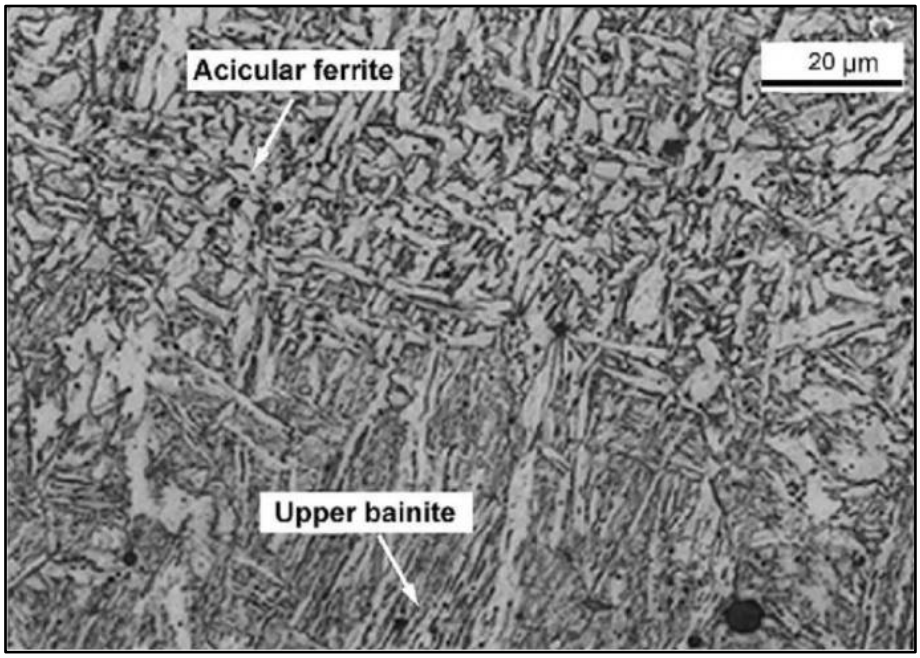

Figure 7: Micrograph showing appearance of upper bainite in a weld metal. The micrograph also shows acicular ferrite (Vezzu et al., 2019).

It is not usually possible to optically discern whether a grain boundary-nucleated lath-like ferrite is Widmanstätten ferrite or bainite. This becomes especially true when the austenite grains and lath-like ferrite grains are also very fine. The term ferrite with second phase aligned (FS(A)) is therefore often used to describe these phases. An example of a region of ferrite laths that would be classified as FS(A) is shown in Figure 8.

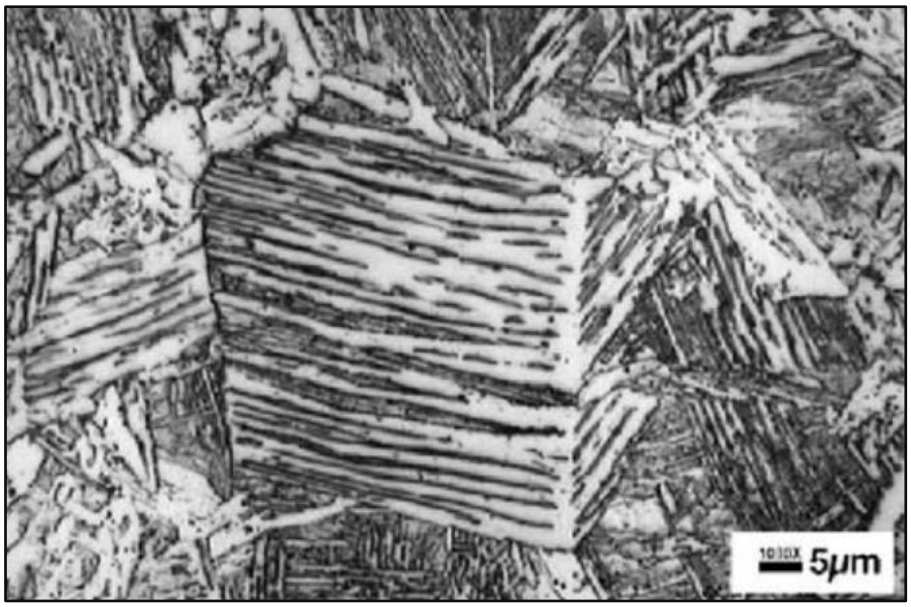

Figure 8: Ferrite with second phase aligned (Byun et al., 2003).

Widmanstätten ferrite and bainite continue to grow from grain boundaries and inclusions as the temperature decreases. Secondary AF will eventually nucleate on primary AF laths. Primary AF is defined as ferritic laths that nucleate on non-metallic inclusions (Babu, 2004; Babu and Bhadeshia, 1990; Kim et al., 2011; Koseki et al., 1997; Koseki and Thewlis, 2005; Rees and Bhadeshia, 1994; Ricks et al., 1982; Thewlis et al., 1997) Secondary AF is AF that nucleates on pre-existing AF, rather than on inclusions. It is likely that this secondary nucleation is largely responsible for the fine interlocking structure of AF (Ricks et al., 1982). Growth and nucleation of both primary and secondary AF will continue until the remaining austenite is too enriched in C for further nucleation or growth to occur. The remaining austenite regions will then transform to interferritic regions (IfRs). The term IfRs refers to regions found in-between AF grains. These regions are high in C due to C rejected from AF and comprise of a mixture of Widmanstätten ferrite, bainite, and martensite with retained austenite (M/A). Carbides are expected to precipitate primarily in this area. The morphology of AF and the tendency for secondary AF or IfRs to form depends on whether the AF nucleated via the Widmanstätten ferrite mechanism or via a true bainite reaction. This is discussed in Section 1.1.2.

1.1.2. Acicular ferrite and interferritic regions

AF is a type of intergranularly nucleated ferrite that grows via a shear mechanism, as was discussed in Section 1.1.1. Although AF is usually described as intergranularly nucleated bainite (Babu and Bhadeshia, 1990), it was shown in Section 1.1.1 that AF can also form and grow via the Widmanstätten mechanism (Thewlis et al., 1997). The AF within a single weld is likely to nucleate as a balance of both mechanisms and a shift in general morphology of AF is likely to be gradual.

The mechanism of primary AF nucleation will not affect the AF in all respects. Both Widmanstätten AF and bainitic AF have high misorientation angles (Lan *et al.*, 2016; Kim *et al.*, 2011) and a small grain size (typically, in the order of 5 μm) (Ricks et al., 1982). However, the nucleation and growth mechanism will affect other characteristics. One such factor is the AF aspect ratio. In the literature, this ratio of AF is reported to range from as low as 3:1 to as high as 11:1 (Farrar and Zhang, 1995). It is likely that low aspect ratios are associated with Widmanstätten AF and higher aspect ratios are associated with bainitic AF (Sugden and Bhadeshia, 1989; Thewlis et al., 1997).

The other factors that are strongly influenced by the type of primary AF nucleation are the extent of secondary AF nucleation and morphology of the IfRs. A schematic of an intergranular region consisting mostly of Widmanstätten acicular ferrite is shown in Figure 9. The schematic shows AF growing from inclusion-nucleated allotriomorphic ferrite. Secondary AF nucleation in this kind of microstructure appears to be limited to the tip of the AF grain, because intergranular regions offer neither sufficient surface area nor low enough C content for the nucleation and growth of ferrite grains. AF grains infringe on one another's growth and limit the grain size. Increased nucleation rate results in a finer grain structure.

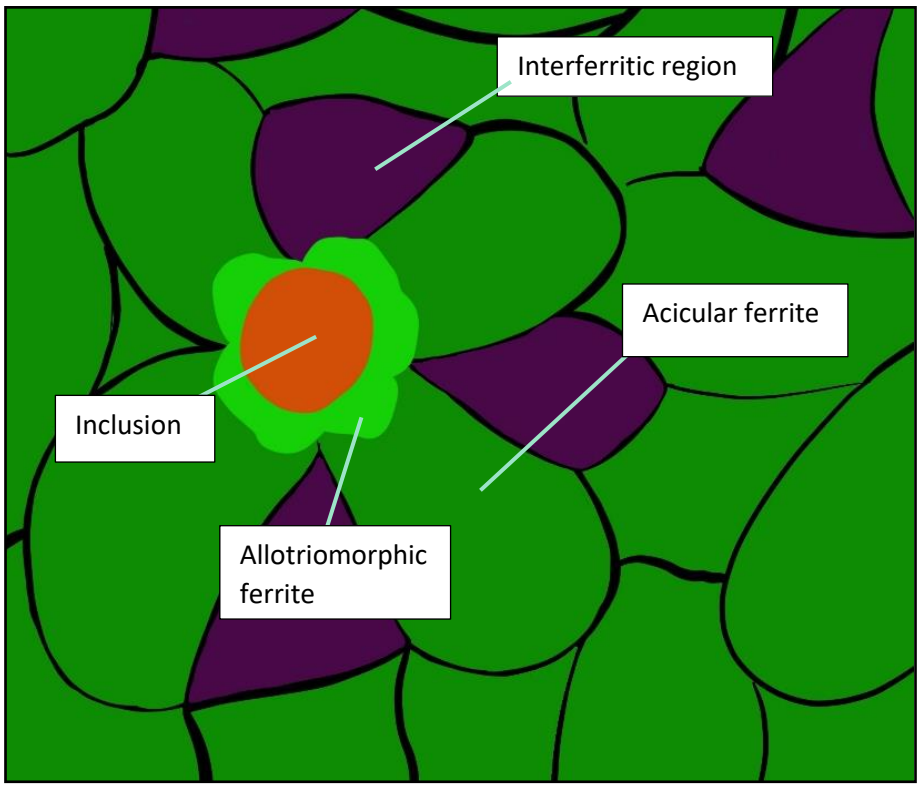

Figure 9: Schematic of Widmanstätten acicular ferrite. An inclusion is shown, surrounded by diffusion-nucleated allotriomorphic ferrite from which the Widmanstätten side plates that eventually grow into acicular ferrite nucleate. Regions of interferritic regions are also shown; these form during the final stages of cooling when the carbon concentration of intergranular regions becomes too high to allow for nucleation of the ferrite. This figure is from the current research.

A schematic of bainitic AF is shown in Figure 10. During bainitic AF growth, the region directly adjacent to the lath does not become as highly enriched in C as is the case with Widmanstätten sheaths. This is because suppressed temperature does not allow for significant diffusion of C. Suppressed C enrichment of surrounding austenite, paired with an elongated surface area, promotes the nucleation of secondary AF perpendicular to the direction of primary lath growth. This mechanism of growth means that the austenite around the AF laths does not become as enriched in C, as is the case with Widmanstätten AF. The remaining austenite will transform to IfRs, but these will be much smaller and not as likely to form hard martensite. Growth of grains in the tangential direction (perpendicular to the surface area of the inclusion) is usually halted by other grains, rather than by C enrichment (Bhadeshia, 2001; Srinivasan and Wayman, 1968).

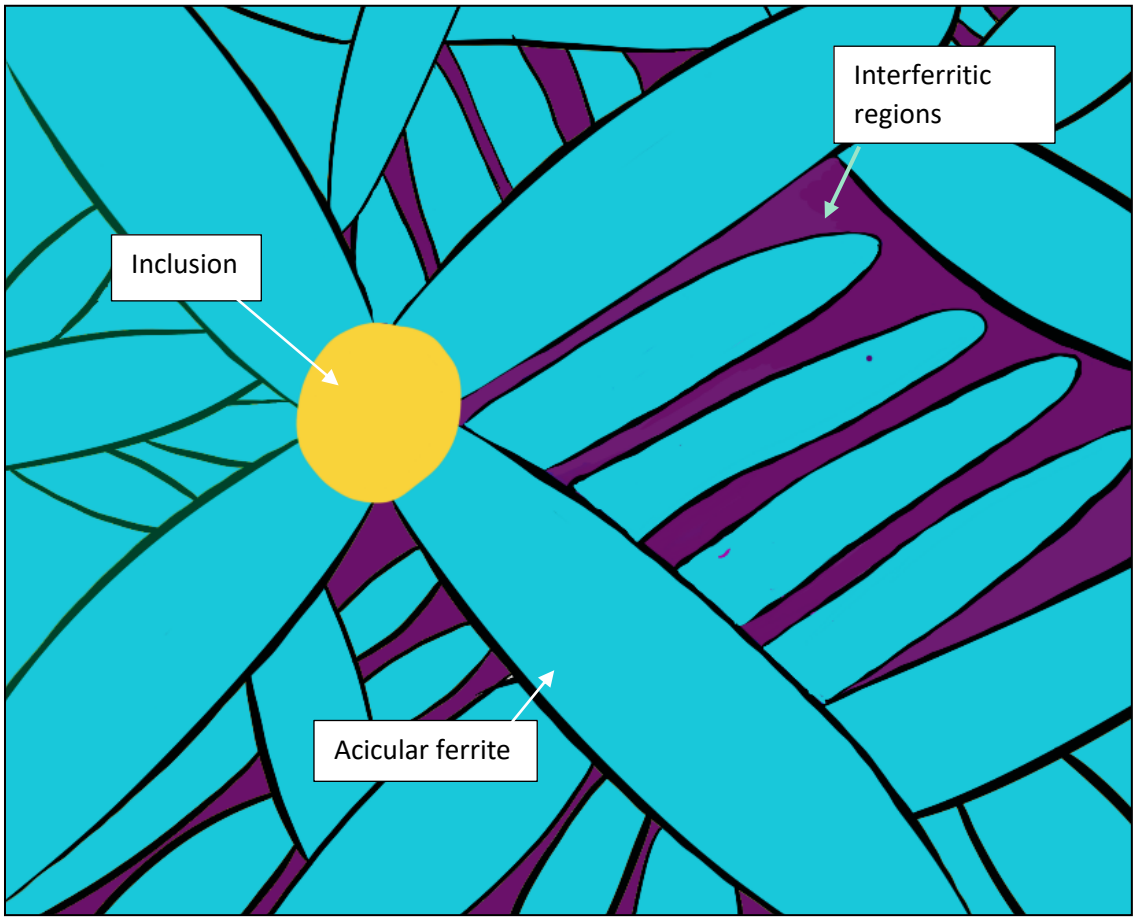

Figure 10: Schematic of bainitic acicular ferrite. An inclusion from which acicular ferrite nucleates directly is shown. This ferrite is considered bainitic because it grows directly from the inclusion rather than from allotriomorphic ferrite. The longer laths and reduced AF allow for the nucleation of secondary AF on the sides of the bainitic AF laths. Small interferritic regions form between the secondary AF laths. This figure is from the current research.

When the temperature falls too low for the continued growth of ferrite laths, the IfRs transform to a cluster of various types of ferrites and martensite with retained austenite (M/A). The exact composition of these regions can be quite diverse, but they always appear to contain some M/A islands. The types of ferrite observed include Widmanstätten ferrite, upper and lower bainite, and martensite (You et al., 2013).

An electron-backscattered diffraction (EBSD) image of an IfR that was found close to an austenite grain boundary is shown in Figure 11. The large grains within the blocky M/A region are believed to be either Widmanstätten ferrite or upper bainite and the congregations of very small grains (labelled Region II) are believed to be lower bainite or martensite or, most likely, combinations of both (You et al., 2013).

Figure 11: EBSD image of an interferritic region (You et al., 2013). Retained austenite refers to austenite that remains as such after solidification. Reverted austenite refers to austenite that underwent a transformation upon cooling. The sample is from a low-carbon HSLA steel that was reheated to simulate the HAZ region of a multipass weld.

1.1.3. Coalesced bainite

Coalesced bainite is a type of bainite that forms along PAGBs in cases where the transformation temperature of bainite is close to the martensite start temperature (M_s). It consists of fine bainite platelets that are identically orientated and can coalesce into a larger subunit (Bhadeshia et al., 2006).

The coalescence starts at the prior austenite grain boundary, and sub-units grow from there. Any factors that reduce C mobility increase bainite coalescence. This is because C precipitation in the interlath regions prevents lath coalescence and low C mobility prevents C precipitation. Scanning electron micrographs of coalesced bainite are shown in Figure 12.

The appearance of coalesced bainite is associated with a dramatic decrease in the toughness of welds and with elevated levels of both Ni and Mn. Coalesced bainite was detected at Mn levels of 2.1 mass % and Ni levels of 2 % in welds that contained about 0.01 mass % C (Bhadeshia et al., 2006).

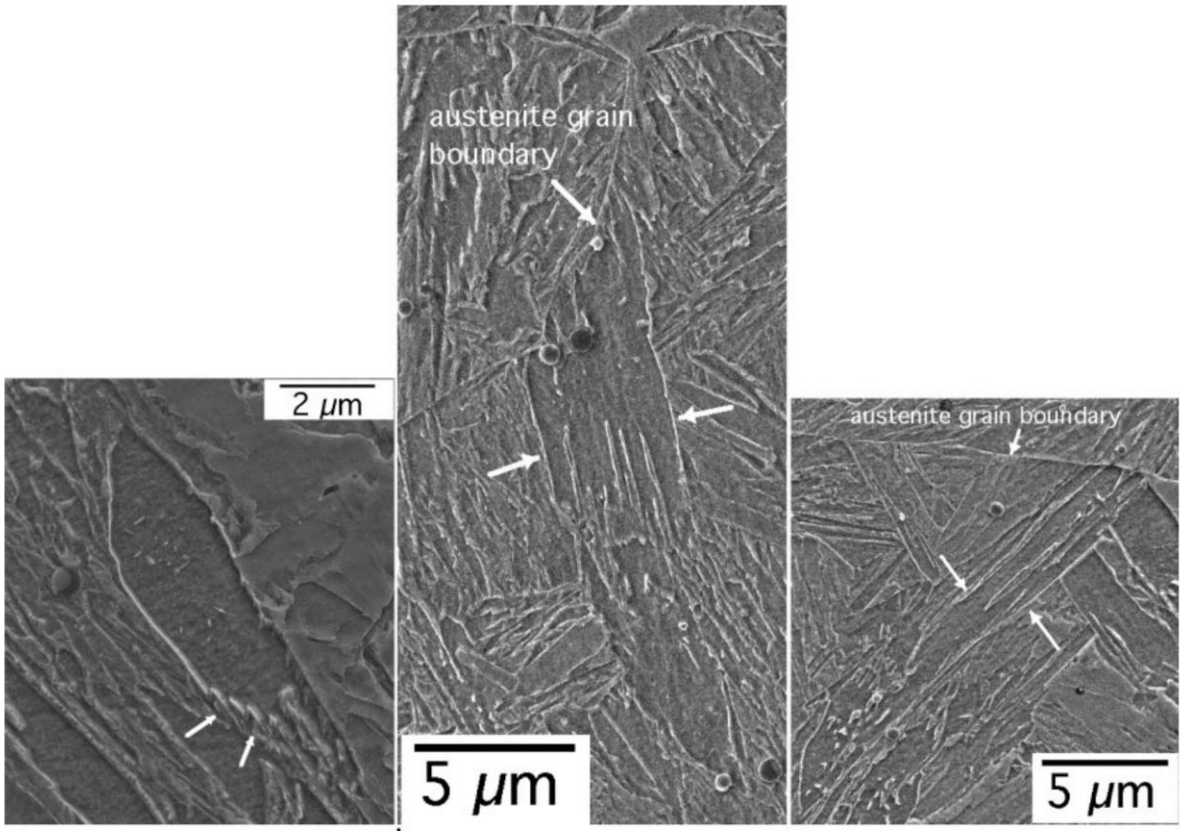

Figure 12: SEM micrographs of coalesced bainite at and near PAGBs (Pak et al., 2008).

1.1.4. Inclusions as acicular ferrite nucleation sites

Non-metallic inclusions are the first solids to form as molten weld metal cools down from the very high temperatures near the arc. Non-metallic inclusions are a result of the deoxidation reactions and can be thought of as slag that has not drifted to the surface of the weld (Dowling, Corbett, and Kerr, 1986).

These inclusions are usually layered because they form across a broad range of temperatures and the thermodynamic stability of phases shifts during cooling (Kang et al., 2016). The chemical composition of each layer of the inclusion is therefore a result of liquid composition and the cooling rate while the weld is still liquid. Once metal has solidified, inclusions will continue to transform; this transformation will be a function of the composition of the surrounding metal matrix. The compositional range of these inclusions is very broad, but they are mainly composed of aluminium (Al), Ti, Mn, silicon (Si), and some combination of oxygen (O) or sulfur (S) (Bhatti et al., 1984; Dowling et al., 1986) Inclusions can be glassy or have an ordered crystalline structure (Koseki and Thewlis, 2005). Inclusions may act as nucleation sites for AF, as stated in Sections 1.1.1 and 1.1.2 (Koseki and Thewlis, 2005; (Bhatti et al., 1984; Dowling et al., 1986).

Four mechanisms have been identified whereby inclusions act as nucleation sites. These mechanisms are complex and depend on many factors, including instantaneous temperature, inclusion geometry, and chemical composition of inclusions. It is usually assumed that one or more of the following nucleation mechanisms are involved in the nucleation of AF:

- Geometric effects;
- Localised stress;
- Crystallographic matching;
- Changes to chemical composition in the surrounding metal matrix.

Geometric effect

The geometric effect of an inclusion refers to the ability of the inclusion to aid nucleation merely by acting as an inert substance with a specific shape, size, and interface energy. The inclusion/γ interface reduces the requisite activation energy required to create an α/γ interface. Inclusions will therefore always be preferred nucleation sites, even if they are considered to be inert substances. The degree to which they increase nucleation potential is a function of their shape, size, and interface energy. This disregards the effect they may have on the surrounding matrix (Lan et al., 2016; Ricks et al., 1982)

The nucleation probability of an inclusion is the probability that a specific inclusion will act as a nucleation site. The nucleation probability of an inclusion will increase as its diameter increases (Babu, 2004), although there will always be a critical point where the beneficial effects of increased surface area are no longer balanced by the increased interfacial energy per unit area (Bott and Rios, 1998). Figure 13 shows a plot of nucleation probability as a function of inclusion size. The image shows that the nucleation probability of inclusions peak at a certain size (Kang et al., 2016). Although there are almost certainly no cases where the geometric effect is the only active mechanism, it is found throughout all inclusion types and weld chemistries.

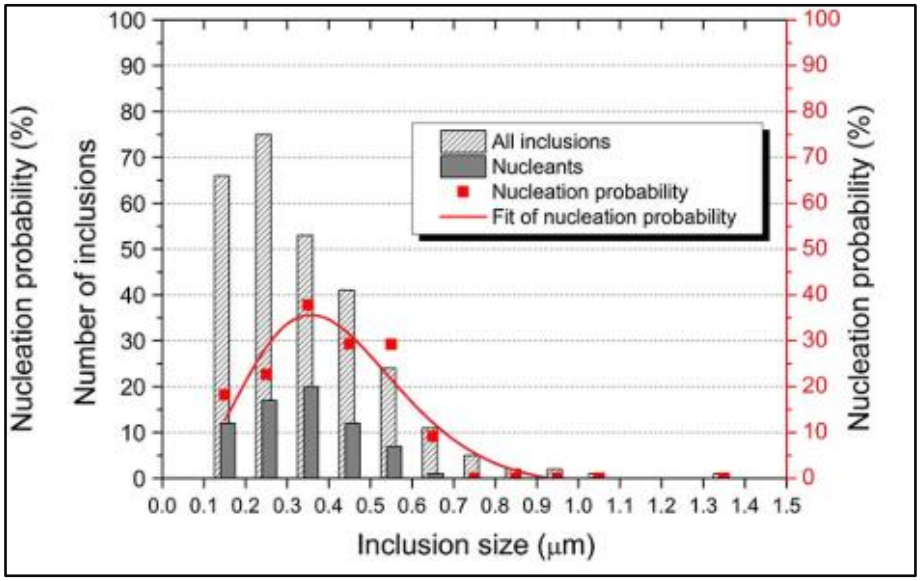

Figure 13: Bar graph showing the number of inclusions of a certain size compared with the number of inclusions of that size that acted as nucleation sites. Superimposed on this is a scatter plot of nucleation probability of each inclusion size (Kang *et al.*, 2016).

Localised stress

The second factor usually considered when discussing the ability of inclusions to nucleate AF is their ability to induce a local stress in the surrounding matrix (Koseki and Thewlis, 2005). Stress fields are created in and around non-metallic inclusions as a result of a differential thermal contraction between the inclusion and the surrounding matrix. The stress produced by this thermal strain is given by Equation 1

$$\sigma = \varphi[(\alpha_m - \alpha_i)\Delta T]$$

Equation 1

Where α_m and α_i are the thermal expansion coefficient of the matrix and inclusion respectively. ΔT is the temperature change and φ is a factor combining the effects of elastic properties as well as, inclusion shape, size, and distribution.

If $\alpha_m > \alpha_i$ then the matrix will contract more than the inclusion and it will be subjected to a triaxial pressure after cooling. Inversely if $\alpha_m < \alpha_i$ the inclusion will contract more than the surrounding matrix and will be under a triaxial tensile stress after cooling (Tweed and Knott, 1987). Strain resulting from elastic stress in the austenite matrix favours the displacive AF transformation. Strain is beneficial for a shear transformation because it contributes to the strain required for the transformation by positioning atoms in a more energetically favourable position (Babu and Bhadeshia, 1992; Dallam and Olson, 1989). Crystallographic matching

The third way in which inclusions aid in AF formation is by good lattice matching between the inclusions and the nucleating ferrite grain. The literature indicates that crystallographic matching strongly aids AF nucleation at inclusions (Koseki and Thewlis, 2005; Ricks et al., 1982). Crystallographic matching can occur only for crystalline inclusions: this explains why glassy inclusions are usually poor nucleation sites (Seo et al., 2019b). Kang *et al.* (2016) showed that AF strictly adopted a Kurdjumov–Sachs relationship with the austenite into which it grows, within a deviation of 5°. This relationship was maintained regardless of transformation characteristics. These results strongly indicate that crystallographic matching could very well be a significant factor in the ability of an inclusion to nucleate AF. The authors also showed that the ferrite and inclusions adopted a Baker–Nutting relationship with $MnTi_2O_4$ inclusions. Other researchers have also shown that this orientation relationship is possible (Okazaki et al., 2012). It was later observed by Nako *et al.* (2014).

For AF to maintain an orientation relationship with both the inclusion and austenite, it is essential that it undergoes a rotation of 5.3° by ferrite during growth. Such rotation would likely be diffusion-controlled and would likely be suppressed as transformation temperatures decreased (Kang *et al*., 2016.).

Altering of surrounding chemical composition

The last mechanism through which inclusions have been shown to aid AF nucleation is by altering the chemical composition of the surrounding matrix. Austenite-forming or stabilizing elements, such as C, Mn, and Si, may be absorbed by the inclusion and resultantly deplete the surrounding matrix of these elements (Koseki and Thewlis, 2005; Ricks et al., 1982)

The depletion of γ-stabilising elements from the matrix results in an increase in the α transformation temperature. This increase drives the γ → α transformation. The most studied elemental depletion is that of manganese (Mn); areas where Mn is depleted are referred to as manganese-depleted zones (MDZ). These zones were detected adjacent to inclusions in weld metal by both Kang *et al.* (2015) and Kang *et al.* (2016). Mn depletion would promote the γ → α transformation; therefore, MDZs are likely to promote AF by the Widmanstätten nucleation mechanism much more strongly than by the bainite transformation. Graphs showing the Mn concentration as a function of distance that was used to confirm the presence of these regions are shown in Figure 14. Similar carbon-depleted regions were detected by Beidokhti, Kokabi, and Dolati (2014). Table 1 shows the nominal compositions of the welds studied by Kang *et al.* (2015) and Kang *et al.* (2016).

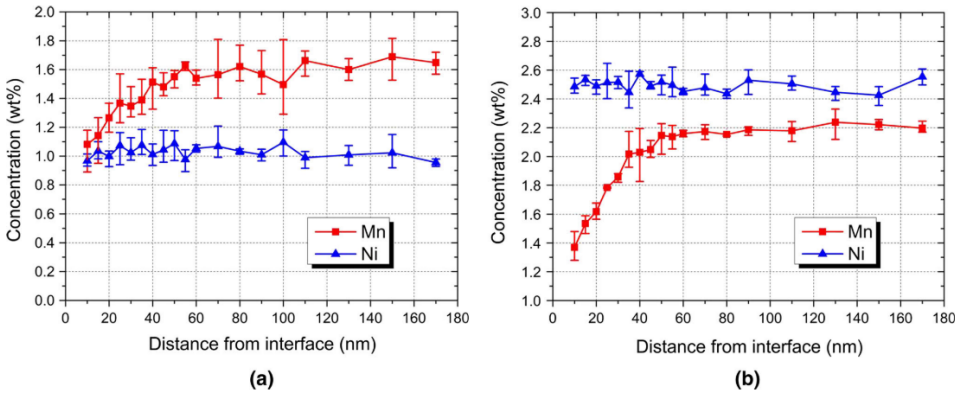

Figure 14: Mn and Ni concentration profiles in the metallic substrate adjacent to a $MnTi_2O_4$ inclusion in a) weld L and b) weld H from Kang *et al*. (2016). Weld L contained 1.6 % Mn and weld H contained 2.1 % Mn.

Table 1: Nominal compositions of welds studied by Kang *et al*. (2015) and Kang *et al*. (2016)

	C	Mn	Ni	Cr	Mo	Ti	[Al]/[O]
Weld L	0.07	2.1	2.4	0.5	1.0	0.04	0.65
Weld H	0.06	1.6	2.8	0.3	0.9	0.07	0.59

Temperature

In addition to the four mechanisms listed above, temperature also affects the nucleation potential of an inclusion. An increase in undercooling, and resultantly the driving force for the transformation, will cause nucleation potentials of all inclusions to increase. As temperature decreases, the mechanisms responsible for nucleation may shift as different $\gamma \rightarrow \alpha$ transformations become active.

The influence of temperature on the effect of the matrix strain mechanism is a good example of this. At higher temperatures, where nucleation is diffusion-controlled, matrix strain does not play a large role. As the temperature decreases, shear nucleation will become more dominant and the effects of matrix strain on nucleation may begin to have a more prominent effect on the nucleation probability of inclusions. In addition, the decrease in temperature will also increase the matrix strain, increasing the dominance of this mechanism even further.

1.1.5. Fracture of HSLA-steel weld metal

Crack initiation

Crack initiation of HSLA-steel weld metal usually occurs at either inclusions or M/A islands. When initiation occurs at an inclusion, it can be a result of either microcrack formation at the inclusion/matrix interface or the inclusion cracking and the crack propagating into the matrix.

Inclusions that nucleate cracks by microcrack formation do so through a mechanism known as microvoid coalescence resulting from the large strain differential between the hard inclusion and the softer surrounding matrix that occurs during loading. (Tweed and Knott, 1987). Elastic misfit strain, resulting from the differential in thermal contraction during cooling will affect the microvoid coalescence mechanism. MnS inclusions usually contract more than the surrounding matrix during cooling (Torkamani et al., 2017) and are therefore likely surrounded by microvoids even prior to the application of external stress. This would promote the likelihood of such inclusions acting as crack initiation sites through microcrack formation. In contrast, oxide inclusions are usually surrounded by a compressive stress which must be overcome for void formation and coalescence to occur as a result of the application of external stress.

Cracks that initiate at the inclusion/matrix interface tend to be ductile in fashion, characterised by a fracture surface dominated by dimples. The dimples will often still contain the inclusions that nucleated the cracks (Ebden and Weatherly, 1983; Kang et al., 2015). Such a fracture surface is shown in Figure 15. Kim *et al.* (1991) suggested that M/A particles would initiate cracks in a similar fashion. Lambert-Perlade *et al.* (2004) detected M/A initiated dimples, shown in Figure 16.

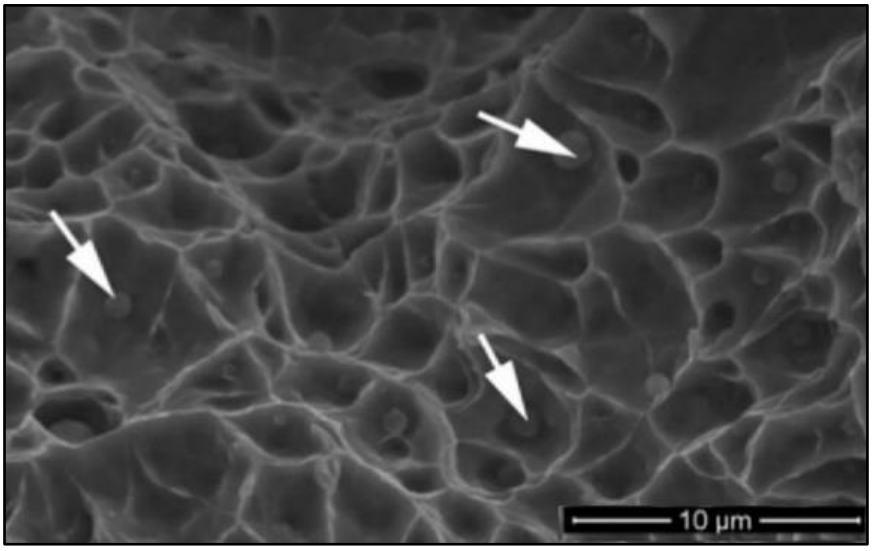

Figure 15: Dimple fracture in an AF weld metal (Lan et al., 2016).

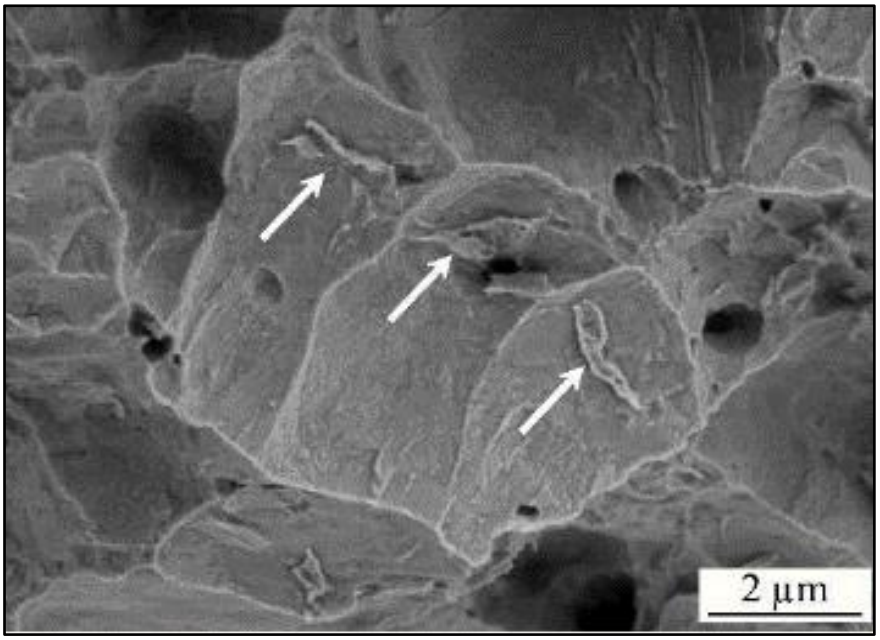

Figure 16: M/A particles initiating microvoids (Lambert-Perlade et al., 2004a).

When inclusions initiate fracture owing to the inclusion itself cracking and propagating into the matrix, these cracks are more likely to propagate in a brittle manner. Fairchild et al. (2000) showed an association between the occurrence of TiN particles and a marked reduction in toughness. Fairchild et al. (2000) went on to show that these TiN particles initiated fracture by crack growth from fractured particles. M/A particles have also been shown to initiate brittle fracture (Davis and King, 1994; Lambert-Perlade et al., 2004b) (Figure 17 and Figure 18), but actually appear more likely to initiate fracture via a ductile mechanism, as discussed earlier in this section. Lambert-Perlade *et al.*

(2004) showed that the degree to which M/A islands were detrimental was strongly dependent on the nature of the particles, as well as fracture conditions. M/A islands resulted in lower toughness only when they consisted mostly of martensite or when low temperatures or high degrees of strain resulted in the transformation of retained austenite to martensite.

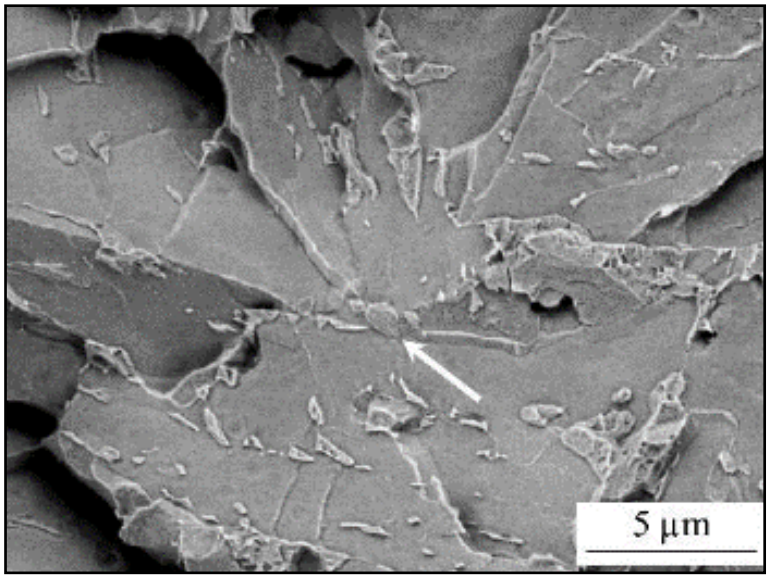

Figure 17: Blocky martensite initiating a cleavage crack (Lambert-Perlade et al., 2004a).

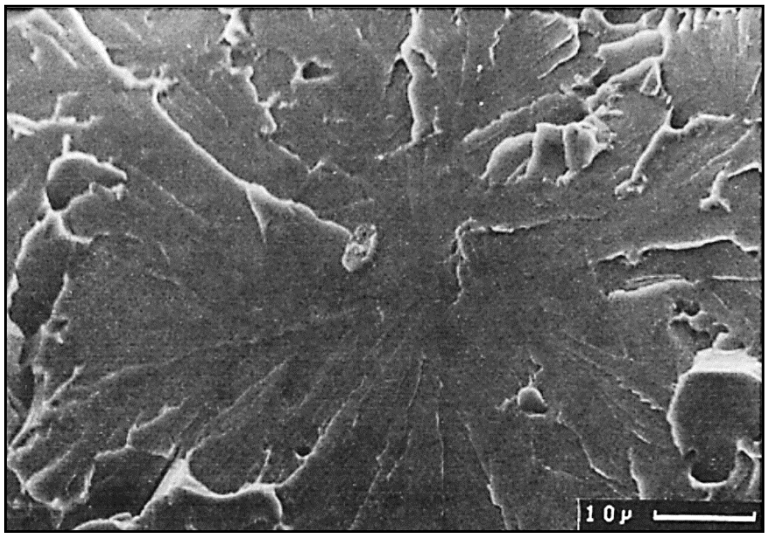

Figure 18: M/A island initiating a brittle fracture (Davis and King, 1994)

Crack growth

A scatter plot showing the relationship between ultimate tensile strength and grain size is shown in Figure 19. Although the manner of crack propagation appears to be related to the mechanism of crack initiation, it is more likely that the extent to which fracture is ductile or brittle will be affected by the inherent fracture toughness of the weld in question. This, in turn, will be a function of inherent matrix properties and grain size. Even if, for example, an inclusion initiates a brittle fracture, a small grain size will inhibit such fracture from propagating (Curry and Knott, 1976).

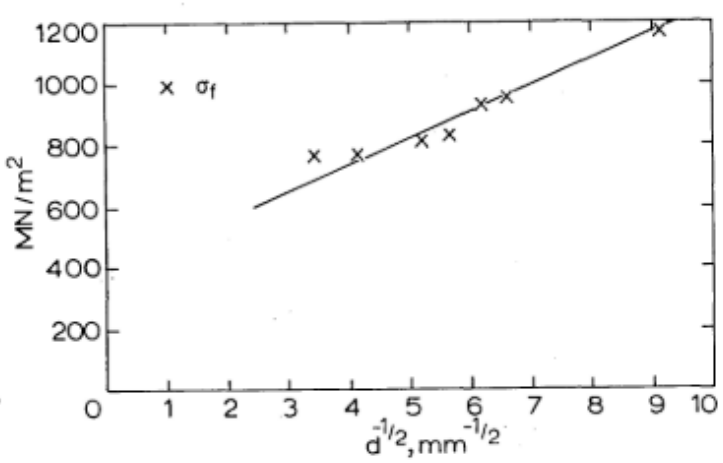

Figure 19: Scatter plot showing the relationship between grain size and ultimate tensile strength in mild steel (Curry and Knott, 1976). The figure shows an increase in fracture strength as the grain size of the steel decreases.

The positive effect that small grain size has on strength is most often expressed by the Hall–Petch equation, shown in Equation 2 (Callister and Rethwisch, 1940):

$$\sigma_y = \sigma_0 + kd^{-0.5}.$$

Equation 2

It would therefore be reasonable to state that the absence of brittle crack initiators will positively influence the impact energy of weld metal. However, the presence of brittle crack initiators will not necessarily lead to the propagation of a brittle crack. If the matrix and strain conditions are not amenable to the propagation of a brittle fracture, then the presence of a crack initiating at an inclusion will not necessarily be detrimental to the impact energy of a weld. It is therefore expected that the general microstructure of the steel, rather than the nature of the inclusions, is likely to be the predominant factor in determining the nature of failure.

HSLA-steel welds usually fracture in a brittle manner along allotriomorphic GBF. Fracture along the regions of AF across PAGBs is then usually reported to occur in a ductile fashion (Tweed and Knott, 1987). An example of brittle fracture along GBF is shown in Figure 20 and an example of ductile fracture across a prior austenite grain is shown in Figure 21.

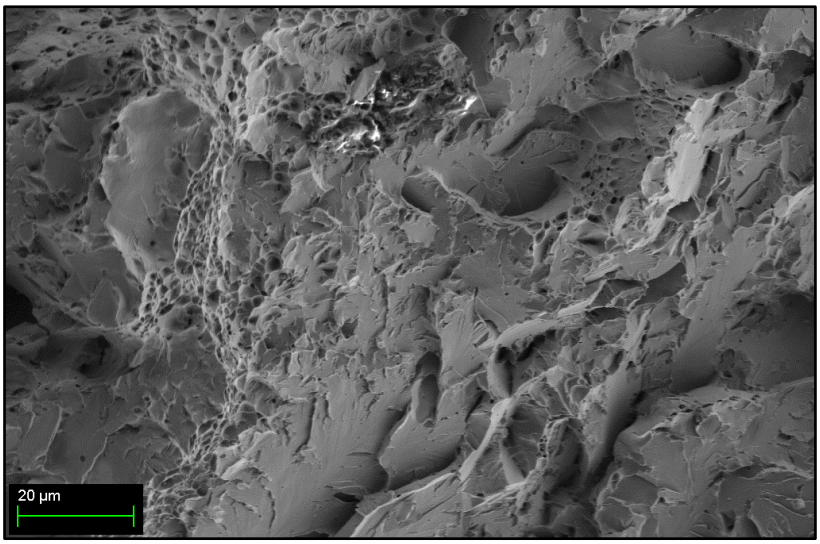

Figure 20: Fracture surface from current study showing brittle fracture along PAGB and ductile fracture across the regions that contained AF. Image taken from current study.

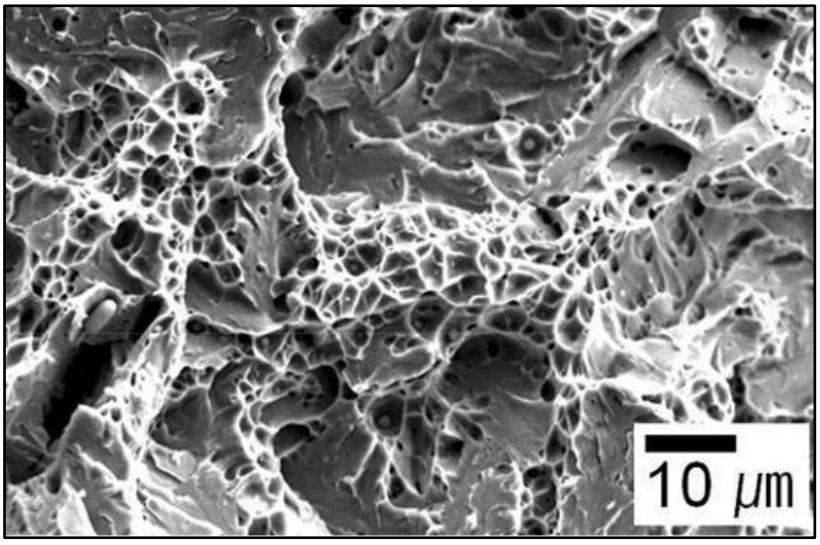

Figure 21: Micrograph of fracture across a prior austenite grain containing primarily AF (Kang et al., 2015). The micrograph shows a primarily ductile fracture mechanism characterised by dimples.

In cases where the intergranular region is predominantly composed of a bainitic ferrite, the fracture across the prior austenite grain will also be brittle. An example of such a fracture surface is shown in Figure 22.

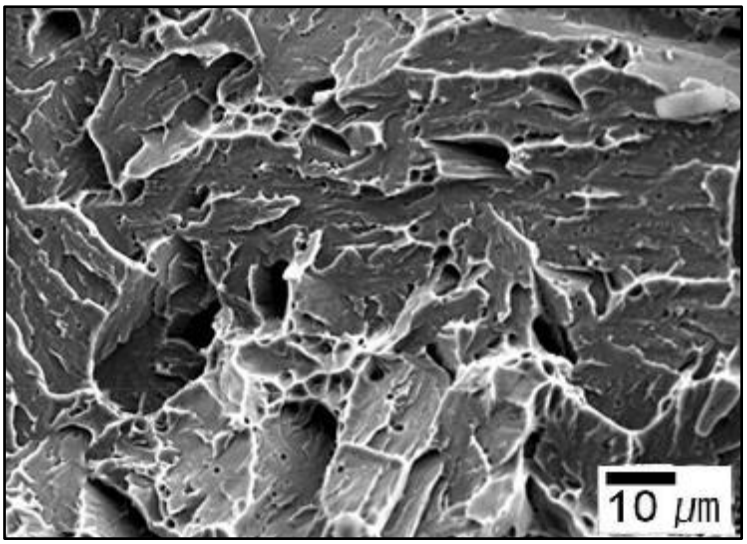

Figure 22: SEM micrograph of a fracture surface across a prior austenite grain that contained bainite and cracked in a brittle manner (Kang et al., 2015).

The role of acicular ferrite

The tendency for fracture to occur in a manner that is primarily ductile across AF and in a brittle manner along both GBF and bainite is likely to be the reason for the strong association between relatively high AF content and good impact properties of weld metals reported in the literature (Lan et al., 2016; Ohkita et al., 1995).

Beidokhti et al. (2009b) found that an increase in AF content from 60 % to 70 % correlated directly to an increase in the Charpy impact energy of HSLA weld metal from 80 J to 120 J. Beidokhti et al. (2009a) reported that, for metal containing 2 % Mn, an increase in AF content from 71 % to 75 % led to an increase in impact energy from 80 J to 110 J (−30 °C) and 100 J to 140 J (−10 °C). The increase in both AF content and impact energy was associated with increased Ti content. For weld metal containing 1.4 % Mn an increase in AF content from 60 % to 75 % was associated with an increase in impact energy from 100 J to 120 J (−10 °C) and 83 J to 110 J (−30 °C). The increased AF content and associated increase in impact energy was associated with an increase in Ti content from 0 % to 0.08 %.

AF is usually assumed to improve mechanical properties by decreasing grain size. This assumption is supported by the fact, often reported in the literature, that an increase in AF is associated with an increase in both strength and impact energy. Such a correlation is usually attributed to a reduction in grain size. Analysis of data published by Fattahi *et al.* (2013), for example, shows that an increase in AF content is very strongly correlated to an increase in impact energy, as shown in Figure 23. These welds contained about 0.1 mass% C, 0.3 mass% Si, 0.6 mass% Mn and 0.02 mass% Ti. These were multi-pass welds deposited using an experimentally coated electrode. The reported increase in impact energy is also associated with an increase in hardness, as shown in Figure 24. The authors themselves did not report this relationship. Their data also showed that an increase in AF content was associated with an increase in hardness (Figure 25).

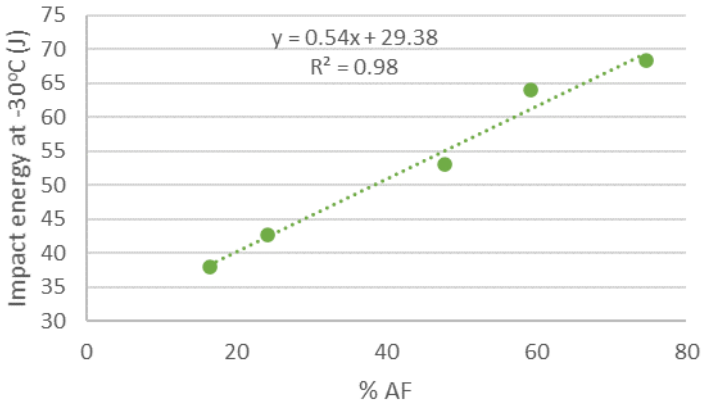

Figure 23: Scatter plot of correlation between %AF and impact energy of weld metal. Graph plotted using data from Fattahi *et al*. (2013).

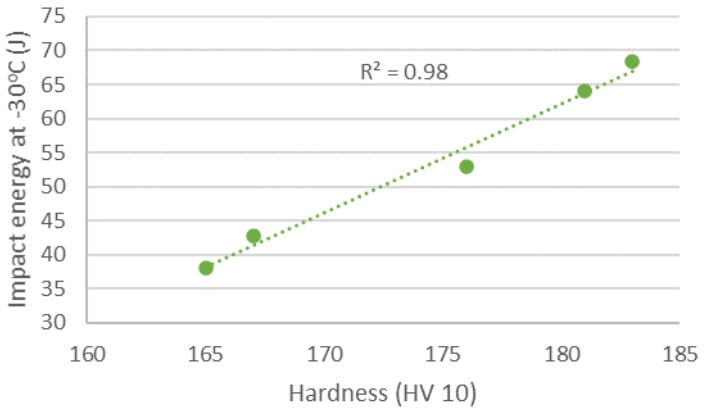

Figure 24: Scatter plot of correlation between impact energy and hardness of weld metal. Graph plotted using data from Fattahi *et al*. (2013)

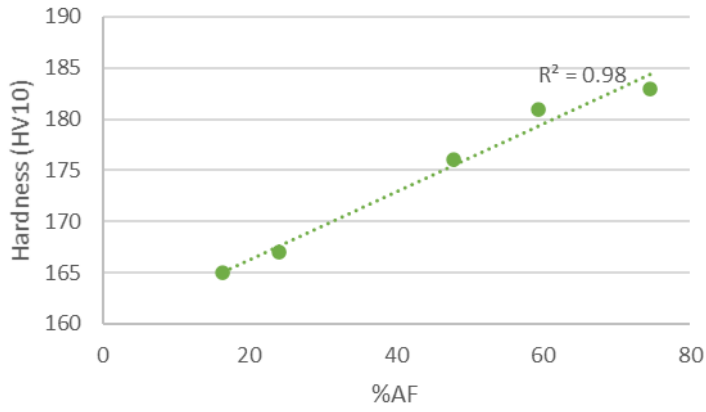

Figure 25: Scatter plot of correlation between hardness and acicular ferrite content of weld metal. Graph plotted using data from Fattahi *et al*. (2013)

The above clearly indicates that AF can be beneficial for the toughness of weld metal, but some exceptions have been reported in the literature. If cracks propagate along PAGBs or GBF, for example, AF will not always benefit toughness. Ebden and Weatherly (1983) produced five welds with microstructures of predominantly AF (> 90 %). Two welds (Weld 2 and Weld 5) produced the lowest upper-shelf impact energy (80 J and 100 J, respectively), despite Weld 5 having only 1 % GBF. In Weld 2, cracks propagated along GBF (Figure 26); in Weld 5, the cracks propagated along PAGBs (Figure 27). Such intergranular fracture along PAGBs has also been noted elsewhere in the literature (Lan et al., 2016).

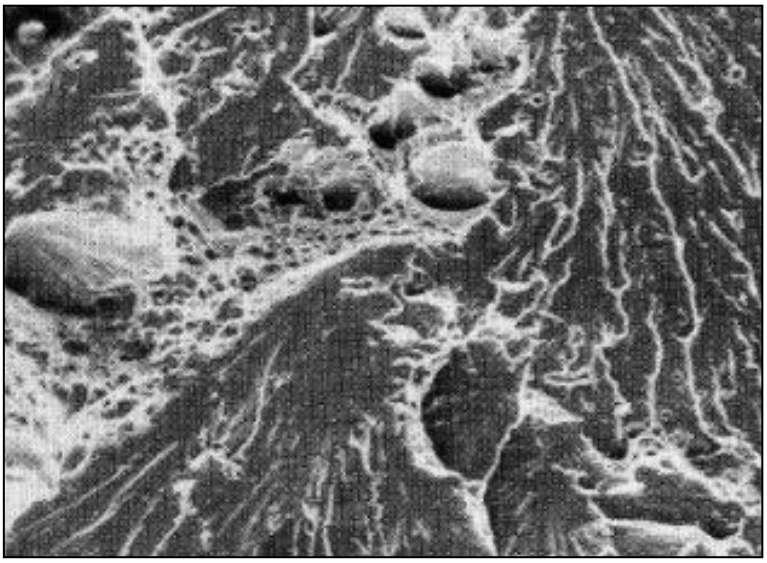

Figure 26: Micrograph of a crack propagating along GBF. The micrograph was taken at 500× magnification (Ebden and Weatherly, 1983).

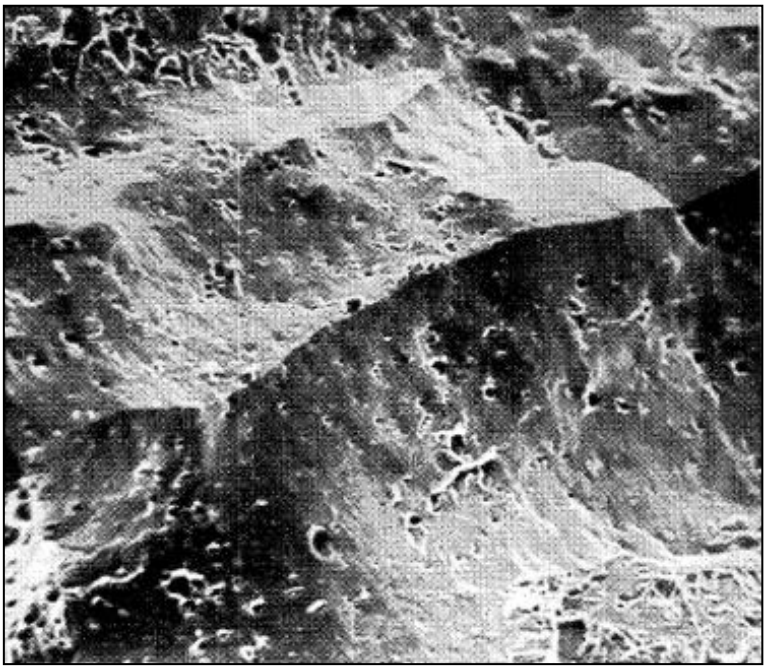

Figure 27: SEM micrograph showing a crack propagating along a prior austenite grain boundary. The micrograph was taken at 500× magnification (Ebden and Weatherly, 1983).

Ebden and Weatherly (1983) attributed the intergranular fracture of the weld in Figure 27 to segregation of S, P, and Mo to PAGBs. Mo is a very common alloying element in HSLA-steel welds and has a known tendency to segregate to austenite grain boundaries and, once there, to influence the free energy of these grain boundaries in a manner that influences the segregation of other elements, namely C and boron (B) (Hua et al., 2018; Maruyama et al., 2003).

Ni has also been associated with segregation to PAGBs and subsequent fracture along these boundaries. Yang *et al.* (2015) found that the addition of 4 mass% Ni to a sample containing 1.6 mass % Mn brought about a segregation structure, as shown in Figure 28. The segregation, in turn, changed the microstructure by shifting it from one dominant in AF to one consisting of bands of AF and polygonal ferrite. Zhang and Farrar (1997) did not report a more notable segregation, but did show that there was a correlation between a Ni content of about 5.5 mass% with fracture modes shifting from across the columnar grains to intergranular failure along the grain boundaries of these grains.

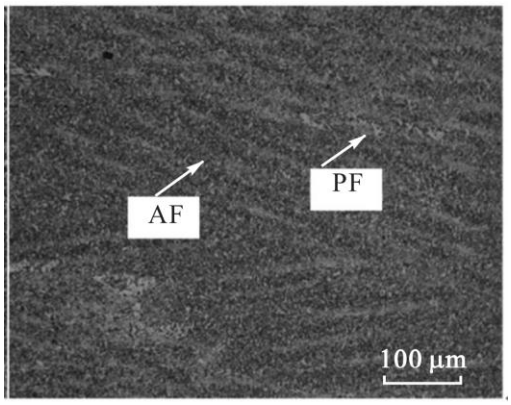

Figure 28: Micrograph showing the segregation structure detected by Yang *et al.* (2015).

Crack propagation can also be affected by hardness differential. Gubeljak (2003) evaluated the effect of overmatched weld metal on crack propagation in HSLA steel. The authors showed that significant differences in hardness created local brittle zones in the weld metal by transferring strain to the softer microstructure. Cracks then propagated in softer regions. The values cited in their work were from a lower hardness region of 240–270 $HV_{0.1}$ versus a higher hardness region of 320–350 $HV_{0.1}$.

1.2. Effect of chemical composition on microstructure, mechanical properties, and transformation temperature of weld metal

1.2.1. Titanium

The addition of Ti to weld metal, in optimum amounts, has been consistently shown to increase the impact energy of welds. This increase in impact energy is usually associated with an increase in AF (Babu, 2004; Beidokhti et al., 2009a, 2009b; Fattahi et al., 2013). Ti has been shown to increase AF content by increasing the nucleation probability of inclusions (Babu, 2004; Beidokhti et al., 2009a; Kang et al., 2016, 2015; Seo et al., 2019a) Ti appears to increase the nucleation probability of inclusions by shifting the nature of inclusions. The nature of this shift depends on the chemical composition of the molten weld metal. In work done by Seo *et al.* (2019) additions of Ti to weld metal resulted in the formation of crystalline oxides forming instead of glassy silicon inclusions. Results of the study are shown in Table 2. The constituent phase in the inclusion is usually determined by X-ray diffraction (XRD) or transmission electron microscopy (TEM), but more recently EBSD has been employed. The results shown in Table 2 were obtained using TEM with selected area diffraction (Seo et al., 2019b).

Table 2: Weld ID, Ti content, and inclusion characteristics (Seo et al., 2015).

ID	Ti (mass%)	Constituent phase in inclusion
0Ti	0.002	$MnSiO_3$. MnS, $MnTi_2O_4$
1Ti	0.023	Mn-silicate, (Mn, Ti)-spinel oxide, MnS
2Ti	0.049	(Mn,Ti)-spinel oxide, Mn-silicate, MnS
3Ti	0.072	Ti_2O_3, γ-Al_2O_3
4TI	0.091	Ti_2O_3, γ-Al_2O_3, TiN

Work done by Dowling et al. (1986) showed that addition of Ti to weld metal shifts the composition of inclusions further away from MnO and closer to Al_2O_3, consistent with the data in Table 2. The authors speculated that these phases are likely to stimulate ferrite nucleation by the crystallographic matching mechanism discussed in Section 1.1.3. These results indicate that it is not necessarily the presence of Ti in the inclusion that affects nucleation probability, but rather that the presence of Ti has an effect on the chemical composition of the inclusion and that this affects the nucleation probability. Ti is a strong deoxidiser, so it is thought that the influence of Ti on the nature of inclusions concerns the effect of Ti on the available oxygen content, reducing available oxygen by forming Ti dioxide.

The exact amount of Ti that is ideal for a given weld metal is quite sensitive to the general composition of that weld, as shown by (Beidokhti et al., 2009b). Their work addressed the combined influence of Ti and Mn on the properties of HSLA submerged arc weld (SAW) (Beidokhti et al., 2009b). Two sets of welds were made, one with a low Mn content (1.4 mass%) and one with a high Mn content (2.0 mass %). Ti content was varied from 0 mass% to 0.17 mass% for each set. The influence of Ti on microstructural constituents is shown in Figure 29 and Figure 30 for the high- and low-Mn groups, respectively, with the relevant weld compositions given in Table 3.

Ti additions led to an initial increase in AF content, but the AF content decreased above some critical Ti level. In both cases, the decrease in AF was associated with an increase in the fraction of secondary phases, which included FS(A) and M/A islands. In both cases, Ti additions did not strongly influence the GBF content. This decrease in AF at the expense of secondary phases is attributed to Ti acting as a reducing agent and increasing Mn pickup. Higher Mn levels increase hardenability and result in poor toughness (Beidokhti et al., 2009a). Figure 31 shows that the increase and decrease of AF was also associated with an increase and with further Ti addition, decrease of impact energy.

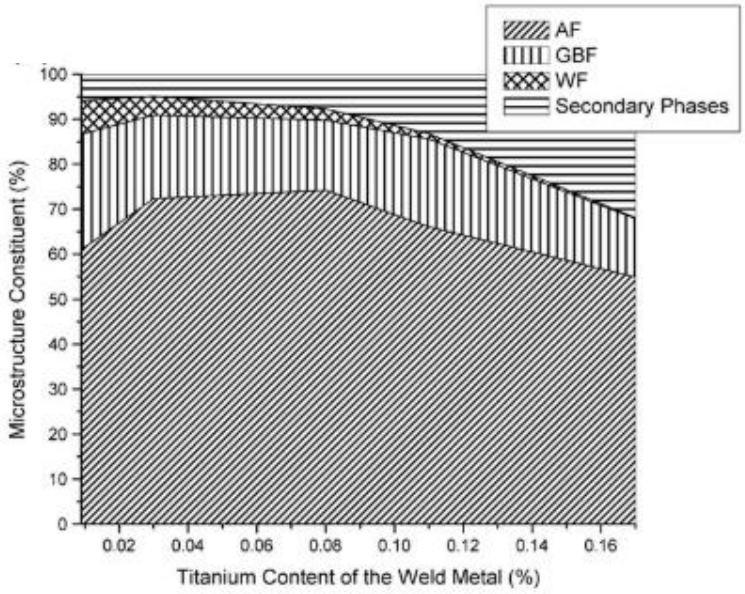

Figure 29: Weld metal constituent as a function of Ti content for welds containing 1.4 mass % Mn. Secondary phases refer to phases such as ferrite with second phase or M/A islands (Beidokhti et al., 2009b). WF refers to Widmanstätten ferrite and secondary phases refer to grain phases not classified as GBF.

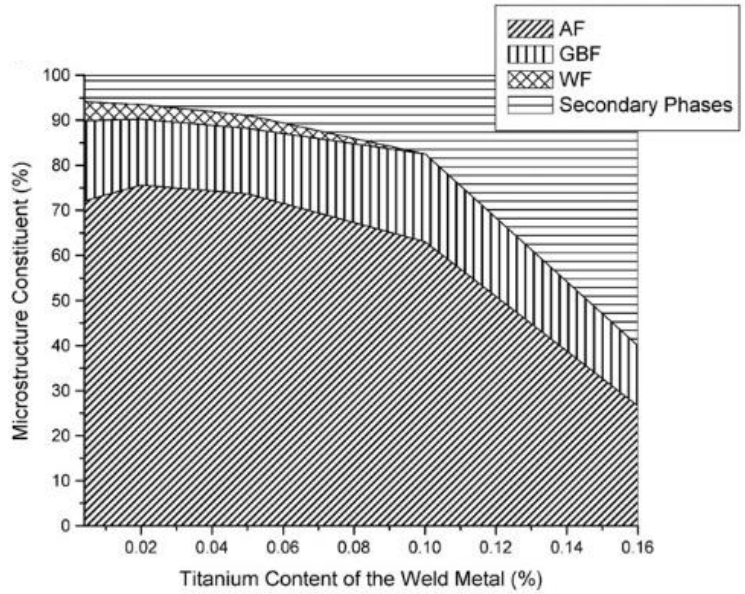

Figure 30: Weld metal constituents as a function of Ti content for welds containing 2.0 mass % Mn. Secondary phases refer to interferritic regions (Beidokhti et al., 2009b). WF refers to Widmanstätten ferrite.

Table 3: Chemical composition and microstructural constituents for welds discussed in Figure 29 and Figure 30 (Beidokhti et al., 2009a).

	C	Si	Mn	Cr	Ni	Mo	V	Ti	AF	GBF	WF	Other
T00	0.06	0.2	1.90	0.08	0.02	0.29	0.008	0.004	70	16	8	6
T10	0.07	0.26	1.92	0.08	0.02	0.28	0.01	0.02	75	14	5	7
T20	0.06	0.26	1.99	0.08	0.02	0.28	0.01	0.05	72	14	6	9
T30	0.06	0.3	2.15	0.08	0.02	0.27	0.01	0.09	61	15	5	20
T40	0.06	0.34	2.23	0.08	0.02	0.28	0.01	0.19	54	13	5	28
T50	0.07	0.35	2.29	0.08	0.02	0.26	0.02	0.22	48	15	4	33

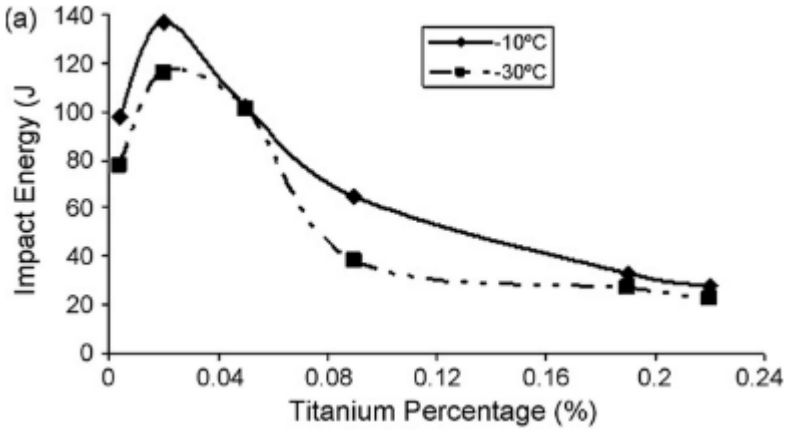

Figure 31: Relationship between Ti content and impact energy (Beidokhti et al., 2009a).

Ti additions to weld metal also pose a risk of leading to TiN precipitation. However, thermodynamic data suggest that TiO_2 will form first and TiN will form only if there is enough Ti remaining after the reaction has gone to completion. This likely explains the importance of the [Al]/[O] ratio in determining AF nucleation, as this ratio will determine the amount of oxygen available for a TiO_2 reaction to occur (Bhatti et al., 1984; Dowling et al., 1986; Seo et al., 2019b).

Ti content selected for the present study was based on work done by Beidokhti et al. (2009a) and Beidokhti et al. (2009b). A Ti content of 0.03 % is likely to be ideal for a weld metal containing 0.1 mass% C and 1.4 mass% Mn. This composition will most likely produce welds with an appreciable amount of AF, whilst it is unlikely to be high enough to lead to embrittlement. The literature also indicates that, at these levels, variability in Ti content due to unstable alloying techniques should not have a significant influence on AF content of the welds. This is shown in Figure 32.

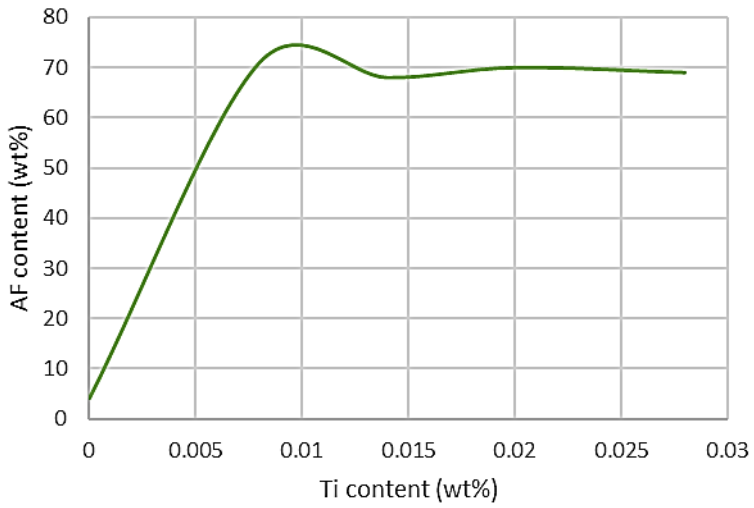

Figure 32: Effect of small changes in Ti content on AF content at selected levels (Seo et al., 2019b).

1.2.2. Nickel

Ni is a common alloying element in weld metal and is often associated with increased toughness. Although Ni is known to improve the intrinsic toughness of ferrite, it can also increase hardenability of weld metal by suppressing the austenite-to-ferrite transformation, which promotes the formation of bainite rather than the softer allotriomorphic ferrite (Guillou et al., 1981). Ni does this by lowering the γ → α transformation temperature (Trzaska, 2016). This shifts the ferrite transformation to a bainite transformation and results in a harder transformation product.

Ni can also be beneficial for toughness in cases where toughness is limited by the presence of martensite. Martensite forms during the cooling of weld metal from austenite that has not transformed to ferrite by the time the martensite start temperature (M_s) is reached (Shi and Han, 2008). The displacive bainite transformation, resulting from increased Ni content, occurs much faster than the diffusion-limited formation of allotriomorphic ferrite. This means that more austenite transforms to bainite, thereby reducing the amount of austenite available to form martensite. The effects are not expected to be very prominent at low levels of Ni. Empirical formulas indicate that the Ac_1 temperature will decrease by 16 K for every 1 mass % Ni added and the Ac_3 temperature by 17 K for every 1 mass% Ni added. It is therefore expected that Ni would need to be added in relatively large amounts to affect mechanical properties by the abovementioned mechanism. Indeed, the literature does indicate that addition of small amounts of Ni does not affect the mechanical properties of weld metal to a statistically significant degree (Kang et al., 2000). These authors showed that an increase from 1.1 mass% Ni to 3.9 mass% Ni led to an increase in hardness from 76 H_{RB} to 83 H_{RB}. The steel contained 0.01 mass %C and about 0.45 mass% Mn. The same authors reported a change in impact energy as a function of temperature with two different Ni additions, which is shown in Figure 33. The graph shows that the effect of Ni on impact energy is negligible. These welds contained about 0.006 mass% C and 0.05 mass% Mn.

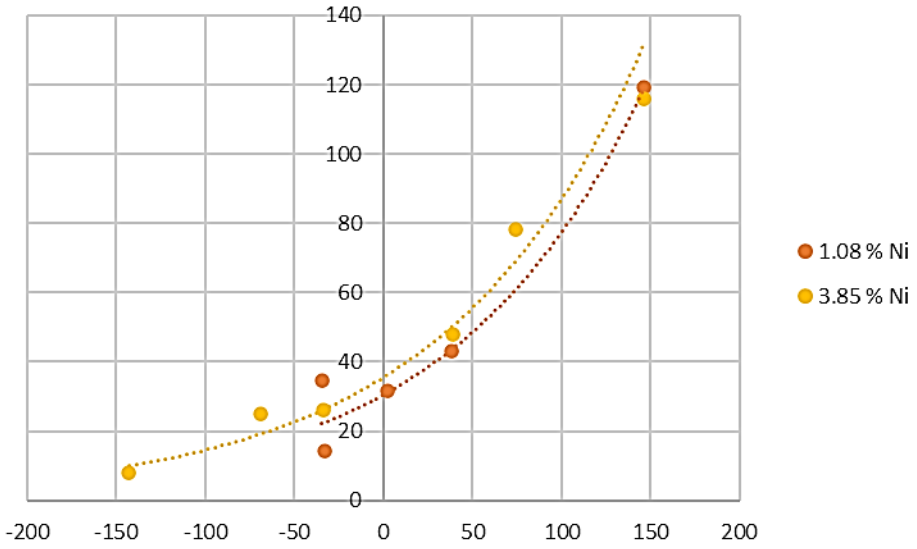

Figure 33: Influence of Ni content on impact energy of welds at different testing temperatures (Kang et al., 2000). The graph shows that Ni additions do not affect impact energy at the temperatures measured.

Other research indicates that the addition of relatively small amounts of Ni can affect the mechanical properties of welds. The influence of Ni on impact energy and microstructure was studied by Yang *et al.* (2015). Their results show that an increase from 2.1 mass% Ni to 2.8 mass% Ni can result in a decrease in impact energy from 84 J to about 54 J. The same change in Ni resulted in an increase in tensile strength from 618 MPa to 655 MPa and yield strength from 532 MPa to 550 MPa. The weld metal contained about 0.03 mass% C.

Yang *et al.* (2015) also studied the impact of changes in Ni content of weld metal across a range of Mn contents. All welds contained 0.03 mass% C and Mn was 0.3 mass%, 0.6 mass%, or 1.6 mass% Mn. The changes in impact energy are shown in Figure 34.

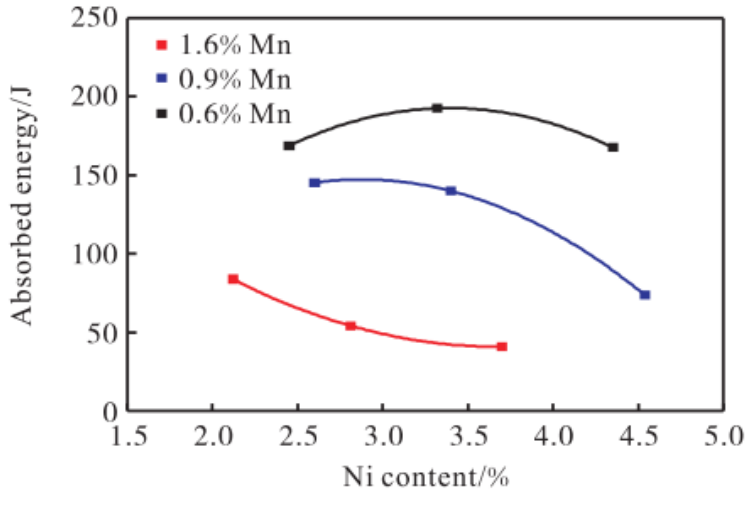

Figure 34: The impact energy of HSLA-steel weld metal content at −60 °C as a function of weld metal Mn and Ni contents. Yield strength of the steel varied from 455 MPa to 575 MPa. Tensile strength of the steel varied from 540 MPa to 674 MPa. Data taken from Yang *et al*. (2015).

Ni also appears to have a limited effect on AF content. Figure 35 and Figure 36 show the effect of Ni content on the as-deposited microstructure of steels containing 1 mass% Mn and 1.8 mass% Mn, respectively (Evans and Bailey, 1997). The welds contained 0.04 mass% C and 0.3 mass% Si. The effect of Ni on AF is not very consistent or significant. Figure 35 showed that the addition of small amounts of Ni (0.5 mass%) led to a decrease in GBF from about 30 % to 20 %. Figure 36 shows that the addition of 3.5 mass% Ni led to the appearance of martensite. This increase in Ni was associated with an increase in both yield and ultimate tensile strength in both cases. Impact energy was not measured, but it is assumed that the formation of martensite would have been detrimental to impact energy.

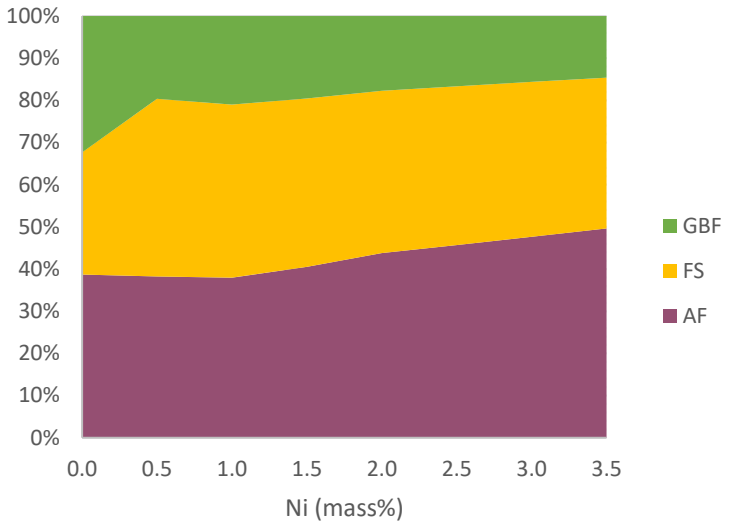

Figure 35: Effect of Ni on as-deposited weld metal microstructure at 1 mass% Mn (Evans and Bailey, 1997).

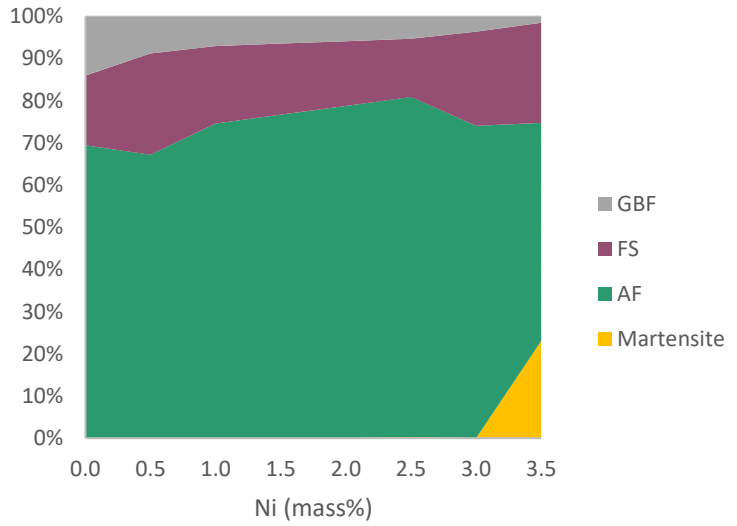

Figure 36: Effect of Ni on as-deposited weld metal microstructure at 1.8 mass% Mn (Evans and Bailey, 1997).

Although Ni does not appear to strongly affect AF content, it does appear to have a notable influence on the morphology of the AF. Work done by Farrar and Zhang (1995) studied the effect of Ni content on morphology and, specifically, the aspect ratios of AF in C–Mn–Ni welds. The chemical composition of the welds, and the aspect ratio of AF in each case, are shown in Table 4. An increase in Ni content is clearly associated with an increase in the AF aspect ratio. Micrographs of welds A1 and A2, containing 1 mass% Ni and 2.5 mass% Ni, respectively, are shown in Figure 37 and Figure 38, respectively. The average aspect ratio only changed from 4:1 to 6.5:1, but the SEM micrographs indicate that the morphology changed significantly. Ni additions of 5.5 mass% and above led to measurable changes in the aspect ratios of the AF laths.

As shown in Figure 37 and Figure 38, increased Ni content does not only change the AF aspect ratio, but also results in a more regular lath morphology. Ni is known to suppress the transformation temperature of steel, so it seems reasonable to assume that Ni additions would have suppressed the transformation temperatures of these welds, an explanation also proposed by the authors. This suppression in transformation temperature likely led to a shift from the Widmanstätten-like AF transformation to a more bainitic AF transformation, as discussed in Section 1.1.2.

Table 4: Chemical compositions and changes in aspect ratio for study of Farrar and Zhang (1995).

Weld code	C	Mn	Mo	Ni	Aspect ratio
A1	0.048	1.68	0.01	0.947	3–5:1
A2	0.041	1.67	0.008	2.482	5–8:1
B1	0.037	0.85	0.008	2.561	3–5:1
B2	0.057	0.67	0.008	3.315	> 3–5:1
B3	0.048	0.78	0.010	5.532	10–15:1
C1	0.034	0.36	0.008	5.577	10:1

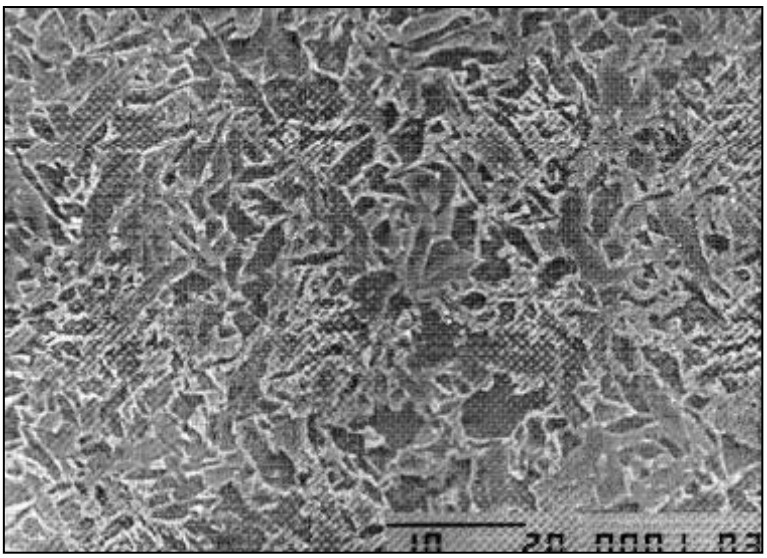

Figure 37: SEM micrograph of A1 (0.9 mass% Ni). Aspect ratio of acicular ferrite needles varied from 3:1 to 5:1 (Farrar and Zhang, 1995).

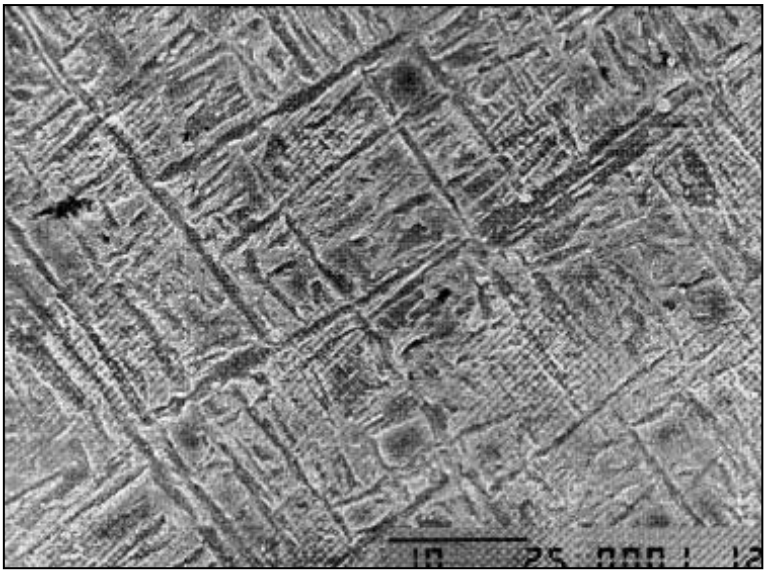

Figure 38: SEM micrograph of A2 (2.5 mass% Ni). Aspect ratio of acicular ferrite needles varied from 5:1 to 8:1 (Farrar and Zhang, 1995).

It was stated in Section 1.1.1 that increased Ni content is associated with increased segregation of both Ni and other alloying elements to PAGBs. It was further noted in Section 1.1.5 that high Ni content has been associated with intergranular fracture along PAGBs in HSLA-steel weld metal.

Zhang and Farrar (1997) showed a correlation between a Ni content of about 5.5 mass% with a shift in the fracture mode from across the columnar grains to intergranular fracture. Kang, Kim, and Hwang (2000) reported similar observations. An increase in Ni content from 2.66 mass% to 7.45 mass% shifted fracture from a brittle, shear mode across prior austenite grains to an intergranular mode along PAGBs, as shown in Figure 39. These results indicate that the effects of Ni on mechanical properties and microstructure are both varied and depend on the chemical composition of the weld.

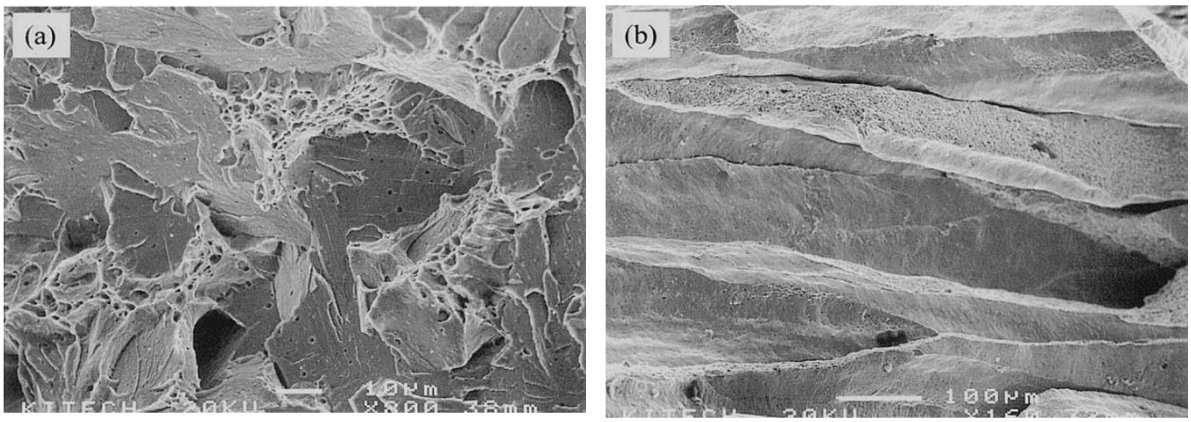

Figure 39: Fracture surfaces of samples from welds with a) 2.66 mass% Ni and b) 7.45 mass% Ni. Samples contained 0.02 mass% C, 1.76 mass% Mn and 0.01 mass% C, 0.91 mass% Mn, respectively (Kang et al., 2000).

1.2.3. Molybdenum

Mo is another alloying element often used to alloy HSLA-steel welding consumables. It is usually associated with increased strength. Mo additions have consistently been shown to increase yield and tensile strength of material. Figure 40 and Figure 41 show the increase in yield and tensile strength resulting from the addition of Mo in work done by Evans and Bailey (1997). Figure 42 and Figure 43 show the increase in yield and tensile strength of as-welded weld metal as a function of Mo content. Graphs were drawn from data published by Surian et al.(2005).

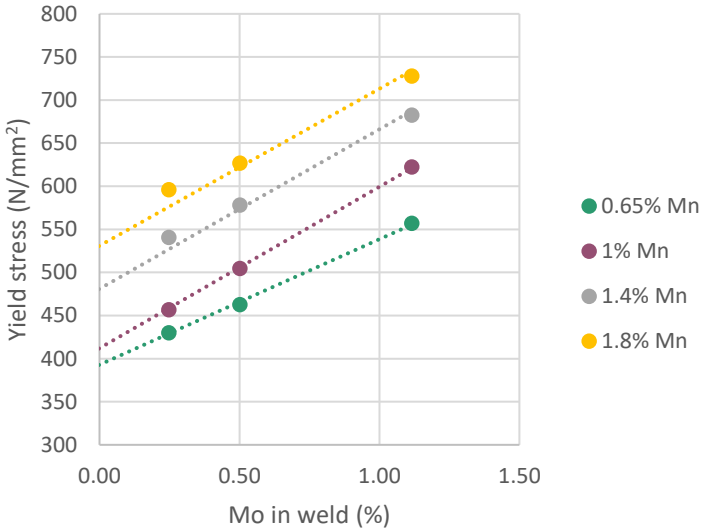

Figure 40: Effect of Mo on the yield strength of as-welded weld metals (Evans and Bailey, 1997). The graph shows a consistent increase in yield strength correlated to an increase in Mo content.

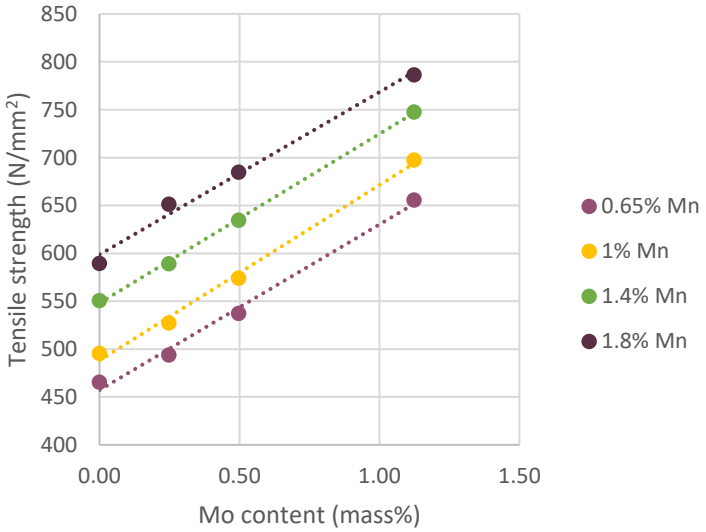

Figure 41: Effect of Mo on the yield strength of as-welded weld metals (Evans and Bailey, 1997). The graph shows a consistent increase in tensile strength correlated to an increase in Mo content.

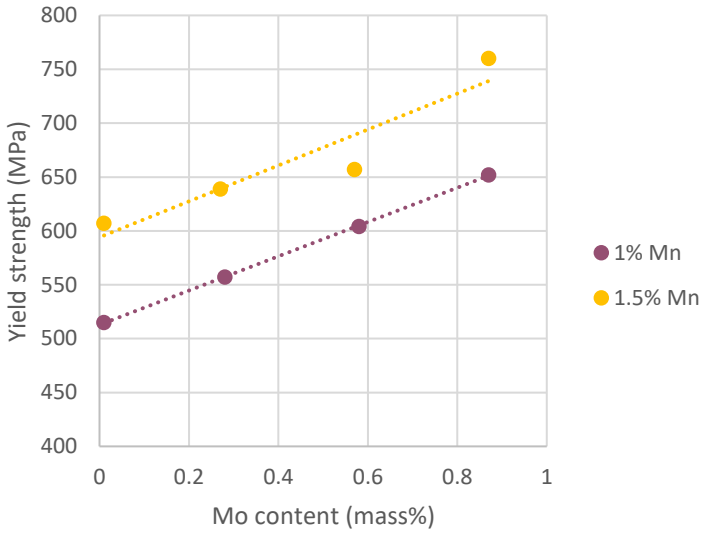

Figure 42: Effect of Mo on the yield strength of as-welded weld metal. Drawn from data obtained from Surian, De Rissone and De Vedia, 2005. The graph shows a consistent increase in yield strength correlated to an increase in Mo content.

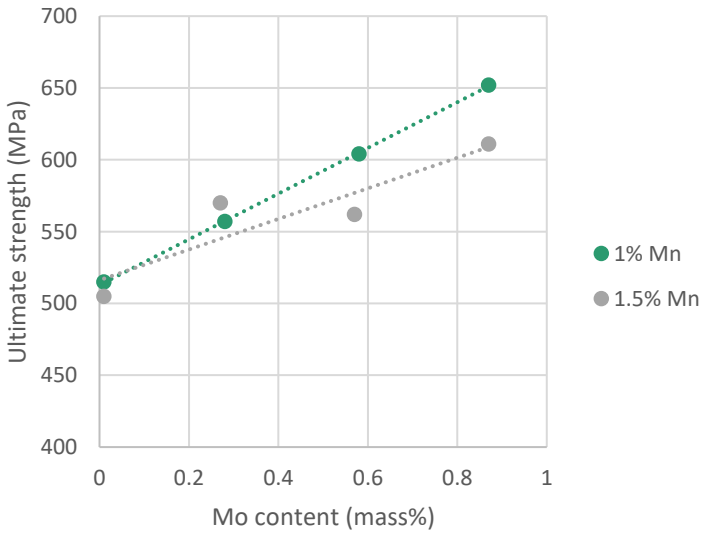

Figure 43: Effect of Mo on the ultimate tensile strength of as-welded weld metal. Drawn from data obtained from (Surian et al., 2005). The graph shows a consistent increase in tensile strength with an increase in Mo content.

The literature also indicates that Mo additions tend to increase AF content of welds. This is, at least in part, probably the reason for the association between increased Mo content and increased strength. However, increases in Mo content have also been shown to increase the martensite content of welds (De Andrés et al., 2013).

The positive effect of Mo on AF content is attributed to an ability to suppress GBF nucleation (Ren et al., 2009; You et al., 2006). Mo appears to segregate to austenite grain boundaries and affect the segregation of other alloying elements, mainly B and C (Guillou et al., 1981; Hua et al., 2018; Maruyama et al., 2003). Mo at grain boundaries also suppresses the $\gamma \rightarrow \alpha$ transformation and increases the ability for intergranular inclusions to compete with grain boundaries as nucleation sites (De Andrés et al., 2013). This suppression of the $\gamma \rightarrow \alpha$ transformation is attributed to the ability of Mo to inhibit C migration necessary for the transformation to occur (Hua et al., 2018). A graph showing the increased Mo concentration at grain boundaries is shown in Figure 44. The steel contained 0.03 mass% C, 0.18 mass% Mo, and negligible levels of Mn.

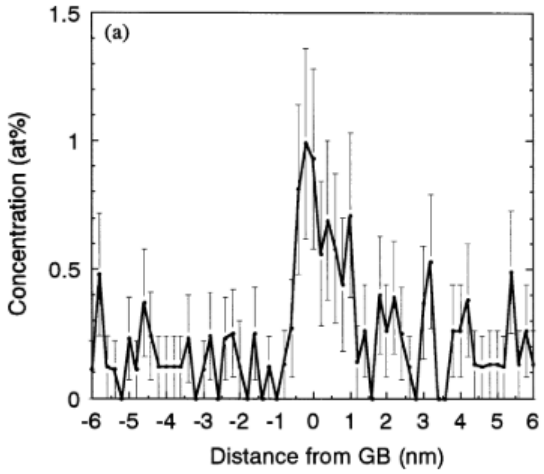

Figure 44: A concentration profile for Mo in the Fe–0.18Mo binary alloy. This alloy is likely a body-centred cubic structure (Maruyama et al., 2003). Composition analysis was carried out using a spark-source atomic emission spectro-chemical analysis technique.

Mo segregation has also been associated with intergranular fracture along PAGBs in HSLA-steel welds, as is the case with Ni (Ebden and Weatherly, 1983). This means that Mo additions leading to an increase in AF will not necessarily be beneficial for impact energy, owing to the resultant shift in fracture mechanism.

Mo also functions as a solid-solution strengthening agent and can lead to carbide precipitation in welds (Grange et al., 1977). Even if Mo additions positively influence impact energy by increasing AF content, they may still have a net negative effect on impact energy due to this carbide precipitation.

In work done by Surian et al. (2005), additions of 0.25 mass% Mo to weld metal containing both 1 mass% Mn and 1.5 mass% Mn led to increased AF content and hardness. The increase in AF content was associated with an increase in impact energy for the weld containing 1.5 mass% Mn, but associated with a decrease in impact energy of the weld containing 1.0 mass% Mn. The chemical composition and hardness of the full set of welds are shown in Table 5. Figure 45 and Figure 47 show the top bead microconstituents of the welds and Figure 46 and Figure 48 show the impact energy of these welds as a function of testing temperature.

Table 5 shows a consistent increase in the hardness of welds as the Mo concentration increases. Figure 45 and Figure 47 indicate that the addition of Mo increased the AF content up to a critical point, whereafter FS(A) increased at the expense of AF. Figure 46 shows that Mo additions had a generally negative effect on impact energy, with the largest decrease resulting from the addition of 0.25 mass % Mo. Hereafter, additional Mo did not have a very strong effect, and the effects are erratic.

Figure 48 shows that, for welds containing 1.5 mass% Mn, the addition of 0.25 mass% Mo has a positive effect on impact energy, whereafter the effects of additional Mo are negligible.

The negative effect of even small Mo additions on impact energy for welds containing 1 mass% Mn occurs despite the increase in AF content associated with Mo additions, shown in Figure 45. This is despite the fact that these small Mo additions do not result in the formation of phases that are expected to be detrimental. The adverse effect observed is therefore likely a result of increased hardness, and possibly carbide precipitation referred to earlier in this section (Grange et al., 1977). The positive effect of Mo on welds containing higher levels of Mn is thought to be a result of the increased AF content associated with Mo additions.

Table 5: Weld compositions for work done by (Surian et al., 2005).

Composition	C	Mn	Ni	Mo	Hardness (HV10)
1 mass% Mn, 0 mass% Mo	0.06	1.03	1.93	0.01	205
1 mass% Mn, 0.25 mass% Mo	0.06	1.11	1.91	0.28	227
1 mass% Mn, 0.50 mass% Mo	0.06	1.03	1.85	0.58	236
1 mass% Mn, 0.90 mass% Mo	0.05	0.95	1.82	0.87	259
1.5 mass% Mn, 0 mass% Mo	0.05	1.54	1.87	0.01	215
1.5 mass% Mn, 0.25 mass% Mo	0.05	1.48	1.89	0.27	249
1.5 mass% Mn, 0.50 mass% Mo	0.06	1.43	1.79	0.57	266
1.5 mass% Mn, 0.90 mass% Mo	0.06	1.45	1.84	0.87	288

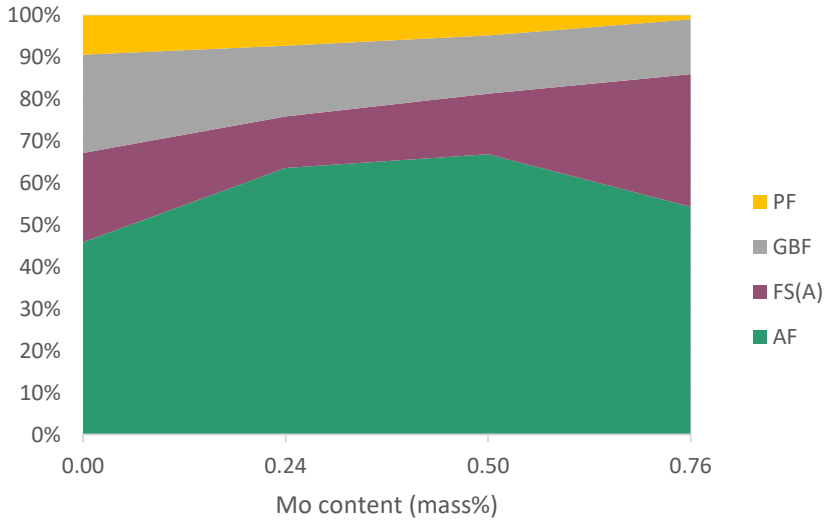

Figure 45: Microstructural constituents as a function of Mo content for 1 mass% Mn (Surian et al., 2005).

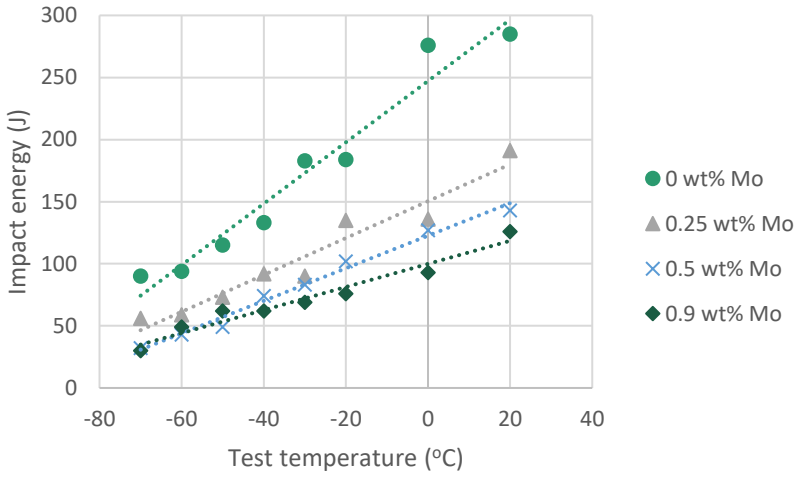

Figure 46: Charpy V-notch impact results for all-weld metals in the as-welded condition for 1 mass% Mn (Surian et al., 2005).

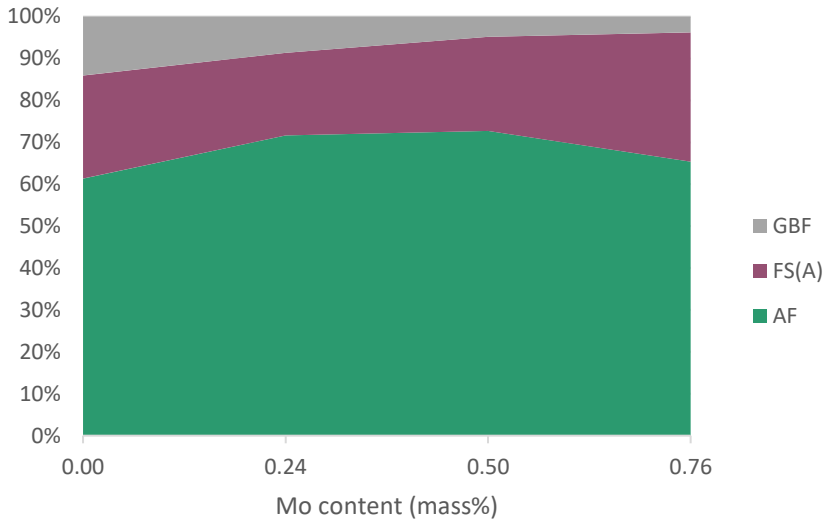

Figure 47: Microstructural constituents as a function of Mo content for 1.5 mass% Mn (Surian et al., 2005).

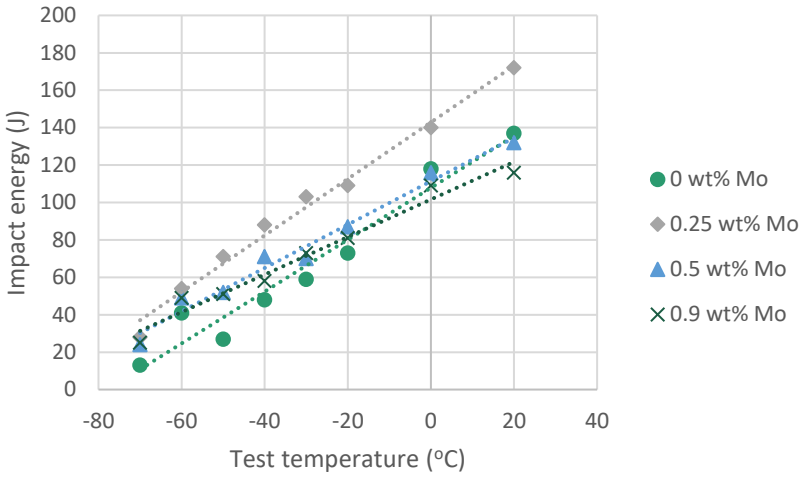

Figure 48: Charpy V-notch impact results for all-weld metals in the as-welded condition for 1.5 mass% Mn (Surian et al., 2005).

Evans and Bailey (1997) evaluated the effect of Mo on 100 J Charpy impact temperature of welds with varying Mn content and obtained equally complex results. In many ways, their results contradict those obtained by (Surian et al., 2005). Figure 49 shows the results of these experiments. The welds contained between 0.03 mass% and 0.05 mass% C. The graph shows that the addition of 0.25 mass% Mo to welds containing 1 mass% Mn or less resulted in a decrease in impact energy, whilst the addition of 0.25 mass% Mo to welds containing 1.5 mass% Mn or more had negligible effect. However, these authors found that addition of 0.5 mass% Mo or more was beneficial for the impact energy of welds containing 1 mass% Mn and that the addition of 0.75 mass% Mo was always beneficial for impact energy.

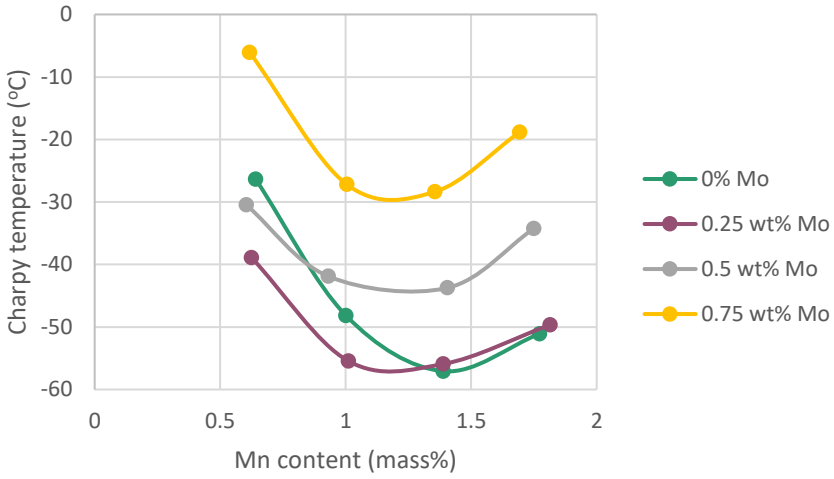

Figure 49: Effect of Mo on 100 J Charpy transition temperature of weld metals with varying Mn contents. Graph drawn from results reported by Evans and Bailey (1997).

These results indicate that, as is the case for Ni, the influence of Mo on impact energy is very complex and highly dependent on weld metal composition. However, it appears likely that, for welds containing 1.5 mass% Mn, the addition of 0.25 mass% Mo should not be detrimental and may be beneficial for impact energy.

1.2.4. Nickel and molybdenum in combination

The interaction effect between Ni and Mo has not often been studied, according to the literature. Work that is available indicates that the presence of Mo may reduce the deleterious effect of Ni on impact energy. Combined addition of Ni and Mo has also been correlated to an increase in AF, but a decrease in impact energy (Bhole et al., 2006; Ren et al., 2009)

Results from a study done by Ren *et al.* (2009) showed that the simultaneous increase in Ni and Mo resulted in a decrease in impact energy. The chemical composition and impact energy of these welds are shown in Table 6. The authors attributed the decrease in impact energy to an increase in bainite.

Table 6: Chemical composition and impact energy of welds (Ren et al., 2009). Impact tests were done at −20 °C in the as-welded condition.

Single wire	C	Mn	Mo	V	Ni	Ti	Nb	Impact energy (J)
S1	0.04	1.43	0.22	0.038	0.18	0.01	0.041	225
S2	0.04	1.41	0.37	0.036	0.32	0.013	0.039	173

Bhole *et al.* (2006) studied the individual effects of Ni and Mo, as well as their combined effects. Table 7 shows the chemical composition of the welds from this study. Figure 50 and Figure 51 show the influence of Ni on the yield and ultimate tensile strength of weld metal in the absence and presence of Ni, respectively. The addition of Ni to samples that contained 0.3 mass% Mo did not significantly change the yield or tensile strength. The spike in tensile strength for the sample containing 2.6 mass% Ni appears to possibly be an anomaly. The addition of Ni to samples that contained 0.8 mass% Mo had no effect on yield strength, but did increase tensile strength from about 800 MPa to about 900 MPa.

Figure 52 and Figure 53 show the effect of an increase in Ni content on elongation and impact energy of welds containing 0.3 mass% Mo and 0.8 mass% Mo, respectively. For welds containing 0.3 mass% Mo, the addition of Ni considerably decreased elongation. For welds containing 0.8 mass% Mo, the addition of 2 mass% Ni had no effect on elongation and the addition of 3 mass% Ni led to only a slight decrease in elongation. Similarly, when Ni was added to welds containing only 0.3 mass% Mo, the impact energy of the welds decreased significantly. However, when Ni was added to welds that contained 0.8 mass% Mo, the impact energy did not reduce significantly.

Table 7: Chemical compositions of weld metal (in percentage by mass) taken from Bhole *et al*., 2006.

Weld sample		C	Mn	Si	Ni	Mo	N	O
A	SLW	0.05	1.65	0.45	0.11	0.294	0.014	0.069
B	LWNi1	0.05	1.59	0.44	1.02	0.289	0.046	0.046
	LWNi2	0.05	1.58	0.45	2.56	0.218	0.044	0.044
	LWNi3	0.05	1.55	0.45	3.75	0.297	0.045	0.045
C	LWMo1	0.06	1.65	0.48	0.07	0.817	0.037	0.037
	LWMo2	0.06	1.59	0.44	0.1	0.881	0.044	0.044
D	LWMoNi1	0.06	1.59	0.47	2.03	0.995	0.042	0.042
	LWMoNi2	0.06	1.59	0.45	2.91	0.7	0.040	0.040

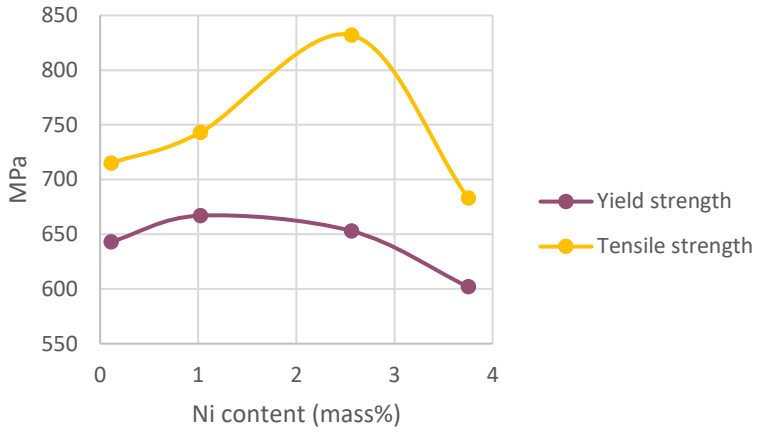

Figure 50: Effect of change in Ni content on yield strength and tensile strength in 0.3 mass% Mo welds (Bhole et al., 2006).

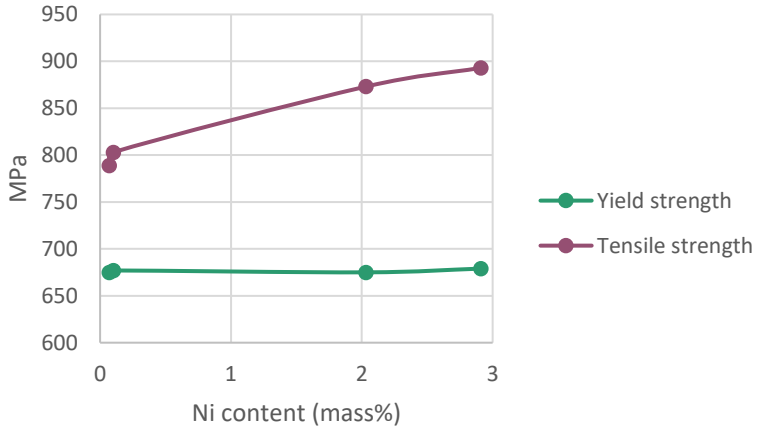

Figure 51: Effect of change in Ni content on yield strength and tensile strength in 0.8 mass% Mo welds (Bhole et al., 2006).

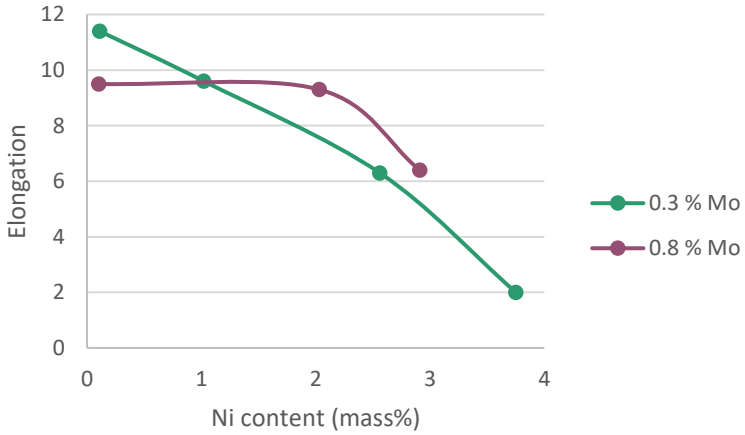

Figure 52: Effect of change in Ni content on elongation with and without the presence of Mo. Drawn from data taken from Bhole *et al*. (2006).

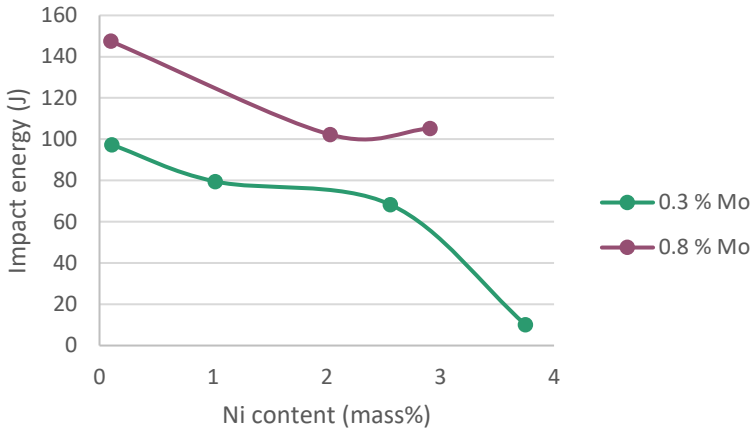

Figure 53: Impact energy as a function of Ni content at 0.3 mass% and 0.8 mass% Mo contents. Impact tests were done at −45 °C. Drawn from data taken from Bhole *et al*. (2006).

Ni and Mo levels for further research

Estimations of ideal Ni and Mo contents are based largely on work done by Bhole *et al.* (2006). The chemical composition, phase composition, impact energy, and strength of each of the applicable welds from this work are given in Table 7. Their work showed that in the presence of about 0.2 mass% Mo and no Ti, additions of 1 mass% and 3 mass% Ni slightly decreased AF content, but significantly decreased impact energy. When Mo content was increased from 0.3 mass% to between 0.7 mass% and 0.9 mass%, Ni additions led to a slight increase in impact energy and a significant increase in strength.

In work done by Surian et al. (2005) in welds containing about 1.5 mass% Mn, increases of 0.2 mass% Mo and 0.3 mass% Mo were found to be beneficial for impact energy, whilst additions above this threshold resulted in the formation of embrittling phases and a loss in impact toughness (Figure 48).

In the correct amount, Mo additions appear to be beneficial for both strength and toughness. The effect of Ni on strength is generally beneficial, but the effect thereof on impact energy is very erratic and often negative. It is suggested that Mo levels from 0 mass% to 0.3 mass% and Ni levels from 0 mass% to 2 mass% be investigated.

1.2.5. Transformation temperatures

Equation 3 and Equation 4 show empirical formulae for calculating A_{c1} and A_{c3} temperatures. They show that Ni additions are expected to decrease these transformation temperatures by 15 °C and 14 °C for each 1 mass% Ni added. Mo additions are expected to increase the Ac_3 temperature by 32 °C for each 1 mass% Mo added. According to Equation 5 and Equation 6, the expected effect of Mo and Ni on B_S is not consistent. This is likely because B_s is not a very stable parameter and is influenced strongly by the cooling rate.

$$Ac_3\ (°C) = 910 - 202\ (mass\%\ C)^{0.5} - 15.2(mass\%\ Ni) + 44.7(mass\%\ Si) + 104(mass\%\ V) + 31.5(mass\%\ Mo) + 31.1(mass\%\ W)$$

Equation 3 (Andrew, 1965)

Ac_1 (°C) = 723 – 10.7(mass% Mn) – 13.9(mass% Ni) + 29(mass% Si) + 16.9(mass% Cr) + 290(mass% As) + 6.38(mass % W)

Equation 4 (Andrew, 1965)

B_s (°C) = 732 − 202(mass% C) + 216(mass% Si) – 85(mass% Mn) – 37(mass% Ni) – 47(mass% Cr) – 39(mass% Mo)

Equation 5 (Kunitakre and Okada, 1998)

B_s (°C) = 656 − 57.7(mass% C) – 75(mass% Si) – 35(mass% Mn) − 15.3(mass% Ni) – 34(mass% Cr) − 41.2(mass% Mo)

Equation 6 (Kirkaldy and Venugopalan, 1984)

B_s (°C) = 830 – 270(mass% C) – 90(mass% Mn) – 37(mass% Ni) – 70(mass% Cr) – 83(mass% Mo)

Equation 7 (Steven and Hayens, 1956)

1.2.6. Industrially available high-strength low-alloy steel welding consumables

An industrially available welding consumable that is close to the chemical composition of interest to this study is ASTM F9A4-EM2-M2-H8. It requires the deposited weld metal to contain a maximum of 0.1 mass% C, a maximum of 0.8 mass% Si, 0.9 mass%–1.8 mass% Mn, 1.4 mass%–2.1 mass% Ni, 0.25 mass%–65 mass% Mo, and a maximum of 0.03 mass% (Ti + V + Zr). A F9A4-EM2-M2-H8 weld consumable is required to have a tensile strength of 620 MPa to 758 MPa, a minimum yield strength of 538 MPa, and a minimum impact energy of 27 J at −40 °C. Welds produced by this consumable are used in the as-welded condition. This consumable is usually used to weld HSLA-80 steel. The Lincolnweld LA-100 electrode is a F9A4-EM2-M2-H8 weld consumable. When a multi-pass weld is produced with a voltage of 28 V, current of 525 A, and travel speed of 41 cm/min, this consumable produces a tensile strength of 700 MPa, yield strength of 640 MPa, and an average impact energy of 125 J at −40 °C.

1.3. Thermal cycling

Industrially produced welds are usually multi-pass welds. When welding involves the deposition of more than one weld bead, the initially deposited bead undergoes thermal cycling. Despite this, a lot of research investigating the effect of chemical composition on mechanical properties makes use only of single-pass welds (Beidokhti et al., 2009a, 2009b; Bhole et al., 2006; Ebden and Weatherly, 1983). In other cases, comparisons are drawn between single- or multi-pass welds without considering the effects of thermal cycling on the mechanical properties of the weld metal (Lan et al., 2016). As shown in Sections 1.3.1 to 0, the thermal cycling to which multi-pass welds are exposed is highly likely to affect their microstructure and, resultantly, their mechanical properties. Studies considering only the effect of chemical composition on weld metal properties may therefore be somewhat incomplete, whilst studies comparing single-pass with multi-pass welds may result in inaccurate conclusions.

Weld thermal cycles involve a quick initial increase in sample temperature to a peak temperature. This peak in temperature will depend on the distance of the point away from the heat source, according to equations published by Rosenthal (1946). The phase transformations that occur in the weld metal during heating, as well as the extent of grain growth at elevated temperatures, are primarily dependent on the peak temperature reached and therefore on the distance from the heat source. Equations published by Rosenthal (1946) could therefore be used to estimate the size of each HAZ region in a weld.

In addition to the utility of these equations in determining peak temperature at a certain point, they can also be used to calculate the critical cooling time between 800 °C and 500 °C, which, in turn, strongly affects the type of $\gamma \rightarrow \alpha$ transformation upon cooling and, resultantly, the final microstructure. A graphical representation of the change in thermal cycle as the distance from the heat source changes is shown in Figure 54. The effects that these thermal cycles might have on microstructure are discussed in Sections 1.3.1 to 1.3.4.

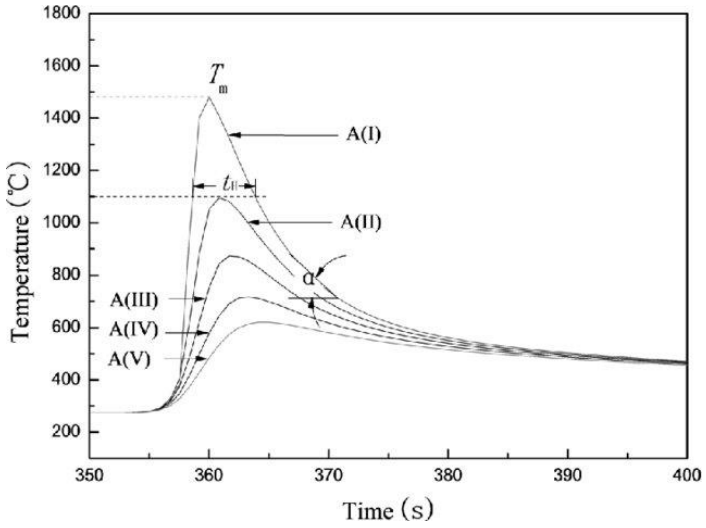

Figure 54: Weld thermal cycle showing different peak temperatures (Bai et al., 2017).

1.3.1. Intercritically reheated heat-affected zone

When the peak temperature of a thermal cycle falls between A_{c1} and A_{c3}, the HAZ is referred to as an intercritically reheated (IR) HAZ. When weld metal is exposed to this thermal cycle, some of the ferrite transforms back to austenite. The regions that transform back to austenite will be a function of local chemical composition, but also of nucleation potential for austenite at grain boundaries. Davis and King (1994) reported that GBF and carbon-saturated regions (like the interferritic) usually transform back to austenite.

The GBF that transforms back into austenite will become more carbon-enriched due to C diffusion from the saturated ferrite towards the unsaturated austenite. Upon cooling, these regions then often transform to bainite, with regions in between bainite laths often transforming to IfRs. The nature of the bainite and the extent of IfRs will be determined by the C content, transformation temperature, and cooling rate. This may lead to networks of IfRs forming along prior austenite grains. The formation of such networks is especially likely if the original GBF network was extensive. Such networks would provide ideal crack propagation sites and may have significant adverse effects on impact energy (Davis and King, 1994).

Networks of IfRs resulting in reduced impact energy have been shown in the HAZ of the parent metal of HSLA-steel welded joints, but not in the heat-affected weld metal section of a multi-pass weld. The parent metal (PM) with which it was associated contained 0.06 mass% C, which is lower than the 0.1 % C stipulated for welding consumables usually used to weld HSLA-80 steels (Mohseni et al., 2012).

It is almost certain that pre-existing IfRs will also transform to austenite on heating. This was shown to occur by Davis and King (1994). If this occurs, homogenisation of C in this region is likely and austenite grains may become larger. The morphology of austenite grains that form upon cooling will likely have a different morphology to that prior to their exposure to the thermal cycle.

1.3.2. Fine-grained heat-affected zone

The part of the HAZ heated to just above the Ac_3 temperature, referred to as the fine-grained (FG) HAZ region, should fully transform to austenite. However, the newly transformed austenite does not experience much, if any, grain growth; therefore, the austenite grain size will be quite small upon cooling. Large grain boundary surface areas may resultantly be available for nucleation of GBF and FS(A) upon cooling.

Regions that consisted of AF prior to heating may then transform via the allotriomorphic $\gamma \rightarrow \alpha$ transformation mechanism and the transformation product will appear similar to that seen prior to thermal cycling. However, the grains would likely be softer (Tweed and Knott, 1987). This would result in improvement in impact energy. There is also the potential that the large grain boundary surface area will result in extensive formation of FS(A), which may be detrimental to impact energy.

Larger regions of ferrite, such as GBF, will transform back into relatively large grains of austenite, which are expected to transform back into ferrite via the process described in Section 1.1.1. If there are regions of austenite that experienced significant grain growth despite the low temperatures, they will also transform back to ferrite in the manner laid out in this section. If this occurs, the nucleation probability of inclusions will be a determining factor in the morphology of AF. Work done by Kang *et al.* (2015) showed that exposure to thermal cycles with peak temperatures of 1350 °C may compromise the ability of inclusions to act as nucleation sites due to homogenization of MDZs. However, Mn diffusion in γ only becomes significant at temperatures well above those associated with the FG HAZ, as shown in Figure 55. It is therefore not likely the homogenization of MDZs would occur when welds are heated to only slightly above the A_{C3} temperature.

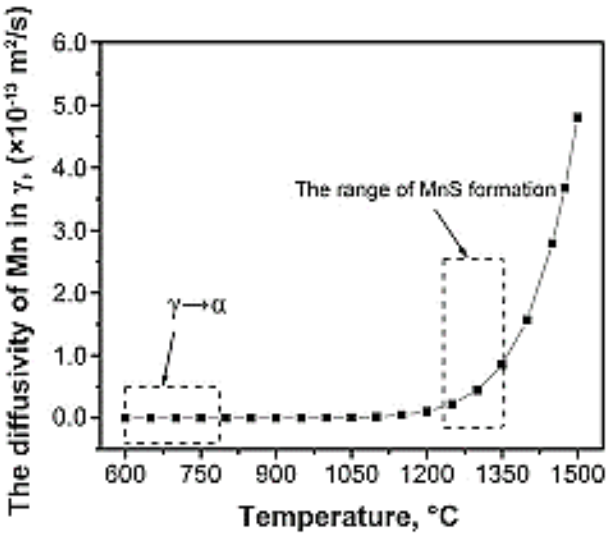

Figure 55: Graph showing the diffusivity of Mn in γ at different temperatures (Song et al., 2019). The graph shows that Mn diffusion in austenite only becomes notable at temperatures above 1200 °C.

The nucleation potential of inclusions, if they are affected by thermal cycling, is more likely to be adversely affected by the absence of, or large reduction in, elastic strain surrounding inclusions when they cool down from temperatures only slightly above the A_{c3} temperature. The difference in thermal expansion coefficients between γ and the inclusion results in the formation of regions of elastic strain around inclusions. Austenite will have formed around inclusions near the A_{c3} temperature, so this strain differential is likely to be lower at any given temperature during cooling from the FG HAZ than it would have been at that same temperature during cooling from the liquid state. The nucleation potential of inclusions relying heavily on a strain differential as a nucleation mechanism may

resultantly be more severely affected by thermal cycling to the FG HAZ region than by thermal cycling to a higher temperature.

1.3.3. Grain-growth heat-affected zone

Weld metal that is exposed to thermal cycles that have peak temperatures well above A_{c3} will transform to austenite and will also experience grain growth such that the weld metal will come to closely resemble the originally deposited weld metal during cooling. In this case, the nucleation probability of inclusions will be the strongest factor determining whether the microstructure of the weld metal, once cooled, resembles the microstructure of the same weld metal prior to thermal cycling. Any suppression of nucleation potential at inclusions will likely increase the probability of FS(A) nucleating at and growing from PAGBs.

In their work, Kang *et al.* (2015) exposed weld metal to weld thermal cycles that had peak temperatures of 1350 °C. This led to the homogenization of MDZs in some welds. An example of such homogenization is shown in Figure 56, with the thermal cycle used in the experiments shown in Figure 57. The chemical compositions of these welds are shown in Table 8.

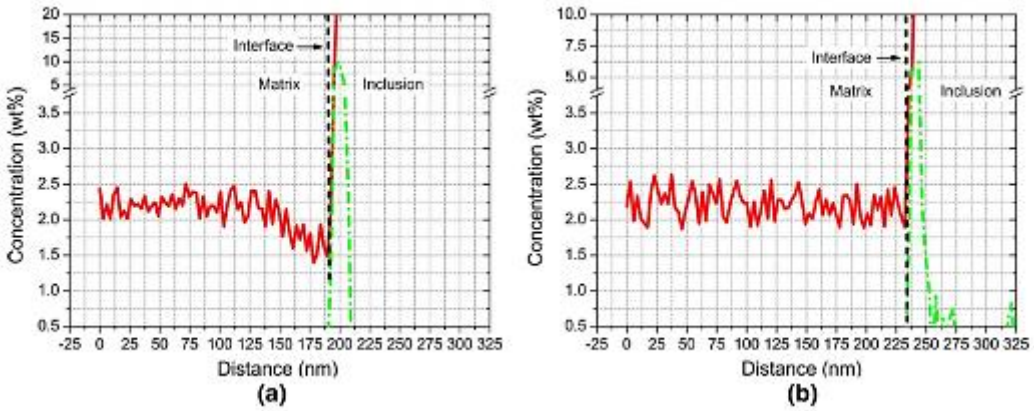

Figure 56: EDS line-scan analysis performed across a matrix/inclusion interface of two specimens (Kang et al., 2015). (a) is from a sample in the as-welded condition and (b) is from a sample that was thermally cycled to the grain-growth region.

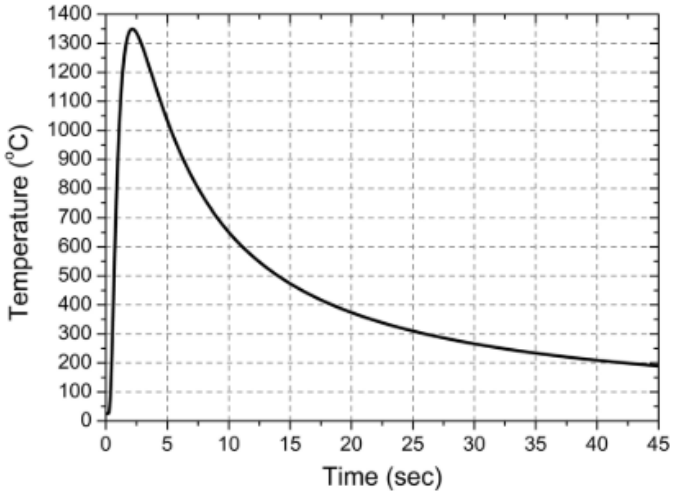

Figure 57: Thermal cycle of welds analysed in Figure 56(Kang et al., 2015).

Table 8: Chemical composition and impact energy of welds from Kang *et al*. (2015). Impact tests were performed on half-size Charpy samples at −40 °C.

	Condition	C	Mn	Ni	Cr	Mo	Ti	[Al]/[O]	Impact energy (J)
S	As-welded	0.07	2.1	2.4	0.5	1.0	0.01	0.65	25.3
RS	GG HAZ	0.07	2.1	2.4	0.5	1.0	0.01	0.65	13.0
I	As-welded	0.06	1.6	2.8	0.3	0.9	0.07	0.59	28.7
RI	GG HAZ	0.06	1.6	2.8	0.3	0.9	0.07	0.59	25.3

The authors went on to show that significantly less AF was nucleated in the weld in which the MDZs had homogenized. This weld also had a significantly lower impact energy than in the as-welded condition. Impact energies of Samples S and I were tested in the weld metal and as-welded condition. Samples RS and RI were extracted from the same welds as Samples S and R, respectively, but were exposed to a weld thermal cycle simulating the grain-growth (GG) HAZ region. The line scans shown in Figure 56 are from Sample R and RS. A similar reduction in impact energy was not seen in Sample I.

SEM micrographs of the four samples are shown in Figure 58. SEM fractography micrographs are shown in Figure 59. Sample RS, which had a low impact energy, broke in a brittle manner. The fracture surfaces of all other samples were dimpled and typical of a ductile fracture. These results confirm the mechanism noted earlier, that thermal cycling may shift the weld from an AF-rich to more bainitic microstructure, likely because inclusions lost their nucleation ability. The authors showed that the inclusions in Sample RI continued to transform and resultantly leached Mn from the surrounding matrix. This led to reestablishment of a Mn-depleted zone around inclusions upon cooling – which, in turn, allowed them to nucleate acicular ferrite. A similar transformation did not occur in Sample RS; Mn was homogenised and inclusions could not act as nucleation sites.

Sample S did not contain Ti, but contained significantly higher levels of Mn than Sample R. Although it is likely that the presence of Ti in Sample I and RI is the reason for the retention of the AF nucleation capability of the inclusions, it is not clear whether this is the reason for its retained impact energy. The high Mn contents of Samples S and RS would have made it more hardneable and may have led to the embrittlement. High Mn content may also have increased the rate of homogenisation of inclusions and contributed to their loss of nucleation probability.

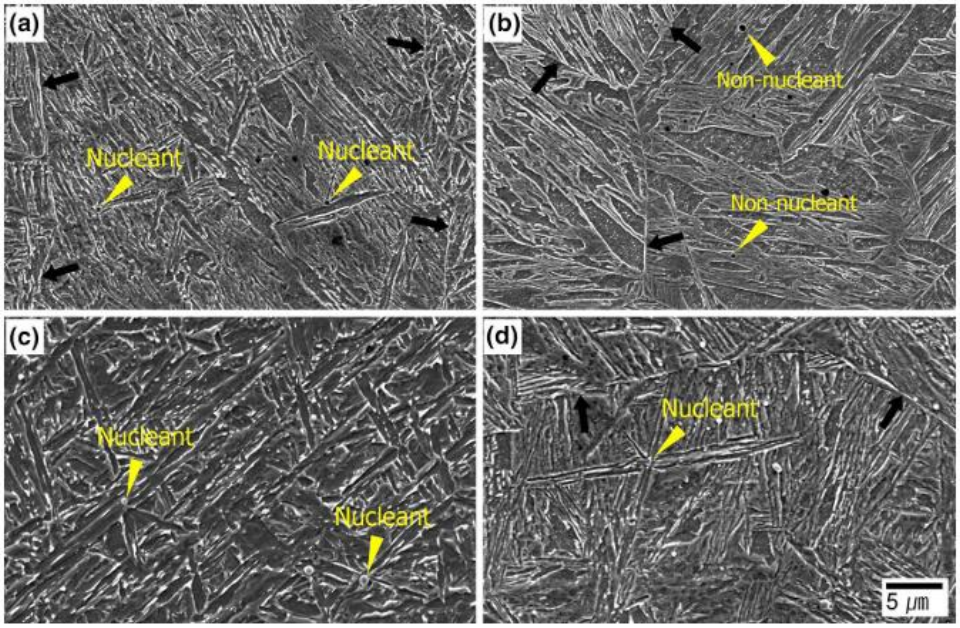

Figure 58: SEM micrographs of the four weld metals analysed by Kang *et al*. (2015). Micrographs marked (a), (b), (c), and (d) show the microstructures of Samples S, RS, I, and RI, respectively.

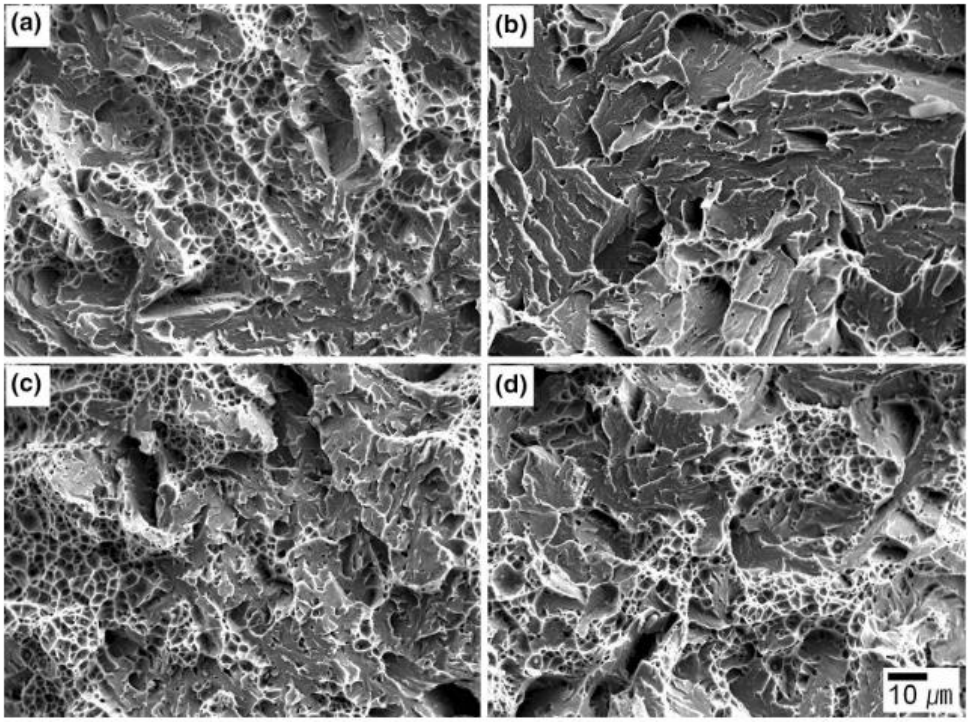

Figure 59: Fracture surfaces of four weld metals with varying Ti content and thermal exposure (Kang *et al*., 2015). Micrographs marked (a), (b), (c), and (d) show the microstructures of Samples S, RS, I, and RI, respectively.

1.3.4. Hardness differential and fracture

The effect of hardness differential within multi-pass weld metal is discussed by Gubeljak (2003). The author detected regions with significantly reduced hardness within multi-pass weld metal (Figure 60). Interactions between these low-hardness regions and surrounding high-strength regions led to local brittle zones (LBZs). The authors attributed the local low-hardness regions to the IR HAZ thermal cycle. During crack tip-opening displacement testing, unstable cracking was initiated at the end of the high-hardness region, propagated through the low-hardness regions, and arrested again in the medium-hardness region.

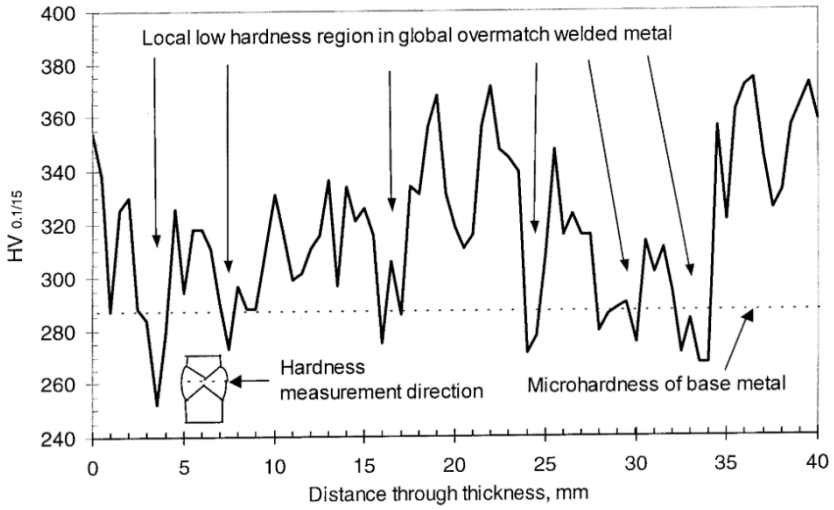

Figure 60: Microhardness traverse of a multi-pass weld (Gubeljak, 2003). The graph shows local low-hardness regions associated with the IR HAZ of thermally cycled weld metal.

The LBZ is believed to have resulted when the stress field of the overmatched region caused strain and resultant hardening of the undermatched region. This hardening resulted in the local matrix being unable to accommodate the strain necessary for crack-tip blunting, and unstable crack growth proceeded during the crack-tip opening displacement test. The unstable crack growth was again arrested at the medium-hardness weld metal. If thermal cycling results in a hardness differential between HAZ regions or between the HAZ and weld metal not exposed to peak temperatures sufficiently high to alter their hardness, the mechanical properties of the weld may therefore be affected.

1.4. Techniques used to change weld metal chemical composition

Research evaluating the effects of chemical composition on weld metal properties is often challenging owing to the complex nature of chemical reactions that determine the final chemical composition of the weld metal. This makes controlled alteration of the chemical composition of weld metal difficult. As is apparent from Section 1.2, interaction effects between various alloying elements can also be quite complex. This means that large experimental matrixes are often desirable when the influence of more than one element is being studied. The sensitivity of microstructure and mechanical properties to alloying element content also makes good control of elemental composition important.

Numerous research techniques are available for altering weld metal chemical composition for the purposes of research, each with advantages and disadvantages. Sections 1.4.1 to 1.4.3 discuss and evaluate methods through which weld metal has been altered or controlled in past experimental work.

1.4.1. Commercial wire/flux combinations

The simplest technique used to alter the chemical composition of weld metal is the use of different commercially available welding wires to obtain different weld metal compositions (Bhatti et al., 1984; Kanjilal et al., 2006; Pandey et al., 1994). This technique is cost-effective and simple, and provides results that are directly commercially applicable, but it does not usually allow for statistical analysis of results because the chemical composition of commercial wires does not usually differ in only a single element, nor does it allow for an extensive experimental matrix. Lastly, the variation in chemical composition that can be evaluated is constrained by commercially available welding consumables. This technique was used by Farrar and Zhang (1995) to investigate the response of AF morphology to different levels of Ni on AF morphology. Table 9 shows the C, Ni, and Mn contents, average Mn content, and range of Mn contents for each weld group. The average Mn content, which would ideally have been zero, ranged from 0 % to 25 %.

Table 9: Average Mn content and range of Mn contents for applicable weld groups (Zhang and Farrar, 1997).

Group	Number	C (mass%)	Ni (mass%)	Mn (mass%)	Average Mn content (mass%)	Range (mass%)	Range (% of average)
A	1	0.048	0.947	1.682	1.68	0.011	1%
	2	0.041	2.482	1.671			
B	1	0.037	2.561	0.852	0.77	0.180	23%
	2	0.057	3.315	0.672			
	3	0.048	5.532	0.783			
T	1	0.083	0.903	0.96	1.1	0.276	25%
	2	0.072	2.248	1.236			

Another way to change weld metal composition is the use of different available fluxes to alter the composition of the weld metal. Beidokhti et al. (2009a) used this method to alter the Ti content of welds. These authors produced welds with varying amounts of Ti, whilst maintaining relatively stable Mn levels, as shown in Table 10.

Table 10: Statistical analysis of chemical consistency of weld metal Mn content (Beidokhti et al., 2009a). Mn range is expressed as a percentage of the average Mn content.

Number	Ti (mass%)	Mn (mass%)	Average Mn content (mass%)	Range (mass%)	Range (% of average)
1	0.004	1.90	2.02	0.39	19%
2	0.02	1.92			
3	0.05	1.99			
4	0.09	2.15			
5	0.19	2.23			
6	0.22	2.29			

1.4.2. Specifically produced welding consumables and base metal

Another method often used to obtain weld metal of varied chemical composition is that of having welding consumables of varying chemical composition drawn specifically for the purposes of the study. This method was used by Ren *et al*. (2009) in their study on the change in impact energy of SAW weld metal in pipeline steel resulting from changes in welding wire composition and welding processes. The chemical compositions of their welds are shown in Table 11.

Table 11: Chemical composition (mass%) of weld metal obtained in experimental work done by Ren *et al*. (2009).

Weld code	Welding method	C	Si	Mn	Ni	Mo	Ti	Cu
S1 (wire 1)	Single wire	0.04	0.27	1.43	0.18	0.22	0.010	0.18
S2 (wire 2)	Single wire	0.04	0.28	1.41	0.32	0.37	0.013	0.23
S3 (wire 1)	Double wire	0.04	0.3	1.42	0.18	0.24	0.013	0.19
S4 (wire 2)	Double wire	0.04	0.28	1.42	0.29	0.25	0.017	0.21

This technique is beneficial as it should allow for very reproduceable weld metal chemical compositions if welding parameters are kept constant. Exact control of the composition of the welding wire is not possible, but this is not the biggest drawback of the technique: the biggest issue with this method is that the creation of a large experimental matrix with this technique is costly and time-consuming.

A similar technique involves having different base-metal chemical compositions cast, rolled, and welded on these plates, thereby altering the chemical composition of the weld metal. This technique has the same issues as discussed above, with the additional drawback that only single-run bead-on-plate welds can be used (Byun et al., 2003; Thewlis, 2000). This method poses the same problems as the wire-drawing method.

1.4.3. Alloy additions to flux

The final method used to alter weld metal chemical compositions of SAW deposits is that of adding powder of a desired alloying element to the flux. This technique was used by Fattahi *et al.* (2013) to alter the Ti content of welds. Varying quantities of Ti oxide nanoparticles were added to the SAW flux. The nanoparticles had an average size of 20 µm. The chemical compositions of the welds are shown in Table 12.

Table 12: Chemical compositions (mass%) of weld metals (Fattahi et al., 2013).

	C	Si	Mn	P	S	Cu	Cr	Ni	Ti
W1	0.13	0.34	0.72	0.015	0.014	0.07	0.02	0.03	0.030
W2	0.12	0.33	0.70	0.014	0.013	0.07	0.02	0.03	0.007
W3	0.09	0.30	0.69	0.015	0.012	0.07	0.02	0.02	0.011
W4	0.09	0.28	0.67	0.013	0.012	0.07	0.02	0.03	0.013
W5	0.07	0.29	0.61	0.012	0.012	0.06	0.02	0.03	0.021

A similar method to that described above was used by Beidokhti, Koukabi, and Dolati, (2009b). The different Ti compositions are shown in Table 13. Two different sets of welds were produced, each with varying Mn content. One set of welds contained 1.4 mass% Mn and the other contained 2 mass% Mn.

To make a fair comparison between the two groups, the Ti content would have needed to remain constant.

Table 13: Ti content of welds containing 1.4 mass% and 2 mass % Mn, and difference between two welds of ideally identical compositions (Beidokhti et al., 2009b).

Weld containing 1.4 mass% Mn	Welds containing 2 mass% Mn	Difference (% of average Ti content)
0.00	0.01	−77
0.02	0.03	−40
0.05	0.08	−46
0.10	0.11	−10
0.10	0.17	−52

Bhole *et al.* (2006) used a similar approach to alter the weld metal chemical composition in their study of the influence of Mo and Ni levels on weld metal chemical composition. They added 99.0 mass% Ni and 99.99 mass% Mo powders to a welded joint using a custom-made powder feeder. The Ni and Mo contents of the welds are given in Table 14. The authors attempted to compare the effects of Mo and Ni on weld metal in isolation from their effect on weld metal when they were added together. Table 14 shows that there were no welds that contained both Ni and Mo that had corresponding Ni and Mo concentrations in either the pure Ni or pure Mo group. This means that a fair comparison between how Ni behaves as an alloying element in the absence of Mo with that in the presence of Mo could not be made. The same can be said of the effect of Mo in the presence and absence of Ni.

Table 14: Comparison of Ni and Mo contents of welds (Bhole et al., 2006).

Only Ni		Only Mo		Ni & Mo	
mass% Ni	mass% Mo	mass% Ni	mass% Mo	mass% Ni	mass% Mo
1.02	0.289	0.11	0.294	2.03	0.995
2.56	0.218	0.07	0.817	2.91	0.7
3.75	0.297	0.10	0.881		

2. Hypothesis and research questions

2.1. Hypothesis

Ni and Mo levels in Ti-containing HSLA-steel SAW metal can be optimized in order to improve both impact properties and hardness.

2.2. Research questions

2.2.1. Weld-alloying technique

Can a novel weld alloying technique be developed that produces welds that have:

- Predictable chemical composition;
- Stable chemical composition throughout a single weld; and
- Stable chemical composition across different welds?

2.2.2. Influence of Ni and Mo

- How do Ni and Mo levels affect the:
    - Microstructure of as-welded weld metal
    - Mechanical properties of weld metal
- Is there a correlation between microstructure and mechanical properties

2.2.3. Thermal-cycling

- Can a single pass weld be used to predict the mechanical properties of a multi-pass of the same chemical composition and produced using the same welding parameters?
- How does the thermal cycling related to different HAZ regions (i.e. IR HAZ, GR HAZ, and CG HAZ) affect the microstructure and mechanical properties of as-welded weld metal.

3. Experimental procedure

3.1. Outline of experimental work

The aim of this research was to determine whether thermal cycling typically experienced during multi-pass SAW had a noticeable effect on the mechanical properties and microstructure of Ti-containing HSLA-steel weld metal at different Ni and Mo levels. A novel weld-metal alloying technique was developed to modify the chemical composition of the weld metal to produce a range of chemical compositions. The compositional range is shown in Table 15.

The weld-metal alloying technique relied on the deposition of beads of alloying elements using laser metal deposition (LMD) over which a single-run, bead-on-plate SAW was made using commercially available filler metal and flux. During the SAW process, the alloying elements deposited with the LMD were mixed into the liquid weld metal to produce an alloyed weld metal of the desired chemical composition. Initial welding was done in two different sessions. Welds 3, 4, and 7 were welded in Session 1 and the remainder of the welds were welded in Session 2. This means that both the LWD and SAW were performed with separate set-ups for Sessions 1 and 2. The same welding parameters were used during both sessions.

The weld metal samples were subjected to Gleeble thermal cycling to simulate the formation of the HAZ sub-regions typically present in the weld metal of multi-pass SAW beads.

Impact energy and hardness testing, as well as microstructural analysis, were performed on the weld metal in the as-welded condition and after reheating to the three peak temperatures to mimic the intercritically reheated (IR), fine-grained (FG), and coarse-grained (CG) heat-affected zones (HAZ) in the weld metal.

The target composition of the alloyed weld metal was 0.1 mass% C, 0.25 mass% Si, 1.4 mass% Mn, and 0.03 mass % Ti, with varying Ni and Mo contents, as shown in Table 15. The reason for the selection of the target chemical compositions was covered in Sections 1.2.1 and 1.2.4.

Table 15: Target Ni and Mo compositions for Welds 1 to 9.

	0 % Ni	1 % Ni	2 % Ni
0 % Mo	Weld 1	Weld 2	Weld 3
0.15 % Mo	Weld 4	Weld 5	Weld 6
0.3 % Mo	Weld 7	Weld 8	Weld 9

Each of the nine welds was thermally cycled to simulate weld metal that had been exposed to a thermal cycle that would produce an IR, FG, and CG HAZ. These samples were labelled Weld x (IR), Weld x (FG), and Weld x (CG). Samples that were not exposed to thermal cycling (as-welded samples) are referred to as Weld x (AW).

3.2. Overview of procedure used to evaluate weld metal

Figure 61 shows a flow chart of the experimental procedure. The welding process by which the nine welds of varying chemical composition were produced is described in Section 3.3. Transformation temperature testing (which was used to select thermal cycles for the HAZ simulations), as well as the thermal cycling itself, is described in Section 3.5. Impact and hardness testing and microscopy were performed on all nine welds in the as-welded state and for all the simulated HAZ regions. Impact and hardness testing are described in Sections 3.6.1 and 3.6.2, respectively.

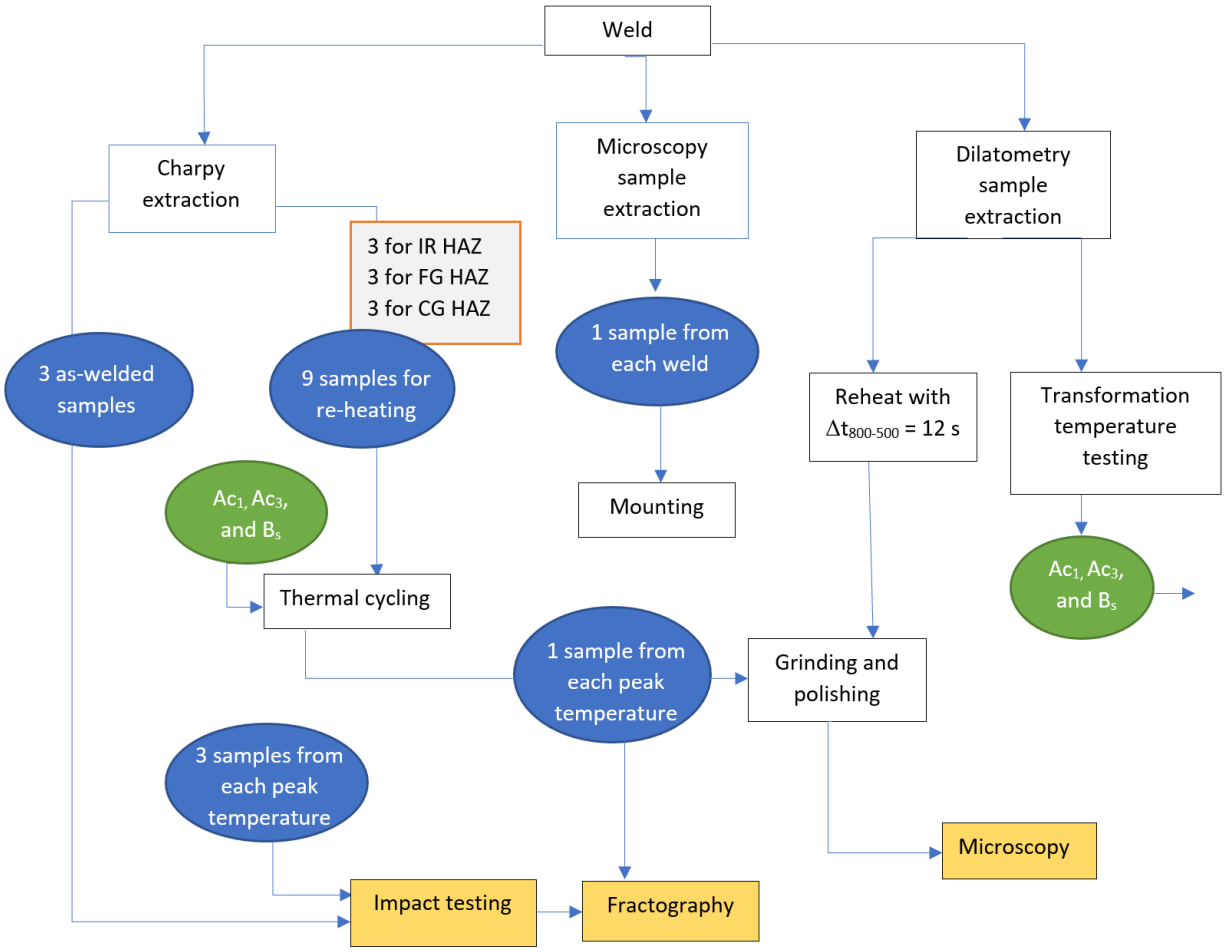

Figure 61: Flow chart of experimental procedure.

3.3. Weld-metal alloying technique

The weld-metal alloying technique used a combination of LMD and SAW. First, LMD was used to deposit pure beads of one or more alloying elements on a base plate of mild steel. Hereafter, Lincolnweld L-61 welding wire and Lincolnweld 860 flux were used to deposit a single-run SAW bead on the plate over the alloying beads. The alloying elements present in the LMD beads were mixed into the SAW metal during welding. A schematic illustration of the weld in the absence of mixing of the alloying beads and the welding metal is shown in Figure 62. A photograph of an actual weld is shown in Figure 63.

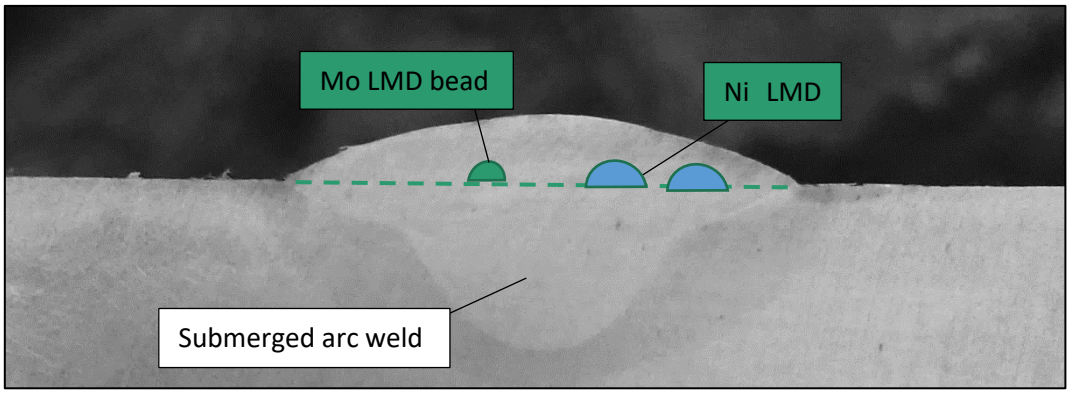

Figure 62: Micrograph of a cross section of a weld, with a superimposed schematic of LWD beads. This schematic is representative of Weld 4. The plate was 20 mm thick.

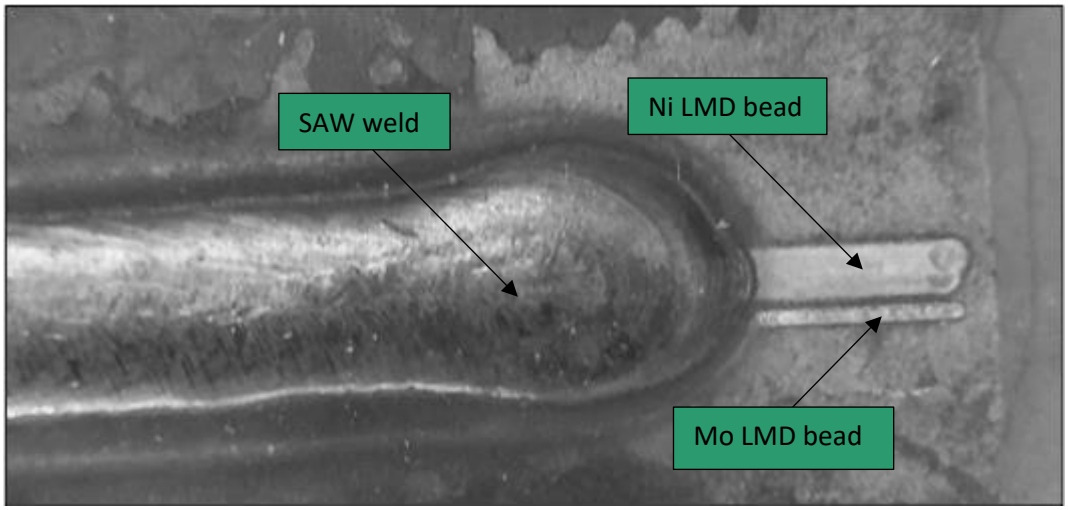

Figure 63: Photograph of a SAW weld metal partially covering three LWD alloying beads. This photograph is of Weld 4, which contained 1 % Ni and 0.02 % Ti as alloying elements.

Prior to the parameter selection process two proof of concept experiments were run that showed that all three elements (Ti, Ni, and Mo) were successfully alloyed. The chemical composition of the welds deposited for the purpose of these experiments can be found in Appendix C.

3.3.1. Laser metal deposition parameters

LMD parameters are shown in Table 16. Bead geometry, measured with a Vernier calliper, is shown in Table 17, with photographs showing the bead dimensions in Figure 64 and Figure 65. Bead width was measured directly, whilst bead height was calculated as the difference between the plate thickness and height measured at the weld. Pure Ni, Mo, and Ti powders were used to deposit LMD beads. One and two LMD beads were used to achieve 0.11 mass% Mo and 0.23 mass% Mo, respectively; two and

four LMD beads were deposited to achieve 1 mass% Ni and 2.3 mass% Ni, respectively. One LMD bead was used to achieve a Ti content of 0.025 mass%.

Table 16: Welding parameters used for LMD.

Parameter	Ti	Mo	Ni
Power (W)	900	900	900
Travel speed (m/min)	1.2	0.2	0.07
Powder feed rate (rpm)	0.5	0.5	0.8

Table 17: Bead dimensions.

Parameter	Ti	Mo	Ni
Spot size (mm)	1	2	4
Typical bead width (mm)	N.A.*	1.5	3.8
Bead height (mm)	0.2	0.5	1

*Not applicable: Ti beads were too small to be measured accurately with a Vernier caliper.

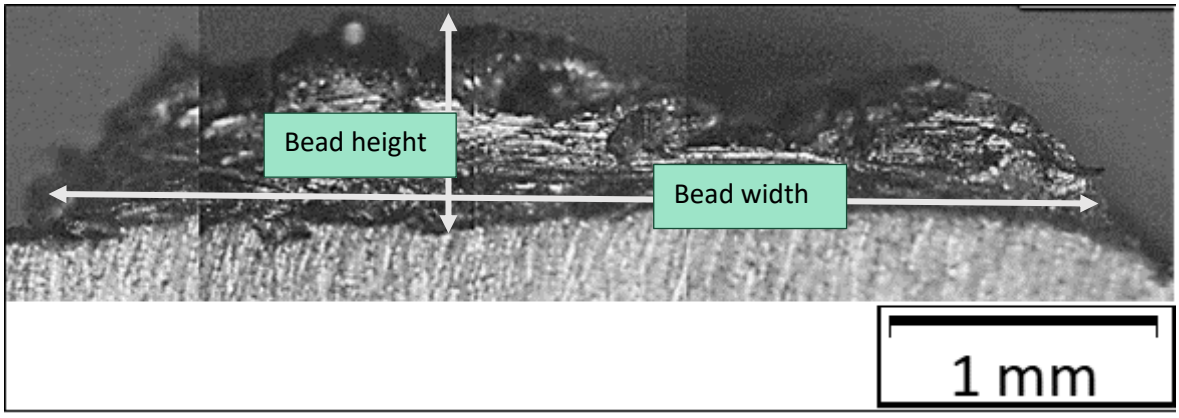

Figure 64: Composite micrograph showing the shape of a Ni laser metal deposition weld bead. Individual micrographs were taken at 50× magnification.

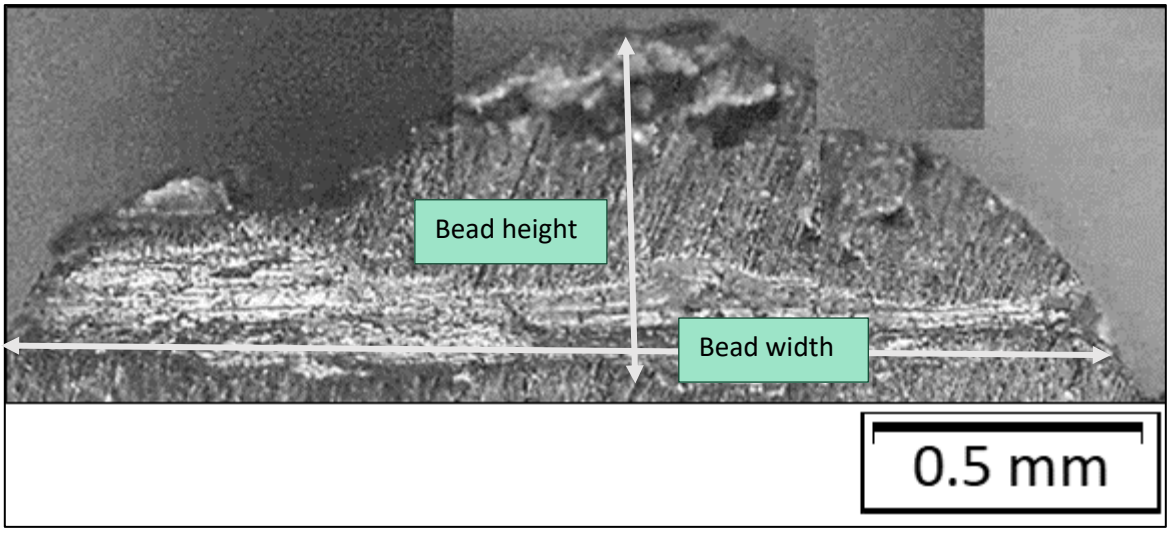

Figure 65: Composite micrograph showing the shape of a Mo laser metal deposition weld bead. Individual micrographs taken at 50× magnification.

3.3.2. Submerged-arc welding parameters

A bead-on-plate SAW procedure using Lincolnweld L-61 welding wire and Lincolnweld 860 flux was used. The unalloyed weld metal produced with these consumables contained 0.1 mass% C and 1.4 mass% Mn. The weld bead did not have any Ni, Mo, or Ti additions. The SAW parameters are shown in Table 18.

Table 18: Welding parameters used for submerged arc welding.

Variable	Value
Current (A)	550
Voltage (V)	30
Travel speed (mm/min)	426
Heat input (kJ/mm)	2.2
Current type	Square wave AC
Offset (%)	75
Balance (%)	50

3.3.3. Parameter selection

The LMD parameters detailed in Table 16 were established to achieve a specific width and thickness of the LMD bead. This enabled the target weld metal composition to be achieved. The desired LMD bead geometry was calculated through the iterative weld method described below.

The cross-sectional surface area of all submerged arc welds ($Area_{(SAW)}$) was assumed to be constant. The chemical composition of the SAW, without any alloying, was assumed to be a function of the chemical composition of the welding wire and dilution. This assumption was based on the fact that the same welding parameters were used for all the SAW beads. This constant $Area_{(SAW)}$ is represented by the cross-sectional surface area of a weld metal produced in the absence of any LMD alloying. The cross-sectional area was quantified using the image processing software *ImageJ,* an open-source Java-written image-processing software. Once $Area_{(SAW)}$ was known, the cross section area of the LMD bead $Area_{(LMD\ bead)}$ theoretically required to achieve a specific alloying content could be calculated according to Equation 9 derived from Equation 8. The correction factor (K) needed to be established

because the density of Ni, Ti, Mo, and steel is different and because the LMD welding beads are porous. The value of K is expressed by Equation 10.

$$\frac{K.Area_{(LMD\ bead)}}{Area_{(SAW\ bead)}} = \frac{mass_{Alloy\ x}}{mass_{SAW\ bead}} = mass\ \%_{Alloy\ element}$$

Equation 8

$$K.Area_{(LMD\ Bead)} = mass\%_{Alloy\ element} \times Area_{(SAW)}$$

Equation 9

Where,

$wt\%_{Alloy\ element}$ = targeted weight percentage of the alloy in the weld metal;

$Area_{(LMD\ bead)}$ = the cross-sectional surface area of the LMD bead; and

$Area_{(SAW)}$ = the cross-sectional surface area of the SAW weld metal in the absence of any LMD alloying.

K = correction factor

$$K = \frac{Measured\ mass\%_{alloying\ element}}{Target\ mass\%_{alloying\ element}}$$

Equation 10

With a known $Area_{(LMD\ bead)}$ the required spot size and bead height could be calculated according to Equation 11 and Equation 12. The ratio between the weld bead width and height is expressed by **Error! Reference source not found.**. This ratio is intentionally selected to achieve a properly adhered bead, with minimal cracking. The areas predicted by these equations are not absolutely accurate because the geometry of the LMD bead is not rectangular, as is seen in Figure 64 and Figure 65. A schematic of the weld bead geometry in relation to the LMD nozzle and laser beads shown in Figure 66.

$$Area_{(LMD\ beads)} = Bead\ height \times Spot\ size$$

Equation 11

$$Spot\ size = 4 \times Bead\ height$$

Equation 12

Figure 66 shows a sketch of the LMD arrangement. Θ is constant for a specific nozzle, so spot size is a function of the focus position distance. Bead height is then a function of travel speed and powder feed rate. A ratio between weld bead width and height of 1:4 is usually used as it tends to ensure a properly adhered bead with minimal cracking.

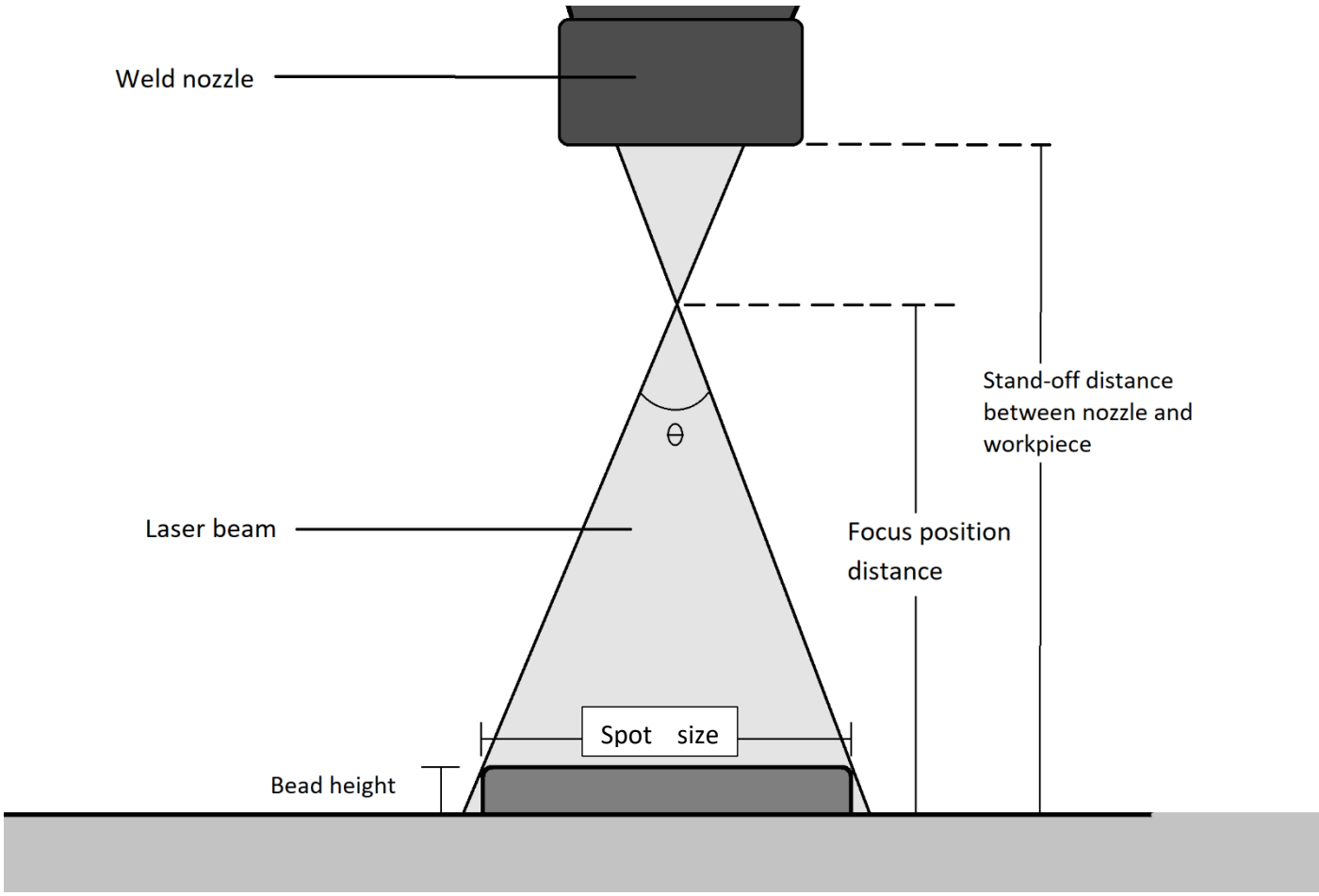

Figure 66: Schematic of laser weld deposition measurements.

LMD beads, with spot size and bead height calculated according to Equation 11 and Equation 12. LMD beads were then deposited on sand blasted plates, whereafter submerged arc welds were deposited over the LMD beads. The chemical composition of the alloyed SAW weld metal was then determined through use of optical emission spectroscopy (OES), using an iCap 6500 Radial induction coupled plasma meter. A new requisite LWD bead size ($Area_{LWD\ Bead(Adjusted)}$) was then calculated according to Equation 16, which was derived from Equation 13 to Equation 15.

$$K = \frac{Measured\ mass\%_{alloying\ element}}{Target\ mass\%_{alloying\ element}} = \frac{Area_{LWD\ bead(Origional)}}{Area_{LWD\ bead(Adjusted)}}$$

Equation 13

$$Area_{LWD\ bead(Adjusted)} = \frac{Area_{LWD\ bead(Origional)}}{K}$$

Equation 14

$$K = \frac{Measured\ mass\%_{alloying\ element}}{Target\ mass\%_{alloying\ element}}$$

Equation 15

$$Area_{LWD\ Bead(Adjusted)} = \frac{Target\ mass\%_{alloying\ element}}{Measured\ mass\%_{alloying\ element}} \times Area_{LWD\ Bead(Origional)}$$

Equation 16

Once requisite bead geometry for a single alloying element was established the requisite geometry for other alloying elements could be calculated according to Equation 17.

$$\frac{Composition\ of\ alloy\ x}{Composition\ of\ alloy\ y} = \frac{Area_{alloy\ x\ \ LWD\ bead}}{Area_{alloy\ y\ \ LWD\ bead}}$$

Equation 17

A full set of welds, with geometry calculated according to the above procedure and expected compositions shown in Table 15, were then deposited.

3.3.4. Sample calculation

An example of the iterative procedure used to adjust the Ni LWD bead size is shown below. The target composition when two weld beads with a spot size of 6 mm and a bead height of 1.5 mm was deposited was 1% Ni. The actual composition, measured by OES, was 2.3%.

Equation 11

$$Area_{(Ni\ LMD\ beads)} = 1.5\ mm\ \times 6\ mm = 9mm^2$$

$$Area_{Ni\ LWD\ Bead(Adjusted)} = \frac{1\%}{2.3\ \%} \times\ 9mm^2$$

$$Area_{Ni\ LWD\ Bead(Adjusted)} =\ 3.9\ mm^2$$

$$Spot\ size = 4 \times Bead\ height$$

$$3.9\ mm^2 = Bead\ height\ \times\ (4 \times Bead\ height) = 4(Bead\ height)^2$$

$$Bead\ height =\ 0.99\ mm$$

$$Spot\ size =\ 3.96\ mm$$

The new bead height was rounded to 1 mm and the new spot size was rounded to 4 mm^2.

Target Mo and Ti bead size was calculated as a function of Ni bead size according to Equation 18Equation 18. The area of the Ni LWD bead was double to accommodate for the fact that two weld beads were used.

$$\frac{Acieved\ Ni\ composition}{Target\ Mo\ composition} = \frac{2 \times Area_{Ni\ LWD\ bead}}{Area_{Mo\ LWD\ bead}}$$

Equation 18

Calculations for the $Area_{Mo\ LWD\ Bead}$:

$$\frac{1\ \%}{0.15\ \%} = \frac{2 \times 4\ \ mm^2}{Area_{Mo\ LWD\ bead}}$$

$$Area_{Mo\ LWD\ bead} = 1.2\ \ mm^2$$

3.4. Chemical analysis

3.4.1. Optical emission spectroscopy

The chemical compositions of all nine welds were tested using OES. OES measurements were taken directly adjacent to the location from which microscopy samples were extracted, as shown in Figure 67. The chemical compositions of these samples were used to report the chemical compositions of Welds 1–9. The accuracy of the OES results of some samples were in doubt; in these cases, OES was also performed on the microscopy samples.

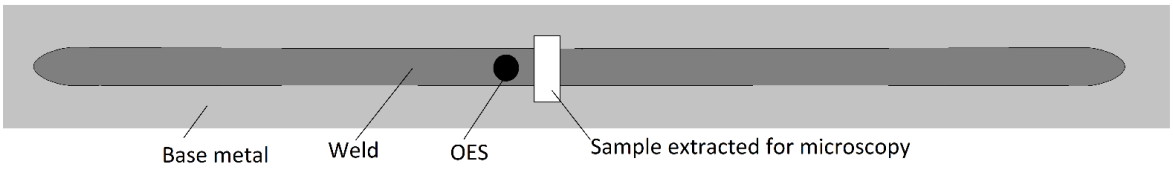

Figure 67: Top view of weld that shows the location of OES measurement relative to that of the sample extracted for microscopy. The reported chemical composition of each weld was obtained from this OES measurement. The total length of a weld bead was typically 450 mm.

An OES traverse was also performed on one of the welds from the trial runs to establish the stability of chemical composition along the length of the weld. A schematic of the OES locations is shown in Figure 68. The chemical composition was determined at five positions along the length of the weld bead, with a distance of 50 mm between measurements, giving complete coverage of the changes in chemical composition along the first 250 mm of the weld bead.

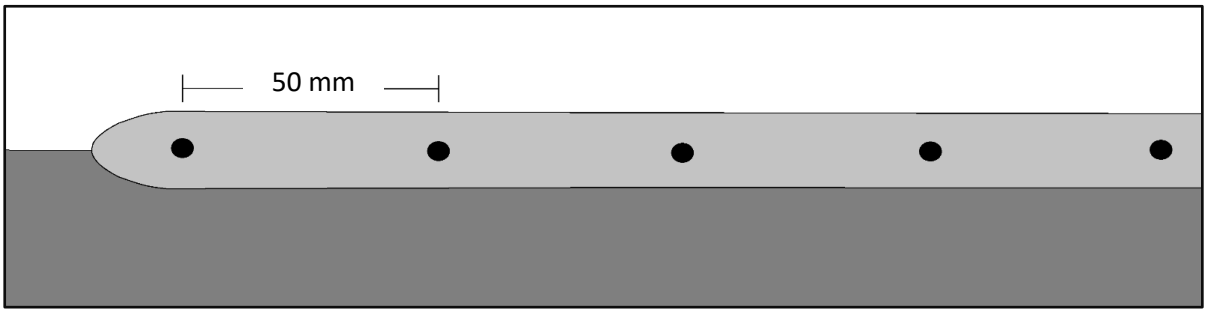

Figure 68: Schematic of a longitudinal cross-section of the weld, showing the locations where measurements were taken for the OES traverse performed along the length of the weld from the trial run.

3.4.2. Scanning electron microscope energy-dispersive x-ray spectrometry

Energy-dispersive X-ray spectrometry (EDS) was also performed on the mounted samples to evaluate the variability of Ni, Mo, and Ti concentrations along the *x*- and *y*-axes of a cross-section of the weld, as shown in Figure 69. EDS was performed using a Zeiss Gemini 2 Crossbeam 540 field-emission gun (FEG) SEM with an EDS detector. The accelerating voltage used was 20 kV, with a working distance of 9 mm, and the acquisition time was 120 s. Mo and Ti concentrations and variability along the cross-section of the welds are reported.

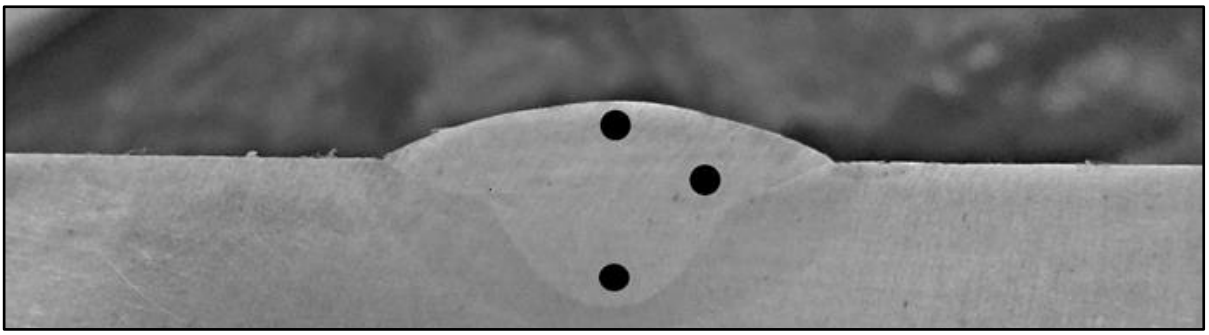

Figure 69: Location on SAW weld where EDS was performed.

The reproducibility of the weld-alloying technique was evaluated by preparing duplicated alloyed welds for Welds 3, 4, and 7. These duplicates were produced in a different weld session (Session 3) from the original set of welds. OES was performed on these welds at the same location, approximately at the centre of the weld bead, as shown in Figure 67.

SEM-EDS was also used to test for segregation of alloying elements to PAGBs in Welds 6 and 9. The average Mn and Ni contents at PAGBs and prior austenite grain centres were calculated from 21 readings from five sites for Weld 6 and 17 readings from seven sites for Weld 9.

SEM-EDS was also used to test whether any of the inclusions in the welds contained significant amounts of S. This was done because MnS is known to have a higher thermal expansion coefficient than steel, whilst Mn, Si, and Ti oxides are known to have a lower thermal expansion coefficient than steel. Inclusions of Welds 2 to 8were analysed. Five inclusions per sample were analysed. Inclusions selected for analysis were selected at random.

3.5. Heat-affected zone simulation

3.5.1. Introduction

Once appropriate chemical compositions of Welds 1–9 were confirmed, Charpy samples were extracted from the weld metal, as described in further detail in Section 3.6.1. The Charpy samples were subjected to thermal cycling simulations described in Section 3.5.3 using a Gleeble 3500 thermomechanical simulator. The purpose of the thermal cycling was to reproduce the three HAZ regions that typically appear in a weld metal during multi-pass SAW as a result of the induced thermal cycling. The mechanical properties of the simulated HAZ regions could then be compared with those of the as-welded weld metal. The peak temperature required to produce each HAZ region was calculated according to measured Ac_1 and Ac_3 transformation temperatures. The procedure used to measure these transformation temperatures is discussed in Section 3.5.2.

3.5.2. Dilatometery

Dilatometry was carried out on samples machined from all nine welds to determine the transformation temperature of each weld, using a Bähr deformation dilatometer 805D. Dilatometry samples were extracted from the weld using wire erosion cutting. Figure 70 shows a schematic of how and where samples were extracted.

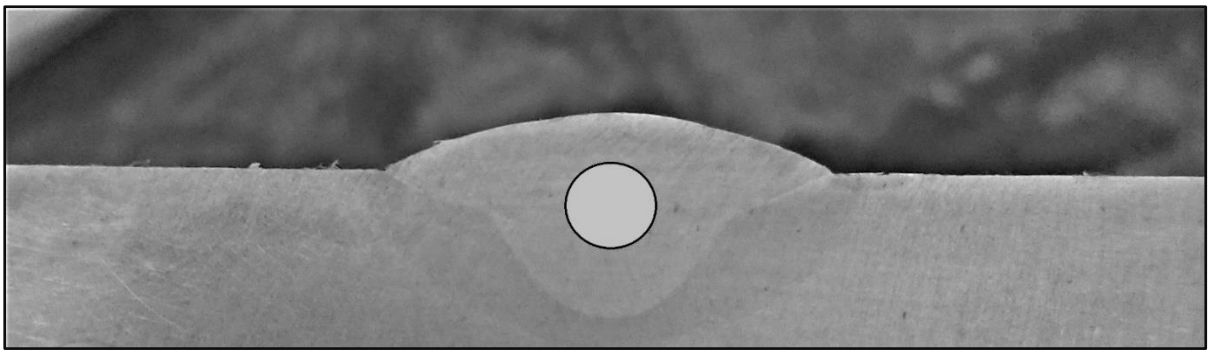

Figure 70: Photograph of weld cross-section with an overlay showing where the dilatometer samples were extracted. Weld bead was about 20 mm wide.

Ac_1 and Ac_3 temperatures were measured using the part of the thermal cycle represented by the solid black line shown in Figure 71. The initial heating rate was 0.17 K/s up to 600 °C. After the sample had reached this temperature, a rate of 0.04 K/s was used for heating through the critical temperature zone to 1000 °C. The faster heating rate of 600 °C could be used because no phase transformation occurred in this temperature range. The heating rate across the critical temperature region was based on previous work that measured transformation temperatures (ASTM Standard A1033 - 18, 2018; De Andrés et al., 2002).

The results of these tests were used to determine the peak temperatures for the thermal cycling experiments. A second set of dilatometry tests were performed to confirm that the calculated peak temperatures were correct and to measure the bainite start temperature (B_s) of each weld. B_s was measured tobetter understand changes in mechanical properties and microstructures of the reheated weld samples. The thermal cycle used for these tests is shown in Figure 71. This included the controlled cooling rate (shown by the dotted line) of 37 K/s. This was calculated from a $\Delta t_{8/5}$ of 8 s, which was used for the Gleeble thermal cycles. $\Delta t_{8/5}$ refers to the time, in seconds, that a weld takes to cool from 800 °C to 500 °C.

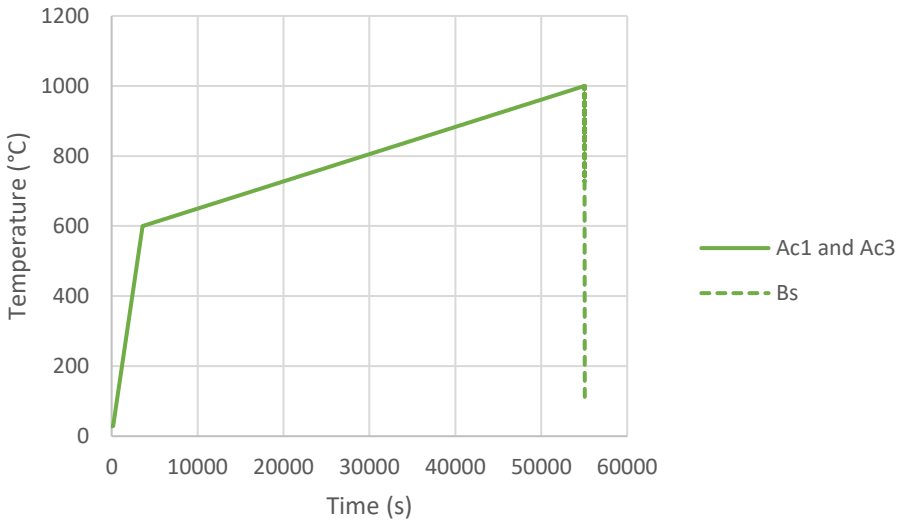

Figure 71: Change in temperature measured during the thermal cycle relative to the time of measurement used to confirm Ac_1, Ac_3 and determine B_s for Welds 1–9.

An example of the output data from the dilatometry experiments and how these were used to determine transformation temperatures are shown in Figure 72. The indent occurring at 600 °C is where the heating rate of the test was slowed from 0.17 K/s to 0.04 K/s, as noted earlier. Points at which B_s Ac_1, and Ac_3 were measured are shown in the figure.

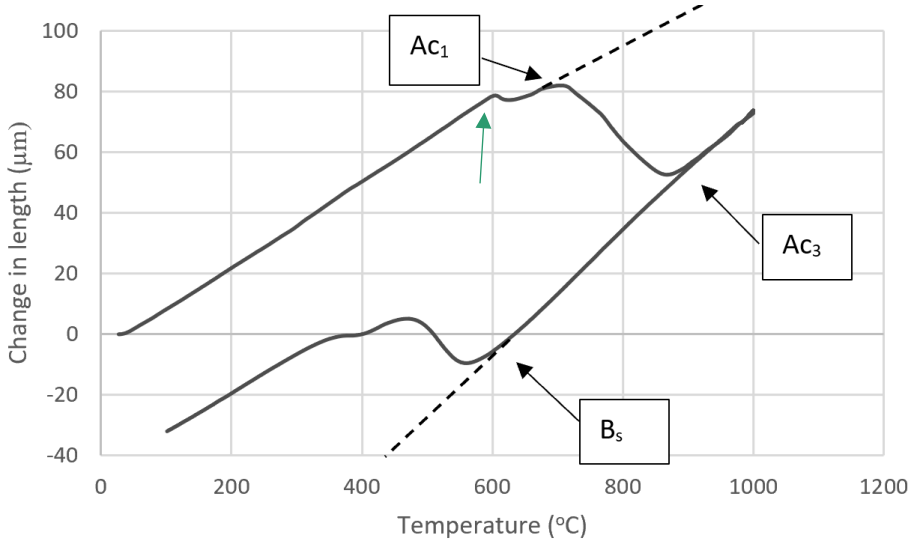

Figure 72: Typical dilatometry curve for the dilatometry tests to which each weld was subjected. This is the curve for Weld 3. The point where heating rate was reduced is indicated with a blue arrow.

3.5.3. Thermal cycling

Twelve Charpy impact samples were machined from each weld. Three were used in the as-welded condition and nine were reheated using the Gleeble 3500 thermomechanical simulator. Details on preparation of Charpy impact test samples and testing can be found in Section 3.6.1. The peak temperature required to produce each HAZ region was calculated according to Equation 19, Equation 20, and Equation 21. T_{IR}, T_{FG}, and T_{CG} refer to temperatures used to simulate the IR HAZ, FG HAZ, and CG HAZ, respectively. Each of these temperatures, as well as the Ac_1 and Ac_3 temperature of each weld, is shown in Table 19.

.

.

$$T_{IR} = \frac{Ac_3 - Ac_1}{2} \,^{o}\mathrm{C}$$

Equation 19

$$T_{GR} = Ac_3 + 75 \,^{o}\mathrm{C}$$

Equation 20

$$T_{GG} = 1350 \,^{o}\mathrm{C}$$

Equation 21

Table 19: Ac_1, Ac_3 temperature of each sample and peak temperatures used to simulate each HAZ region.

Weld	Actual A_{c1} temperature (°C)	Actual A_{c3} temperature (°C)	Peak temperature		
			Intercritical region (T_{IR}) (°C)	Grain-refinement region (T_{GR}) (°C)	Grain-growth region (T_G) (°C)
1	717	890	804	965	1350
2	707	869	788	944	1350
3	746	930	838	1005	1350
4	697	893	795	968	1350
5	709	893	801	968	1350
6	651	906	779	981	1350
7	718	956	837	1031	1350
8	730	957	844	1032	1350
9	727	876	802	951	1350

The $\Delta t_{8/5}$ of the original SAW was estimated to be 10 s, and this was the intended $\Delta t_{8/5}$ for these experiments. The estimation was based on results derived from solutions to the equations published by Rosenthal (1946), as discussed in Section 1.3. Thermal conductivity was taken to be 45 J/sK (Peet et al., 2011); volume thermal capacity used was 4.5×10^6 J/m^{3}K (Babu et al., 1999); and heat input (HI) used was 2.2 kJ/mm. Output data from Gleeble cycling, shown in Figure 73, shows that the actual $\Delta t_{8/5}$ achieved was 8 s.

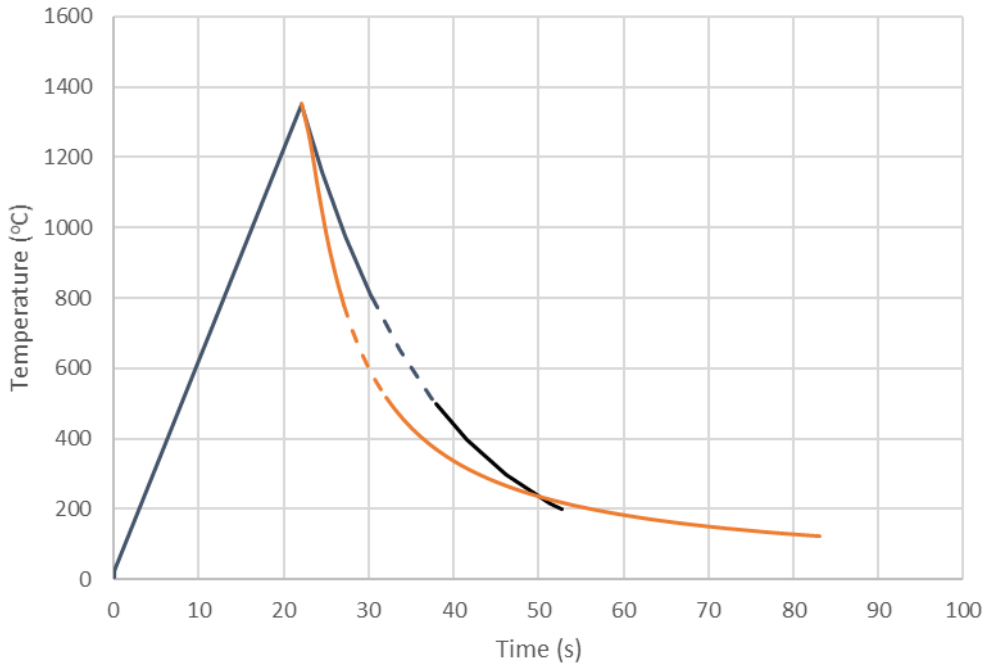

Figure 73: Line graph showing the change in temperature as a function of time, as reported by the Gleeble (black line). As calculations indicate, this would have occurred during actual welding (orange line), as estimated using equations published by Rosenthal (1946). The dotted segment of each line shows the cooling time from 800 s to 500 s. These results come from the temperature measured during Gleeble thermal cycling for the GG HAZ for all welds.

Additional thermal cycling work was done using the dilatometer to establish the sensitivity of the microstructure and hardness to the $\Delta t_{8/5}$. The thermal cycle was the same as shown in Figure 73, but with a $\Delta t_{8/5}$ of 12 s.

3.6. Mechanical testing

3.6.1. Impact testing

As part of the development of the experimental programme, the ductile-to-brittle transition temperature (DBTT) of Weld 1 was measured by testing impact energy of this weld at 10, 0, −10, −20, and −30 ˚C, as shown in Figure 74. Impact testing was done using full size Charpy specimens (10 mm × 10 mm × 55 mm) and a KV8 (V-notch 10 x 5.0) impactor size was used. DBTT is usually defined as the temperature where the impact energy shifts from the upper-shelf region to the lower-shelf region. These tests were done to ensure that Charpy impact tests were carried out at sufficiently low temperatures. The intended testing temperature was −40 ˚C (Kang et al., 2015). The results of these experiments showed that this temperature is well below the DBTT of Weld 1. Had this not been the case, a different testing temperature would have been considered.

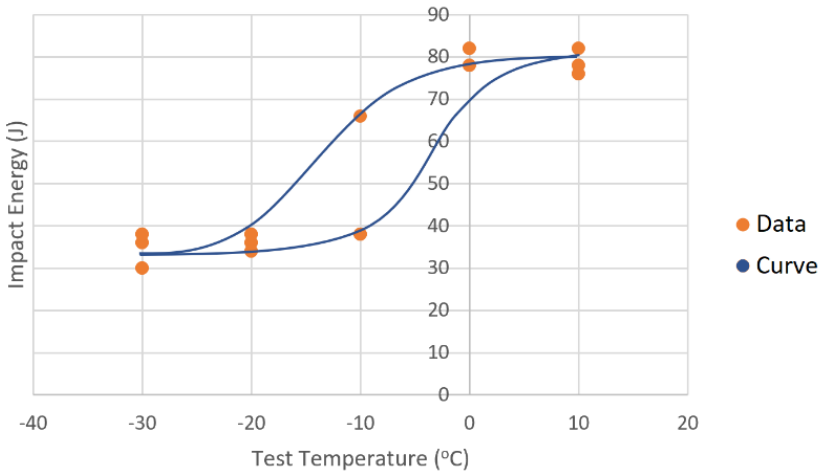

Figure 74: Graph showing how the DBTT of Weld 1 was measured. Samples were full-size coupons.

Charpy testing was also performed on each sample in the as-welded condition and on all thermally cycled samples. The machined samples exposed to each thermal cycle for a specific weld were selected at random so that the location of each Charpy impact test was effectively random along the weld line. This is indicated in Figure 75. Samples were machined as shown in Figure 76. Hereafter, they were thermally cycled and, after thermal cycling, were milled to a thickness of 5 mm. Equation 22,derived from Table 6 in ASTM A370, was used to calculate the full-size Charpy impact energy.

$$IE_{Full\ size} = 2 \times \left(IE_{Half\ size}\right) + 0.0367$$

Equation 22

During milling, damage occurred to one of the welds from Weld 1 (IR), Weld 1 (CG), Weld 6 (IR), and Weld 8 (CG); therefore, only two Charpy impact tests were done for these samples. There was insufficient weld metal for the sample requirements of Welds 3, 4, and 7 and additional welds had to be made. Thermal cycling to the CG HAZ was performed with these samples. The chemical composition of the second weld of Weld 3 was out of specification so Weld 3 CG HAZ results are omitted.

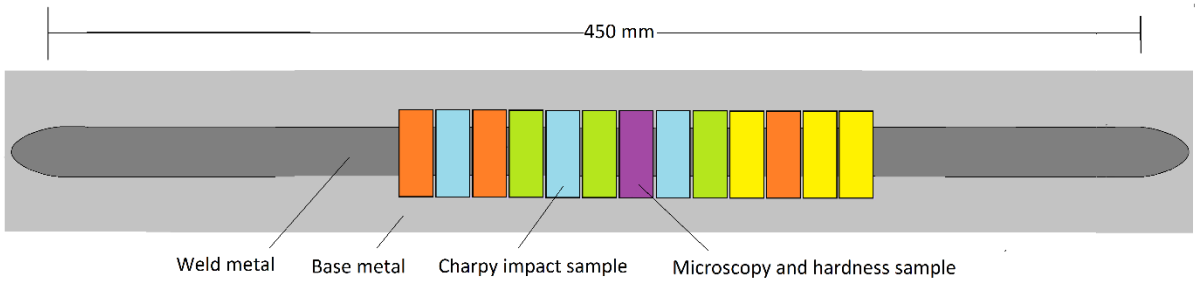

Figure 75: Schematic showing where Charpy impact test samples were extracted and random location of a specific reheated sample. Welds were extracted from the centre of the weld to avoid variation in chemical composition, which was confirmed to occur at the start of the weld bead (Figure 87). The total weld length used for the impact toughness samples was about 180 mm.

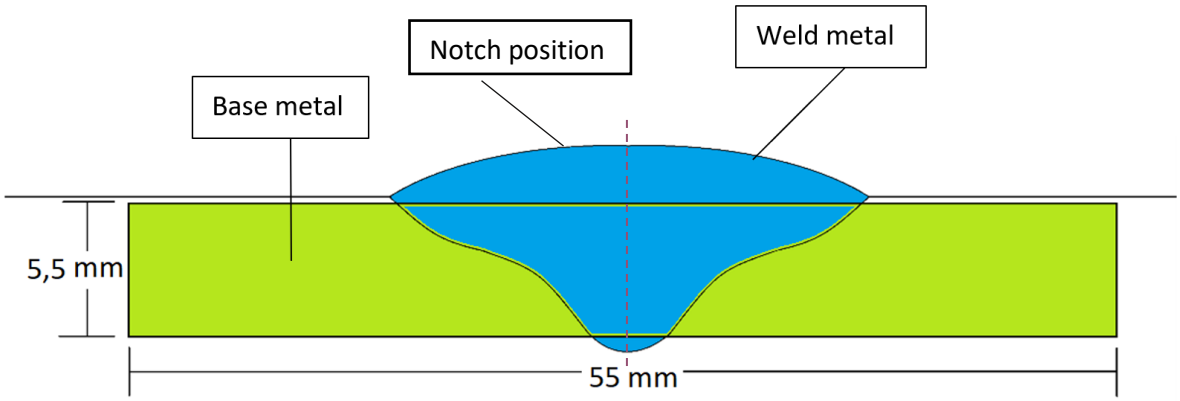

Figure 76: Schematic cross-section of the extraction of Charpy impact test pieces from as-welded samples.

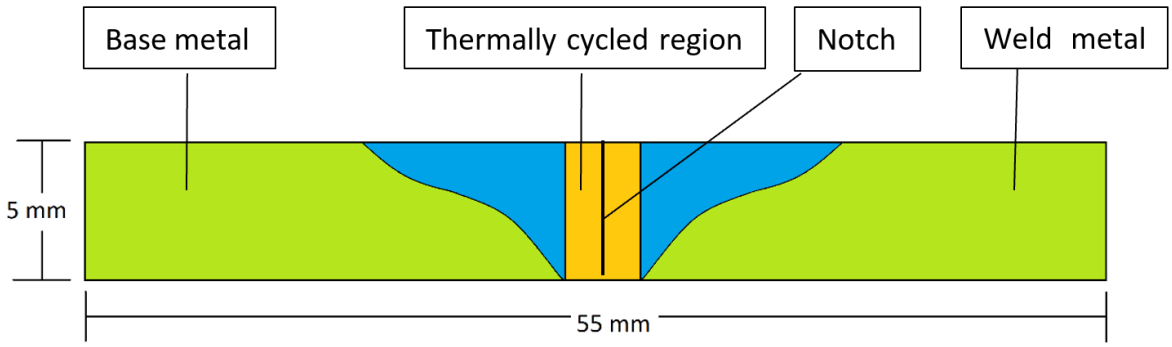

Figure 77: Schematic of the extraction of Charpy impact test samples from thermally cycled samples.

3.6.2. Hardness testing

Hardness tests were performed on samples after microscopy, in the polished and etched condition. Future-Tech (FM-700) Vickers microhardness tester was used. Etching ensured that hardness measurements fell in the correct location. Eight indentations were made on each sample. Indentations were made in the thermally cycled region for thermally cycled welds and hardness measurements of as-welded welds were limited to the same region, i.e., the centre of the weld. Hardness was measured with a Vickers hardness tester and a 10 kg load. A minimum distance of three times the diameter of an indentation was left between indentations.

Hardness measurements were used to estimate the tensile strength of samples according to the hardness conversion table from ASTM E140-12B (2019)e1. This standard provides a table that allows one to read off the ultimate tensile strength associated with a certain hardness. The table starts at a hardness of 80 HV10 and increases in multiples of 5. Interpolation was used to calculate the tensile strength if a hardness reading was not a multiple of 5. Standard deviation was calculated using the "Std.Dev()" function in *Excel* and the 95 % confidence interval (*CI*) was calculated according to Equation 23:

$$95\%\ CI = \pm \frac{t \times \sigma}{\sqrt{n}},$$

Equation 23

where t = 2.365, σ is the standard deviation, and n = number of fields measured.

3.7. Microscopy

3.7.1. Surface preparation

As-welded samples were extracted and mounted in black Bakelite, then ground and polished. The thermally cycled samples were ground and polished without further machining or mounting. Orientation of the sample is shown in Figure 78.

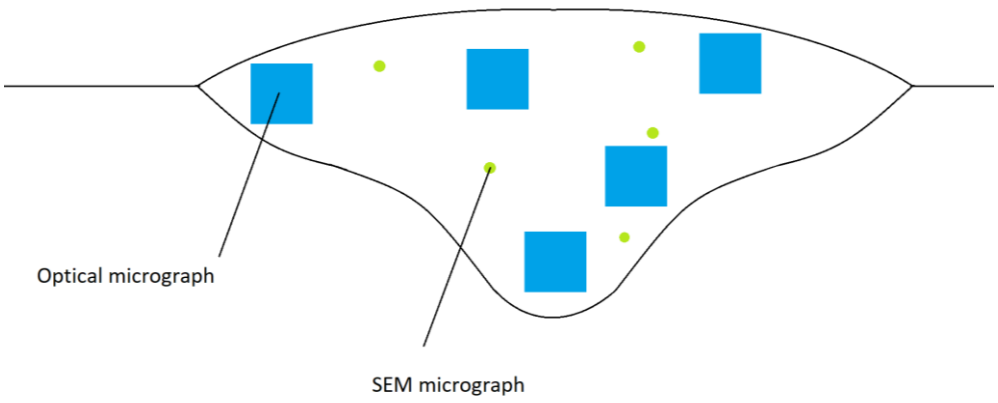

Figure 78: Schematic of the orientation of microscopy samples, also showing random locations of optical microscopy and SEM analyses.

All samples were ground using 150 µm, 90 µm, 40 µm, 30 µm, 25 µm, 15 µm, and 8 µm grinding paper. The samples were then polished with 3 µm diamond solution and etched using a 2 % Nital solution. This step was repeated twice. The final etching time was carefully controlled to expose the microstructure. The same sample preparation was used for the optical and scanning electron microscopy analyses.

3.7.2. Optical microscopy

Optical microscopy was performed on all weld samples in the as-welded condition and following thermal cycling. Optical microscopy was performed using an Olympus BX51M instrument. Bias with regards to micrograph location was avoided by moving the sample to a new location without looking through the eye piece of the microscope (Figure 78). Fraction grain boundary products (GBPs) were measured using optical microscopy.

3.7.3. Scanning electron microscopy

SEM metallography was performed on all weld samples in the as-welded condition and following thermal cycling, using a Zeiss Gemini 2 Crossbeam 540 FEG SEM. SEM locations were selected at random by reducing the magnification of the sample to the minimum possible and then moving the platform to a random location before increasing magnification again and capturing the image. This was done to avoid bias. Ferrite grain size and fraction of IfRs were measured using SEM.

3.7.4. Quantitative metallography

Optical microscopy was used to qualitatively study the GBPs of each sample. Samples were also quantitatively studied by performing a point count on optical micrographs that had been taken at 200× and 500× magnification. A grid of 108 points per field was used with 10 fields per sample, in accordance with ASTM Standard E 562 (2011). Five of the fields were taken at 200× and five at 500× magnification. Percentage GBP was calculated using the results of the point counting. Low-voltage high-resolution SEM microscopy was used to measure the ferrite grain size and the fraction of IfRs decorating the areas between AF and GBP grains.

SEMs are usually operated at an accelerating voltage of about 20 kV. An example of an image obtained at this accelerating voltage is shown in Figure 79(a). Low-voltage high-resolution SEMs, such as the Zeiss Gemini 2 Crossbeam 540 FEG SEM, are usually operated at 0.5 kV to 2 kV. Owing to the lower accelerating voltage, electrons do not penetrate very deeply into the sample and allow for a truer representation of the surface. An example of such a micrograph is shown in Figure 79(b). It should be noted that, because of the sensitivity of this instrument, the micrograph captured at 20 kV is more detailed than a similar micrograph would have been if a conventional SEM had been used.

The drawback of high-resolution microscopy is that surface preparation becomes very important, as even very fine scratches will show up. The benefit, however, is that the difference between scratches and grain boundaries is more clearly discernible, as shown in Figure 79.

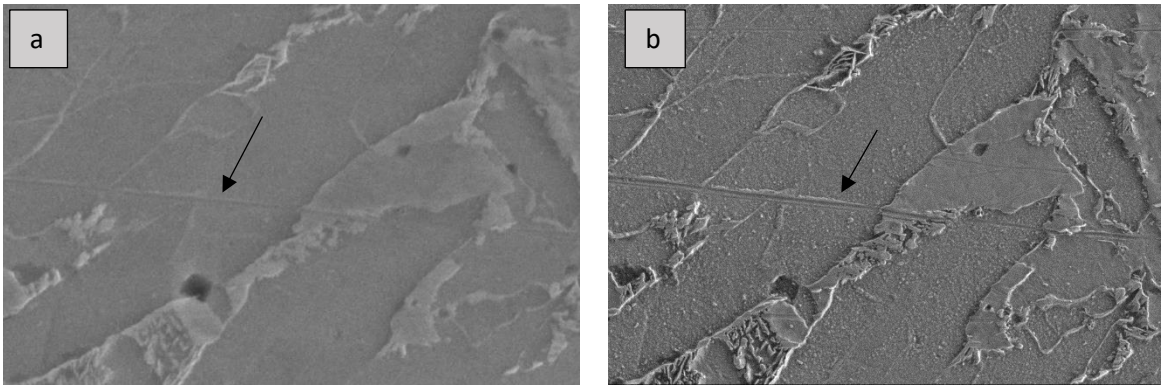

Figure 79: Scanning electron micrograph captured at an accelerating voltage of a) 20 kV and b) 2 kV using a Zeiss Gemini 2 Crossbeam 540 FEG SEM. A scratch is indicated by a black arrow.

Image analysis was performed using micrographs taken at 10 000× magnification with the SEM. ASTM Standard 1382-97, (2010) stipulates that a magnification be used such that a minimum of 50 grains are visible and that discernment between grains is possible. Clear discernment of IfRs was possible at 10 000× magnification, without losing an impression of the AF morphology. Locations at which each micrograph was taken were selected by reducing magnification to the lowest possible level, moving the stage around at random, and then increasing magnification again. This ensured that areas for analysis were selected at random and prevented areas of interest from selectively being used for analysis.

Images were processed using *Procreate* image-processing software, which allows for digital tracing of grains and phase regions by hand, as opposed to reliance on hue and contrast adjustments used in more conventional techniques. The software was used to create processed images (Figure 81) from the original (Figure 80). *Image J* was used to analyse grain size and the percentage interferritic phases.

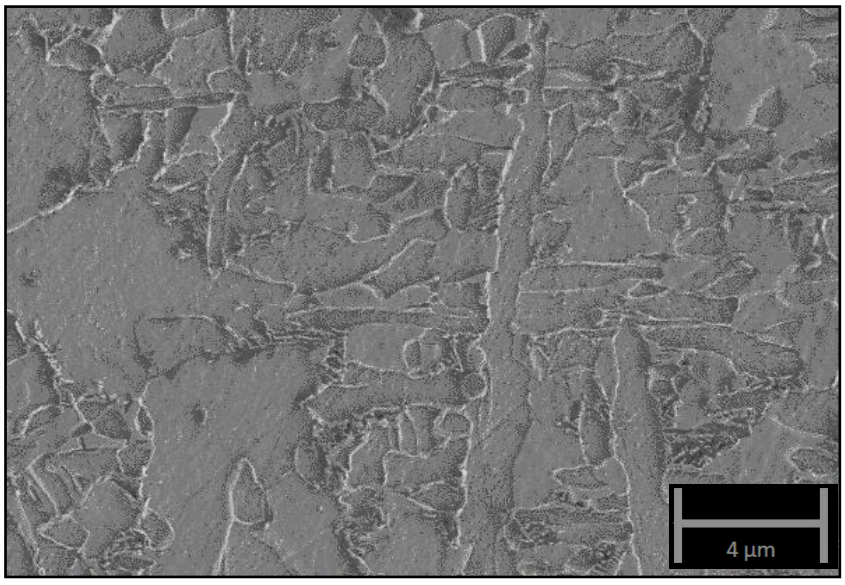

Figure 80: Original SEM micrograph (Sample 1 AW).

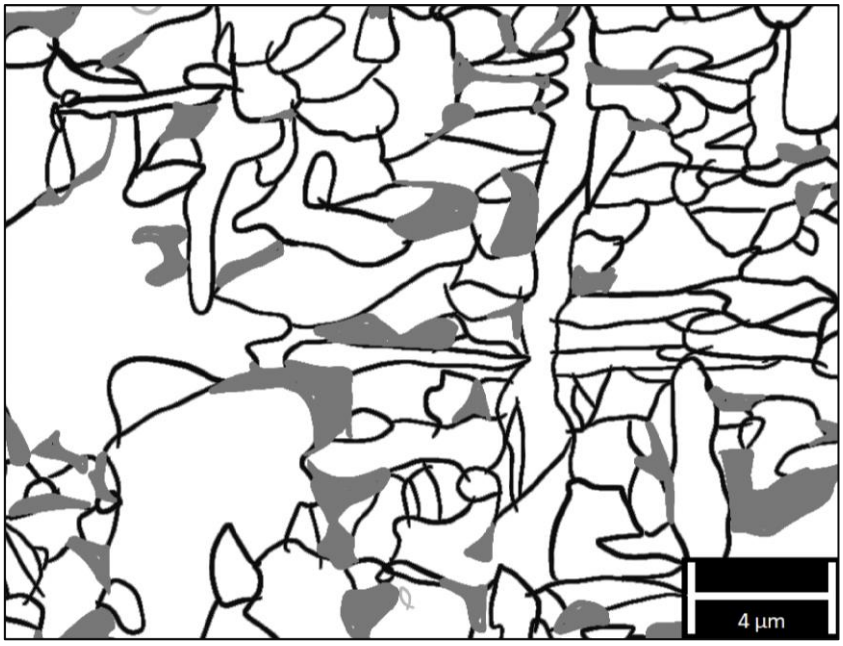

Figure 81: Processed SEM micrograph (Sample 1 AW). Grey grains represent M/A regions.

In most cases grain boundaries were clearly discernible, as shown in Figure 80 and Figure 81. Grain boundaries were either slightly raised regions between two grains or they were identified as the junction between two grains where one grain was slightly raised in relation to the adjacent grain.

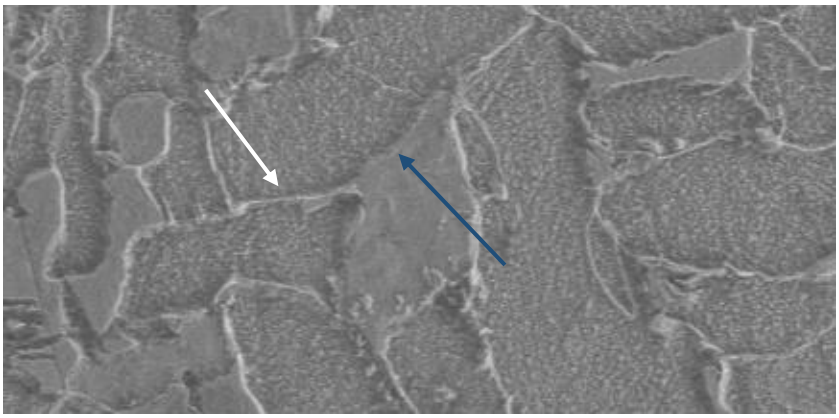

Figure 82: Micrograph showing how grain boundaries were identified. The white arrow shows a grain boundary that appeared as a raised region between two grains. The dark blue arrow shows a grain boundary separating a grain that was slightly raised in relation to the grain adjacent to it.

In some samples, the transition from secondary AF to IfRs was not noticeably clear. Regions were classified as AF if clear grain boundaries were discernible. Figure 83 shows a region of fine secondary AF on the left and an area classified as an interferritic on the right. The region of fine secondary AF has clear grain boundaries, whilst the IfRs does not.

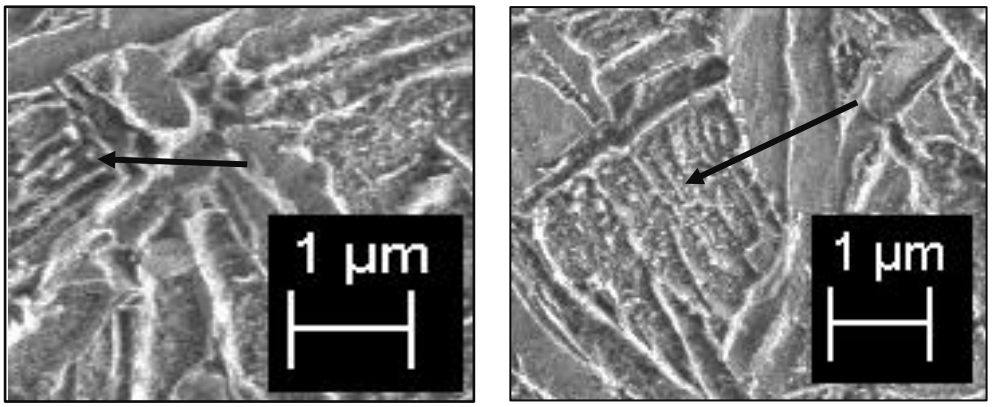

Figure 83: SEM micrographs showing (left) a region of very fine secondary acicular ferrite and (right) an interferritic M/A region.

Results of both optical and SEM microscopy were used to calculate the AF fraction. AF is conventionally quantified and reported in the literature according to Equation 24 (Beidokhti et al., 2009b). The percentage GBP referred to in the equation includes GBF, Widmanstätten ferrite, and bainite. The martensite in this equation refers to austenite that transformed to pure martensite and does not include M/A particles found in IfRs (Evans and Bailey, 1997). Martensite was not formed in any samples in the present study but is shown in the equation because it would have been considered in the manner shown had it formed.

$$\%AF_{Conventional} = 100\% - \%GBP - \%Martensite,$$

Equation 24

where

$\%AF_{Conventional}$ = percentage acicular ferrite according to how it is traditionally measured;

$\%GBP$ = percentage grain boundary products

The AF content calculated according to Equation 24 and reported in the literature does not distinguish between true AF and IfRs that contain various forms of ferrite and M/A islands. Figure 84 shows an example of such phases. True AF here refers to ferrite that nucleates from intergranular inclusions and grows via a shear mechanism (primary AF) and ferrite that nucleates and grows, also via shear, from these primary AF laths. The reason for this lack of distinction is likely because conventional SEM is not sensitive enough to allow for discernment between these two phases. This is described in more detail in Section3.7.1.

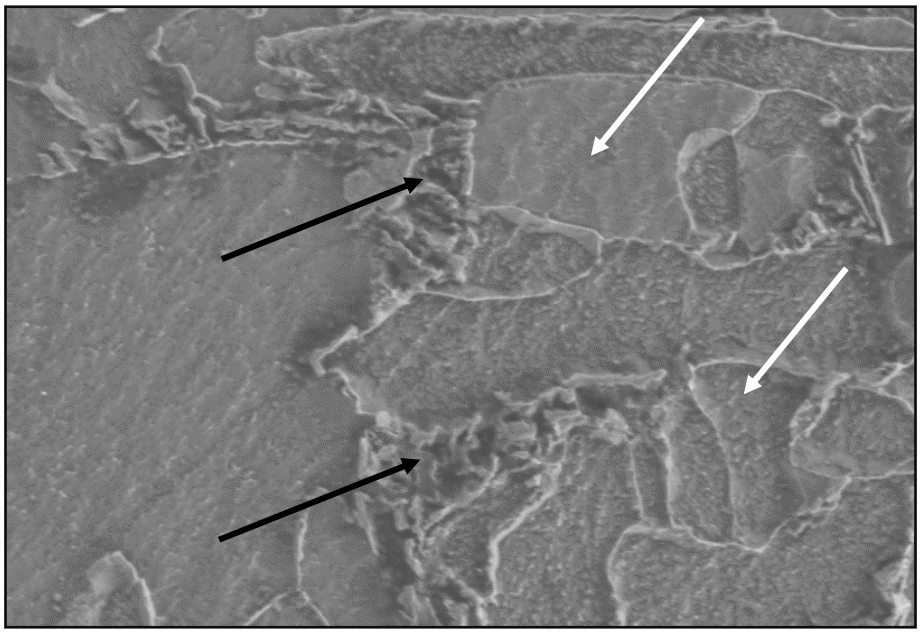

Figure 84: SEM micrograph showing a microstructure region of what would conventionally be M-A regions (black arrows) within the overall ferrite (AF) regions (white arrows).

Figure 84 shows a SEM micrograph of a microstructural region that would traditionally be classified as consisting of AF only; however, it is clear that this region contained true AF (indicated by black arrows) and IfRs. A detailed discussion on IfRs can be found in Section 1.1.2. In this research, an approach was followed to differentiate between true AF and IfRs; thereby quantifying the percentage of true AF present by using Equation 25. IfR region content was determined using high-resolution SEM analysis, as described in Section3.7.3. This means that true AF could also be expressed by Equation 25:

$$\%\ AF_{True} = \%AF_{Conventional} - \ \%IfR$$

Equation 25

$$\%AF_{True} = 100 - (\ \%\ GBP + \ Martensite + \%IfR)$$

Equation 26

where

% $AF_{(True)}$ = percentage true acicular ferrite

% $AF_{(Conventional)}$ = percentage AF according to conventional measurement

% GBP = percentage grain boundary products (determined by optical metallograph)

% IfR = interferritic region (determined by scanning electron microscopy)

The confidence interval for both GBP and IfR was calculated according to Equation 27.

$$95\ \%\ CI = 1.96\ \frac{(P_p)}{\sqrt{P_\alpha}},$$

Equation 27

where P_p = estimated volume fraction and P_α = number of points in α.

The grain size analysis tool from *Image J* produces an *Excel* spreadsheet with the grain size of each individual grain for a given area. Grain size was reported in pixels and calculated as the product of the number of pixels in the *x*- and *y*-directions, which were then converted to μm^2 and then μm. Grain size analysis was separately done to measure the grain size of AF and M/A grains. This spreadsheet was used to determine the 95 % confidence intervals according to Equation 27.

Different magnifications had to be used to calculate the GBP and IfRs contents because of the difference in their grain sizes: a magnification that was high enough to discern IfRs was too high to accurately measure the volume fraction of GBF, bainite, and Widmanstätten ferrite. Because the use of different magnifications to measure the phases was unavoidable, the decision was made to use the equipment that would allow each phase to be measured most accurately. This means that, statistically, GBP content and IfRs need to be considered as independent estimates and the variance of $\%AF_{(True)}$ must be calculated according to Equation 28. Standard deviation could then be calculated according to Equation 28 and 95 % confidence interval according to Equation 29.

$$Variance_{\%AF_{True}} = StDev_{\%\ GBP}{}^2 + StDev_{\%IfR}{}^2$$

Equation 28

$$Standard\ deviation_{\%AF_{True}} = \sqrt{Variance_{\%AF_{True}}}$$

Equation 29

3.7.5. Fractography

Fractography was performed on the fracture surfaces of Charpy impact samples of interest. All fractographs were taken on the Mode 1 flat fracture area. Samples evaluated are shown in Table 20. Samples 1, 3, 4, and 7 (AW) were evaluated to understand the fracture behaviour of as-welded samples that had high impact energy values. The fracture surfaces of Welds 6 and 9 (AW) were evaluated because these samples had lower impact energy values than the other as-welded samples. The remainder of the samples were selected because they showed either a dramatic change in microstructure without accompanying loss in impact energy (Weld 6) or because they showed an accompanying decrease in impact energy after exposure to a weld thermal cycle.

Table 20: Welds on which fractography was performed and reason for analysis.

	As-welded	IR HAZ	GR HAZ	GG HAZ
Weld 1	Reference			
Weld 2				
Weld 3	Only high-Ni sample that did not have a low impact energy			
Weld 4	Reference	Reduction in impact energy		
Weld 5		Reduction in impact energy		
Weld 6	Low impact energy	Impact energy did not change	Impact energy did not change	Impact energy did not change
Weld 7	Reference	Reduction in impact energy		
Weld 8			Reduced impact energy	Reduced impact energy
Weld 9	Low impact energy			Reduced impact energy

3.8. Statistical Analysis

3.8.1. Regression analysis

Multiple linear regression analyses were performed to evaluate all possible correlations between changes in chemical composition and mechanical properties and microstructural changes. Interaction effects between Ni and Mo contents were also evaluated. Further interaction effects were not evaluated because there were not enough data points to accommodate for more than three variables in the multiple regression analysis. A minimum of 10 data points per *x*-variable of the linear regression analysis is required to prevent false correlation effects (Statistics solutions, 2020). Correlation between mechanical properties and microstructural properties was also evaluated. The regression analysis function of *Excel* was used and only linear regression was evaluated. Variables tested are shown in Table 21. The influence of chemical composition was evaluated for impact energy, hardness, GBP content, true AF content, IfRs content and grain size, to establish if controlled variables (chemical composition and peak temperature during thermal cycling) alone could predict mechanical properties or microstructure. Microstructural measurements, chemical composition, and a combination of both were tested to see if they could predict mechanical properties. This was to test if the expected relationships between microstructural and mechanical properties were valid. The correlation between hardness and chemical composition on impact energy was tested because this would be a very valuable correlation with regard to impact energy estimation.

Table 21: *x*-variable combinations checked for statistical influence on impact energy, hardness, and microstructure.

Y-variable	X-variables		
Impact energy	mass % Ni	mass % Mo	
	mass % Ni	mass % Mo	mass % Ni x mass % Mo
	Hardness		
	Hardness	mass % Ni	mass % Mo
	% GBP		
	% GBP	mass % Ni	mass % Mo
	% $AF_{(True)}$		
	% $AF_{(True)}$	mass % Ni	mass % Mo
	% M/A		
	% M/A	mass % Ni	mass % Mo
	Grain size		
	Grain size	mass % Ni	mass % Mo
	% $AF_{(True)}$	Grain size	
	Peak temperature		
	Peak temperature	mass % Ni	mass % Mo
Hardness	mass % Ni	mass % Mo	
	mass % Ni	mass % Mo	mass % Ni x mass % Mo
	% GBP		
	% GBP	mass % Ni	mass % Mo
	% $AF_{(True)}$		
	mass % Ni	mass % Ni	mass % Mo
	% M/A		
	% M/A	mass % Ni	mass % Mo
	Grain size		
	Grain size	mass % Ni	mass % Mo
	% $AF_{(True)}$	Grain size	
	Peak temperature		
	Peak temperature	mass % Ni	mass % Mo
% GBP	mass % Ni	mass % Mo	
	mass % Ni	mass % Mo	mass % Ni x mass % Mo
	Peak temperature		
	Peak temperature	mass % Ni	mass % Mo
% $AF_{(True)}$	mass % Ni	mass % Mo	
	mass % Ni	mass % Mo	mass % Ni x mass % Mo
	Peak temperature		
	Peak temperature	mass % Ni	mass % Mo
% M/A	mass % Ni	mass % Mo	
	mass % Ni	mass % Mo	mass % Ni x mass % Mo
	Peak temperature		
	Peak temperature	mass % Ni	mass % Mo
Grain size	mass % Ni	mass % Mo	
	mass % Ni	mass %% Mo	mass % Ni x mass % Mo
	Peak temperature		
	Peak temperature	mass % Ni	mass % Mo

4. Results

4.1. Chemical composition

The OES results of Welds 1–9 are shown in Table 22. These welds were performed in two different weld sessions. Welds 3, 4, and 7 were welded during the first weld session and the remainder during the second session. The welding parameters of the two different weld sessions were identical and welds deposited during the two different sessions were not expected to vary. Table 22 indicates that the Mo concentrations for welds made during the first session were notably higher than comparable welds made during the second weld session. Weld 4, deposited during the first session, contained 0.18 mass% Mo whilst Welds 5 and 6, deposited during the second session, contained 0.11 mass% and 0.12 mass % Mo respectively. Similarly Weld 7, deposited during the first session, contained 0.3 mass% Mo, whilst Welds 8 and 9, deposited during the second session, contained 0.22 mass% and 0.23 mass% Mo, respectively. Given the fact that identical welding parameters were used for all welds, and given the fact that Mn and C content remained fairly stable across the 9 welds; dilution was assumed to be constant across the 9 welds. Any dilution effects that may have affected. The average O/Ti ratio was 15, with a maximum of 13.1 for weld 5 and 16.8 for Weld 7.

Table 22: Chemical compositions (mass%) of Welds 1 to 9.

Weld	Session	C	Mn	Si	Mo	Ni	Al	Ti	N	O	S	P
Base plate		0.24	0.65	0.23	0	0.02	0.002	0.001			0.016	0.15
1	2	0.11	1.4	0.27	0.01	0.01	0.028	0.027	0.096	0.45	0.011	0.029
2	2	0.12	1.4	0.23	0.01	1.05	0.027	0.022	0.070	0.36	0.012	0.030
3	1	0.11	1.4	0.26	0.01	2.17	0.028	0.019	0.065	0.32	0.013	0.029
4	1	0.12	1.5	0.30	0.18	0.01	0.030	0.021	0.078	0.35	0.013	0.029
5	2	0.12	1.4	0.26	0.11	1.13	0.030	0.026	0.080	0.34	0.012	0.026
6	2	0.10	1.4	0.26	0.12	2.34	0.032	0.025	0.064	0.39	0.008	0.021
7	1	0.11	1.5	0.31	0.30	0.01	0.031	0.020	0.065	0.32	0.009	0.024
8	2	0.11	1.4	0.24	0.22	0.95	0.033	0.029	0.077	0.34	0.009	0.022
9	2	0.11	1.4	0.23	0.23	2.44	0.025	0.030	0.062	0.39	0.008	0.021
Minimum		0.10	1.4	0.23	0.01	0.01	0.025	0.019	0.062	0.32	0.008	0.021
Maximum		0.12	1.5	0.31	0.3	2.44	0.033	0.030	0.096	0.45	0.013	0.030
Average		0.11	1.4	0.26	0.13	1.03	0.03	0.024	0.07	0.36	0.016	0.026

4.1.1. Consistency of chemical composition across different welds

shows the average Ni content and range of Ni contents of welds that were supposed to have the same amount of Ni. Ni alloying for the 1.1 mass% Ni group was done by depositing two LMD beads according to the parameters shown in Table 16; that for the 2.3 mass% Ni group was done by depositing four LMD beads according to the parameters in Table 16. The range in Ni content in the 1.1 mass% Ni group was about 13.5 mass% of the average alloying content. As a reference, in the same group, the range of Mn contents was 10 mass% of the average Mn content. Figure 85 shows the relationship between individual weld chemical composition and the average for each group.

Table 23: Average Ni content and range of Ni content for welds with the same intended Ni content. Individual Ni content of each weld is also shown. Range is expressed as a mass percentage of alloying element and as a percentage of the average Ni content.

Weld	Intended Ni content (mass%)	Ni content (mass%)	Average Ni content (mass%)	Range (mass%)	Range (% of average alloy content)
2	1.00	1.05	1.04	0.18	15
5	1.00	1.13			
8	1.00	0.95			
3	2.00	2.17	2.32	0.27	12
6	2.00	2.34			
9	2.00	2.44			

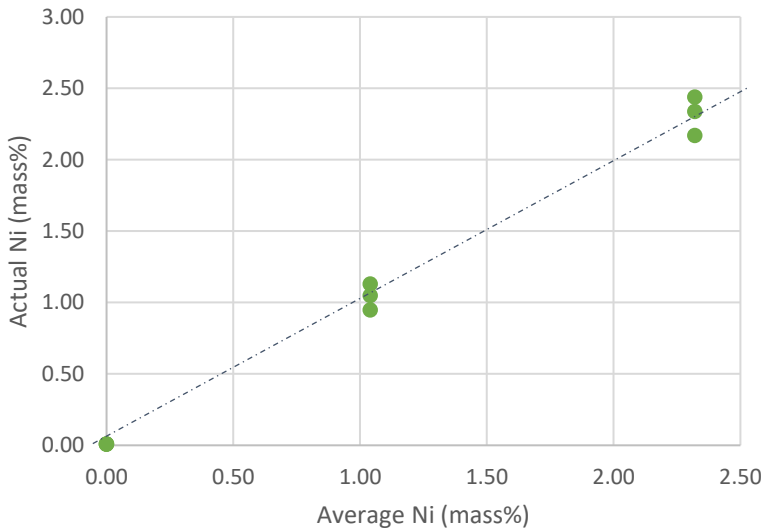

Figure 85: Graph showing average Ni content in relation to the individual Ni content for Welds 1 to 9. Average content was taken across those welds that had the same intended Ni content. The dashed line shows where all points would have fallen if the relationship had been ideal.

The average Mo content and range of Mo content for welds with the same intended Mo content are shown in Table 24. The range, expressed as a percentage of the average Mo content of welds with the same intended alloying content, is quite large. A graph showing the correlation between the individual content of each weld and the average Mo content of welds with that intended Mo content is shown in Figure 86.

Table 24: Average Mo content and range of Mo content for welds with the same intended Mo content. Individual Mo content of each weld is also shown. Range is expressed as a percentage of alloying element in weight and as a percentage of the average Mo content.

Weld	Intended Mo content (mass%)	Mo content (mass%)	Average Mo content (mass%)	Range (mass%)	Range (% of average alloy content)
2	0.15	0.18	0.14	0.07	50
5	0.15	0.11			
8	0.15	0.12			
3	0.30	0.34	0.26	0.11	42
6	0.30	0.22			
9	0.30	0.23			

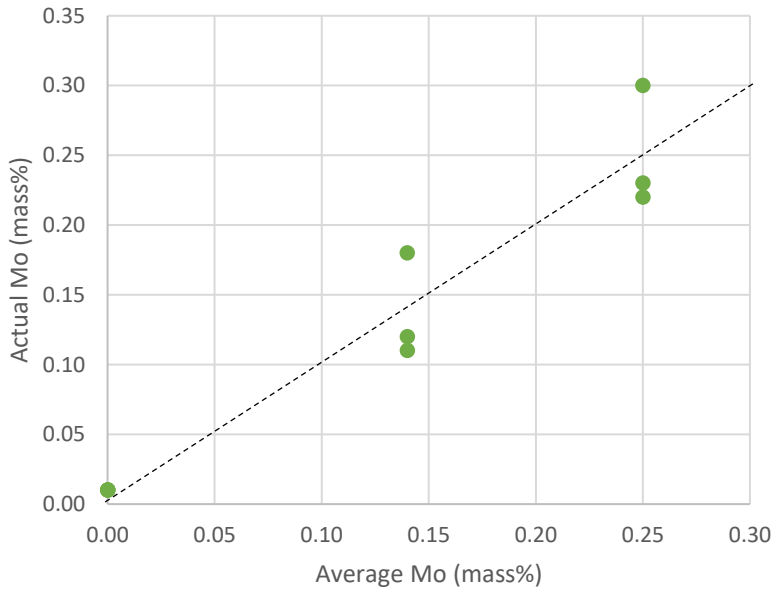

Figure 86: Graph showing the average Mo content in relation to the individual Mo for Welds 1-9. Average content was taken across those welds that had the same intended Mo content. The dashed line shows where all points would have fallen if the relationship had been ideal.

The three welds produced in Session 1 (Welds 3, 4, and 7) were welded again in Session 3. Table 25 compares the alloy content of each weld produced in Session 1 to its counterpart produced in Session 3. There were no differences in the welding parameters between the different sessions. There was a very small difference in the Ni content of Weld 3 and a notable difference between the Mo contents of Weld 4 and Weld 7, welded in Sessions 1 and 3.

Table 25: Comparison of Mo contents of Welds 4 and 7, welded in Session 1 and Session 3.

Weld	Element	Session 1 (mass%)	Session 3 (mass%)	Difference (mass% points)	Difference (% of average)
3	Ni	2.17	2.02	−0.15	−5
4	Mo	0.18	0.15	−0.03	−18
7	Mo	0.30	0.36	0.06	18

Table 26 shows the intended, individual, and average Ti content of Welds 1–9. The range of Ti contents was low, but high enough to be of concern when expressed as a percentage of the average Ti content.

Table 26: Range and standard deviation of Ti concentrations across Welds 1 to 9, expressed as both percentage by mass and as a percentage of the average concentration. The intended Ti content was 0.03 % for all welds.

Weld	Ti content (mass%)	Average Ti content (mass%)	Minimum	Maximum	Range (mass%)	Range (% of average alloy content)
1	0.027	0.025	0.019	0.030	0.011	46
2	0.022					
3	0.019					
4	0.021					
5	0.026					
6	0.025					
7	0.020					
8	0.029					
9	0.030					

The possibility that the variation in chemical composition between various welds had resulted from variation in dilution across different welds was considered. However, if variation in chemical composition of alloying elements added by LMD had resulted from changes in dilution similar variation would have been seen in alloying elements that were already present in the parent metal and filler metal, for example Mn. Since Mn levels were largely stable, and the variation in Mn levels did not correlate to variation in LMD alloying elements, the effect of a variation in dilution along a weld bead was considered not to have been significant.

4.1.2. Chemical consistency within a single weld

To evaluate the chemical consistency along the length of a single weld, an OES traverse was performed on one of the welds from the trial welds produced during the refinement of the weld-alloying technique. The points were 35 mm apart, with point 1 falling 100 mm from the start of the weld. The weld length was about 400 mm.

Figure 87, Figure 88, and Figure 89 show the Mo, Ni, and Ti contents of the OES traverse as a function of the distance from the starting point of the weld. The graphs show that the chemical composition of the welds stabilized about 150 mm away from the starting point of the weld.

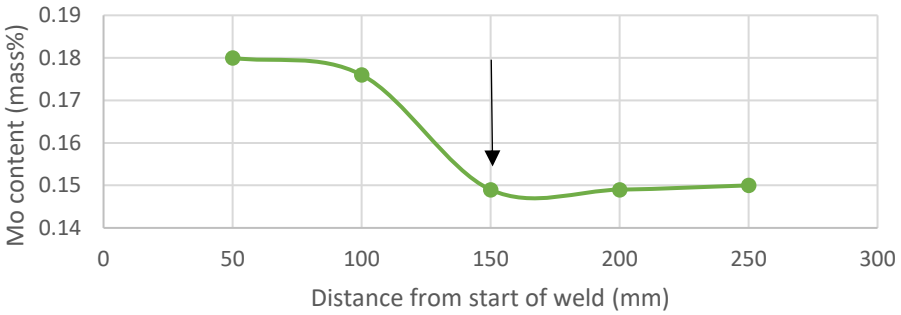

Figure 87: Plot of Mo content of a weld from a trial run as a function of the distance from the start of the weld. Average Mo content of the weld was 0.16 mass%.

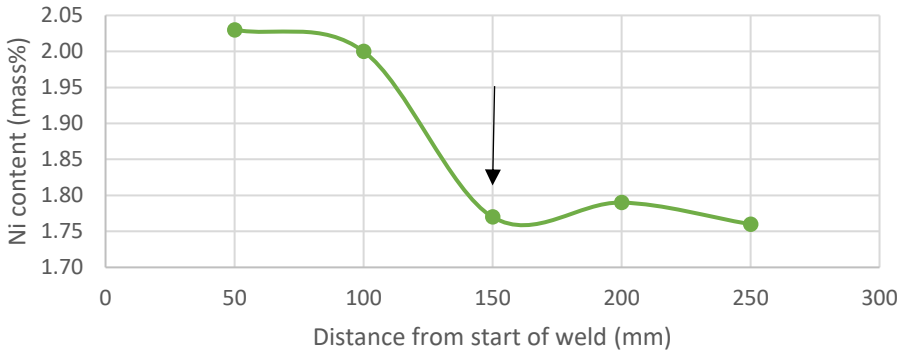

Figure 88: Plot of Ni content of a weld from a trial run as a function of the distance from the start of the weld. The average Ni content of the weld was 1.77 mass%.

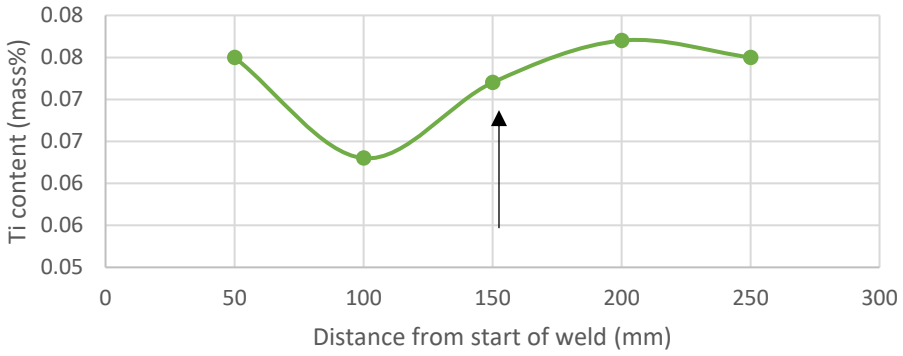

Figure 89: Plot of Ti content of a weld from a trial run as a function of the distance from the start of the weld. The average Ti content of the weld was 0.07 mass%.

Table 27 shows the concentration of weld metal at three locations after stabilisation had occurred. The range in concentration of alloying elements was very low and not of concern provided sampling close to the starting point of the weld is avoided (as was done in this study; Figure 75).

Table 27: Concentration of alloying elements added with LMD at three locations down the length of a weld. Mn concentration is shown to allow comparison between LMD alloys and those present in the welding wire and base metal.

	Distance from start of weld (mm)			Range (mm)	Range (%)
	150	200	250		
Mn	1.38	1.36	1.35	0.03	2
Mo	0.149	0.149	0.150	0.001	0.7
Ni	1.77	1.79	1.76	0.03	2
Ti	0.072	0.077	0.075	0.01	7

The consistency of Ni and Mn contents along the *x*- and *y*-axes of a single weld was evaluated by measuring the concentration of these elements at three different locations on a cross-sectional microscopy sample using EDS. The results are shown in Table 28. The Ni range (expressed as a percentage) was equal to or lower than the Mn range. The Mo content was too low to be accurately measured with EDS.

Table 28: Difference between the Ni and Mn ranges measured by EDS. Position of Points 1, 2, and 3 are shown in Figure 69.

	Ni content (mass%)				Mn content (mass%)			
Weld	Point 1	Point 2	Point 3	Range (% of average)	Point 1	Point 2	Point 3	Range (% of average)
Weld 1	0.00	0.00	0.00	Not detected	1.48	1.62	1.59	0.09
Weld 2	1.18	1.20	1.28	8.2	1.58	1.61	1.49	0.08
Weld 3	2.28	2.29	2.23	2.2	1.50	1.68	1.55	0.11

4.1.3. Accuracy of equations used to predict chemical composition.

The difference between the Mo and Ni contents predicted by Equation 16Equation 17 and those measured by OES are shown in Table 29. The smallest difference was 4 mass% and the largest difference was 20%. This difference is largely attributed to irregular bead shape shown in Figure 64and
Figure 65 (Section 3.3.1). The fact that the actual chemical composition was used for the analysis of results meant that this disparity was not an issue with regards to interpretation of results.

Table 29: Comparison of expected alloying element concentration of in welds according to Equation 16Equation 17 and measured alloying element content

Welds	Alloying element	Calculated alloy content (mass%)	Measured alloy content (mass%)	Difference (% of calculated alloy content)
4, 5, 6	Mo	0.15	0.14	6
7, 8, 9	Mo	0.3	0.25	17
2, 5, 8	Ni	1	1.04	4
3, 6, 9	Ni	2	2.3	15
1-9	Ti	0.03	0.024	20

4.1.4. Inclusion analysis

SEM-EDS was performed to analyse the chemical composition of 5 inclusions from Welds 2 to 8. SEM-EDS readings were corrected by eliminating Fe from the analysis. Of the inclusions analysed only 3 inclusions contained S. One inclusions from Weld 4 (0.18 mass% Mo and 0 mass% Ni) contained S. The corrected reading from the EDS indicated that this inclusion contained about 30 mass% S. Two inclusions from Weld 8 (0.22 mass% Mo and 0.95 mass% Ni) contained S. The corrected reading from the EDS indicated that these inclusions contained about 18 mass% and 50 mass% S respectively. The readings from these EDS measurements were not intended to quantitative, but were merely used to obtain an idea of the degree to which S was present in inclusions. One of the expected effects of adding Ti to weld metal is the reduction in MnS containing inclusions (Kang et al., 2015; Seo et al., 2015).

It was noted in Section 1.2.1 that Ti(N) may form in weld metal if the O/Ti ratio is too low, i.e. if all the free Ti does not react with oxygen. Ti(N) were not expected to form in this weld metal because the O/Ti ratio (15) was between 10 and 100. No Ti(N) particles were observed.

4.2. Thermo-Calc

The fraction of liquid, δ-ferrite, and austenite present in a weld metal under equilibrium conditions at specific temperatures, as calculated by *Thermo-Calc*, is shown in Figure 90. *Thermo-Calc* is a phase diagram and thermo dynamic property calculation software (Andersson et al., 2002). An increase in Ni results in partial suppression of the formation of δ-ferrite and an increase in the degree to which austenite is in balance with liquid. At 2.3 mass% Ni, there is very little overlap between δ-ferrite and γ. In addition, γ is in balance with the liquid to a much greater extent than at lower Ni concentrations.

Figure 90 also shows that an increase from 0 to 1.1 mass% Ni did not have the same effect on welds with different concentrations of Mo. The *Thermo-Calc* calculations used the measured chemical composition of Welds 1–9. These results indicate that there were slight variations in the C, N, and Mn contents of the welds. The variation in the concentrations of elements other than Ni and Mo are likely responsible for the apparent inconsistent response of weld metal to Ni.

The database TCFE7: Steels/Fe-Alloys v7.0 was used. Only the liquid, austenite, and ferrite data was plotted as this was what was considered to be valuable to the discussion regarding solidification mechanism. Thermo-Calc was only run down to 145°C. Mineral phases were part of the Thermo-Calc output, but were not included in graphs as they did not add value to the discussion.

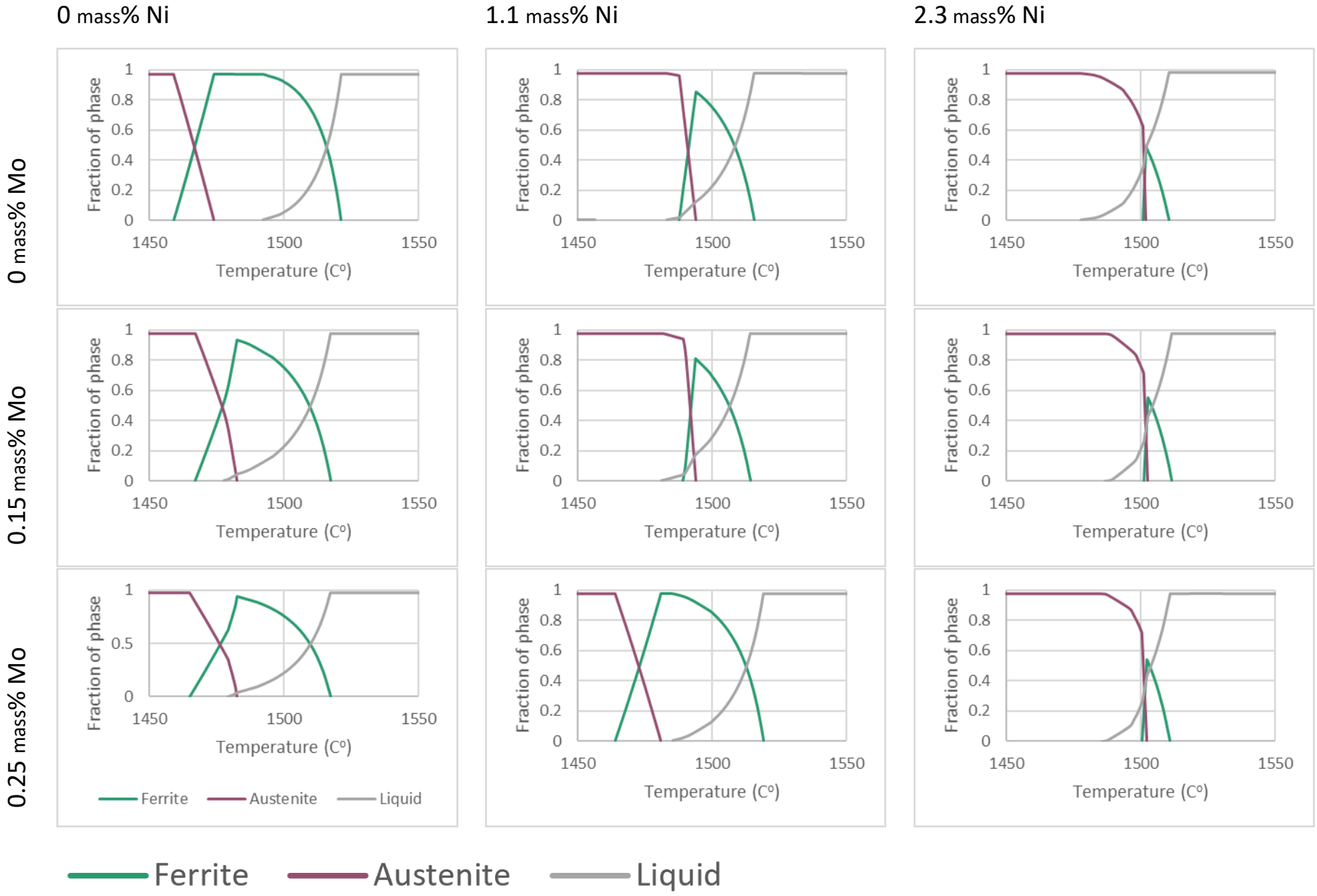

Figure 90: Graphs showing the fraction of specific phases at temperatures for Welds 1 to 9. Plotted from data obtained by *Thermo-Calc* calculation.

4.3. Properties of welds in the as-welded condition

4.3.1. Transformation temperature

Dilatometry was performed using the thermal cycle shown in Section 3.5.2 to measure the Ac_1, Ac_3, and B_s temperatures of Welds 1–9. Table 30 shows the results of these experiments. The correlations between measured and predicted A_{c1}, A_{c3}, and B_s temperatures of each weld are shown in Figure 91, Figure 92, and Figure 93, respectively. The expected A_{c1}, A_{c3} temperatures were calculated according to equations published by Andrew (1965) (Equation 3 and Equation 4). The expected B_s temperature was calculated according to an equation published by Kunitake and Okada (1998) (Equation 5). B_s was also calculated according to empirical formulae set out by Kirkaldy and Baganis (1978) and Steven (1956), but these results were omitted as they proved to be poor estimates.

Figure 91 indicates that, with the exception of Weld 9, there is a reasonably good correlation between the transformation temperatures predicted by Equation 3 and those measured during this study. Figure 92 indicates that Equation 4 was a relatively poor predictor of Ac_3 temperature. Figure 93 shows that Equation 5 predicted B_s quite well, with the exception of Welds 1 and 2.

Table 30: Measured transformation temperatures of Welds 1 to 9.

Weld	Mo (mass%)	Ni (mass%)	Ac_1 (°C)	Ac_3 (°C)	B_s (°C)
1	0.01	0.0	717	890	
2	0.01	1.0	705	877	641
3	0.01	2.2	670	909	595
4	0.18	0.0	703	897	620
5	0.11	1.1	697	891	568
6	0.12	2.3	662	889	511
7	0.30	0.0	728	934	591
8	0.22	1.0	716	920	548
9	0.23	2.4	715	876	492

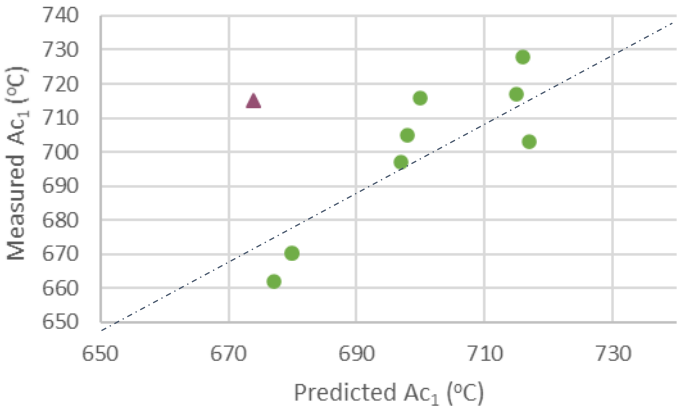

Figure 91: Correlation between predicted and measured Ac_1 temperatures. The triangular marker indicates Weld 9, which was an outlier.

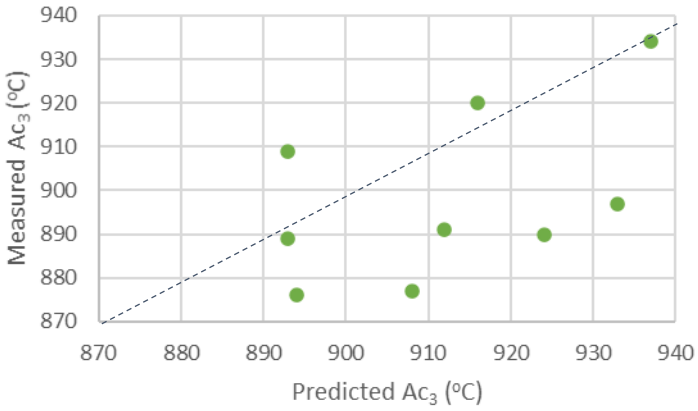

Figure 92: Correlation between predicted and measured Ac_3 temperatures.

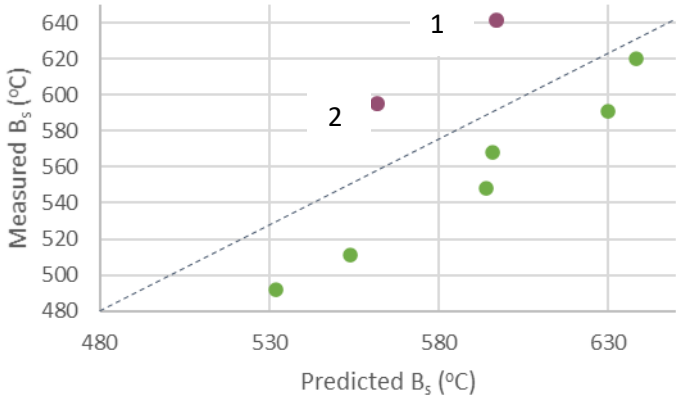

Figure 93: Correlation between predicted and measured B_s temperatures. Two outliers (Welds 1 and 2) are indicated by purple markers.

4.3.2. Microstructure

Qualitative microscopy

Composite micrographs of Welds 1–9 (AW) are shown in Figure 94 and Figure 97, taken at 100× and 500× magnification, respectively. The optical micrographs revealed that all welds consisted of varying amounts of GBP decorating the PAGBs. Prior austenite grain centres appeared to consist of AF, as the term is conventionally used. An etch effect was detected on what was later confirmed to be PAGBs of Welds 6 and 9 (AW). Micrographs showing the etch effect on Welds 6 and 9 (AW) are shown in Figure 95 and Figure 96, respectively. Low-magnification SEM microscopy revealed that the etch effect was associated with PAGBs, as shown in Figure 98.

SEM revealed that the regions of all welds that were not covered by GBPs in the as-welded condition, with the exception of Welds 6 and 9 (AW), consisted of a balance of true AF and IfRs. Welds 6 and 9 (AW) also contained AF and IfRs, but regions of coalesced bainite were also detected on and near the PAGBs of these welds. Some bainite was also detected on Weld 6 (AW). Composite SEM images of Welds 1–9 (AW) before and following image processing are shown in Figure 99 and Figure 100, respectively. Micrographs showing the coalesced bainite in Welds 6 and 9 (AW) are shown in Figure 101, Figure 102, and Figure 103. The bainite observed in Weld 6 is shown in Figure 104.

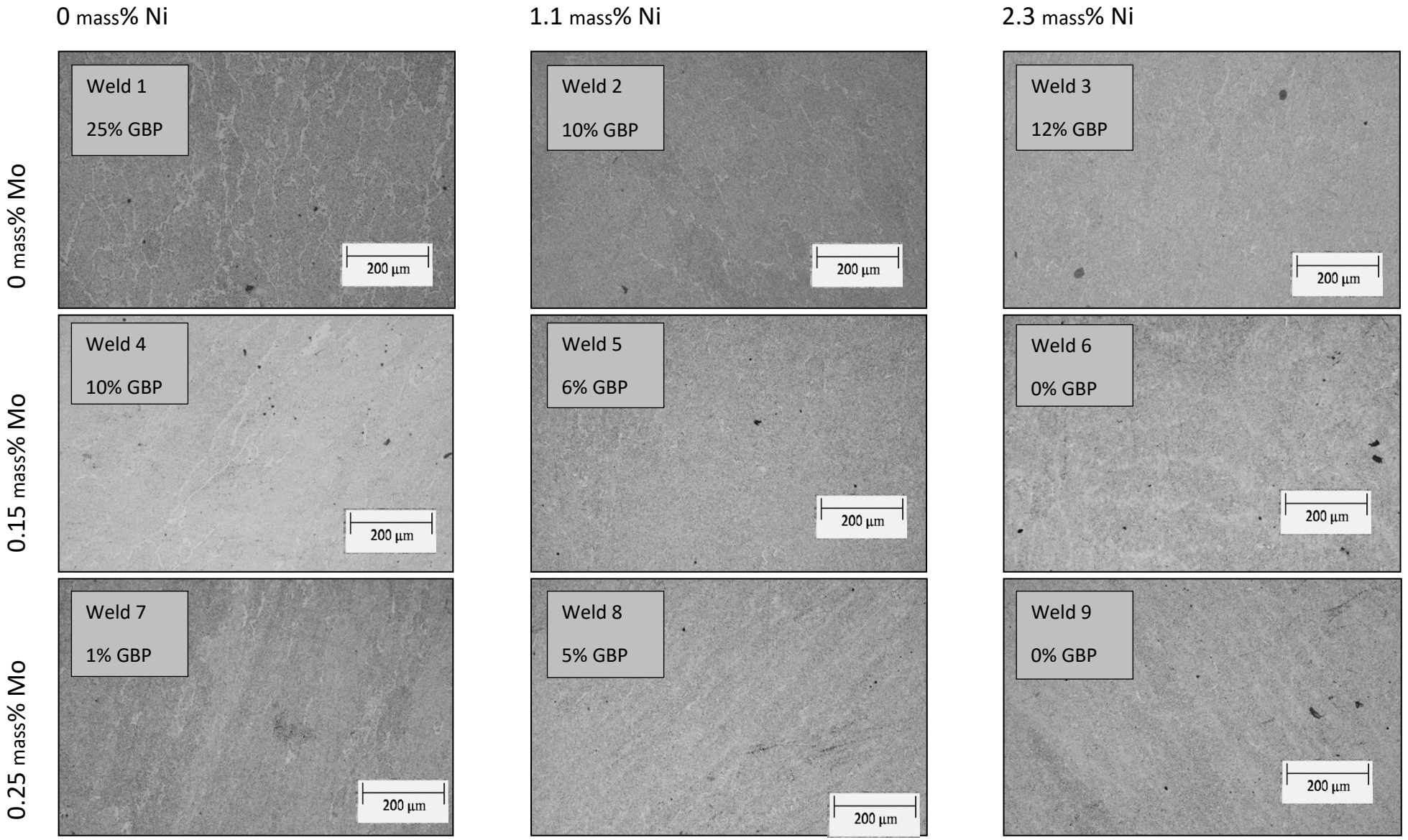

Figure 94: Composite figure of optical micrographs of Samples 1 to 9 (AW). Percentage grain boundary product is indicated on each micrograph. The micrographs were captured at 100× magnification. Grain boundary products are clearly visible on Welds 1, 2, and 4 (AW). The orientation of the micrographs is shown in Figure 84. The figure shows an etch effect on what appears to be the PAGBs of Welds 6 and 9 AW.

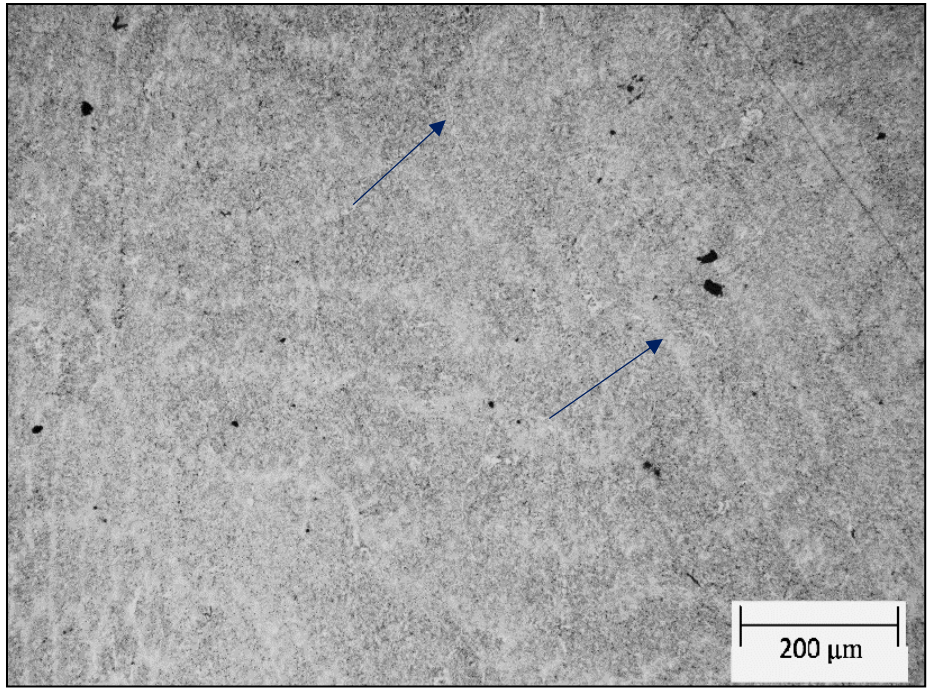

Figure 95: Optical micrograph of Weld 6, taken at 100× magnification. The micrograph shows an etch effect that appears to follow the PAGBs, which are indicated by arrows.

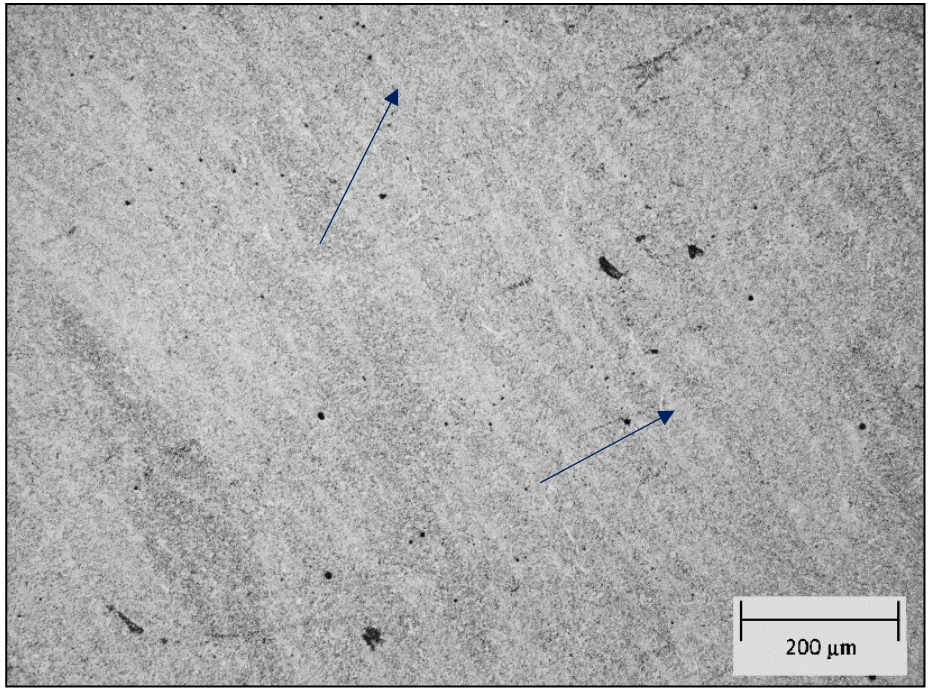

Figure 96: Optical micrograph of Weld 9, taken at 100× magnification. The micrograph shows an etch effect that appears to follow the PAGBs.

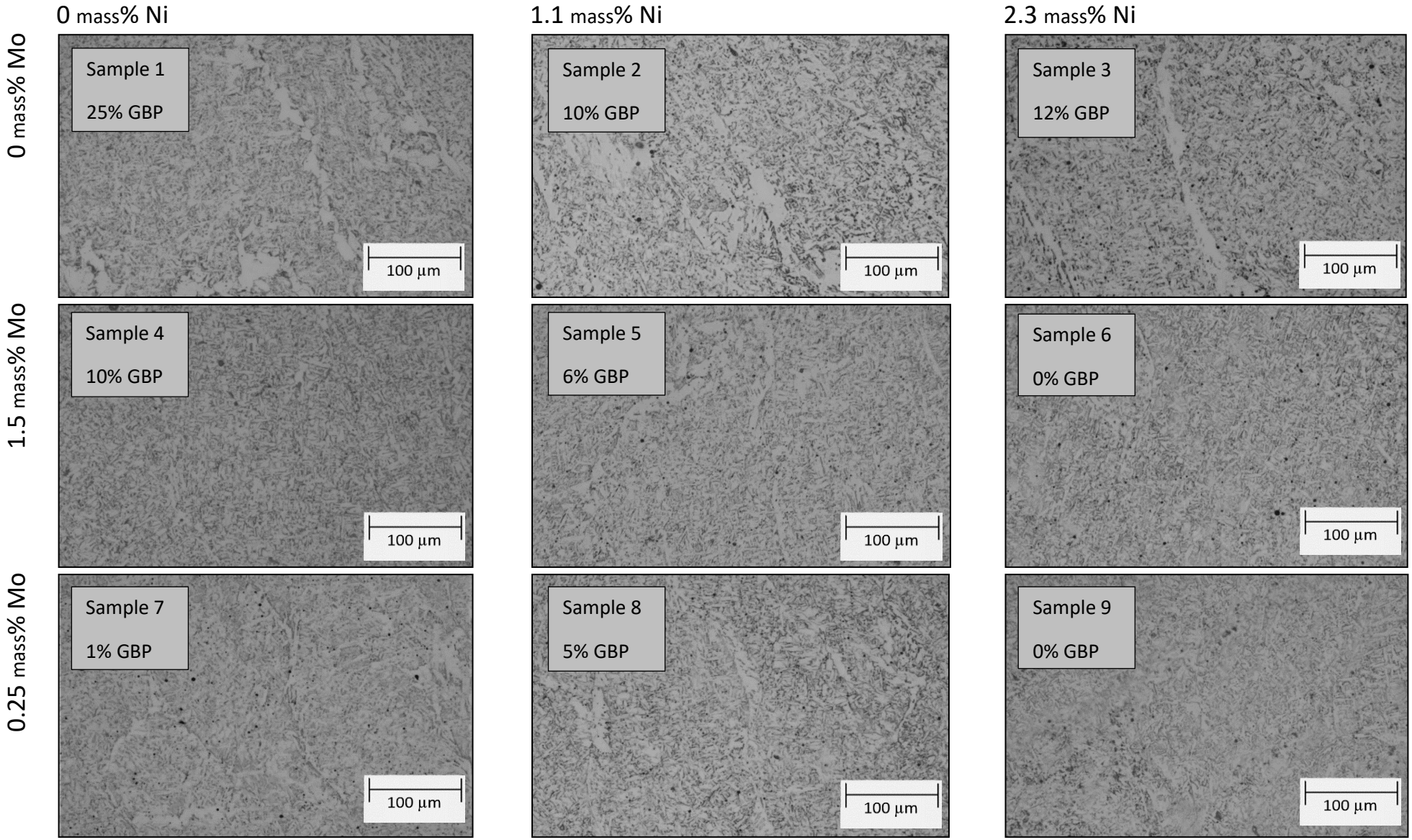

Figure 97: Composite figure of optical micrographs of Samples 1 to 9 (AW). Percentage grain boundary product is indicated on each micrograph. The micrographs were captured at 500× magnification. Grain boundary products are apparent on Samples 1, 2, 3, 5, and 7 (AW). Low- and high-Ni groups had an average of 1.0 mass% Ni and 2.3 mass% Ni, respectively. Low- and high-Mo groups had an average of 0.14 mass% Mo and 0.25 mass% Ni, respectively.

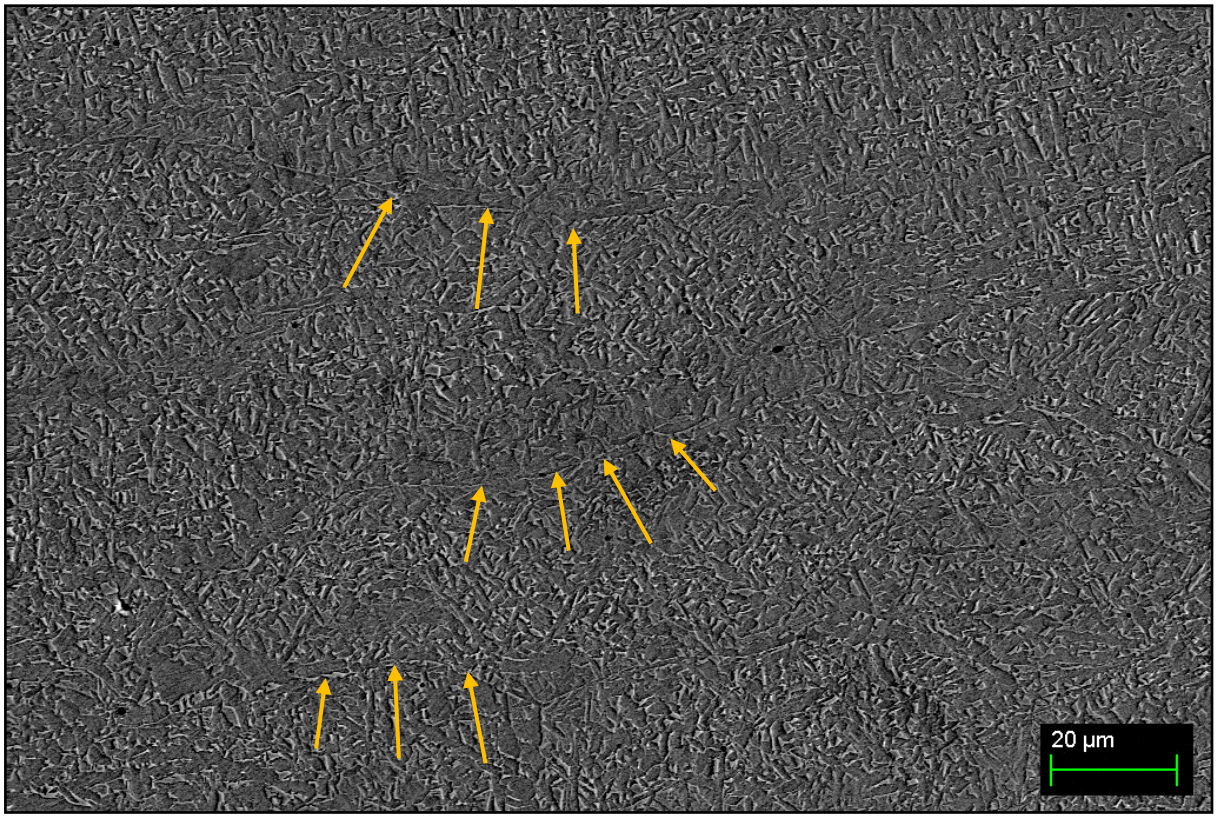

Figure 98: SEM micrograph of Sample 9 (AW) showing that the etch effect visible on optical microscopes is a result of a less severe etch on PAGBs. PAGBs are indicated by arrows. The micrograph was taken at 600× magnification at a working distance of 7.9 mm and accelerating voltage of 15 kV. The contrast of the image was increased to make the etch effect more visible.

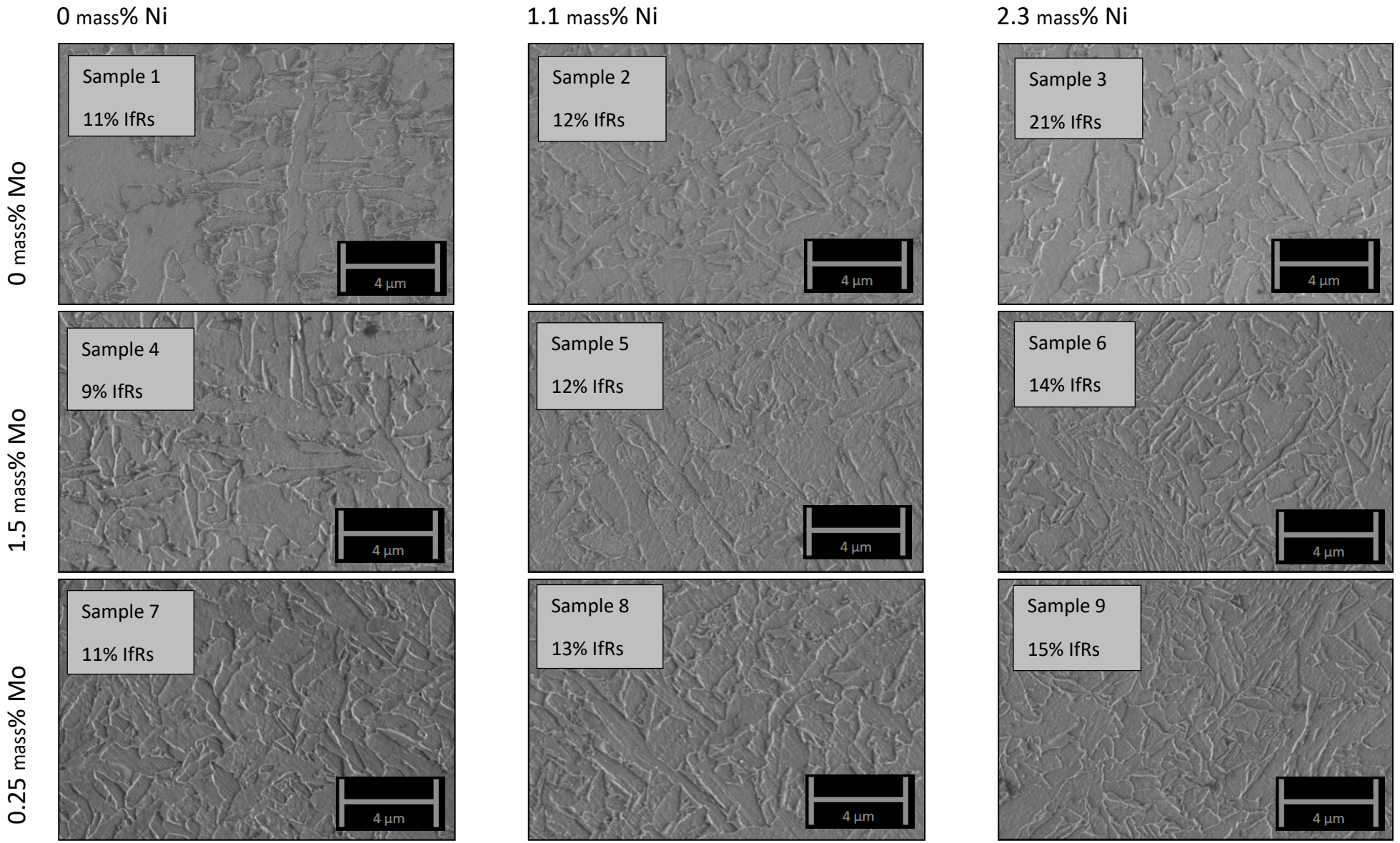

Figure 99: Composite figure of SEM micrographs of Samples 1 to 9 (AW). The percentage interferritic region (IfRs) is indicated on each micrograph. Samples 6 and 9 (AW) have small grain sizes when compared with other samples and regions of ferrite with second phase aligned.

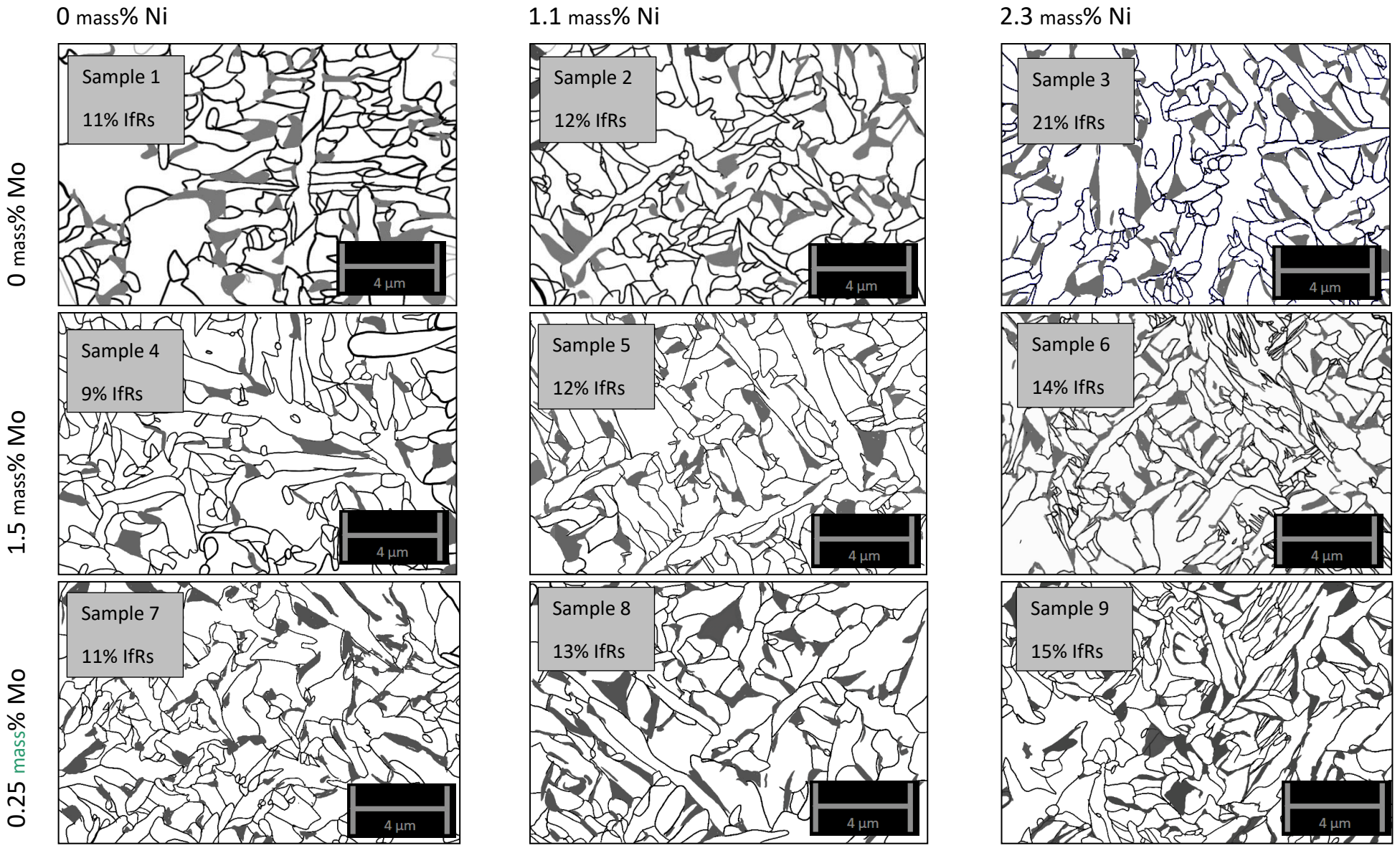

Figure 100: Composite figure of processed SEM micrographs of Samples 1 to 9 (AW). The percentage of IfRs is indicated on each micrograph. Samples 6 and 9 (AW) have small grain sizes when compared with other samples and regions of ferrite with second phase aligned.

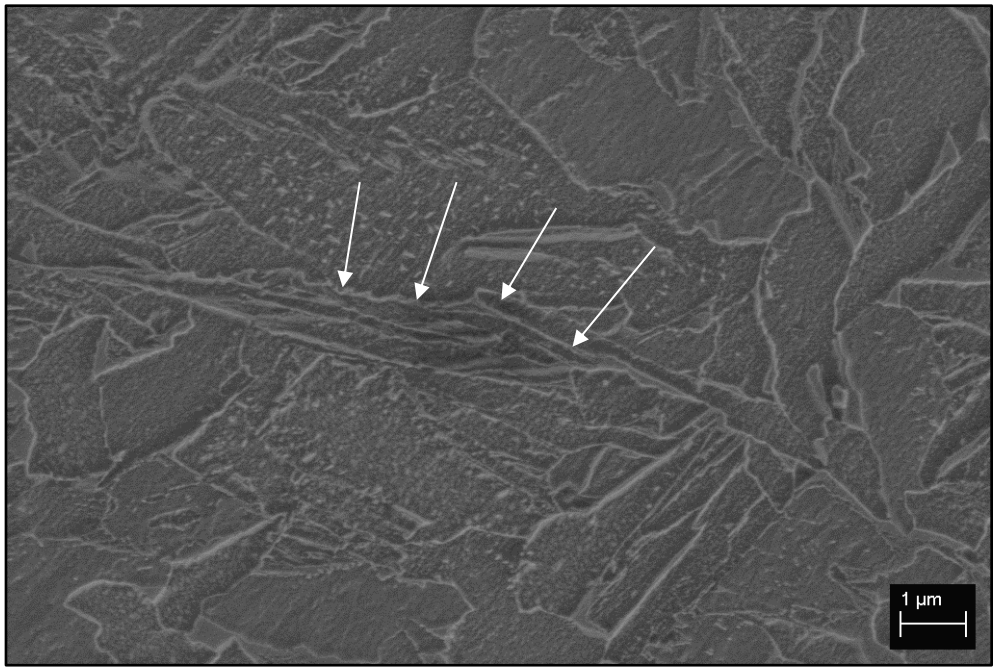

Figure 101: Micrograph of regions of coalesced bainite from Weld 6 (AW). The prior austenite grain boundary is indicated by arrows.

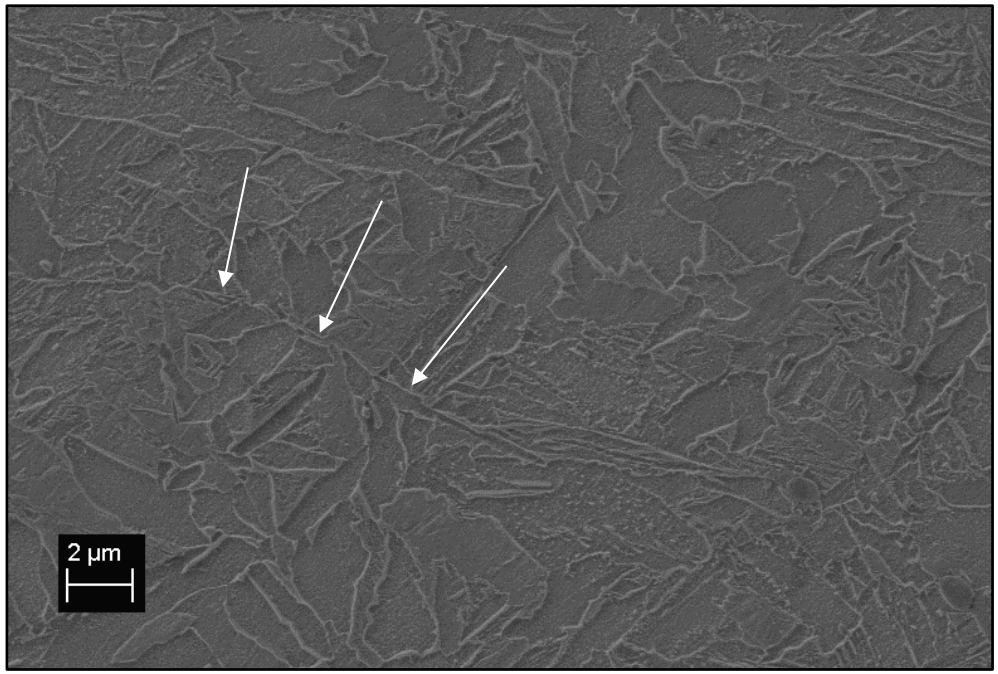

Figure 102: SEM micrograph of Weld 6 (AW) showing regions consisting of coalesced bainite and partly coalesced AF on a grain boundary. The prior austenite grain boundary is indicated by arrows.

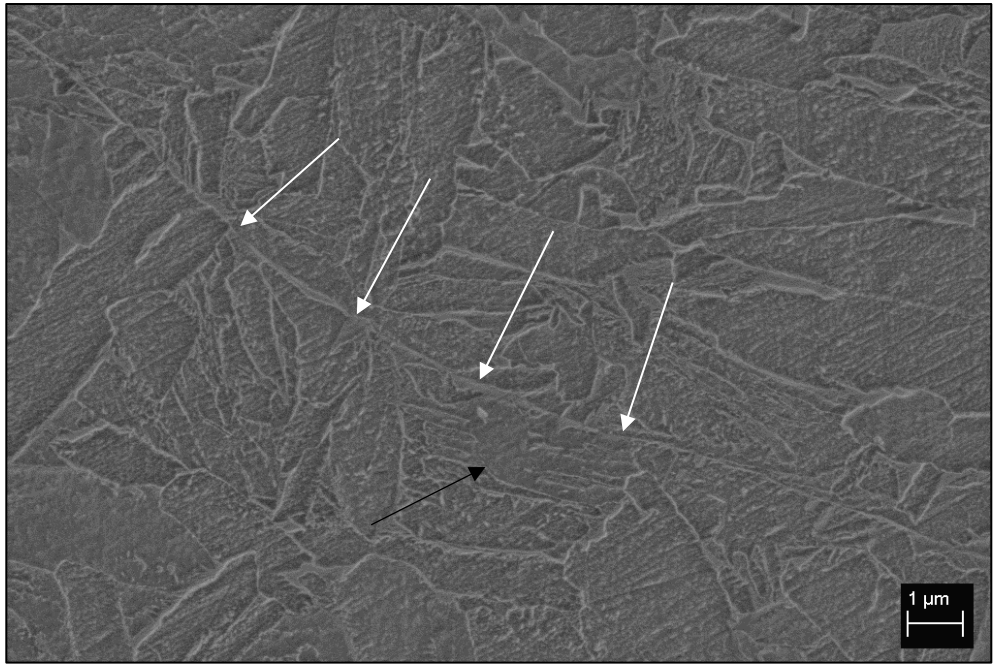

Figure 103: Micrograph of Weld 9 (AW). Micrograph shows regions of coalesced bainite on a prior austenite grain boundary. The prior austenite grain boundary is indicated by white arrows. Coalesced bainite is indicated with a black arrow.

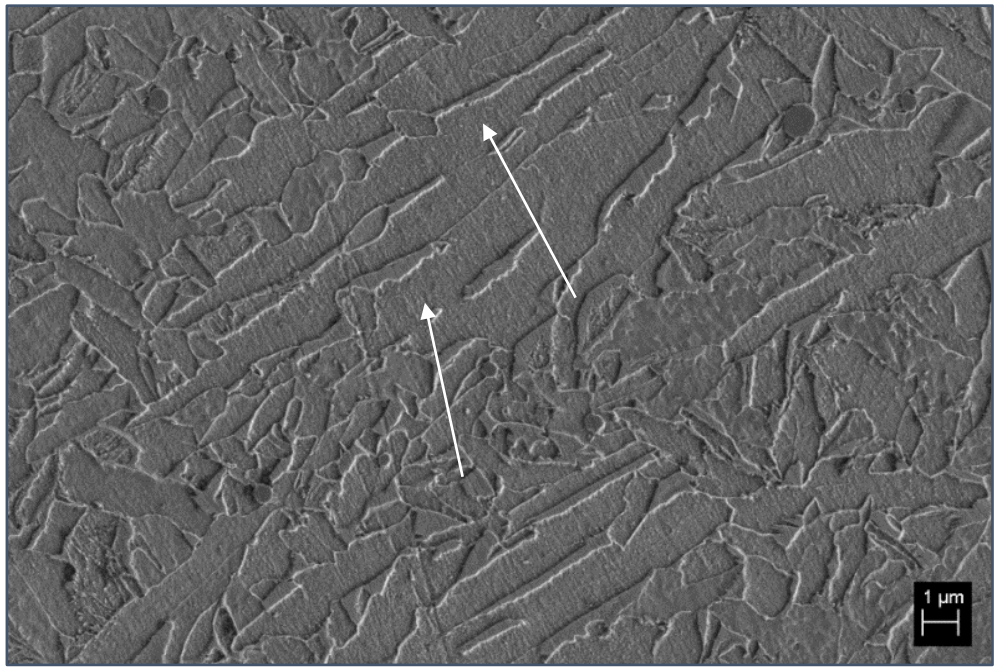

Figure 104: SEM micrograph of Sample 6. White arrow shows sheaths of either bainite or Widmanstätten ferrite. Taken at 10 000× magnification.

Quantitative metallography

Table 31 summarises the chemical composition of each weld, grain size, and microstructural constituents. It is noted that the identification of IfRs was subjective and that this may have resulted in a larger uncertainty than was calculated here. Change in chemical composition did not have a consistent effect on grain size, fraction of $AF_{(true)}$, or fraction of IfRs. The measured GBP fraction was affected by changes in composition. The percentage $AF_{(conventional)}$ is not reported because of the direct relationship that it has with percentage GBP in this study, as expressed by Equation 30. This direct relationship would not have existed if martensite had formed in the samples, as discussed in Section 3.7.

$$\%AF_{Conventional} = 100\% - \%GBP$$

Equation 30

Table 31: Summary of chemical composition and microstructural evaluation of Welds 1 to 9. 95% confidence interval (CI) is also shown.

Sample	%Ni	%Mo	Grain size (µm)	$\%AF_{(True)}$	$\%AF_{(Conventional)}$	%GBP	%IfRs
			Mean ± 95% CI	Mean ± StDev	Mean ± 95 % CI	Mean ± 95 % CI	Mean ± 95 % CI
Weld 1	0.01	0.01	2.0 ± 0.33	64 ± 0.022	75 ± 0.022	25 ± 0.022	11 ± 0.001
Weld 2	0.01	1.05	1.8 ± 0.19	78 ± 0.019	90 ± 0.019	10 ± 0.019	12 ± 0.001
Weld 3	0.01	2.17	1.7 ± 0.16	68 ± 0.017	88 ± 0.017	12 ± 0.017	20 ± 0.001
Weld 4	0.18	0.01	1.4 ± 0.11	81 ± 0.02	90 ± 0.020	10 ± 0.020	9 ± 0.001
Weld 5	0.11	1.22	1.6 ± 0.09	82 ± 0.025	94 ± 0.025	6 ± 0.025	12 ± 0.001
Weld 6	0.12	2.17	1.4 ± 0.11	86 ± 0.074	100 ± 0.074	0 ± 0.074	14 ± 0.001
Weld 7	0.30	0.01	1.8 ± 0.23	89 ± 0.036	99 ± 0.036	1 ±0.036	11 ± 0.001
Weld 8	0.22	0.95	1.6 ± 0.08	82 ± 0.038	95 ± 0.038	5 ± 0.038	13 ± 0.001
Weld 9	0.23	2.44	1.1 ± 0.06	85 ± 0.069	100 ± 0.069	0 ± 0.069	15 ± 0.001

A multivariant linear analysis was performed on the correlation between GBP content and chemical composition of the welds. Individual GBP measurements were used as *y*-variables for the analysis. These results are shown in Table 32 and the equation derived from the results is shown in Equation 31. A scatter plot between the measured GBP content and the values predicted by Equation 31 is shown in Figure 105. The results show that there is a notable correlation between GBP content and chemical composition.

Table 32: Regression statistics and coefficients, standard error, and P-value of the linear multiple regression of the influence of mass% Ni, mass% Mo, and their product on GBP content.

Multiple *R*	0.84		
***R* squared**	0.71		
Adjusted *R* squared	0.70		
Standard error	3.95		
Observations	90		
	Coefficients	Standard error	P-value
Intercept	19.88	1.10	4.48E-31
Mo (mass%)	−63.55	5.66	4.77E-11
Ni (mass%)	−5.87	0.78	1.60E-18
Ni (mass%) × Mo (mass%)	13.85	4.41	0.002323

$$\%GBP = 19.9 - 63.6(mass\%\ Mo) - 5.9(mass\%\ Ni) + 13.9(\text{mass}\%\ Mo\ \times \text{mass}\%\ Ni)$$

Equation 31

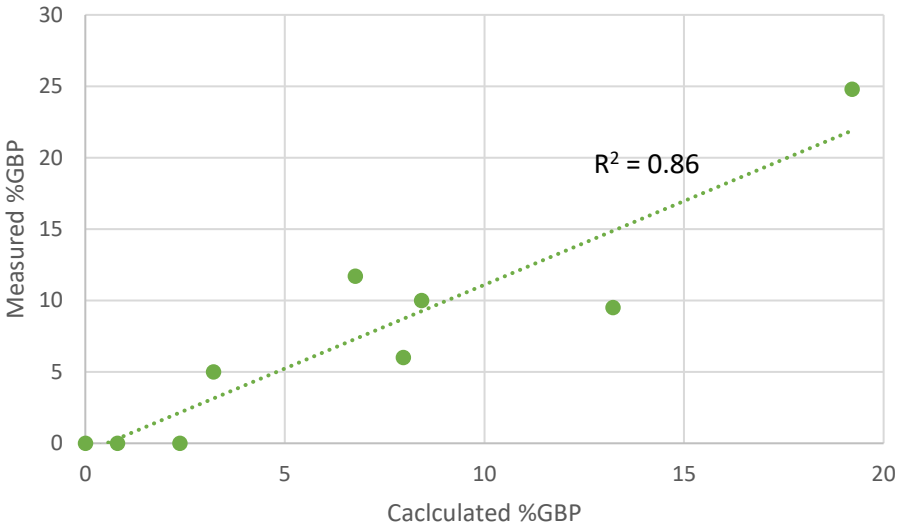

Figure 105: Scatter plot of relationship between calculated and measured % GBP.

A regression analysis was used to test whether the addition of Ti as a variable to the regression model shown in Table 32 would improve the R^2 value. The results are given in Table 33. These show that the R^2 value remained the same whilst the standard error increased slightly. The P-value of the mass% Ti variable is also very close to 1. This shows that Ti content did not have a statistically significant effect on the GBP content of the welds.

Table 33: Regression statistics and coefficients, standard error, and test on individual regression coefficients (t Stat) of the linear multiple regression done of influence of mass% Ni, mass% Mo, the product between mass% Ni and mass% Mo, and mass% Ti on GBP content.

Multiple *R*	0.84		
***R* squared**	0.71		
Adjusted *R* squared	0.70		
Standard error	3.97		
Observations	90		
	Coefficients	Standard error	P-value
Intercept	19.89	1.14	7.15E-30
Mo (mass%)	−5.87	0.78	6.2E-11
Ni (mass%)	−63.56	5.70	2.53E-18
Ni (mass%) × Mo (mass%)	13.85	4.44	2.46E-3
Ti (mass%)	−0.015	0.42	0.972

4.3.4. Scanning electron microscopy energy-dispersive X-ray spectroscopy

SEM showed that the etch effect observed during optical microscopy (Figure 95, Figure 96, and Figure 98) was associated with the presence of coalesced bainite (Figure 101 and Figure 102) on and directly adjacent to the PAGBs of Welds 6 and 9. However, it was not clear if the etch effect was a result of the coalesced bainite, which may be more etch-resistant, or the result of some variation in the chemical composition at the PAGBs and their centres. Therefore, SEM-EDS was used to test for segregation of alloying elements to the PAGBs in these welds.

SEM-EDS measurements were taken on grain boundaries and at grain centres. The average Mn and Ni contents at PAGBs and prior austenite grain centres were calculated from 21 readings from five sites for Weld 6 and 17 readings from seven sites for Weld 9. Mo concentration was too low to allow for an accurate comparison between Mo levels at the grain centre and those at the grain boundary. The EDS results are shown in Table 34. The results confirm that the etch effect observed at grain boundaries was the result of segregation of Ni to PAGBs. The results also showed that Mn diffused away from PAGBs in Weld 6 and towards PAGBs in Weld 9. EDS did not indicate that any other elements segregated to grain boundaries. An example showing where PAGBs and grain centres were measured is shown in Figure 106.

Table 34: Ni and Mn concentrations and PAGBs and prior austenite grain centres of Welds 6 and 9.

Sample	Ni (mass%)			Mn (mass%)		
	Grain boundary	Grain centre	Difference	Grain boundary	Grain centre	Difference
Weld 6	2.24 ± 0.03	2.07 ± 0.02	0.17 (8 %)	1.47 ± 0.03	1.70 ± 0.02	0.23 (15%)
Weld 9	2.15 ± 0.05	1.84 ± 0.03	0.31 (16%)	1.61 ± 0.04	1.41 ± 0.05	0.2 (13 %)

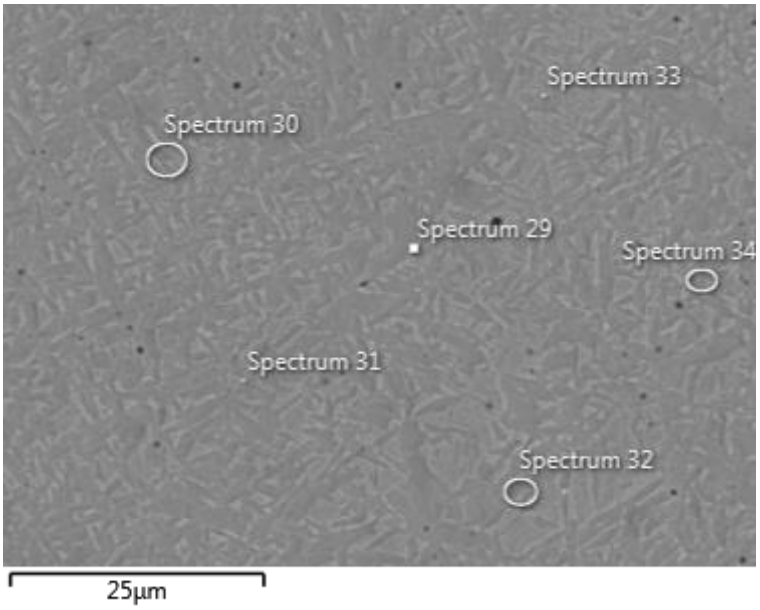

Figure 106: Micrograph from Weld 6, showing where readings on PAGBs and grain centre measurements were taken. Spectra indicated by points were taken on the grain boundary; spectra indicated by small circles were taken at grain centres.

4.3.5. Fractography

Fractography showed that all welds in the as-welded condition, with the exception of Welds 6 and 9 (AW), fractured in a brittle manner along the GBPs that decorated the PAGBs and in a ductile manner across regions containing AF and IfRs. Examples of such fractures are shown in Figure 107, Figure 108, and Figure 109. Welds 6 and 9 (AW) fractured intergranularly along PAGBs, which is shown in Figure 110. This fracture appeared to have occurred along the coalesced bainite that was identified in these samples (Figure 112).

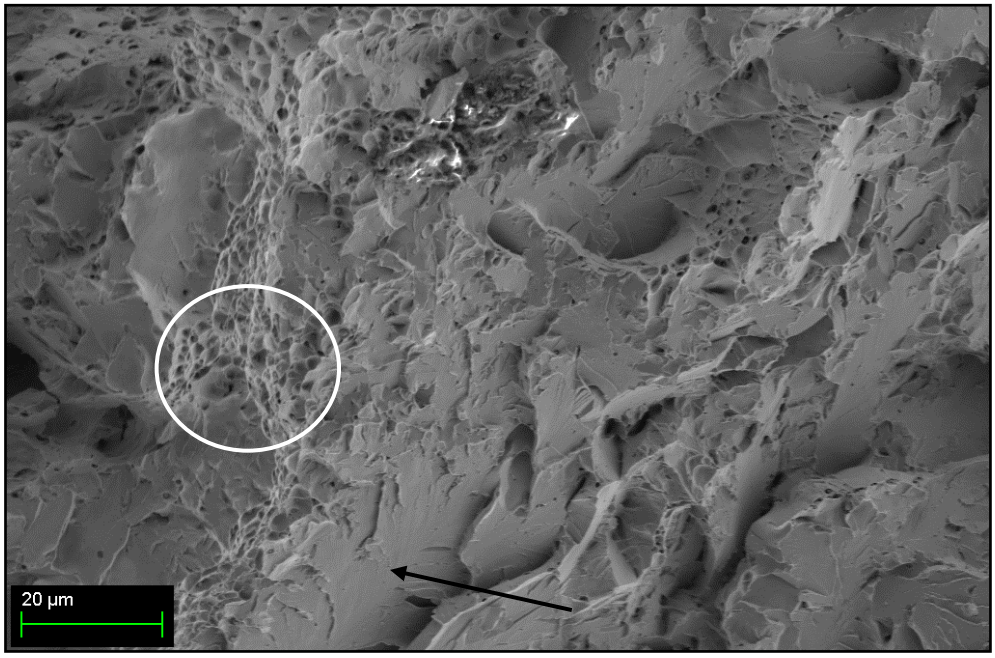

Figure 107: SEM micrograph of the fracture surface of Weld 1 (AW). The micrograph shows brittle fracture along GBF (indicated by a black arrow) and ductile fracture in areas where fracture propagated across regions of acicular ferrite (indicated by a white circle). The sample contained 0.017 mass% Ti and no Mo or Ni. The sample had an impact energy of 41 $J_{(5mm)}$ and a hardness of 208 HV10. Average grain size of the sample was 2 µm. The sample contained 25 % GBPs.

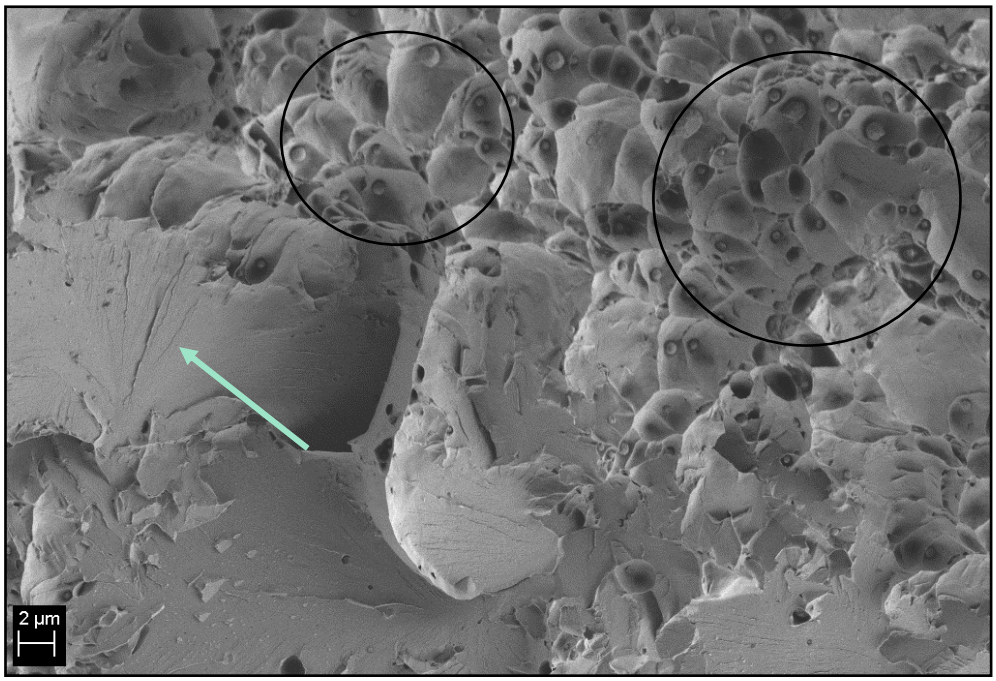

Figure 108: Higher magnification SEM image showing the fracture surface of Weld 1 (AW), the same sample as in Figure 107. An arrow indicates the cleavage fracture associated with GBF and circles indicate the regions of ductile fracture.

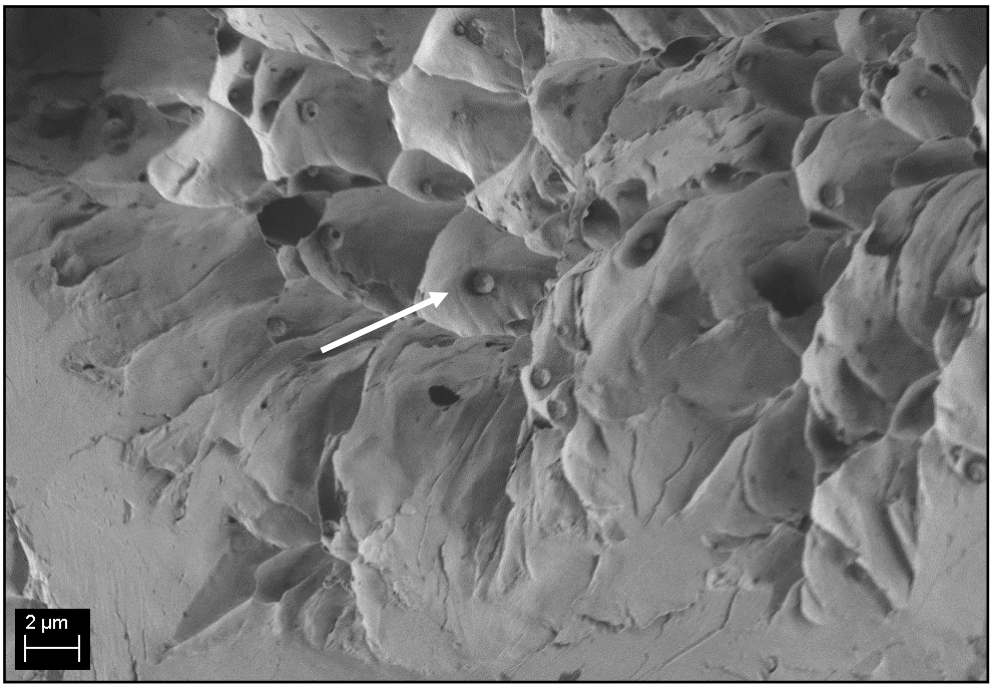

Figure 109: SEM micrograph of the fracture surface of Weld 1 (AW). An arow indicates one of the inclusions that resulted in dimple fracture. The sample contained no Mo or Ni. The sample had an impact energy of 41 $J_{(5mm)}$ and a hardness of 208 HV10. Average grain size of the sample was 2 µm. The sample contained 25 % GBPs.

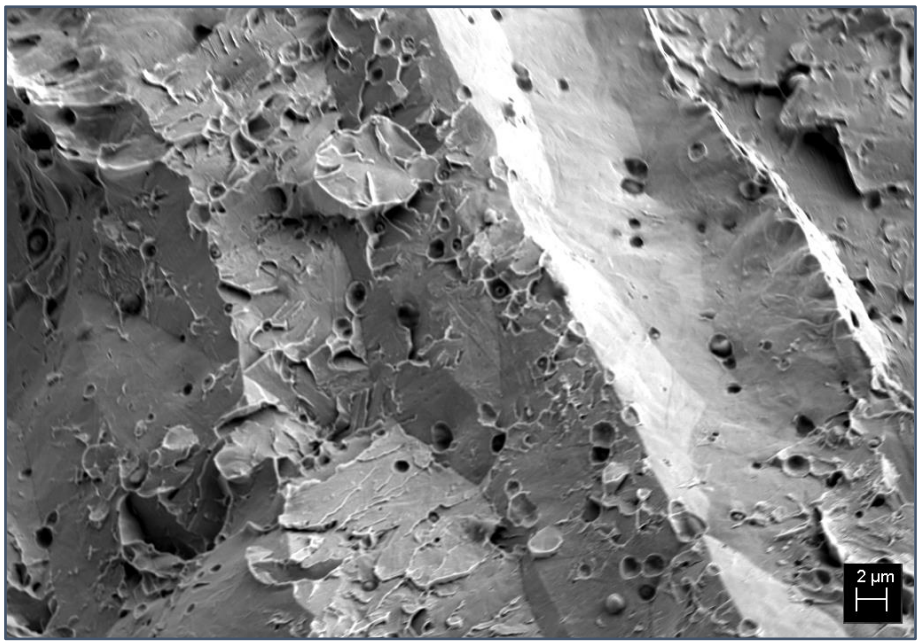

Figure 110: SEM micrograph of the intergranular fracture on the fracture surface of Weld 6 (AW). The sample contained 0.12 mass% Mo and 2.34 mass% Ni. The sample had an impact energy of 29 $J_{(5mm)}$ and a hardness of 261 HV10. The sample contained no GBPs.

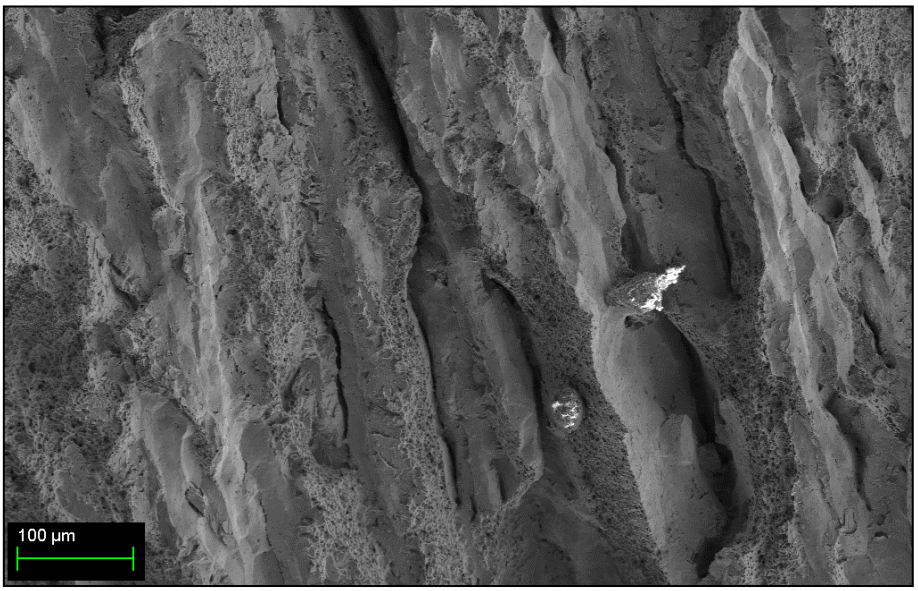

Figure 111: SEM micrograph of the fracture surface of Sample 9 (AW). The sample contained 0.23 mass% Mo and 2.44 mass% Ni. The sample had an impact energy of 31 $J_{(5mm)}$ and a hardness of 271 HV10. Average grain size of the sample was 1.1 µm. The sample contained 100 % $AF_{(Traditional)}$ and 85 % $AF_{(True)}$. The sample shows intergranular fracture along PAGBs.

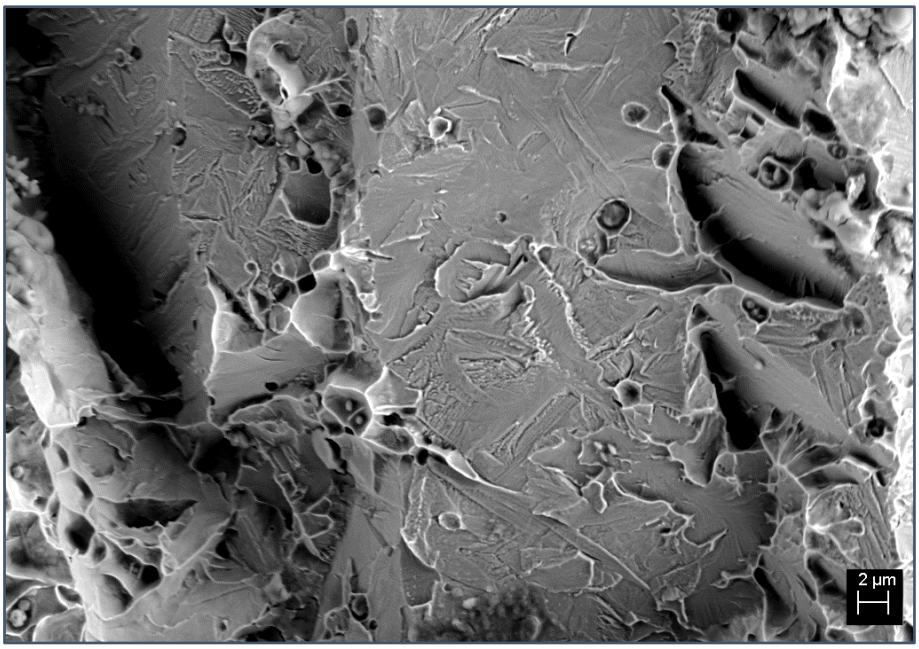

Figure 112: SEM micrograph of intergranular cracks propagated along coalesced bainite on the fracture surface of Sample 9 (AW). The sample contained 0.23 mass% Mo and 2.44 mass% Ni. The sample had an impact energy of 31 $J_{(5mm)}$ and a hardness of 271 HV10. The sample contained no GBPs.

4.3.6. Mechanical properties

Table 35 summarises the chemical composition and impact properties of Welds 1–9, and the full-size Charpy estimations, as calculated according to Equation 22 (derived from ASTM A370). Scatter plots of the impact energy of each weld in relation to the Ni and Mo contents of that weld are shown in Figure 113 and Figure 114.

$$IE_{Full\ size} = 2 \times \left(IE_{Half\ size}\right) + 0.0367$$

Equation 14

No statistical correlations were found between the chemical composition of a specific weld and its impact energy of that weld or between any of the variables measured during quantitative microscopy and impact energy. The reason for this appears to be that, with the exceptions of Welds 6 and 9, impact energy did not vary to a significant degree across welds. This can be seen clearly in Figure 115. The only distinct correlation observed was between the presence of coalesced bainite in Welds 6 and 9 and the distinctly low impact energy values of these two samples. These samples fractured in a brittle manner along the coalesced bainite found along the PAGBs of these samples, as shown in Figure 110 and Figure 112.

Table 35: Summary of chemical composition and impact properties of Welds 1 to 9 in the as-welded condition. Impact energy was measured at −40 °C and samples were 5 mm × 10 mm × 55 mm in size. Equation 22 was used to calculate the full-size Charpy values.

Weld	Mo (mass%)	Ni (mass%)	IE 1 (J_{5mm})	IE 2 (J_{5mm})	IE 3 (J_{5mm})	Average impact energy (J_{5mm})	Full-size impact energy (J)
1	0.01	0.01	40	48	36	41	82
2	0.01	1.05	38	40	38	39	78
3	0.01	2.17	38	46	46	43	86
4	0.18	0.01	48	44	44	45	90
5	0.11	1.22	42	54	44	47	94
6	0.12	2.17	22	28	36	29	58
7	0.3	0.01	50	46	50	49	98
8	0.22	0.95	40	42	42	41	82
9	0.23	2.44	36	26	32	31	62

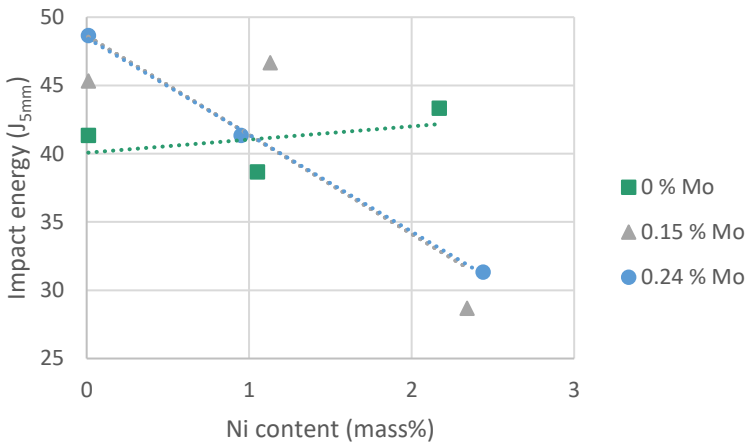

Figure 113: Scatter plot showing impact energy as a function of Ni content at different Mo levels. The trend lines of the 0.15 mass% Mo and 0.24 mass% Mo welds overlap. Sample size was 5 mm × 10 mm × 55 mm.

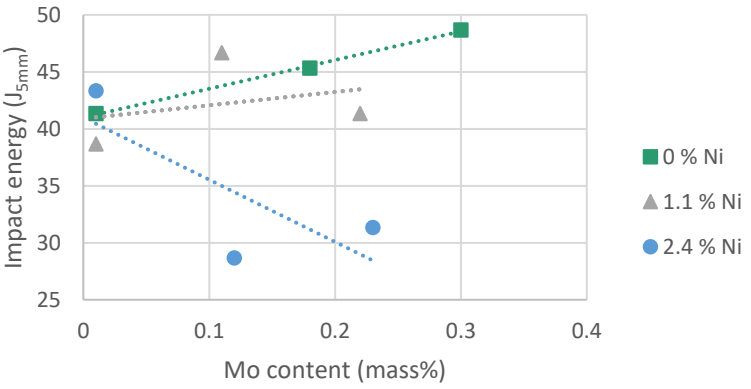

Figure 114: Scatter plot showing impact energy as a function of Ni content at different Mo levels. Sample size was 5 mm × 10 mm × 55 mm.

Table 36: Summary of chemical composition, microstructural evaluation, and impact energy values of Welds 1 to 9.

Weld	Mo (mass%)	Ni (mass%)	Grain size (µm)	%GBP	$\%AF_{(True)}$	% IfRs	Impact energy (J_{5mm})
1	0.01	0.01	2.0	25	64	11	41
2	0.01	1.05	1.8	10	78	12	39
3	0.01	2.17	1.7	12	68	20	43
4	0.18	0.01	1.4	10	81	9	45
5	0.11	1.13	1.6	6	82	12	47
6	0.12	2.34	1.4	0	86	14	29
7	0.3	0.01	1.8	0	89	11	49
8	0.22	0.95	1.6	5	82	13	41
9	0.23	2.44	1.1	0	85	15	31

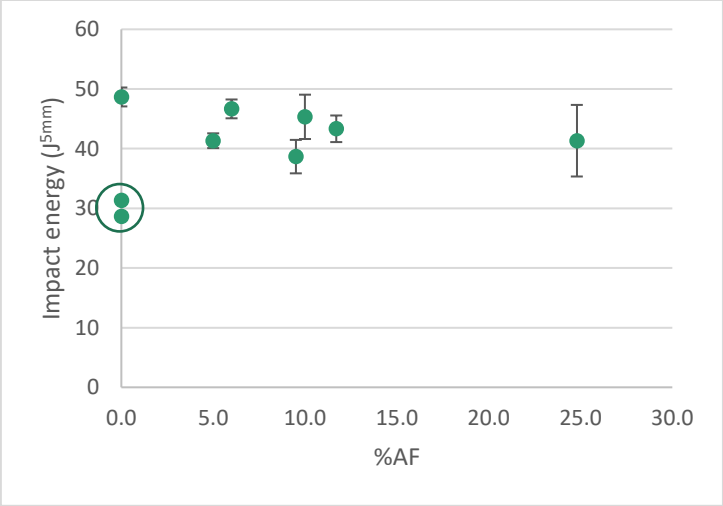

Figure 115: Scatter plot of relationship between impact energy and GBPs. Welds 6 and 9 are circled and show that $AF_{(True)}$ content does not explain the reduction in impact energy of these two welds.

Hardness

The chemical composition, results of quantitative metallography, hardness, and estimated tensile strength of Welds 1–9 (AW) are shown in Table 37. Hardness was converted to ultimate tensile strength (UTS) using the hardness conversion table from ASTM E140-12B (2019)e1. Welds 6 and 9 (AW) had notably higher hardness values and Weld 1 (AW) had a significantly lower hardness than other welds. The high hardness of Welds 6 and 9 is attributed to the coalesced bainite observed and shown in Figure 101, Figure 102 and Figure 103. The bainite observed in Weld 6 may also have contributed to the high hardness; however, the very limited degree to which it was observed makes this unlikely. The low hardness of Weld 1 is attributed to the high GBP content of this weld.

Table 37: Summary of chemical composition, hardness, and UTS calculated as a function of the hardness measurements of Welds 1 to 9 (AW).

Sample	Mo (mass%)	Ni (mass%)	Grain size (µm)	%GBP	$\%AF_{(True)}$	% IfR*	Hardness (HV 10)	UTS (based on hardness)
Weld 1	0.01	0.01	2.0	25	64	11	208 ± 4	681
Weld 2	0.01	1.05	1.8	10	78	12	227 ± 3	751
Weld 3	0.01	2.17	1.7	12	68	20	225 ± 4	742
Weld 4	0.18	0.01	1.4	10	81	9	242 ± 3	768
Weld 5	0.11	1.22	1.6	6	82	12	240 ± 7	763
Weld 6	0.12	2.34	1.4	0	86	14	261 ± 4	828
Weld 7	0.3	0.01	1.8	0	89	11	240 ± 5	742
Weld 8	0.22	0.95	1.6	5	82	13	244 ± 3	776
Weld 9	0.23	2.44	1.1	0	85	15	271 ± 5	857

*Interferritic regions

Two multivariant regression analyses were used to test the relationship between hardness and chemical composition. The first analysis took only the Ni and Mo concentrations into account; the second took the Ni and Mo concentrations, as well as their product, into account. The results of these regression analyses are shown in Table 38 and Table 39, respectively. The equations produced by the results of the regression analyses are shown in Equation 32 and Equation 33.

The multivariant regression was performed using individual hardness measurements. This was necessary because there is a minimum number of *y*-data points required for every additional *x*-variable added to such an analysis. The first multivariant regression had an R^2 value of 0.67; that of the second analysis was 0.74. This indicates that there is an interaction effect between Ni and Mo, which is confirmed by the P-value of the product of Ni and Mo contents.

The equation produced by the multivariant regression reported in Table 39 is shown in Equation 33 and was used to calculate the hardness of each weld in this study. These values were then compared to the measured values, as shown in Figure 116. The trendline of this graph had an R^2 value of 0.82. The P-values of the independent variables in both regression models were extremely low, which indicates that both mass% Mo and mass% Ni in the first case, and mass% Mo, mass% Ni, and the product of mass% Ni and mass% Mo in the second case, were statistically significant.

Table 38: Regression statistics and coefficients, standard error, and P-value of linear multiple regression of the influence of the correlation between mass% Ni and mass% Mo on hardness.

Multiple *R*	0.83		
***R* squared**	0.68		
Adjusted *R* squared	0.67		
Standard error	11.01		
Observations	72		
	Coefficients	Standard error	P-value
Intercept	208	2.79	9.08E−68
Mo (mass%)	14.14	1.39	1.97E−15
Ni (mass %)	104.50	12.89	1.27E−11

$$HV10 = 208 + 14.14(mass\%\ Mo) + 104.5(mass\%\ Ni)$$

Equation 32

Table 39: Regression statistics and coefficients, standard error, and P-value of linear multiple regression of the influence of the correlation between mass% Ni, mas % Mo, and mass% Ni × mass% Mo on hardness.

Multiple *R*	0.87		
***R* squared**	0.75		
Adjusted *R* squared	0.74		
Standard error	9.87		
Observations	72		
	Coefficients	Standard error	P-value
Intercept	216	3.07	2.79E−65
Mo (mass%)	58.71	15.82	0.003598
Ni (mass %)	6.57	2.18	0.000416
Ni (mass%) × Mo (mass%)	52.19	12.32	6.97E−05

$$HV10 = 216 + 58.7(mass\%\ Mo) + 6.6(mass\%\ Ni) + 52.2(mass\%\ Mo \times mass\%\ Ni)$$

Equation 33

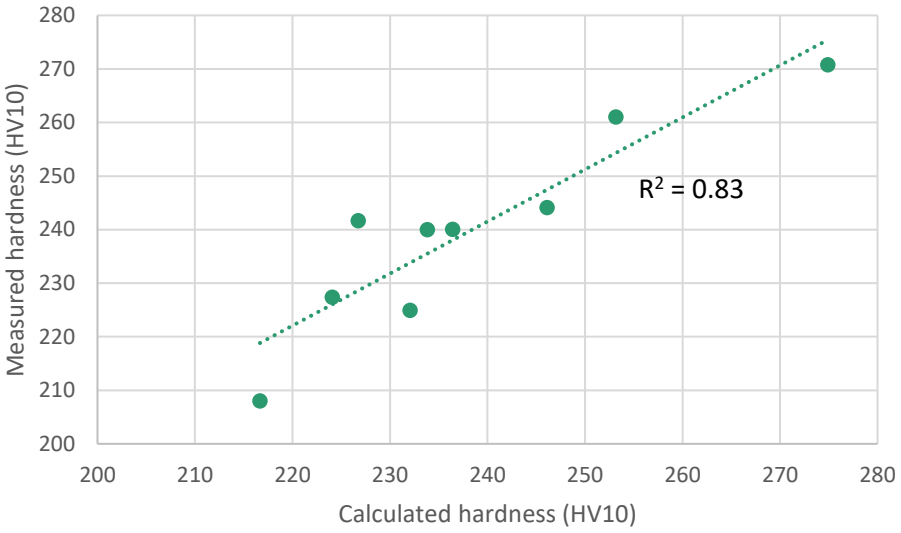

Figure 116: Scatter plot of relationship between the hardness predicted by Equation 33 and the measured hardness values of each weld.

A multivariant regression analysis was performed that included Ti content as a variable, in addition to the Ni and Mo contents and their product. The results of this regression are shown in Table 40. The adjusted R^2 value of this regression model is slightly higher than that without Ti as a variable (Table 39); however, the standard error of the model is higher.

Table 40: Regression statistics and coefficients, standard error, and test on individual regression coefficients (t Stat) of linear multiple regression of the influence of the correlation between mass% Ni, mass% Mo, mass% Ni × mass% Mo, and Ti on hardness.

Multiple *R*	0.88		
***R* squared**	0.77		
Adjusted *R* squared	0.76		
Standard error	9.49		
Observations	72		
	Coefficients	Standard error	P-value
Intercept	290.59	29.35	7.63E−96
Mo (mass%)	−3.42	4.43	6.88E−09
Ni (mass%)	−0.86	27.83	1.28E−18
Ni (mass%) × Mo (mass%)	140.15	36.39	4.90E−05
Ti (mass%)	−2809	1099	0.778

A scatter plot of the relationship between hardness and GBP content is shown in Figure 117. The relationship between hardness and traditional acicular ferrite content is shown in Figure 118. There is a strong tendency for hardness to decrease as the fraction of GBPs decreases and the fraction of $AF_{(True)}$ content increases. There was no correlation between the percentage IfRs and hardness.

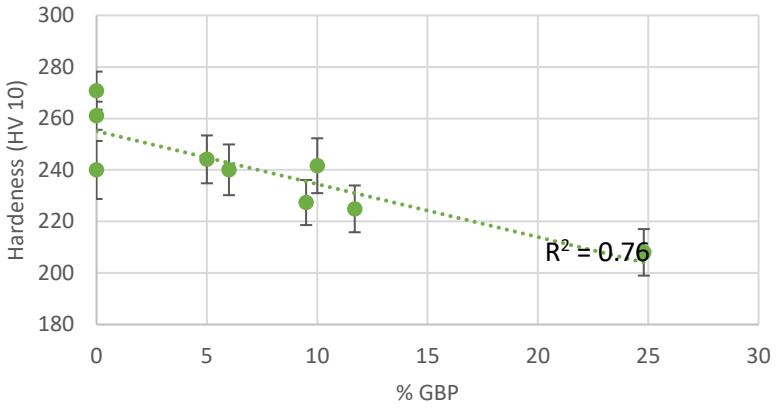

Figure 117: Scatter plot of relationship between hardness and grain boundary product content.

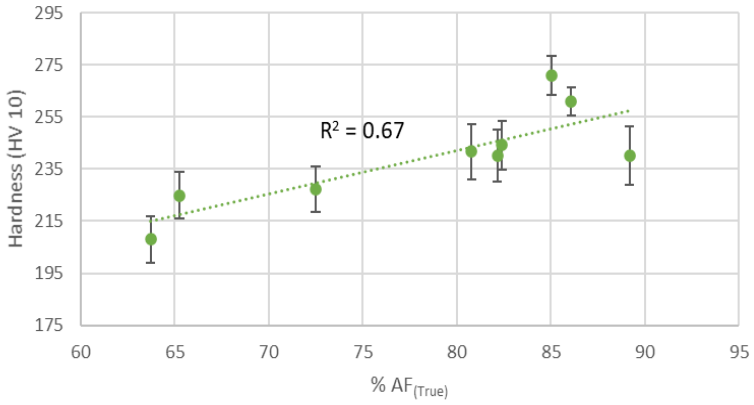

Figure 118: Scatter plot of relationship between hardness and true acicular ferrite content. There is a relatively good, positive correlation between the two variables.

A Hall–Petch plot of the results is shown in Figure 119. This plot indicates that the Hall–Petch effect, where the expected increase in strength is expressed as a function of grain size (Equation 2), appears to be responsible for a significant amount of the increase in hardness observed in the samples.

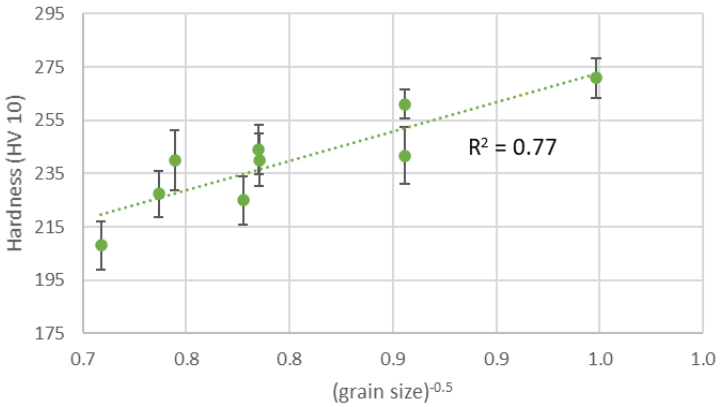

Figure 119: Hall–Petch plot of the relationship between hardness and the inverse of the square root of grain size.

The results therefore indicated that hardness was primarily affected by two main factors: grain size and GBP content. However, grain size and GBP content are not independent variables and a multivariant linear regression was necessary to determine an equation that could be used to evaluate whether these two factors altered hardness independently. The results of the multivariant linear regression are shown in Table 41. Individual hardness readings were used as *y*-variables whilst average (grain size)$^{-0.5}$ and GBP content readings were used as *x*-variables.

The equation produced by the multivariant regression is shown in Equation 34. A scatter plot showing the relationship between the hardness predicted by this equation in relation to the measured hardness of each sample is shown in Figure 120. The R^2 value of the trendline is 0.90. This is significantly higher than the R^2 value of the relationship between hardness and both (grain size)$^{-0.5}$ and GBP content independently. This shows that the influence of GBP content on hardness is not merely a result of its influence on grain size.

Table 41: Regression statistics and coefficients, standard error, and P-value of linear multiple regression done on the influence of (grain size)$^{-0.5}$ and GBP content on hardness.

Multiple *R*	0.92		
***R* squared**	0.84		
Adjusted *R* squared	0.83		
Standard error	7.85		
Observations	72		
	Coefficients	Standard error	P-value
Intercept	−65.4	26.83	4.38E−32
(grain size)$^{-0.5}$	411.9	34.80	3.37E−19
%GBP	−0.80	0.15	6.58E−10

$$HV10 = -65.4 + 411.9(grain\ size)^{-0.5} - 0.8(\%\ GBP)$$

Equation 34

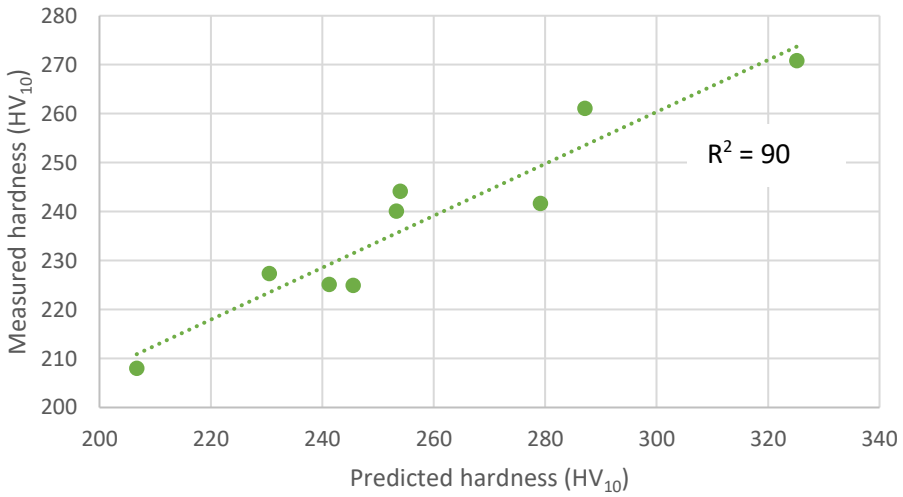

Figure 120: Scatter plot showing relationship between the hardness predicted by Equation 34 and the measured hardness of each sample. The R^2 value of the correlation between these two values is 0.90.

Hardness and impact energy

A scatter plot of the relationship between hardness and impact energy of Welds 1–9 is shown in Figure 121. The graph clearly shows the binary nature of the impact energy values across the hardness range shown. It also shows that the two welds that had low impact energy values had higher hardness than the remainder of the welds. This indicates that there may be some critical hardness level above which impact energy begins to decrease. Both high hardness welds contained Mo and high levels of Ni. Weld 6 contained 0.12 mass% Mo and 2.2 mass% Ni and Weld 9 contained 0.23 mass% Mo and 2.4 mass% Ni.

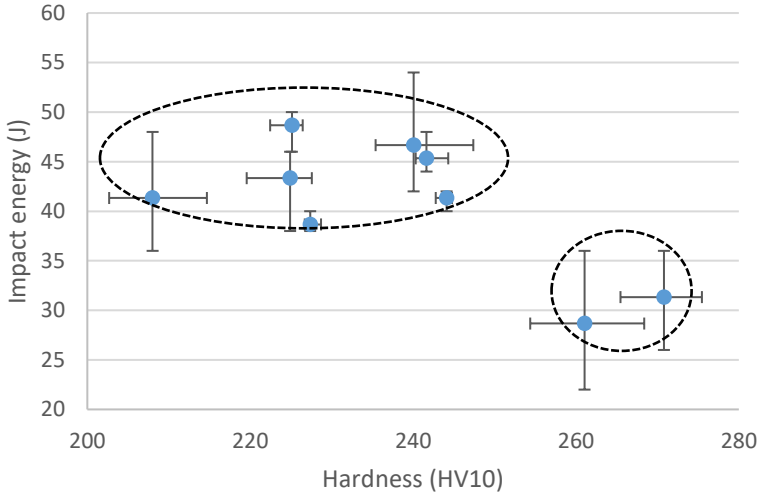

Figure 121: Scatter plot showing the relationship between hardness (HV10) and impact energy (J) of Welds 1 to 9 in the as-welded condition. Error bars of the hardness measurements represent standard deviation and the error bars of the impact energy represent the range of impact energy readings. Weld 6 and Weld 9 are to the bottom right of the image.

4.4. Thermal cycling

4.4.1. Outline of experimental work

Samples from each weld were exposed to three thermal cycles, intended to represent the thermal cycling to which weld metal is exposed during multi-pass welding. The peak temperatures of each thermal cycle corresponded to the peak temperature associated with the IR HAZ, FG HAZ, and CG HAZ. Changes in ferrite grain size, GBP content, M/A region content, and $AF_{(True}$ content after thermal cycling are shown in Figure 122, Figure 123, Figure 124, and Figure 125, respectively. The graphs show that there are notable changes to all variables in at least some of the welds for each thermal cycle, but that no discernible trends are present. The average hardness and Charpy impact test results of Welds 1–9 in all heat treatment conditions are shown in Table 42.

.

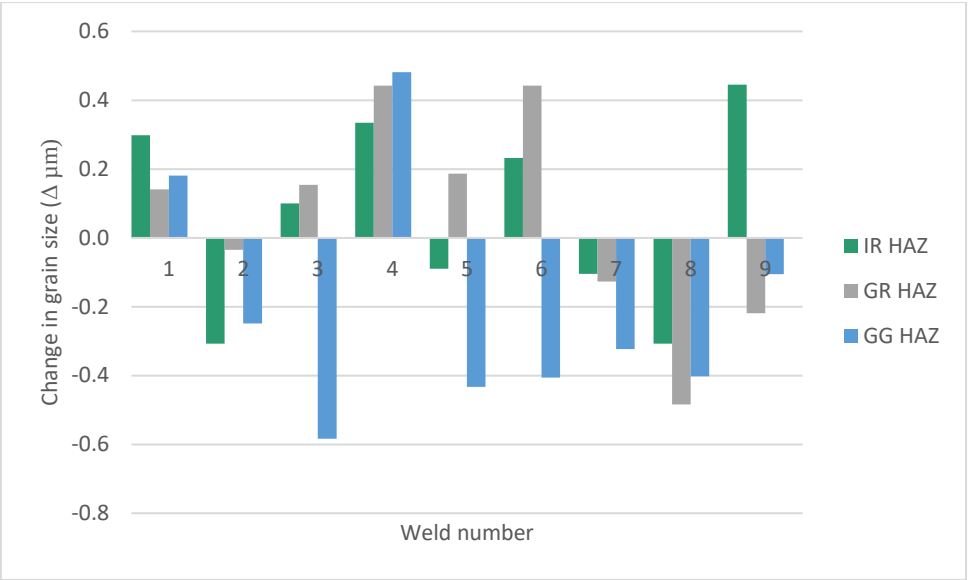

Figure 122: Bar graph of changes in ferrite grain size measurement of Welds 1 to 9 following thermal cycling to simulate various HAZ regions.

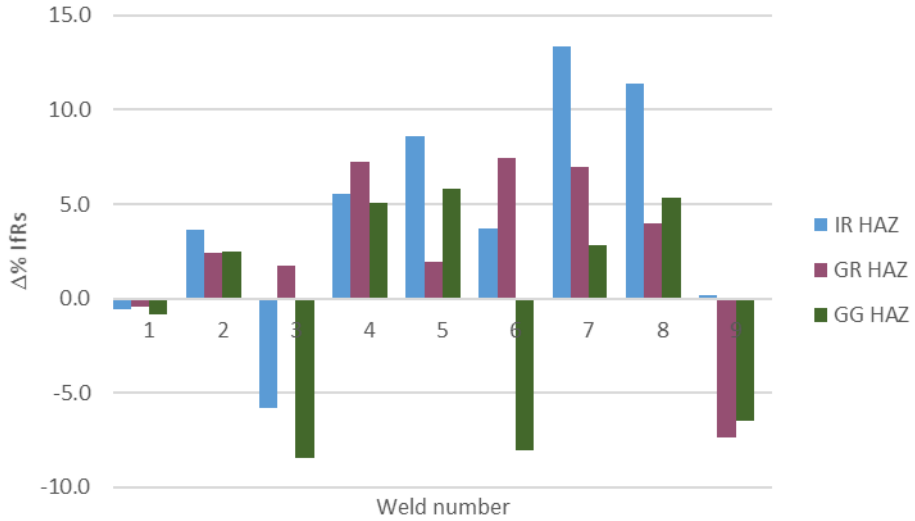

Figure 123: Bar graph of the change in fractions of interferritic regions in Welds 1 to 9 following thermal cycling to simulate various HAZ regions.

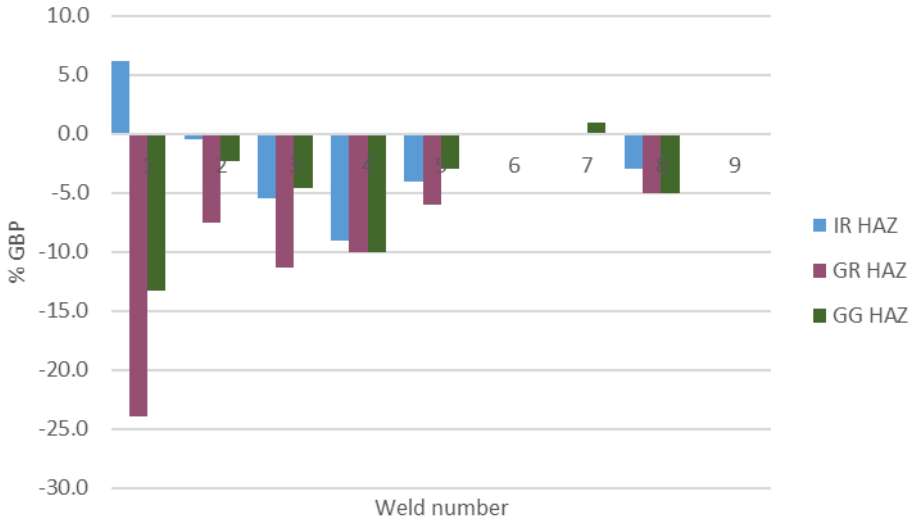

Figure 124: Change in fraction of GBP in Welds 1 to 9 following exposure to various thermal cycles.

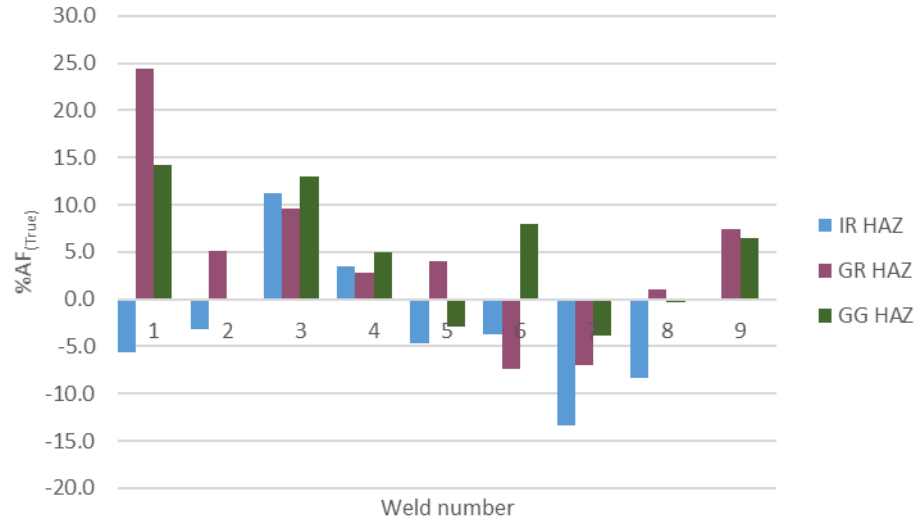

Figure 125: Change in fraction of $AF_{(True)}$ in Welds 1 to 9 following exposure to various thermal cycles.

Table 42: Average hardness and Charpy impact test results of Welds 1 to 9 (AW), (IR HAZ), (GR HAZ), and (GG HAZ). 95 % confidence interval of the hardness is also quoted.

Weld	Heat treat-ment	Ni (mass%)	Mo (mass%)	Hardness (HV10)		Impact 1 (J_{5mm})	Impact 2 (J_{5mm})	Impact 3 (J_{5mm})	Average impact (J_{5mm})
				$\Delta t_{(800-500)}$ = 8 s	$\Delta t_{(800-500)}$ = 12 s				
1	AW	0.01	0.01	208 ± 3.2		40	48	36	41
	IR	0.01	0.01	204 ± 2.6		34	34		34
	GR	0.01	0.01	196 ± 3.2		60	56	50	55
	GG	0.01	0.01	226 ± 2.8		44	40		42
2	AW	1.05	0.01	227 ± 6.4		38	40	38	39
	IR	1.05	0.01	252 ± 3.9		30	40	24	31
	GR	1.05	0.01	250 ± 4.7		26	40	38	35
	GG	1.05	0.01	260 ± 2.9		32	28		30
3	AW	2.17	0.01	225 ± 4.4		38	46	46	43
	IR	2.17	0.01	229 ± 1.1		36	36	40	37
	GR	2.17	0.01	224 ± 3.1		36	46	40	41
	GG	2.17	0.01	254 ± 2.6		40	38	36	38
4	AW	0.01	0.18	242 ± 2.4		48	44	44	45
	IR	0.01	0.18	241 ± 8.5	249 ± 3.4	28	30	26	28
	GR	0.01	0.18	252 ± 3.6	210 ± 7.3	40	40	32	37
	GG	0.01	0.18	234 ± 9.6	238 ±7.1	40	50	46	45
5	AW	1.13	0.11	240 ± 20		42	54	44	47
	IR	1.13	0.11	246 ± 10	268 ± 9.5	34	28	32	31
	GR	1.13	0.11	250 ± 2.8	252 ± 2.3	38	40	42	40
	GG	1.13	0.11	269 ± 7.7	275 ± 3.3	30	30		30
6	AW	2.34	0.12	261 ± 5.9		22	28	36	29
	IR	2.34	0.12	276 ± 3.1	285 ± 2.6	32	42		37
	GR	2.34	0.12	312 ± 7.3	285 ± 3.4	32	22	26	27
	GG	2.34	0.12	340 ± 12	310 ± 2.1	30	30		30
7	AW	0.01	0.3	225 ± 7.3		28		22	49
	IR	0.01	0.3	268 ± 8.3	239 ± 4.8	32	28	20	27
	GR	0.01	0.3	291 ± 14	250 ± 8.0	36	30	30	32
	GG	0.01	0.3	271 ± 3.0	257 ± 4.3	42	40	42	41
8	AW	0.95	0.22	244 ± 5.8		40	42	42	41
	IR	0.95	0.22	292 ± 7.8	257 ± 3.4	34	32	32	33
	GR	0.95	0.22	274 ± 6.8	264 ± 10	30	34	26	30
	GG	0.95	0.22	291 ± 7.4	271 ± 3.5	28	26		27
9	AW	2.44	0.23	271 ± 7.7		36	26	32	31
	IR	2.44	0.23	270 ± 4.3		26	26	26	26
	GR	2.44	0.23	339 ± 4.7		24	16	18	19
	GG	2.44	0.23	352 ± 4.0		18	16	20	18

The change in hardness for each weld (ΔHV10) and the HAZ region at which this hardness occurred are shown in Table 43. Four of the welds (Welds 6, 7, 8, and 9) experienced a significant change in hardness (> 40 HV10)).

Table 43: Difference between average hardness of the as-welded weld metal and average hardness of the simulated HAZ region that had the highest hardness for each weld. Low- and high-Ni groups had an average of 1.0 mass% Ni and 2.3 mass% Ni, respectively; low- and high-Mo groups had an average of 0.14 mass% Mo and 0.25 mass% Ni, respectively.

	0 % Ni				1.0 % Ni				2.3 % Ni			
HAZ region	Sample	IR	FG	CG	Sample	IR	FG	CG	Sample	IR	FG	CG
0 % Mo	1	−4	−12	**18**	2	25	22	**33**	3	4	−1	**29**
0.15 % Mo	4	4	−1	**29**	5	−1	**10**	−8	6	6	10	**29**
0.25 % Mo	7	15	51	**79**	8	43	**66**	46	9	−1	**68**	81

Scatter plots showing the relationships between the impact energy of welds in the as-welded condition and following thermal cycling to simulate the IR HAZ, FG HAZ, and CG HAZ are shown in Figure 126, Figure 127, and Figure 128, respectively. The graphs show that there is no relationship between the impact energy of welds in the as-welded condition and the impact energy of those same welds following thermal cycling. This means that, except in very general terms, the impact energy of a single-pass weld cannot be used to predict the impact energy of a multi-pass weld. Each HAZ region affected the impact energy of welds in a different way, as shown in Sections 4.4.2, 4.4.3, and 4.4.4. All welds that underwent significant changes in impact energy due to thermal cycling contained Mo; however, the presence of Mo did not result in a reduction in impact energy in all cases, nor did higher levels of Mo result in a larger decrease in impact energy. There was no general trend with regards to the effect of Ni on the sensitivity of weld metal to reheating.

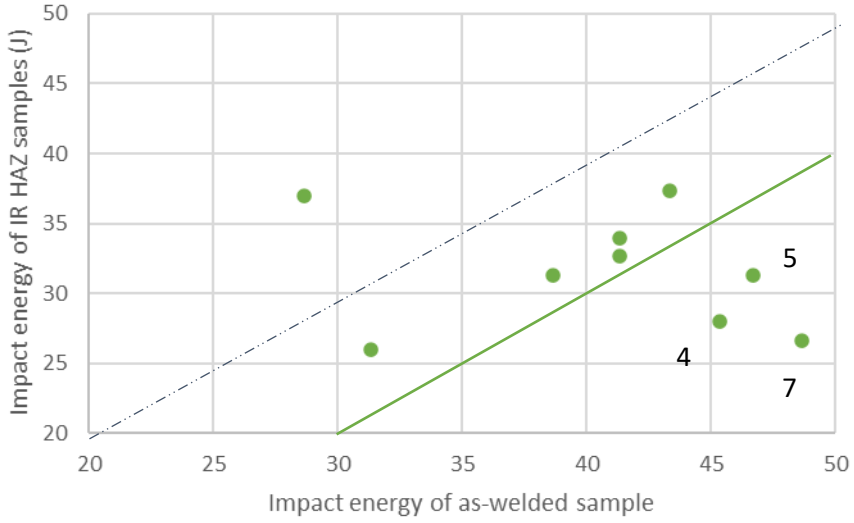

Figure 126: Scatter plot of relationship between the impact energy of welds in the as-welded condition and the impact energy following thermal cycling with peak temperature in the IR HAZ region. The graph shows that there is no relationship between the two values. Data points below the solid line indicate welds for which impact energy was reduced by more than 10 $J_{(5mm)}$ after exposure to the IR HAZ thermal cycle compared with the as-welded condition.

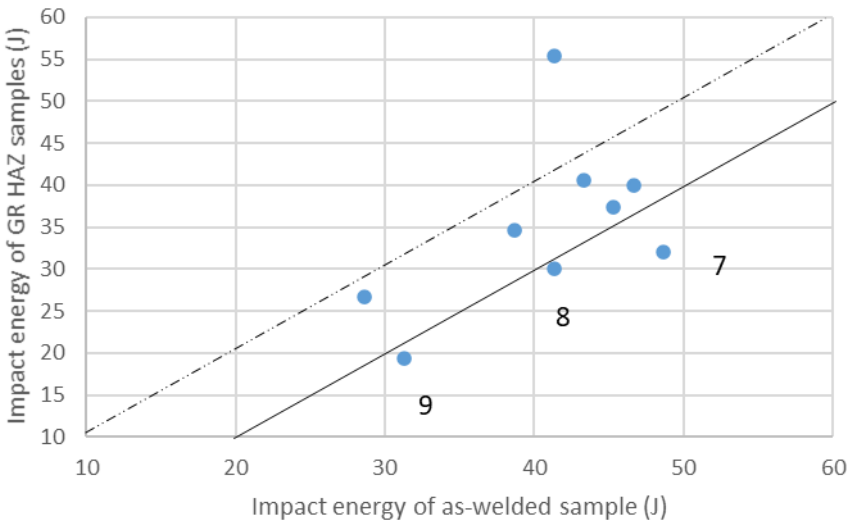

Figure 127: Scatter plot of relationship between the impact energy of welds in the as-welded condition and the impact energy following thermal cycling with peak temperature in the GR HAZ region. The graph shows that there is no relationship between the two values. Data points below the solid line indicate welds for which the impact energy was reduced by more than 10 $J_{(5mm)}$ after exposure to the FG HAZ thermal cycle compared with the as-welded condition.

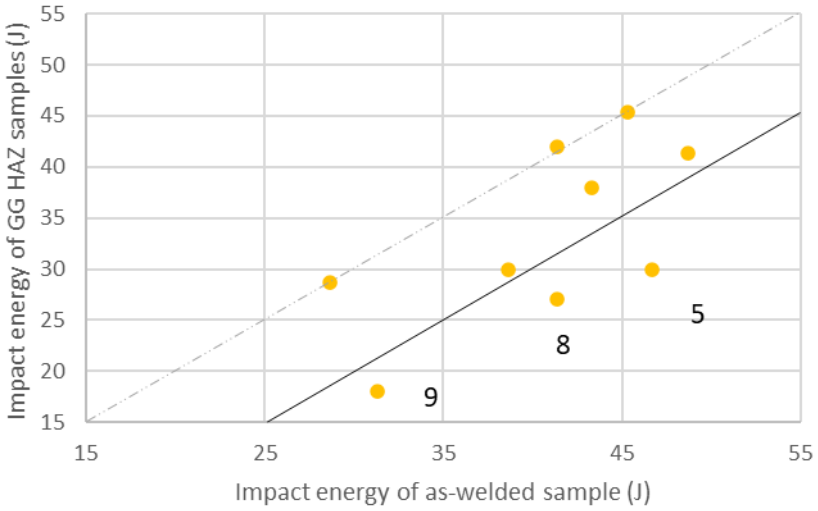

Figure 128: Scatter plot of relationship between the impact energy of welds in the as-welded condition and the impact energy following thermal cycling with peak temperature in the GG HAZ region. The graph shows that there is no relationship between the two values. Data points below the solid line indicate welds for which the impact energy was reduced by more than 10 $J_{(5mm)}$ after exposure to the CG HAZ thermal cycle compared with the as-welded condition.

4.4.2. Response of weld metal to reheating to the intercritically reheated heat-affected zone

The impact energy of each IR HAZ sample is shown in Table 44. Changes in hardness and impact energy of Welds 1–9 after reheating to the IR HAZ are shown in Figure 129 and Figure 130, respectively. Welds 7 and 8 showed significant changes in hardness (greater than 40 HV10). There was a significant reduction in the impact energies of Welds 4, 5, and 7 (less than −10 $J_{(5mm)}$).

Table 44: Impact energy (IE) and change in impact energy in relation to the as-welded sample of that weld (ΔIE) for Welds 1 to 9 (IR HAZ). ΔIE values in bold indicate that this was the largest change in impact energy across all heat-treatment conditions for that particular weld.

	0 mass% Ni			1.0 mass% Ni			2.3 mass% Ni		
	Weld	IE ($J_{(5mm)}$)	ΔIE ($J_{(5mm)}$)	Weld	IE ($J_{(5mm)}$)	ΔIE ($J_{(5mm)}$)	Weld	IE ($J_{(5mm)}$)	ΔIE ($J_{(5mm)}$)
0 mass% Mo	1	34	−7	2	31	−7	3	37	**−6**
0.15 mass% Mo	4	28	**−15**	5	31	**−17**	6	37	8
0.25 mass% Mo	7	27	**−22**	8	33	−9	9	26	−5

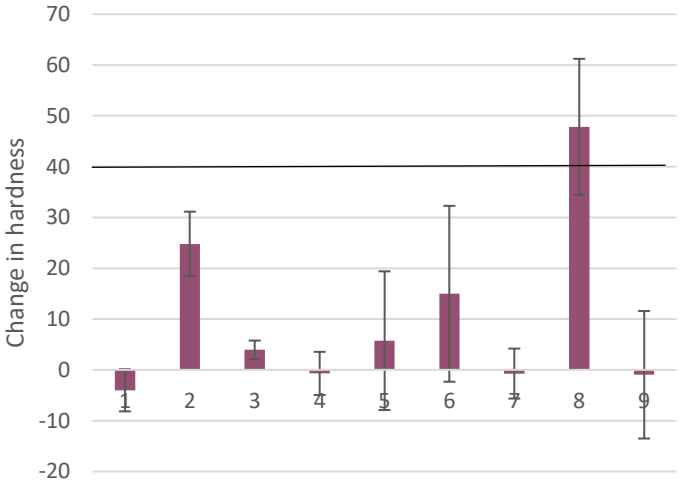

Figure 129: Change in hardness of each weld following reheating to the IR HAZ region.

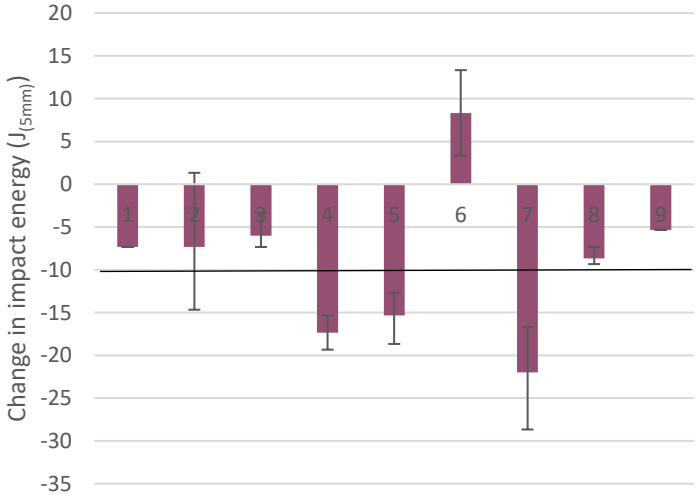

Figure 130: Change in impact energy of each weld following reheating to the IR HAZ region.

SEM microscopy of Welds 4, 5, and 7 (IR) revealed IfRs. The IfRs had undergone no etching and no evidence of a substructure was apparent. Examples of such regions are shown in Figure 131 and Figure 132. In contrast, the IfRs of Weld 8 had undergone etching and showed evidence of a substructure. This structure appears similar to the coalesced bainite observed in Weld 9 (AW) (Figure 103). An example of such an IfR is shown in Figure 133. The ferrite regions of this sample also contained small precipitates. It is likely that these are the result of carbide precipitation that occurred when austenite transformed to ferrite. The increase in hardness of Weld 8 (IR HAZ) was therefore associated with the precipitation of what appears to be carbides within ferrite grains. The decrease in impact energy was associated with a change in morphology of the IfRs.

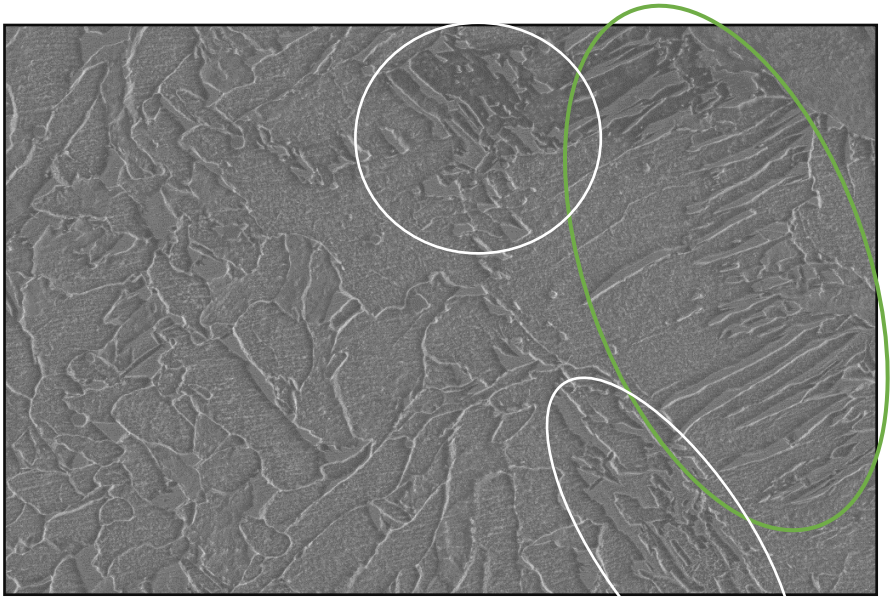

Figure 131: SEM micrograph of Weld 4 (IR HAZ). The micrograph shows regions of M/A in between bainite laths (indicated by a green oval) and in between ferrite grains (indicated by white ovals). The sample contained 0.18 mass% Mo and no Ni. The sample had an impact energy of 28 $J_{(5mm)}$ and a hardness of 241 HV10.

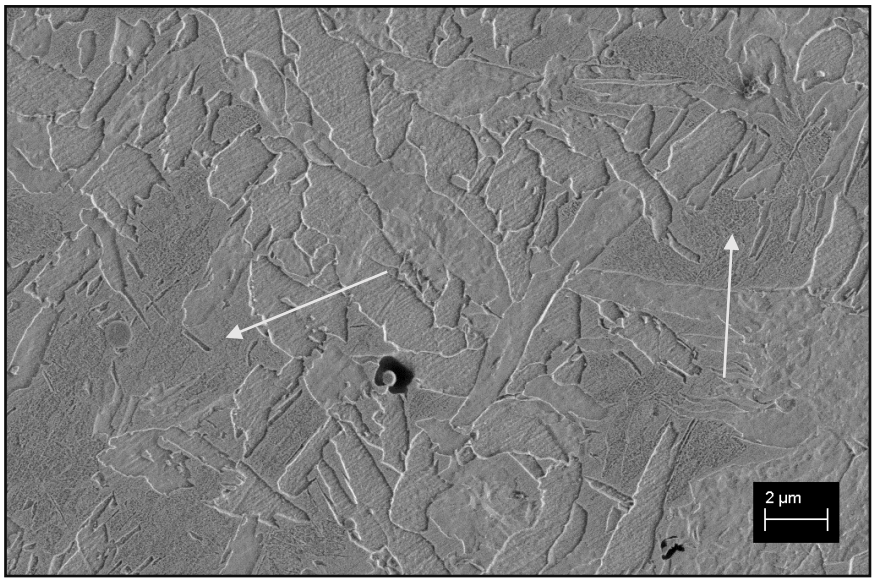

Figure 132: Micrograph of the interferritic region of Weld 7 IR HAZ. The micrograph shows extensive M/A region coverage (indicated by white arrows) The sample contained 0.3 mass% Mo, and 0 mass% Ni. The sample had an impact energy of 27 $J_{(5mm)}$ and a hardness of 268 HV10.

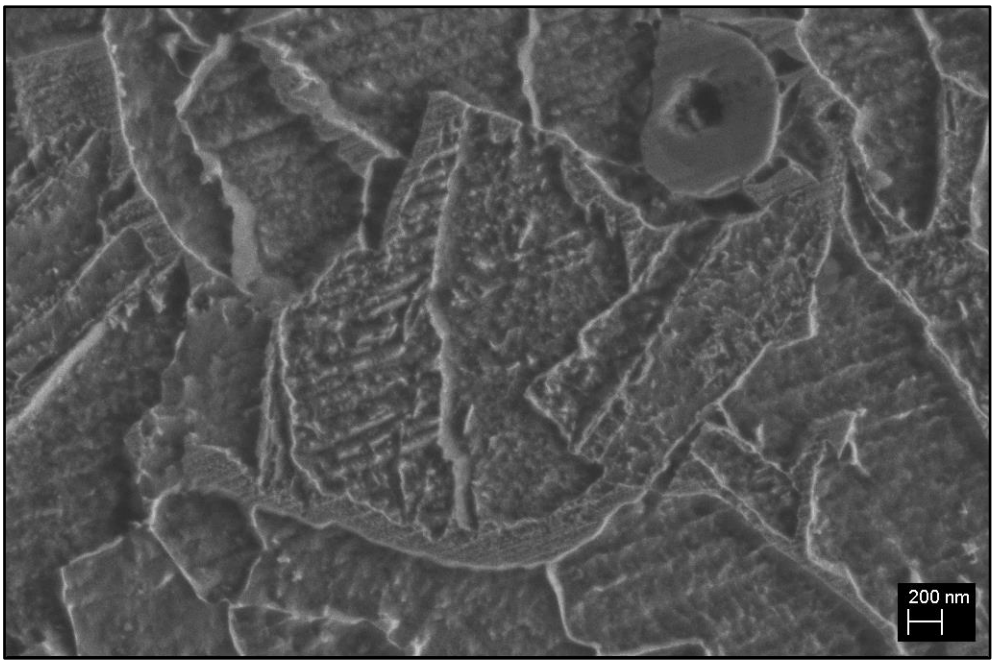

Figure 133: SEM micrograph of an M/A regions from Weld 8 (IR) The sample contained 0.22 mass% Mo and 0.95 mass% Ni. The sample had an impact energy of 33 $J_{(5mm)}$ and a hardness of 292 HV10. The M/A region shows evidence of a substructure.

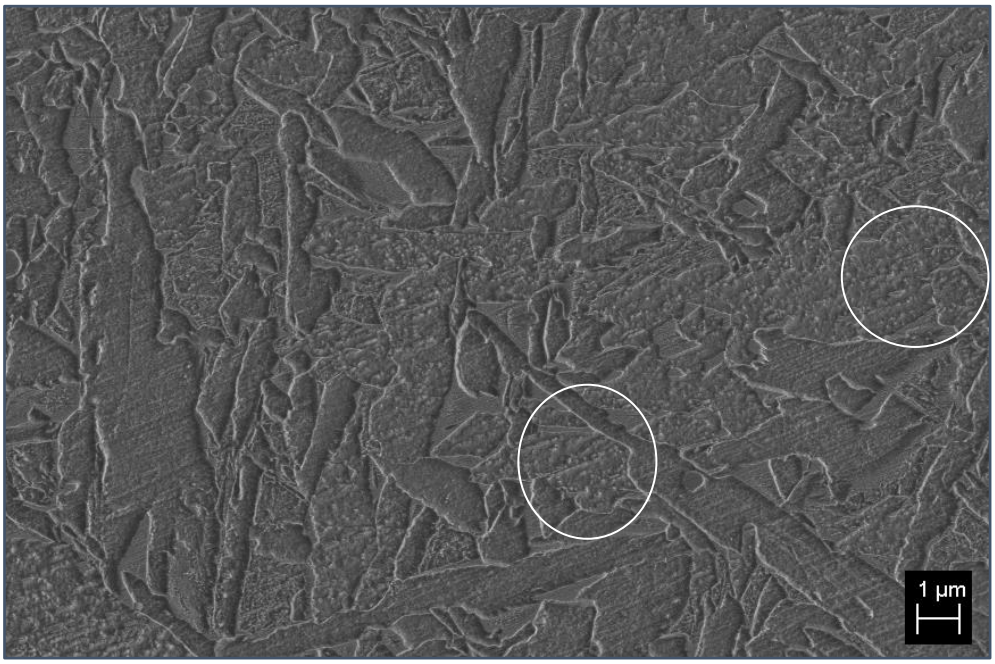

Figure 134: SEM micrograph of Weld 8 (IR) The sample contained 0.22 mass% Mo and 0.95 mass% Ni. The sample had an impact energy of 33 $J_{(5mm)}$ and a hardness of 292 HV10. The micrograph shows extensive carbide precipitation in some of the ferrite regions. Some of these regions are circled.

The fracture surface of Weld 4 (IR HAZ) is shown in Figure 135. The fracture surface shows extensive regions of brittle fracture interspersed with regions of ductile fracture. The brittle fracture is too extensive and broad to be associated with PAGBs. The same fracture surface is shown at higher magnification in Figure 136. There are, what appear to be, extensive M/A particles across the fracture surface. It is noted that these particles are much smaller than the microscopically detected IfRs. M/A islands are usually associated with IfRs (see Section 1.1.2). The possible M/A particles detected on the fracture surface are thought to be responsible for the brittle fracture associated with the IR HAZ samples.

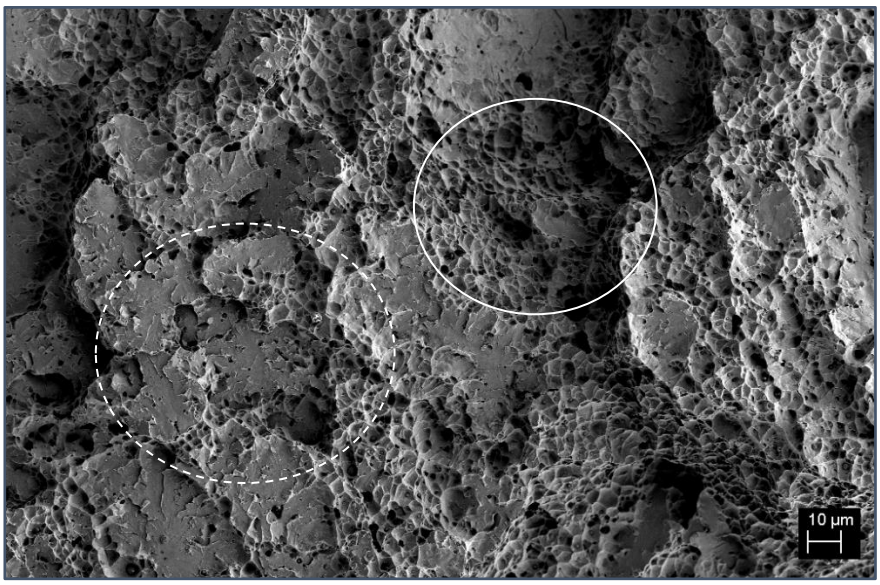

Figure 135: SEM micrograph of the fracture surface of Weld 4 (IR HAZ). The sample shows regions of extensive brittle fracture interspersed with ductile fracture. Brittle fracture is indicated by the dashed circle and ductile fracture is indicated by the solid circle. The sample contained 0.18 mass% Mo and no Ni. The sample had an impact energy of 28 $J_{(5mm)}$ and a hardness of 241 HV10.

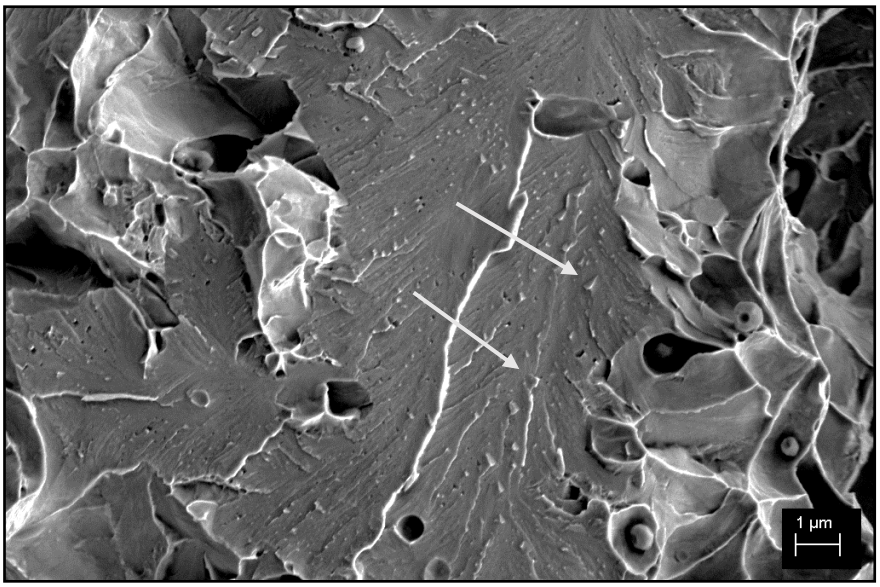

Figure 136: SEM micrograph of the fracture surface of Weld 4 (IR HAZ). The sample shows extensive M/A particles on the brittle fracture surface. The sample contained 0.18 mass% Mo and no Ni. The sample had an impact energy of 28 $J_{(5mm)}$ and a hardness of 241 HV10.

4.4.3. Response of weld metal to reheating to the fine-grained heat-affected zone

The impact energy of each FG HAZ sample is shown in Table 45. The average impact energy of these samples was 35 $J_{(5mm)}$, with a range of 36 $J_{(5mm)}$ and a standard deviation of 10 $J_{(5mm)}$. There was no consistent trend with regard to the absolute value of impact energy for samples exposed to this temperature region, but all samples that contained high levels of Mo had low impact energies. The impact energy of the high-Mo high-Ni weld metal was very low (19 $J_{(5mm)}$).

Table 45: Impact energy (IE) and change in impact energy for Welds 1 to 9 (FG HAZ) compared with the as-welded sample of that weld (ΔIE)). ΔIE values in bold indicate that this was the largest change in impact energy across all heat-treatment conditions for that particular weld.

	0 mass% Ni			1.0 mass% Ni			2.3 mass% Ni		
	Weld	IE ($J_{(5mm)}$)	ΔIE ($J_{(5mm)}$)	Weld	IE ($J_{(5mm)}$)	ΔIE ($J_{(5mm)}$)	Weld	IE ($J_{(5mm)}$)	ΔIE ($J_{(5mm)}$)
0 mass% Mo	1	55	**14**	2	35	−4	3	41	−3
0.15 mass% Mo	4	37	−8	5	40	−7	6	27	**−2**
0.25 mass% Mo	7	32	−17	8	30	−11	9	19	−12

The changes in hardness and impact energy of FG HAZ samples are shown in Figure 137 and Figure 138, respectively. There was a significant increase in the hardness of Welds 6 and 9 (> 40 HV10) following reheating to the GF HAZ region. Welds 7, 8, and 9 experienced significant changes in impact energy (< −10 $J_{(5mm)}$) following thermal cycling. Welds 7, 8, and 9 (FG HAZ) had significantly decreased impact energy when compared with their as-welded counterparts. They also had low overall impact energy. The impact energy of Weld 6 (FG) was also low, but not lower than in the as-welded condition.

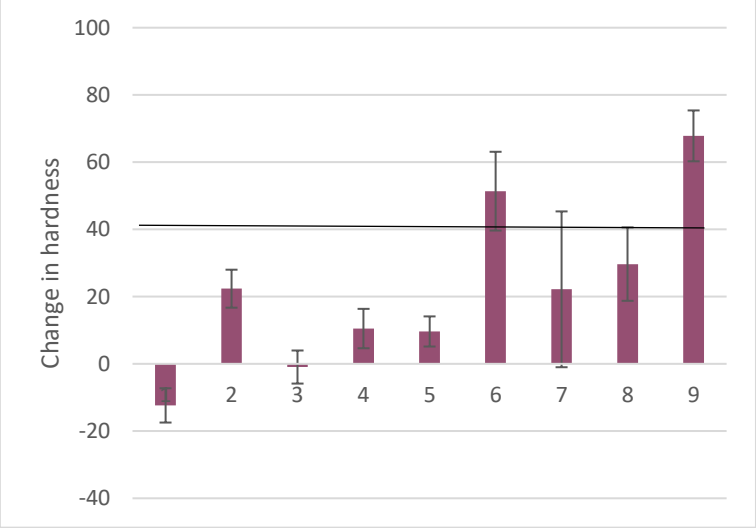

Figure 137: Bar graph showing change in the hardness of weld metal following reheating to the FG HAZ region.

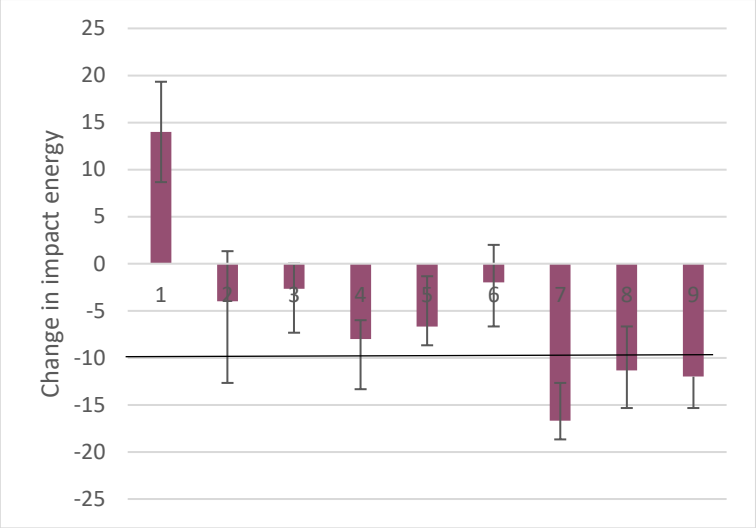

Figure 138: Bar graph showing change in the impact energy of weld metal following reheating to the FG HAZ region.

Microscopy of Welds 7, 8, and 9 (FG) showed that all these samples contained regions of long, thin AF needles interspersed with secondary AF. An example of such a microstructure is shown in Figure 140. The microstructures of Welds 7 and 9 (FG) consisted almost entirely of these regions, whilst those of Welds 6 and 8 were interspersed with regular AF. Weld 9 also contained what appeared to be martensite, as shown in Figure 141. It is likely that these regions of ferrite resulted in the lower impact energy of Weld 9 in relation to Welds 7 and 8 (FG).

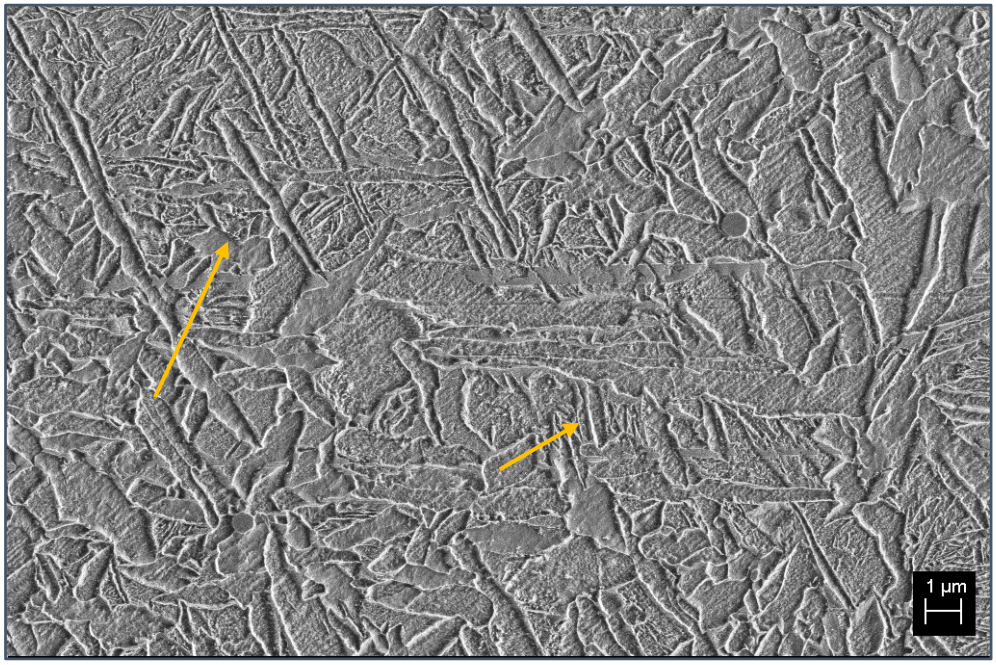

Figure 139: SEM micrograph of Weld 6 FG HAZ. The micrograph shows regions of acicular ferrite with very high aspect ratios and significant degrees of secondary ferrite (indicated by arrows). The sample contained 0.12 mass% Mo and 2.34 mass% Ni and had an impact energy of 27 $J_{(5mm)}$.

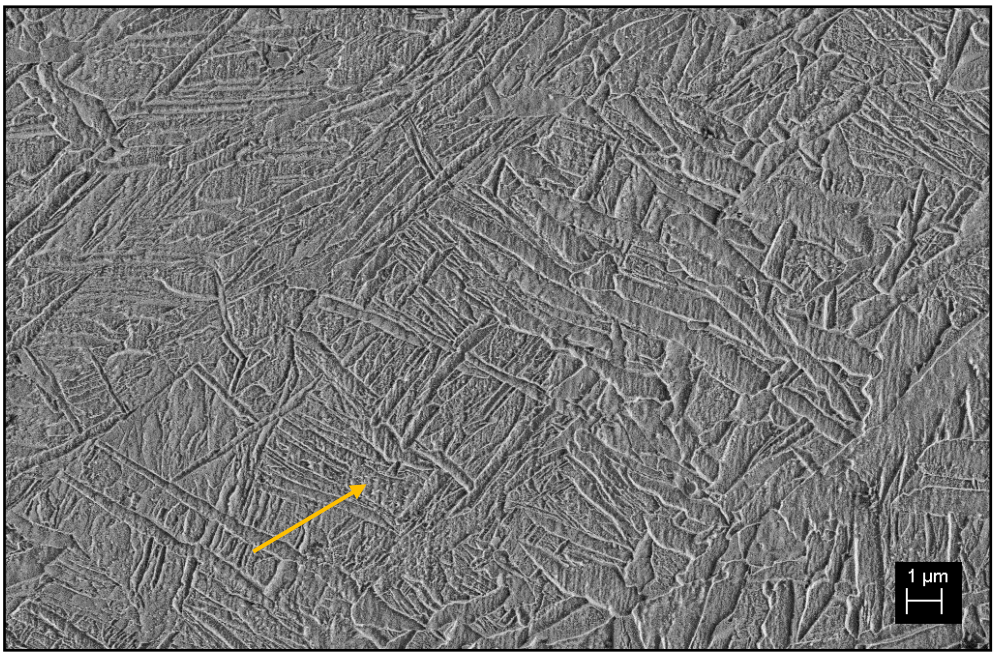

Figure 140: SEM micrograph of Weld 7 GR HAZ. The micrograph shows regions of acicular ferrite with very high aspect ratios and significant degrees of secondary ferrite. The sample contained 0.3 mass% Mo, and 0 mass% Ni and had an impact energy of 32 $J_{(5mm)}$.

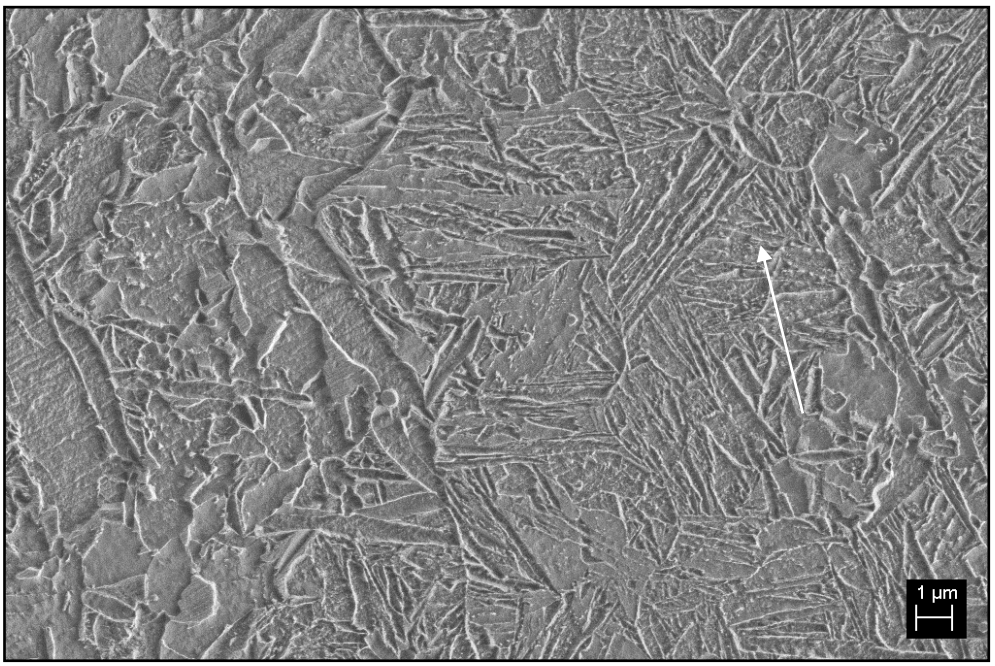

Figure 141: SEM micrograph of Weld 9 GR HAZ. The micrograph shows regions of acicular ferrite with very high aspect ratios and significant amounts of acicular ferrite. The sample also contains martensite, as indicated by the white arrow. The weld contained 0.23 mass% Mo and 2.44 mass% Ni and had an impact energy of 18 $J_{(5mm)}$.

Fractography of Welds 7, 8, and 9 (FG) revealed that all samples fractured extensively in a brittle manner, interspersed with regions of ductile cup-and-cone fracture. Examples of this fracture are shown in Figure 142 and Figure 143. Regions of brittle fracture are assumed to be associated with regions of bainitic AF, whilst the regions of ductile fracture are assumed to be associated with regions of more typical AF.

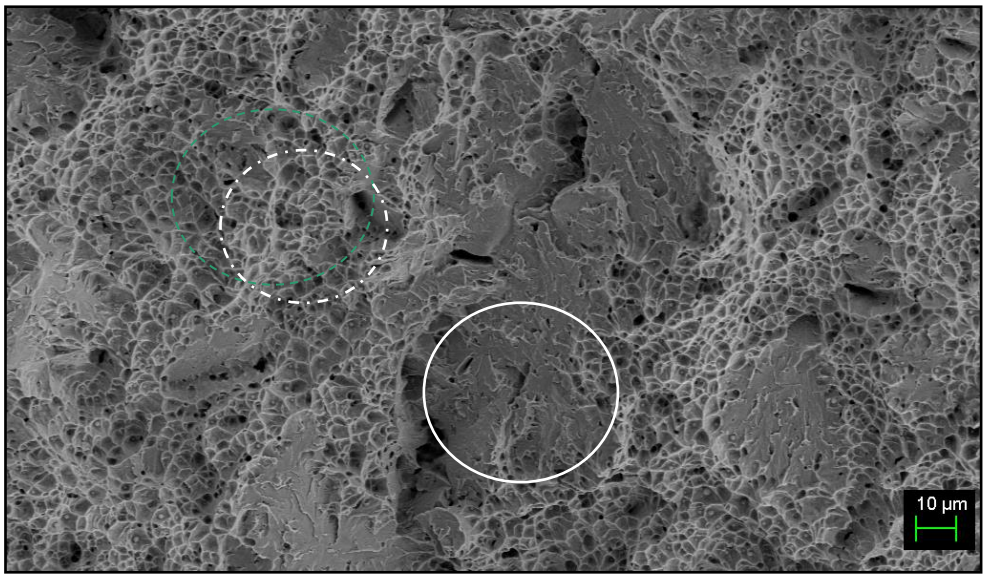

Figure 142: SEM micrograph of the fracture surface of Weld 7 (GR HAZ). The sample contained 0.3 mass% Mo, and 0 mass% Ni and had an impact energy of 32 $J_{(5mm)}$. The dashed circle indicates a region of ductile fracture and the solid circle indicates a region of brittle fracture.

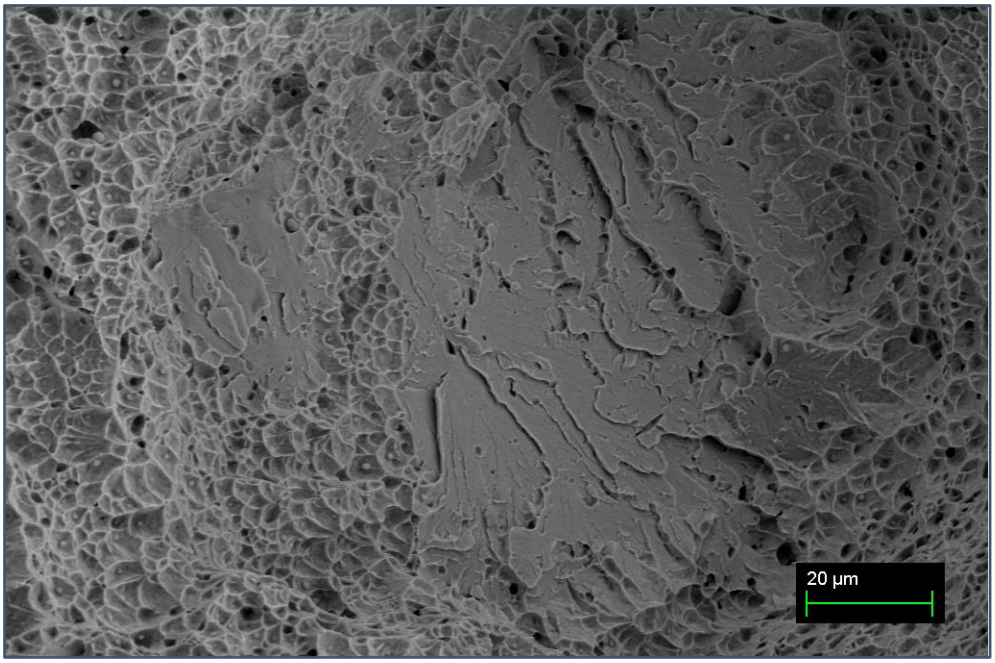

Figure 143: SEM micrograph of the fracture surface of Weld 9 GR HAZ. The sample contained 2.34 mass% Ni and 0.23 mass% Mo. The micrograph shows a region of brittle fracture.

4.4.4. Response of weld metal to reheating to the coarse-grained heat-affected zone

The impact energies of Welds 1–9 (CG) are shown in Table 46. The only observable trend was that Ni additions lowered the impact energy for the high-Mo group.

Bar graphs showing the change in hardness and impact energy of welds following CG HAZ thermal cycling are shown in Figure 144 and Figure 145, respectively. The hardness of Welds 6, 8, and 9 increased significantly following thermal cycling and the impact energies of Welds 5, 8, and 9 decreased significantly.

Table 46: Impact energy (IE) and change in impact energy in relation to the as-welded sample of that weld (ΔIE) for Welds 1 to 9 (CG HAZ). ΔIE values in bold indicate that this was the largest change in impact energy across all heat-treatment conditions for that particular weld.

	mass% Ni			mass% Ni			mass% Ni		
	Weld	IE ($J_{(5mm)}$)	ΔIE ($J_{(5mm)}$)	Weld	IE ($J_{(5mm)}$)	ΔIE ($J_{(5mm)}$)	Weld	IE ($J_{(5mm)}$)	ΔIE ($J_{(5mm)}$)
mass% Mo	1	42	1	2	30	**-9**	3	38	-5
mass% Mo	4	45	-5	5	30	0	6	29	0
mass% Mo	7	41	-7	8	27	**-14**	9	18	**-13**

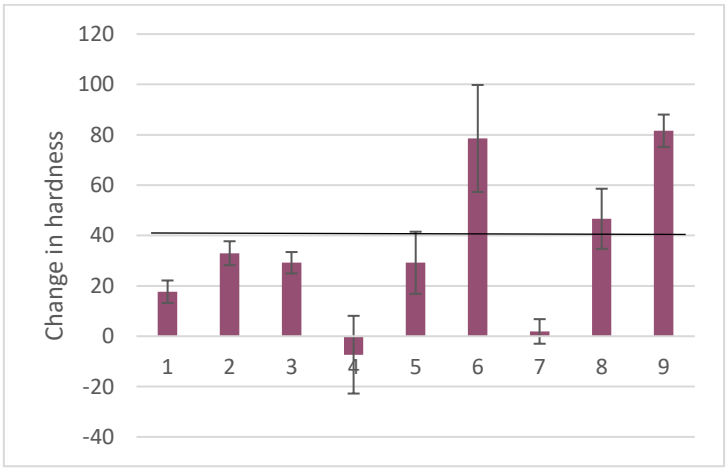

Figure 144: Bar graph of change in hardness of Welds 1 to 9 after reheating to the GG HAZ region.

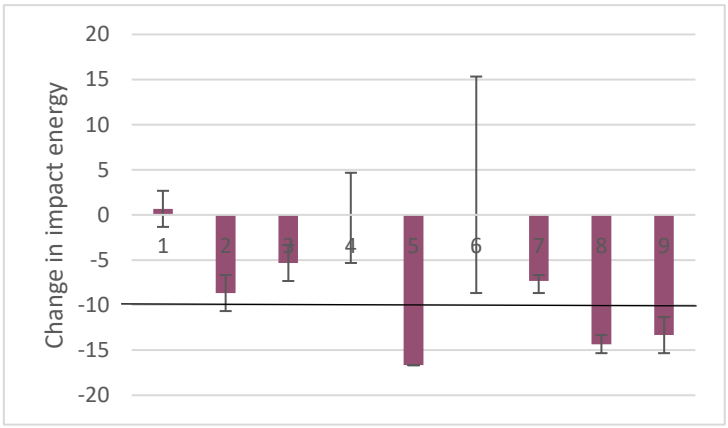

Figure 145: Bar graph of change in impact energy of Welds 1 to 9 after reheating to the GG HAZ region.

Weld 5 (CG) had a microstructure tending towards bainitic AF and contained some bainite. A micrograph of this sample is shown in Figure 146. The AF structures in Welds 6, 8, and 9 (CG) were fully bainitic. An example of such an AF region is shown in Figure 147. The increase in hardness of Welds 6, 8, and 9 is attributed to this microstructure. The decrease in impact energies of Welds 8 and 9 is attributed to the same microstructure.

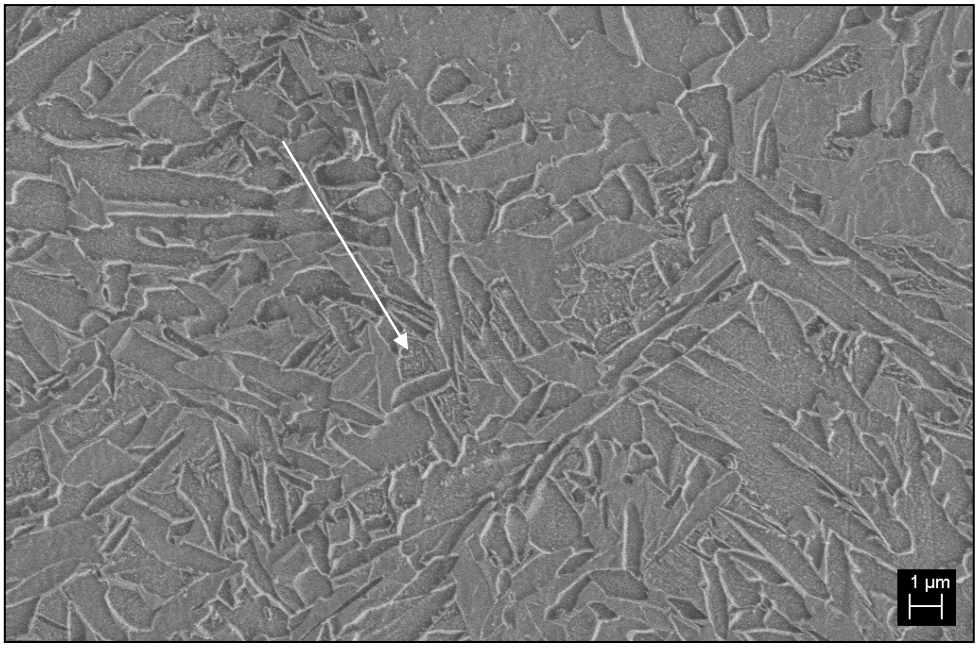

Figure 146: SEM micrograph of Weld 5 (CG HAZ). The micrograph shows a fine AF with relatively high aspect ratio and bainite. Regions of secondary AF are indicated by an arrow. The weld contained 0.11 mass% Mo and 1.13 mass% Ni. It had a hardness of 269 HV10 and an impact energy of 30 $J_{(5mm)}$.

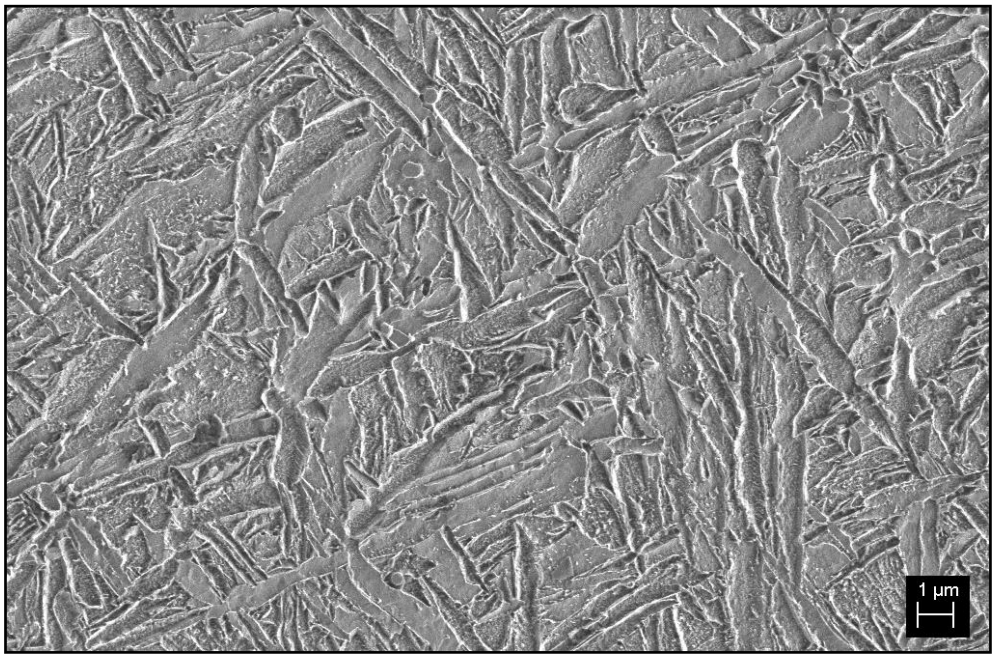

Figure 147: SEM micrograph of Weld 9 GG HAZ. The micrograph shows regions of acicular ferrite with very high aspect ratios and significant amounts of acicular ferrite and secondary AF. The weld contained 0.23 mass% Mo and 2.44 mass% Ni and had an impact energy of 18 $J_{(5mm)}$.

Fractography of Weld 6 (CG) showed that, despite the presence of bainitic AF, the weld fractured largely intergranularly across prior austenite grains, as shown in Figure 148. Fractography of Welds 8 and 9 indicates that the bainitic AF resulted in extensive brittle fracture across AF regions, as shown in Figure 149.

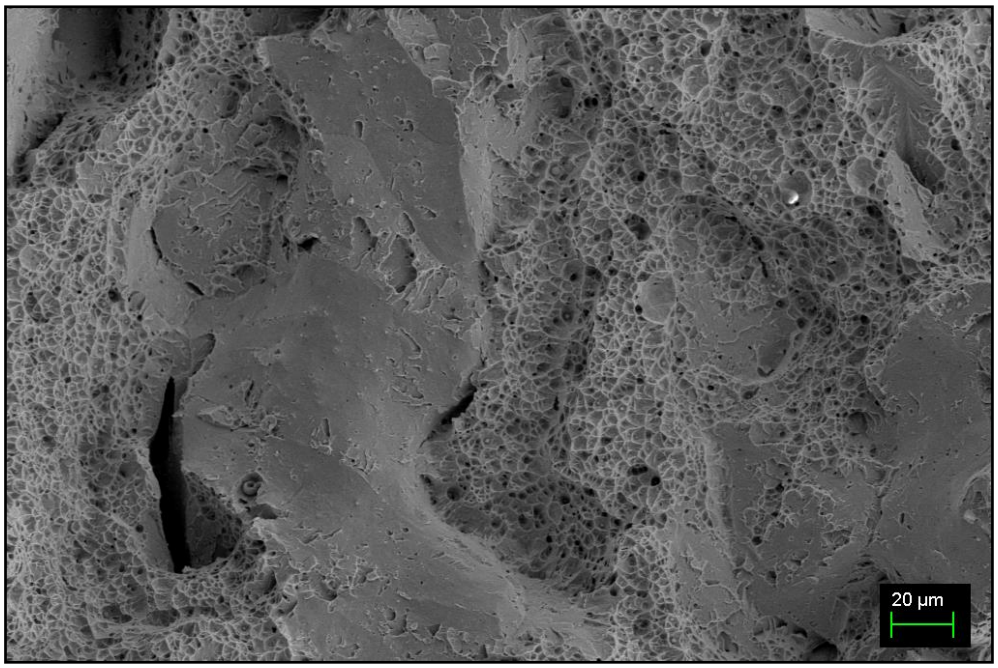

Figure 148: Micrograph of fracture surface of Weld 6 GG HAZ. The micrograph shows evidence of intergranular fracture and grain separation along PAGBs. The weld contained 0.12 mass% Mo and 2.2 mass% Ni and had an impact energy of 29 $J_{(5mm)}$.

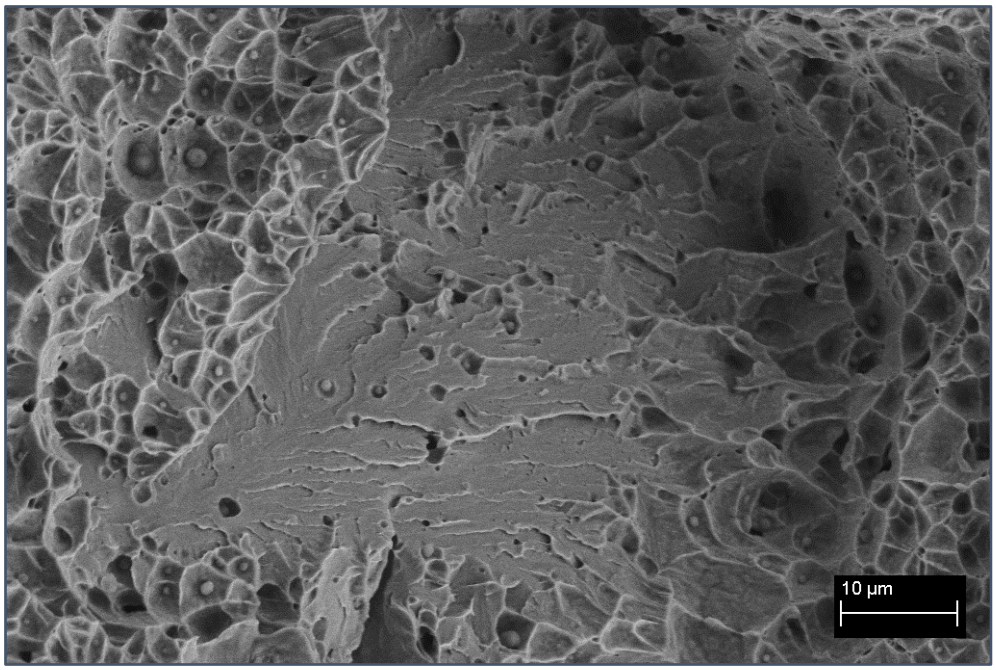

Figure 149: Micrograph of fracture surface of Weld 9 GG HAZ. The micrograph shows a region of brittle fracture along what appears to be an austenite grain boundary. Crack propagation appears to have occurred along similarly orientated slip planes. The weld contained 0.23 mass% Mo and 2.44 mass% Ni and had an impact energy of 18 $J_{(5mm)}$.

4.4.5. Impact energy as a function of hardness and grain size

A Hall–Petch plot of the data is shown in Figure 150. A scatter plot of the relationship between impact energy and hardness is shown in Figure 151. A scatter plot of the correlation between impact energy and grain size is shown in Figure 152. The graph shows a general tendency for impact energy to increase with grain size. The relationship is not very strong. This is the opposite trend to that generally expected.

Figure 150 shows that the Hall–Petch relationship could only partly explain the change in weld metal hardness. This indicates that some of the changes in hardness are likely a result of changes in grain size, but that the influence of grain size is not a dominating effect. Impact energy tended to decrease with an increase in hardness. This is also an expected relationship. However, smaller grain size was associated with a reduction in impact energy. Although the relationship was not strong, this is the opposite relationship to that usually expected. This indicates that the decrease in grain size is associated with a change in microstructure that has a negative influence on impact energy.

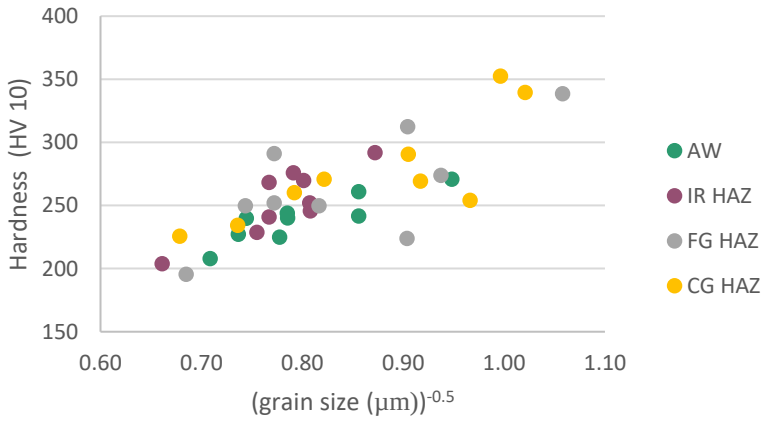

Figure 150: Hall–Petch plot showing a good correlation between an increase in hardness and (grain size)$^{-0.5}$.

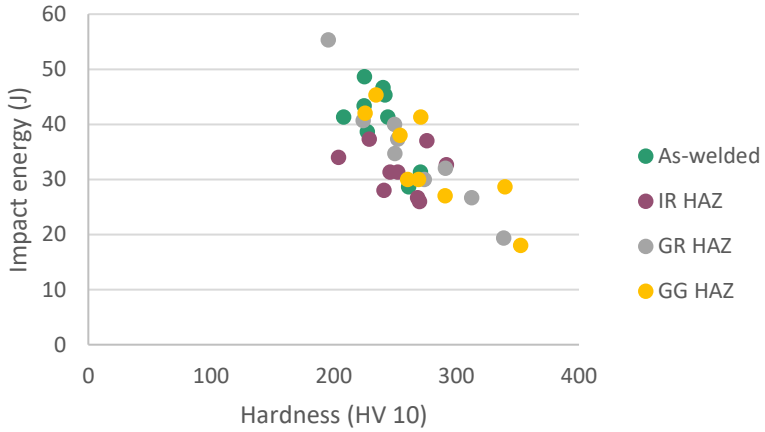

Figure 151: Scatter plot showing relationship between impact energy and hardness for all samples. Different weld region simulations are plotted in different colours. The graph shows a general tendency for impact energy to decrease with an increase in hardness.

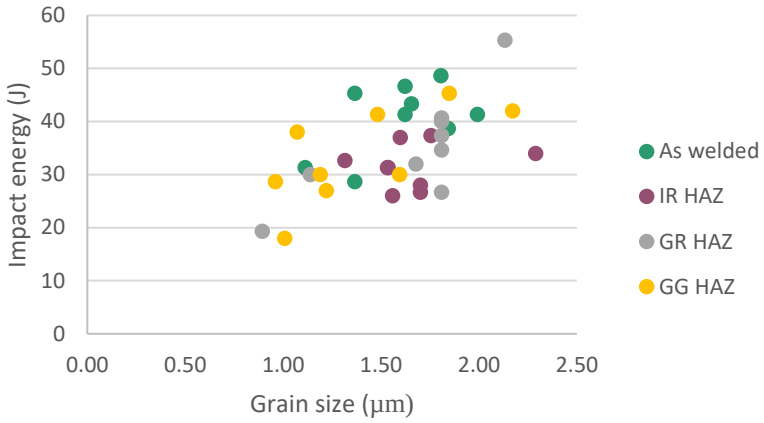

Figure 152: Scatter plot showing relationship between impact energy and grain size for all samples. Different HAZ region simulations are plotted in different colours.

4.4.6. Cooling rate sensitivity

Additional thermal cycling experiments were done to test the influence of cooling time from 800 °C to 500 °C ($\Delta t_{8/5}$) on the microstructure of the thermally cycled weld metal. Gleeble thermal cycling used a $\Delta t_{8/5}$ of 8 s; the calculated $\Delta t_{8/5}$ of the initial weld was 12 s. Additional testing was done on all three thermal cycles of Welds 4–8. Welds 1–3 were omitted because neither the hardness nor impact energy of these welds changed significantly during initial thermal cycling.

Table 47 shows the average hardness (HV10) of samples exposed to the two different thermal cycles. The difference in microstructure between the two samples is noted where applicable. Notable differences in microstructure were noted only in samples that showed significant differences in hardness. A difference of 20 HV10 was considered a significant difference in hardness. Figure 153 compares the microstructure of Weld 5 (FG) at faster and slower cooling rates. Figure 154 compares the microstructure of Weld 7 (FG) at faster and slower cooling rates. The hardness of Welds 5 and 6 (IR) was higher with a lower cooling rate than with a faster one. In the case of Weld 5, this increase in hardness is associated with more extensive IfRs. It is not clear why the hardness of Weld 6 increased with a reduced cooling rate.

Some IfRs contained or showed evidence of a substructure. These substructures were identified by a textured etch effect that could be seen on the IfRs.

Table 47: Difference in hardness between welds exposed to a thermal cycle with a $\Delta t_{(8/5)}$ of 8 s cycled in a Gleeble, and those with a $\Delta t_{(8/5)}$ of 12 s cycled in a dilatometer. The difference in microstructure of samples with a hardness difference exceeding than 20 HV10 is also noted. No other samples showed a difference in microstructure.

Weld		ΔIE ($J_{(5mm)}$)	Hardness (HV10)			
	HAZ region	$\Delta t_{(8/5)}$ = 8 s	$\Delta t_{(8/5)}$ = 8 s	$\Delta t_{(8/5)}$ = 12 s	Change associated with change in $\Delta t_{(8/5)}$	Difference in microstructure
4	As-welded		242 ± 2.8			
	Intercritically reheated	−17	241 ± 2.4	249 ± 3.4	No statistically significant change	No notable difference
	Fine-grained	−8	252 ± 3.1	210 ± 7.3		Larger grains with M/A regions of different appearance
	Coarse-grained	0	234 ± 6.8	238 ±7.1	No statistically significant change	No notable difference
5	As-welded		240 ± 6.4			
	Intercritically reheated	−15	246 ± 8.5	268 ± 9.5	Increase	More extensive M/A structure
	Fine-grained	−7	250 ± 7.3	252 ± 2.3	No statistically significant change	No notable difference
	Coarse-grained	−17	269 ± 7.4	275 ± 3.3	No statistically significant change	No notable difference
6	As-welded		261 ± 3.9			
	Intercritically reheated	8	276 ± 3.6	285 ± 2.6	Increase	No notable difference
	Fine-grained	−2	312 ± 13.2	285 ± 3.4	Decrease	More evidence of grain growth and more extensive M/A regions
	Coarse-grained	0	340 ± 7.7	310 ± 2.1	Decrease	More evidence of grain growth
7	As-welded		225 ± 9.6			
	Intercritically reheated	−22	268 ± 4.7	239 ± 4.8	Decrease	No notable difference
	Fine-grained	−17	291 ± 7.3	250 ± 8.0	Decrease	Lower aspect ratios
	Coarse - rained	−7	271 ± 4.3	257 ± 4.3	Decrease	No notable difference
8	As-welded		244 ± 2.9			
	Intercritically reheated	−9	292 ± 20.8	257 ± 3.4	Decrease	Slightly larger grains
	Fine-grained	−11	274 ± 8.3	264 ± 10.4	No statistically significant change	No notable difference
	Coarse-grained	−14	291 ± 4.7	271 ± 3.5	Decrease	No notable difference

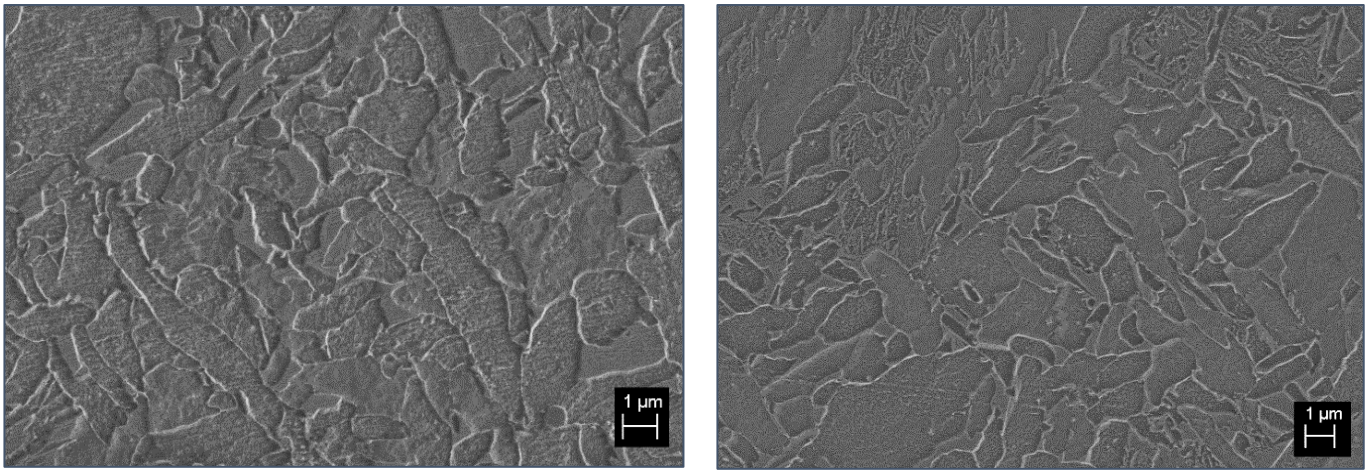

Figure 153: Micrograph of Weld 5 after thermal cycling to a peak temperature in the FG HAZ region and $\Delta t_{(8/5)}$ of (left) 8 s and (right) 12 s. The micrograph from the sample subjected to the slower cooling rate has more extensive IfRs. The M/A regions on the right also show evidence of a substructure that is not apparent in the sample subjected to the faster cooling rate.

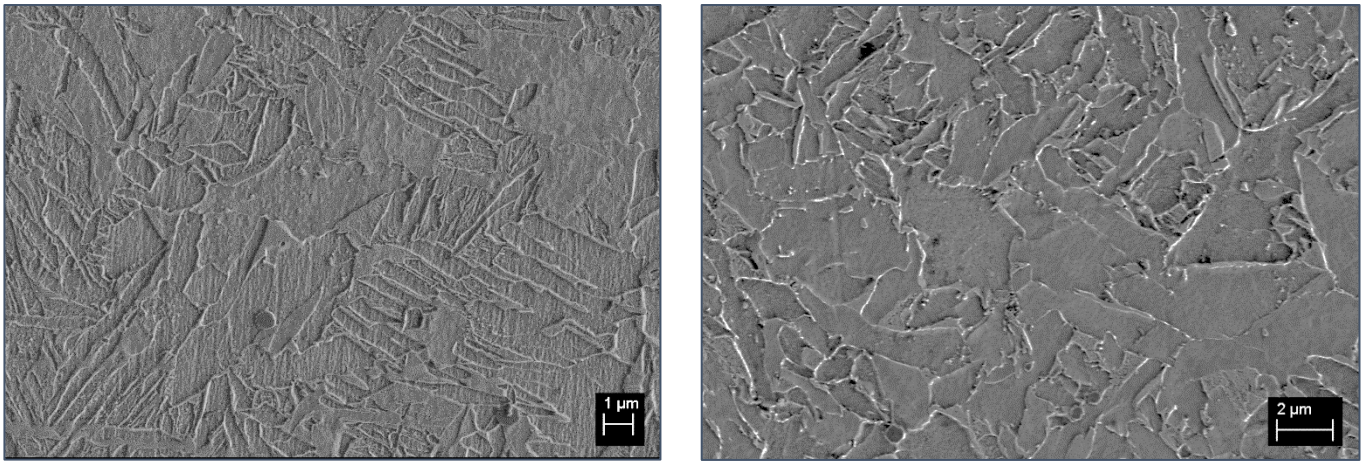

Figure 154: Micrograph of Weld 7 after thermal cycling to a peak temperature in the FG HAZ region and $\Delta t_{(8/5)}$ of (left) 8 s and (right) 12 s. The micrograph from the sample that was subjected to the slower cooling rate shows lower aspect ratios.

5. Discussion

5.1. Chemical composition

5.1.1. Weld metal chemistry

The results reported in Section 4.1 show that the weld alloying method developed for the purposes of this study can produce welds of consistent and reproducible chemical composition. However, the consistency of chemical composition (as quantified using the range in alloy content) deteriorates significantly below an alloy content of 0.1 mass%.

The consistency of chemical composition across the nine welds is reported in Section 0. These results show that the Ni content was very stable (Table 23), but variability of Mo (Table 24, Table 25, and Figure 86) and Ti was notable (Table 26). The consistency of chemical composition across the nine welds is reported in Section 0. The instability in Mo and Ti alloy contents is attributed to a loss in the stability of powder feed rate in g/mm when the rotation rate of the powder feeder was reduced from 0.8 rpm to 0.5 rpm (Table 16).

The chemical composition of individual welds was shown to be consistent across the length and cross-sectional area of that specific weld. However, weld compositions only stabilised 150 mm from the start of the weld. To avoid variation in the chemical composition of samples, all samples were extracted within the chemically stable range of the weld, as shown in Figure 75.

Section 4.1.3 showed that the equations used to predict the chemical composition of a weld were not extremely accurate. This discrepancy was attributed, at least in part, to the fact that the cross-sectional area of the LMD beads was not rectangular. As a consequence, the weld metal chemical composition of welds needs be confirmed via OES or a similar technique if this method of weld metal composition control is to be used in future research. OES verification was used for this study. The difference between the predicted chemical composition and the achieved chemical composition was not large enough to negatively impact the study.

5.2. As-welded weld metal

5.2.1. Microstructure and fracture

With the exceptions of Welds 6 and 9, which are discussed in Section 5.2.6, all welds consisted of varying degrees of GBPs, decorated PAGBs. The remainder of the microstructure consisted of a balance of AF and IfRs. The GBPs consisted almost exclusively of GBF, with the exception of Weld 6, where some bainite was detected.

Fractography of as-welded samples indicated that fracture occurred in a brittle fashion along GBF and in a ductile cup-and-cone manner, where fracture propagated across a region of acicular ferrite (Figure 107 to Figure 109). This was true of all evaluated welds, except for Welds 6 and 9, which fractured intergranularly along PAGBs.

These observations are in line with the literature, where fracture in weld metal initiated at and propagated along GBF is usually brittle (Tweed and Knott, 1987) and fracture initiated at inclusions in the AF region usually has a dimple morphology (Ebden and Weatherly, 1983; Kang et al., 2015). Tweed and Knott (1987) showed that brittle fracture along GBF occurs because strain is transferred along the soft GBF during the initial loading. The hardness of GBF then increases until it is equal to that of the AF, at which point it is very brittle, and tends to fracture by a cleavage mechanism.

Cracks initiated at M/A islands are expected to have the same morphology as cracks initiated at inclusions (Davis and King, 1994). The brittle fracture associated with GBF is a function of the grain size of these structures in relation to the AF.

The fact that fracture along GBPs appears to be primarily brittle in nature explains why the fraction of AF, as it is conventionally measured in the literature, is so often found to be a dominating factor in determining weld metal toughness. All cases reported in the literature where this correlation was found contained less than 80 % AF (Beidokhti et al., 2009b; Lan et al., 2016; Ohkita et al., 1995) However, for the results of the current study, where the AF content of Welds 2–9 were higher than 88 % and Weld 1 was 75 % (Table 31), AF content did not have a statistically significant correlation to the impact energy. This indicates that above some critical level of AF, the AF content of a weld ceases to be a dominant factor in determining weld metal impact energy.

Weld 3 (AW) contained a larger amount of IfRs than other welds. The weld metal contained high concentrations of Ni, which likely lowered the transformation temperature, resultantly suppressing AF growth. This simply means that less austenite would have transformed to ferrite when the temperature became too low for austenite to transform to ferrite via the AF mechanism, at which point the remaining austenite transformed to IfRs. The same increase in IfRs did not occur in Welds 6 and 9. The reason for this appears to be that the formation of coalesced bainite is promoted when high levels of Ni are present along with Mo. The mechanism whereby this occurred is discussed in Section 5.2.6.

5.2.2. Effect of chemical composition on grain boundary product content

The results of this study showed that the GBP content of a specific weld could be predicted with an accuracy of 86 % when Ni content, Mo content, and the product of Ni and Mo contents were used as *x*-variables in an equation produced by a multivariant linear regression analysis. The addition of both Ni and Mo led to a decrease in the fraction of GBPs. There was also an interaction effect between the two variables. These results are supported by the literature, which indicates that increases in both Ni and Mo contents are expected to result in a decrease in the GBP content of a weld (Bhole et al., 2006; Ren et al., 2009; Yang et al., 2015)

The decrease in the fraction of GBPs related to Mo may be the result of a tendency of this element to segregate to PAGBs (Dumoulin et al., 1980; Guillou et al., 1981; Hua et al., 2018). Once present at the grain boundary, Mo has been shown to suppress the $\gamma \rightarrow \alpha$ transformation. The suppression of this transformation at the grain boundaries enables intragranular inclusions to compete as nucleation sites for ferrite (Koseki and Thewlis, 2005). This suppression of the $\gamma \rightarrow \alpha$ transformation was demonstrated by Hua *et al.* (2018) to be the result of suppressed C migration caused by the presence of Mo.

The effect of Ni on the GBP content of welds is attributed to the role that this element plays as an austenite stabiliser, in combination with its tendency to result in segregation of alloying elements to PAGBs. The tendency of Ni to promote segregation was shown in the literature (Kadoi et al., 2020) and in this study (Section 4.3.2). Because Ni acts as an austenite stabiliser, the higher levels of Ni at PAGBs will suppress ferrite formation at these grain boundaries.

5.2.3. Effect of Ni and Mo contents on mechanical properties

Both Ni and Mo were shown in Section 4.3.6 to affect the hardness of the weld metal. It was also shown that there is an interaction effect between these two elements. The effects of Mo and Ni on hardness in samples from this study appear to be comparable to those reported in the literature. The results from this study are compared with results from the literature in Table 48 and Table 49. The

change in hardness for the results from the Evans and Bailey (1997) study were converted using from ASTM E140-12B (2019)e.

An increase in Mo concentration from 0 mass% to 0.25 mass% (in a weld containing no Ni) resulted in similar changes in hardness to those welds deposited and studied by Surian et al. (2005). These welds did not contain Ni. In the presence of Ni, changes in hardness were not comparable to these results, which supports the conclusion made earlier in this section that there are interaction effects between Ni and Mo.

The measured effects of Ni on hardness, for the current study, are comparable with results reported in the literature only when Mo levels are low. This also supports the conclusion drawn earlier in this section that there is an interaction effect between Ni and Mo. Furthermore, the fact that the results from this study are comparable with those in the literature indicates that the presence of Ti, at the levels used in this study, did not impact the effect of Ni or Mo on hardness.

Table 48: Change in hardness with Mo content: comparison between published data and results of the present study.

Source	C (%)	Ti (%)	Mn (%)	Ni (%)	Change in Mo content (%)	Change in hardness
Evans and Bailey (1997)	0.04	0.0	1.4		0.25–0.5	13 HV10*
Surian, De Rissone, and De Vedia (2005)	0.05		1.5		0–0.27	34 HV10
Present study	0.1	0.027 0.019	1.5		0–0.25	32 HV10
	0.1	0.021 0.025	1.5	1	0–0.25	17 HV10
	0.1	0.020 0.030	1.5	2.2	0–0.25	46 HV10

*Converted from ASTM E140-12B (2019)

Table 49: Change in hardness with Ni content: comparison between published data and results of the present study.

Source	Mn (%)	C (%)	Ti (%)		Mo (%)	Change in Ni content	Change in hardness (HV10)*
			No Ni	High Ni			
Evans and Bailey (1997)	1.4	0.04				0.05–2.25	18
Present study	1.5	0.1	0.027	0.031		0–2.17	17
	1.5	0.1	0.022	0.033	0.1	0–2.34	19
	1.5	0.1	0.019	0.030	0.2	0–2.44	31

*Converted from ASTM E140-12B (2019)

The chemical composition, hardness and impact energy values of some welds from the current study are compared with those of comparable welds from the literature in Table 50. Except for Weld 9, all

welds from this study had hardness and impact energy values comparable with welds from the literature that did not contain Ti. This indicates that the presence of Ti, in the levels that were used in this study, does not have a significant influence on the mechanical properties of weld metal when other alloying elements, like Ni and Mo, are present.

The difference between the impact energy of Weld 9 (64 $J_{(5mm)}$) and the welds from the literature with which it is compared in Table 50 (welds from Viano et al. (2000), Surian et al. (2005), and ASTM F9A4-EM2-M2-H8) is attributed to the coalesced bainite that formed in Weld 9. It is likely that the higher C content of Weld 9, in relation to the welds from the literature with which it is compared, contributed to the formation of this phase. The high C content of other welds did not have a similarly deleterious effect because the concentrations of other alloying elements (Mo and Ni) were not high enough to lead to the formation of coalesced bainite.

Table 50: Comparison between hardness values of welds in the current study and those found in literature. Impact energies of welds from the current study were adjusted for sample thickness according to ASTM A370.

Group	Source	C	Mn	Ni	Mo	Ti	Hardness	Impact energy
1	Viano, Ahmed, and Schumann (2000)	0.07	1.60	1.49	0.23	0.00	230 HV5	100 J (−51 °C)
	Current study (Weld 8)	0.1	1.40	1	0.22	0.03	244 HV10	84 J (−40 °C)
2	Viano, Ahmed, and Schumann (2000)	0.06	1.51	1.35	0.16	0.00	210 HV5	100 J (−51 °C)
	Current study (Weld 5)	0.1	1.40	1	0.11	0.03	227 HV10	108 J (−40 °C)
3	Viano, Ahmed, and Schumann (2000)	0.05	1.75	1.67	0.36	0.00	250 HV10	100 J (−51 °C)
	Surian, De Rissone, and De Vedia (2005)	0.05	1.48	1.89	0.27	<0.01	250 HV10	90 J (−40 °C)
	ASTM F9A4-EM2-M2-H8	0.05	1.52	1.76	0.41	<0.03*	230 HV10 **	125 J (−40 °C)
	Current study (Weld 9)	0.10	1.41	2.2	0.23	0.03	271 HV10	63 J (−40 °C)

* Ti+V+Zr

** Converted from Hardness Rockwell B

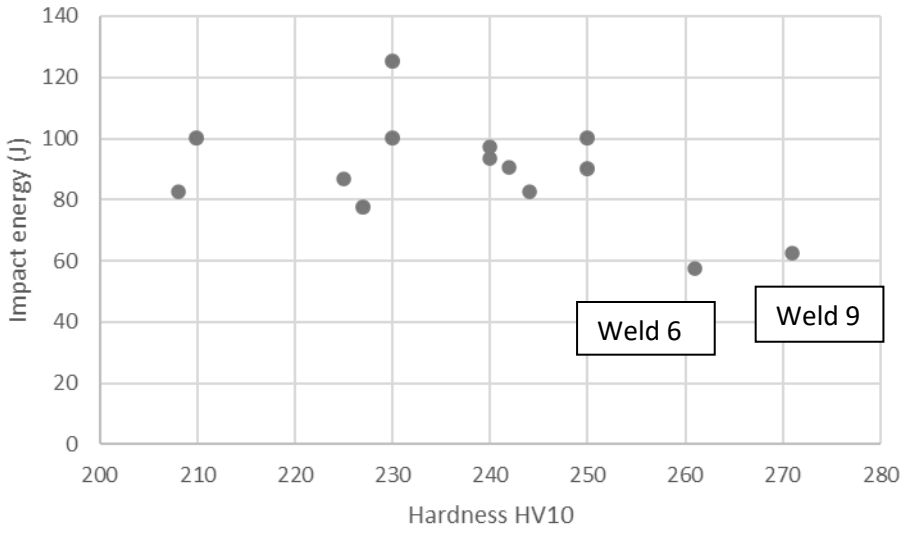

Figure 155: Scatter plot showing correlation between hardness and impact energy.

5.2.4. Influence of microstructure on hardness

Equation 34, the multivariant equation drawn up to predict hardness as a function of (grain size)$^{-0.5}$ and the fraction of GBPs, is 90 % accurate. The hardness of samples was predicted with 77 % accuracy when (grain size)$^{-0.5}$ alone was used as a variable and was only 66 % accurate when the fraction of GBP was used as a variable. This means that the correlation between GBP and hardness was not merely a result of the correlation between GBP content and grain size, but that the fraction of GBPs affected hardness independent of its effect on grain size.

In the current research, GBPs were almost exclusively GBF. GBF is an allotriomorphic ferrite that forms via a reconstructive mechanism at high temperatures. This type of ferrite is expected to be softer than even Widmanstätten-like AF, which grows via a displacive mechanism. This would explain the correlation between hardness and GBP content independent of its effect on grain size.

5.2.5. Influence of Ti

It was noted in Section 5.1 that the variability in Ti was significant. However, statistical analysis showed that this variability did not influence either the microstructure (Table 33) or mechanical properties. Results from the literature support these findings. Work done by (Beidokhti et al., 2009a) showed that, for the Ti ranges applicable to this study, Ti variation was not expected to influence impact energy (Figure 151). Work done by Seo et al. (2019b) also indicates that, for the Ti ranges applicable to this study, Ti variation should not influence $AF_{(Conventional)}$ content (Figure 152). Figure 158 and Figure 159 show that the results of this study confirmed this prediction.

AF content of welds in this study was, on average, much higher than those of Seo, Kim, *et al.* (2019). These higher levels of AF content are attributed to the additions of Ni and Mo, which were not present in the study of Seo, Kim, *et al.* (2019), nor in the outlier in this study (Weld 1), which contained similar levels of AF as reported by these authors.

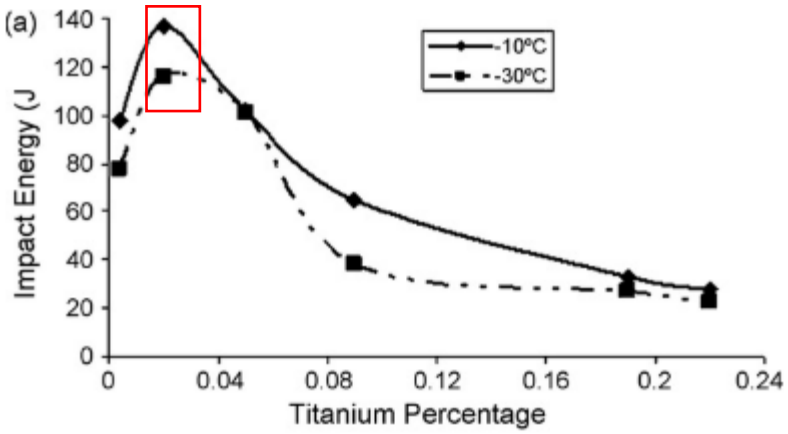

Figure 156: Relationship between Ti content and impact energy (Beidokhti, Koukabi, and Dolati, 2009a). The Ti content applicable to this study is indicated by the red box.

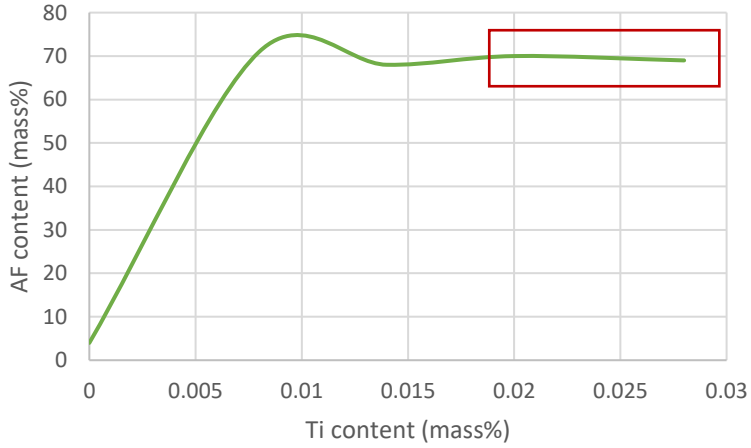

Figure 157: Effect of small changes in Ti content on AF content (Seo et al., 2019b). The Ti content applicable to this study is indicated by the red box.

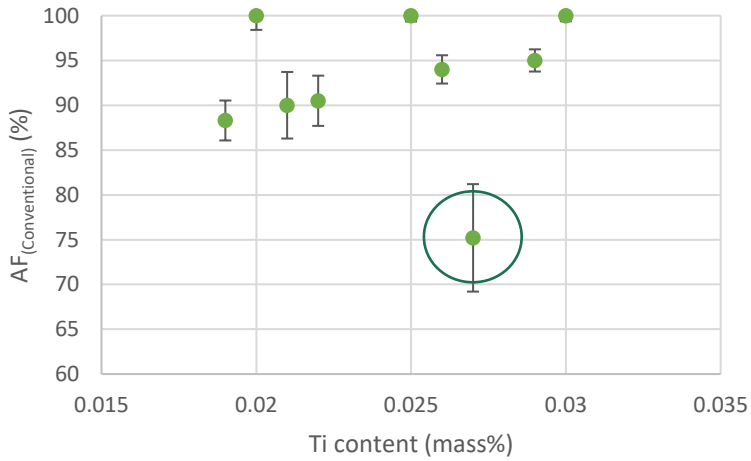

Figure 158: Scatter plot showing the relationship between AF content and Ti content from welds in this study. The circled outlier is Weld 1.

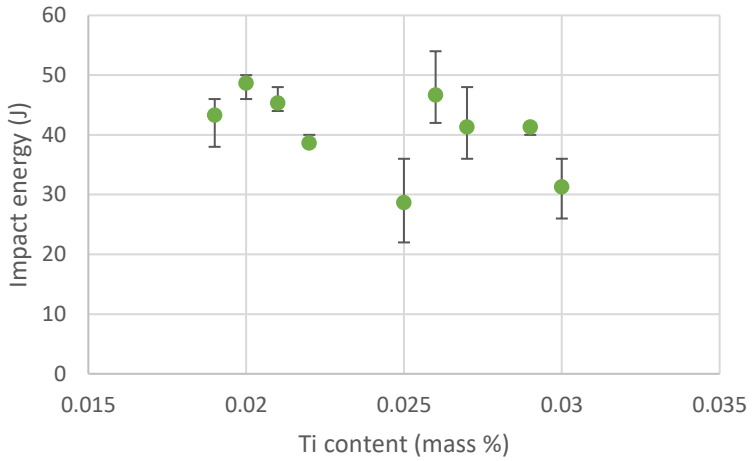

Figure 159: Scatter plot showing the relationship between impact energy and Ti content from welds in this study.

5.2.6. Microstructure and fracture of Welds 6 and 9

The impact energies of Welds 6 and 9 were shown to be significantly lower than those of the other welds in this study (Table 35). The low impact energies of these welds is attributed to regions of coalesced bainite that had formed on and near the PAGBs of these welds. This coalesced bainite appears to have resulted in the intergranular fracture along the PAGBs (Figure 110 and Figure 112). Coalesced bainite is believed to have formed as a result of Mn and Ni segregation to PAGBs. Ni segregation is believed to be a result of the high Ni content of these welds. A schematic representation of these arguments is shown in Figure 160.

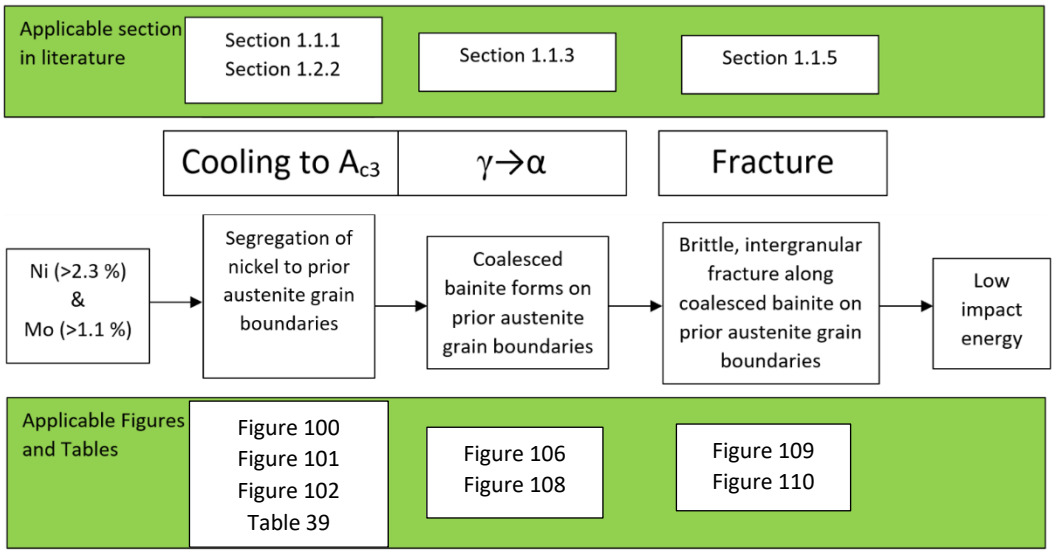

Figure 160: Schematic representation of the explanation for the low impact energies of Welds 6 and 9. The flow chart shows that segregation of Ni and Mn to PAGBs occurred whilst the weld metal was cooling and that this segregation led to the formation of coalesced bainite at these PAGBs. The coalesced bainite resulted in the brittle, intergranular fracture that occurred during impact testing and resulted in the low impact energy of the weld.

Segregation

Optical microscopy showed an etch effect on Welds 6 and 9 (AW), which appear to indicate that alloying elements had segregated to grain boundaries. The etch effect was that of a lighter etch on what appeared to be prior austenite grains. This indicated a higher concentration of alloying elements at the location where the etch effect was observed. Similar etch effects were not seen in other weld metals. SEM and EDS were used to confirm that the etch effect was the result of segregation of Mn and Ni to PAGBs. In Weld 6, the Ni concentration varied from 2.07 mass% to 2.24 mass% between grain centres and grain boundaries. In the same weld, the Mn content decreased from 1.70 mass% to 1.47 mass% from the centre of the grain to the grain boundary. For Weld 9, the Ni concentration increased from 1.84 mass% to 2.15 mass%. For the same weld, the Mn concentration increased from 1.41 mass% to 1.61 mass%. The average Mo content was below the detection limit of the SEM-EDS equipment.

The limitations of EDS analysis are discussed in Section 3.4.2. It is noted in this section that, due to the depth of penetration of an EDS analysis, the readings are not necessarily a representation of the point analysed, but of an average area below the surface of the sample. This means that when EDS fails to confirm segregation, for example, segregation can not necessarily be ruled out. However, in cases where segregation is confirmed, as is the case in this study, the inherent limitation of EDS does not limit the validity of the results.

The segregation of Ni to PAGBs is attributed to the extent to which the weld metal solidifies as γ (Figure 90). Kadoi *et al.* (2020) showed that the degree of Ni segregation in a weld metal is related to the degree to which a weld solidifies as γ. Other authors have also reported Ni segregation to PAGBs to be associated with increased Ni content (Yang et al., 2015).

The Ni segregation is therefore likely a result of a shift in solidification mode, in turn resulting from the high Ni content of welds The etch effect seen in Weld 6 and 9 appears to have resulted from the presence of coalesced bainite (discussed below) and was not believed to be a direct result of Ni segregation. This would explain why no such etch effect was detected on Weld 3.

Formation of coalesced bainite

Regions of coalesced bainite were detected on or near the PAGBs of Welds 6 and 9. Similar regions of coalesced bainite are reported in the literature and are often associated with increased Ni content in weld metal and, in some cases, with Mo (Bhadeshia *et al.*, 2006; Pak *et al.*, 2008). The coalesced bainite is believed to have formed because of the higher Ni levels.

The formation of coalesced bainite is described in Section 1.1.3. Bainite laths coalesce during growth. This coalescence can occur only if diffusion rates of C prevent its precipitation between adjacent laths. Such precipitation would prevent coalescence. Therefore, low C mobility increases the likelihood of bainite coalescence because it prevents the diffusion required for C to be precipitated between laths (Bhadeshia *et al.*, 2006). Mo has been shown to limit C mobility (Hua et al., 2018), and is likely why coalesced bainite formed only in welds that contained Mo (such as Weld 6 and Weld 9).

Fracture along prior austenite grain boundaries

The intergranular fracture of Welds 6 and 9 (AW) was shown to propagate along regions of coalesced bainite (Figure 110 and Figure 112). The shift in fracture mechanism of Welds 6 and 9 is attributed to the formation of coalesced bainite at and near PAGBs. The appearance of this apparently brittle type of AF near PAGBs appears to be the result of segregation of Ni to these grain boundaries. The segregation of these elements was, in turn, attributed to the high Ni content of the welds. The

literature also indicates that high Ni content may be associated with both increased segregation (Yang *et al.*, 2015) and intergranular fracture along PAGBs (Zhang and Farrar, 1997).

5.3. Thermal cycling

5.3.1. Change in hardness of welds

Thermal cycling resulted in significant changes in the hardness of Welds 6, 7, 8, and 9 only. Significant changes in hardness were considered to be those exceeding 40 HV10. The largest change in hardness of Weld 6 was after exposure to the GG HAZ and was 79 HV10. The largest change in hardness of Weld 7 occurred after reheating to the GG HAZ region and was 79 HV10. The largest changes in the hardness of Welds 6 and 9 occurred after exposure to the FG HAZ and were 51 HV10 and 68 HV10, respectively. The susceptibility of Welds 7, 8, and 9 to increased hardness resulting from thermal cycling is attributed to the high Mo levels of these welds. The susceptibility of Weld 6 to increased hardness is attributed to the high levels of Ni. High levels of Ni would also have contributed to the susceptibility of Weld 9 to increased hardness resulting from thermal cycling.

It was noted in Section 3.5.3 that the cooling rate of dilatometry experiments was slightly higher ($\Delta t_{(8/5)}$ = 8 s) than the cooling rate that the actual weld metal was likely to have experienced ($\Delta t_{(8/5)}$ = 10 s). Some of the welds were therefore exposed to thermal cycling in a dilatometer to evaluate how the microstructure would respond to lower cooling rates. The cooling rate used for these experiments was $\Delta t_{(8/5)}$ = 12 s. Results in Section 4.4.6 showed that the cooling rate did affect the hardness of thermally cycled welds. These results indicate that the higher hardness of thermally cycled samples taken from Weld 8, when compared with the weld in the as-welded condition, may have been a result of the higher cooling rate used during Gleeble thermal cycling.

When the change in hardness is evaluated according to results shown in Section 4.4.6, only Weld 6 showed a significant increase in hardness (49 HV10 for Weld 6 (GG)) due to thermal cycling. Owing to insufficient material, Weld 9 could not be evaluated, but, given its high alloy content, it seems reasonable to assume that it would also have experienced an increase in hardness equal to or greater than that of Weld 6.

Gubeljak (2003) showed that significant differences in hardness could cause local brittle zones to form in weld metal by transferring strain to the softer microstructure – where cracks then propagated. The values cited in their work were in a lower hardness region of 240–270 $HV_{0.1}$ and higher hardness region of 320–350 $HV_{0.1}$. It is therefore expected that multi-pass welds of chemical composition similar to Welds 6 and 9 would experience unstable crack growth due to the difference in hardness between different HAZ regions.

5.3.2. Change in impact energy of welds

Reheating led to a significant decrease in the impact energies of Welds 4 and 5 as well as Welds 7, 8, and 9. For Welds 4, 5, and 7, the largest decrease in impact energy was associated with the IR HAZ region and for Welds 8 and 9, the largest decrease was associated with the CG HAZ. There was no identifiable correlation between the impact energy of welds in the as-welded condition and the impact energy of welds following reheating to any of the HAZ regions.

The increase in the hardness of many welds appears to have been a result of the higher cooling rates used for thermal cycling in comparison with the estimated cooling rates of the original welds. This does not appear to be the case for impact energy. This is supported by the fact that changes in impact energy were not related to changes in hardness, but rather to microstructure.

The microstructure of welds that had significantly lowered impact energy values following a specific thermal cycle were unaffected by cooling rate (Table 47). This indicates that the changes in impact energy were likely not to have been a result only of the difference in cooling rate between the as-welded samples and the thermally cycled samples.

Changes in impact energy detected during this study were likely a function of peak temperature and not merely cooling rate, and because these changes in impact energy can be significant, it must be concluded that the results of mechanical testing and microstructure of as-welded weld metal cannot be used to estimate the impact properties of multi-pass welds.

The mechanical properties of Weld 3 (AW), for example, were not particularly noteworthy with respect to the other as-welded samples in the study. The average hardness of Weld 3 (AW) (225 HV10) was lower than those of Welds 4 and 5 (AW) (240 HV10 and 242 HV10, respectively). The impact energy of Weld 3 (AW) (43 J) was also lower than those of Welds 4 and 5 (AW) (45 J and 47 J, respectively). Evaluation of weld metal based purely on the as-welded properties would resultantly indicate that the composition of Weld 3 results in less-favourable mechanical properties than those of Welds 4 and 5. However, the IE_{min} (37 J) of the weld is higher than that of either Weld 4 or 5 (28 J and 30 J, respectively). $IE_{(min)}$ refers to the lowest impact energy across all heat-treatment conditions. The reader is reminded that the impact tests were performed on half size (5 mm x 10 mm x 55 mm) samples.

Two more examples that illustrate this point are Welds 6 and 7. The impact energy of 7 (AW) was 49 J. This was the second-highest impact energy measured. However, the IE_{min} of Weld 7 was 27 J, which is close to the lowest end of all measured impact energy values. Weld 6 had the lowest impact energy of all welds in the as-welded condition (29 J), but the IE_{min} of the welds was also 27 J. Whilst this was still low, it was comparable with the IE_{min} of most other welds and, in combination with the high hardness value, may provide a favourable strength/impact toughness balance.

It is also noted that no trends could be detected with regard to correlation between chemical composition, microstructure, and mechanical properties. There was a general tendency for hardness to increase with a decrease in grain size and for impact energy to decrease when hardness increased.

5.3.3. Effect of reheating to the intercritically reheated heat-affected zone on impact energy

Exposure to a thermal cycle with a peak temperature in the IR HAZ led to significant decrease in the impact energies of Welds 4, 5, and 7. Decreased impact energy was not associated with an increase in hardness. Microscopy showed that the morphology of the IfRs of Samples 4, 5, and 7 differed significantly from that of their as-welded counterparts. The IfRs of these samples did not respond to etching and showed no evidence of the substructures that were seen in the welds in the as-welded condition.

The shift in IfR morphology was likely a result of a $\alpha \rightarrow \gamma$ transformation that occurred in these regions when they were heated to the IR HAZ. Owing to the high C content of the IfRs, they are most likely to transform to austenite upon heating (Davis and King, 1994). C homogenisation and further C enrichment of the newly formed γ from the surrounding α is likely to occur following the initial transformation. Grain growth of the γ grains may also occur. The extent of all these transformations is a function of time spent at elevated temperatures. C diffusion is driven by the high temperatures and increased mobility of C in γ, whilst C enrichment of γ by surrounding α results from the comparatively carbon-saturated state of this α (Davis and King, 1994).

With the exception of Weld 8 (IR), the IfRs of all welds that were exposed to an IR HAZ thermal cycle showed a similar change in morphology. This indicates that the mechanism responsible for the shift in IfR morphology is relatively consistent across all welds. The fact that not all welds that underwent a change in IfR morphology experienced a decrease in impact energy indicates that this shift in morphology is not always detrimental to impact energy.

The fracture surfaces of welds that were adversely affected by the new IfR morphology (Welds 4, 5, and 7 (IR)) all showed evidence of extensive brittle fracture. The regions where brittle fracture occurred were decorated with small protrusions that appeared to be small M/A islands. The particles were identified as M/A islands because they are similar in appearance to those shown in literature and because their presence in consistent with IfR morphology. It would have been beneficial to confirm the nature of these particles via a method such as electron backscatter diffraction (EBS-D). These M/A islands are usually associated with brittle fracture (Kim et al., 1991; Lambert-Perlade et al., 2004a; Mohseni et al., 2012) and are believed to result in a decrease in the principal stress required for fracture (Davis and King, 1996). Networks of IfRs containing M/A islands have been shown to reduce the impact energy of the PM of HSLA-steel welds, but have not been identified in the heat-affected weld metal sections of multi-pass welds (Mohseni et al., 2012). The associated PM contained 0.06 mass% C, which is lower than the 0.1 mass% C used in this study.

5.3.4. Effect of reheating to the fine-grained heat-affected zone on impact energy

Exposure to FG HAZ thermal cycles resulted in a decrease in the impact energy of Welds 7, 8, and 9. The low impact energies of these welds are attributed to regions of long, thin AF needles interspersed with secondary AF (Figure 139, Figure 140, and Figure 141). These regions of AF were classified as bainitic AF. The fracture surfaces of these welds consisted of extensive regions of brittle fracture, interspersed with ductile cup-cone fractures (Figure 142 and Figure 143). The regions of brittle fracture are believed to be associated with the regions of bainitic AF and to have resulted in the low impact energy of these three welds.

The appearance of bainitic AF is believed to be associated with suppressed AF transformation temperature during the cooling stage of thermal cycling. This suppression, in turn, is believed to result from a reduction in the nucleation potential of inclusions during thermal cycling.

One of the mechanisms by which inclusions act as nucleation sites for AF is by the formation of local regions of elastic strain that form around the inclusions due to the difference in thermal expansion coefficients between the inclusion and the surrounding matrix during cooling (Kang et al., 2016). This was discussed in detail in Section 1.1.4.

When the weld metal cools from the liquid phase, as in the as-welded samples, the elastic strain surrounding the inclusions can become quite large. However, the peak temperature reached by samples is much lower during the FG HAZ thermal cycle and the elastic strain surrounding inclusions at a given temperature during cooling is likely to be much smaller than during welding. Elastic strain surrounding an inclusion is expected to be directly correlated to the nucleation potential of that inclusion. Therefore, a decrease in elastic strain surrounding an inclusion is expected to result in a reduction in the nucleation potential of that inclusion. The lower peak temperature associated with the FG HAZ thermal cycle, in relation to the as-welded weld metal, which cooled from the liquid phase, is likely to be associated with a decrease in the nucleation potential of any given inclusion. The degree to which nucleation potential is suppressed will be a result of the degree to which the nucleation potential of a certain inclusion was initially influenced by the surrounding elastic strain. The decrease in nucleation potential of inclusions at any given temperature will then suppress the temperature at which inclusions become active nucleation sites and decrease the AF nucleation temperature and the

number of active nucleation sites. It is believed that a decrease in the nucleation temperature of inclusions resulted in the bainitic AF sheaths observed in Welds 7, 8, and 9. Lower nucleation temperatures likely resulted in longer, thinner AF sheathes (Farrar and Zhang, 1995), whilst the reduction in active nucleation sites, and therefore a number of primary AF laths, reduced grain impingement. Long thin sheathes also provide the large surface areas required for the extensive nucleation of secondary AF that was observed.

Furthermore, the decrease in the number of active nucleation sites prevents AF grains from impinging one another's growth and further contributes to the large aspect ratio of the needles. The large aspect ratios of AF result in significant surface area, allowing for the nucleation of secondary AF. The extensive secondary AF may be a significant contributor to the decrease in impact energy because the parallel growth of the sheaths likely results in an increase in the effective grain size of the metal.

It was noted in Section 4.1.4 that S containing inclusions were detected in Weld 4 and Weld 8. It was noted in Section 1.1.4 that MnS has a larger thermal contraction coefficient than than steel whilst the thermal contraction coefficient of Mn-oxides, Ti-oxides and silicates is lower than that of steel (Torkamani et al., 2017). This means that the strain that develops around a MnS inclusion will be tensile whilst the strain that develops around an oxide inclusion will be compressive. The amount of S measured in at least two of these inclusions (28 mass% for Weld 4 and 50 mass% for Weld 8) indicates that they consisted predominantly of MnS.

Elastic strain surrounding an inclusion is understood to assist nucleation of bainitic-type ferrite (such as AF) by shifting the Fe atoms in the γ to a position that is more thermodynamically favourable for the displacive transformation to take place. It is therefore not clear whether the nature of the strain (that is to say whether it is tensile or compressive) will affect this mechanism.

However, it has been noted by Kang et al.(2016) that the size range at which an inclusion is an effective AF nucleation site is limited by the effect that inclusion size has an effect on the strain field surrounding it. As an inclusion becomes larger the strain surrounding it also increases. At some point this strain becomes so large that plastic strain occurs. Some literature indicates that plastic strain inhibits bainite nucleation. It is believed that plastic strain in γ surrounding a larger inclusion is the reason why nucleation potential of inclusions decreases with size after some critical point (Figure 13). The nature of an inclusion (that is to say its mineral composition) is therefore likely to have an effect on the size range at which it can act as a nucleation site. Given that the elastic strain surrounding an inclusion is then also a function of the temperature differential (i.e. peak temperature in the case of weld metal exposed to thermal cycling during multi-pass welding) this size range will then also be a function of peak temperature.

5.3.5. Effect of reheating to the coarse-grained heat-affected zone

The impact energies of Welds 5, 8, and 9 had lower values following exposure to the CG HAZ thermal cycles than in the as-welded condition. Bainitic AF was detected in these welds (Figure 146 and Figure 147) and the fracture surfaces of the samples contained extensive regions of brittle fracture (Figure 149). In some areas, the regions of brittle fracture showed that fracture had occurred across what appeared to be secondary AF (Figure 148 and Figure 149). A decrease in impact energy of these samples is therefore attributed to the brittle fracture along regions of bainitic AF.

Bainitic AF was also observed in Weld 6 (CG HAZ) but did not result in a change in the impact energy of this sample. Fractography of Weld 6 (CG HAZ) showed that the sample had fractured intergranularly along the PAGBs of these samples. Bainitic AF, therefore, did not result in a decrease in the impact energy of Weld 6 because it did not change the fracture mechanism. This indicates that the bainitic AF

that formed in Weld 6 was not as brittle as the coalesced bainite, and further indicates that brittle fracture across bainitic AF resulted in lower impact energy values than intergranular fracture along coalesced bainite on PAGBs. Bainitic AF therefore appears to be more brittle than the coalesced bainite that formed in Welds 6 and 9 (AW).

As was the case for the appearance of bainitic AF in the CG HAZ, the change in AF morphology is attributed to a decrease in the nucleation potential of an inclusion at a specific temperature. However, in the case of samples that were cycled to the CG HAZ region, this reduction in nucleation potential is not attributed to a reduction in strain energy surrounding inclusions.

The decrease in nucleation potential of inclusions in samples exposed to the CG HAZ thermal cycles that results from a decrease in the elastic strain energy surrounding inclusions, when compared with the same inclusions in the as-welded condition, would not have been as severe as for samples exposed to the FG HAZ. Therefore, a decrease in elastic strain energy surrounding inclusions is not considered the reason for the decrease in nucleation potential of inclusions; instead, MDZ homogenization is thought to have caused this apparent decrease in the nucleation potential of inclusions.

In research by Kang *et al.* (2015), the authors showed that the nucleation potential of some welds exposed to thermal cycles with a peak temperature of 1350 °C decreased as a result of this thermal cycling. The authors concluded that the reason for this decrease was the homogenization of MDZs that occurred during thermal cycling. The decrease in nucleation potential of inclusions was also associated with a decrease in the impact energy of a specific weld. This research is discussed in more detail in Section 1.1.4. The same mechanism is not believed to have been active in welds exposed to the FG HAZ microstructure because Mn diffusion only becomes active at about 1300 °C (Song et al., 2019).It is noted that the EDS of inclusions showed that all tested inclusions, from all tested welds, contained Ti. Since Ti-containing inclusions are those inclusions most commonly associated with MDZ-related AF nucleation it is reasonable to assume that this nucleation mechanism was active in the initial as-welded microstructure.

5.4. Reporting of interferritic region

It was noted in Section 3.7 that the fraction of IfRs in a microstructure is not usually measured or reported in the literature. The results of this study found that, with the exception of Weld 3 (AW), this component did not vary significantly between welds in the as-welded condition; however, thermal cycling did appear to result in non-negligeable variation in the fraction of this microstructural phase.

An increase in the amount of IfRs appears to have resulted in brittle fracture of some welds exposed to IR HAZ thermal cycles, although no direct correlation could be found between the percentage of IfRs and either impact energy or hardness. This is likely because the morphology of the IfRs is as large a determinant in the influence that their content will have as the IfRs content itself. Another reason for the lack of correlation may be the inaccuracy in determining the amount of IfRs, given the subjective nature of the techniques used to determine their volume fraction. Further study into the influence of these regions on impact energy of welds that contain high levels of $AF_{(Conventional)}$ would be beneficial.

6. Conclusions

6.1. Alloying technique

The weld alloying technique developed for the purposes of this research shows significant promise as an alloying method to be used in future research. It was shown to have the capability to produce welds of stable, reproducible chemical composition in a low-cost and effective manner that would, in turn, allow for the evaluation of complex experimental matrixes that the current techniques do not allow. This may allow for a more nuanced understanding of the influence of chemical composition on the mechanical properties of welds.

6.1.1. Predictability of chemical composition

The study showed that the iterative approach used to establish LMD welding parameters for the purposes of alloying the SAW metal was relatively reliable, with a maximum deviation from the expected chemical composition of 20 %. This value could likely be reduced by increasing the amount of iterations used to determine welding parameters.

6.1.2. Stability of chemical composition throughout a single weld

The chemical composition of a single weld was relatively stable throughout the length of the weld.

6.1.3. Stability of chemical composition across different welds

The chemical composition across different welds was acceptably stable when the expected alloying content was ≥ 1 mass %. When the alloying content was ≤ 0.2 mass % the stability of the chemical compositions decreased significantly. There is thus a lower limit, with regards to intended alloying content, below which this alloying technique is not feasible. The lower limit can likely be improved by using a larger SAW wire or by using an Fe-alloy powder for the LMD instead of a pure alloying element powder.

6.2. Effect of chemical composition

6.2.1. Effect of Ni and Mo on microstructure

The most notable effect of chemical composition on microstructure was the appearance of coalesced bainite on and adjacent to prior austenite grain boundaries when Ni levels exceeded 2 mass % and Mo was present. Chemical composition of welds also had a predictable correlation to GBP content. There was no correlation between chemical composition and any other microstructural changes. However, microstructural changes were mostly limited to changes in GBPs and the appearance of coalesced bainite.

6.2.2. Effect of Ni and Mo on mechanical properties

Hardness of weld metal in the as-welded condition could be predicted reasonably well as a function of the chemical composition of the weld (R^2 = 8.3 from Figure 116). With the exception of Weld 6 and 9, the chemical composition of the welds did not change the impact energy to any statistically significant degree.

The influences of Mo and Ni in the current study appear to be comparable to changes reported in the literature where Ti was not present in weld metal. This indicates that the presence of small amounts of Ti does not influence the behaviour of Ni and Mo in as-welded weld metal.

6.2.3. Correlation between microstructure and mechanical properties

Hardness could be predicted as a function of the grain size and fraction of GBPs.

The low impact energy values of Weld 6 and 9 were attributed to intergranular fracture along the PAGBs observed on the fracture surfaces of both these welds. This intergranular fracture, in turn, is attributed to the presence of coalesced bainite that was observed at these PAGBs. These structures were not observed in any other welds. EDS confirmed that Ni and Mn had segregated to PAGBs and the proportionally higher concentration of these alloying elements is believed to have resulted in the formation of embrittling coalesced bainite structures.

6.3. Thermally cycled weld metal

6.3.1. Use of a single pass weld to predict the mechanical properties of a multi-pass weld.

The results of this study clearly show that the mechanical properties of a single pass weld cannot be used to predict the mechanical properties of a multi-pass weld of the same chemical composition and deposited with the same welding parameters.

6.3.2. The effect of thermal cycling related to different HAZ regions (i.e. IR HAZ, GR HAZ, and CG HAZ) on the microstructure and mechanical properties of as-welded weld metal.

Thermal cycling did not have a strong effect on the hardness of welds but did lower the impact energy of some welds to a non-negligible degree. No definitive trend could be identified with regard to the effect of weld metal on the impact energy of welds, but there appear to be some consistent mechanisms involved that affect the change in the microstructure of the welds.

7. Follow-up work

7.1. Alloying method

The alloying method shows clear promise as a research and development tool, but does require refinement. The procedure is currently limited in two main areas. The first is that it cannot reliably produce welds of identical chemical composition when the welds are not produced during the same weld session. This problem should be relatively easy to solve and it is recommended that a more reliable means of controlling powder feed rate be developed. It is also highly likely that the use of multiple, smaller LWD beads would produce more stable welds. Whether this is true, and the extent to which it is true, should be tested. This can be done by producing welds with the same intended alloying composition and varying the number/size of weld beads used to produce a certain weld chemical composition.

The second area of limitation with regards to the alloying method is that the current procedure allows for the production of single-pass welds only. This work successfully showed that the mechanical properties of single-pass welds are not necessarily representative of multi-pass welds and that a study evaluating the effects of weld metal chemical composition cannot be considered comprehensive unless multi-pass welds are evaluated. It would be very easy to expand the procedure that is captured in this document to one that can be used to produce multi-pass welds for the purposes for research. In short, LWD beads would need to be deposited prior to every subsequent SAW run and dilution effects would need to be considered.

7.2. Coalesced bainite

The results of this study indicate that coalesced bainite formation may be promoted by the segregation of alloying elements. It is recommended that this hypothesis be studied by first confirming that the observed structure is, in fact, coalesced bainite. Thereafter the local chemical composition of welds in this study at regions where coalesced bainite formed should be evaluated in relation to regions where it did not form.

Mo also appears to have contributed to the formation of coalesced bainite, possibly as a result of the suppression of C diffusion at PAGBs. A study evaluating the local chemical composition at locations where coalesced bainite did and did not occur would be valuable as a starting point to such a study. However, information on the C distribution in relation to Mo content would be required to evaluate this hypothesis in a meaningful way. An atomic-dispersion spectroscopy study would be required for such work.

8. References

Andersson, J.O., Helander, T., Höglund, L., Shi, P., Sundman, B., 2002. Thermo-Calc & DICTRA, computational tools for materials science. Calphad 26, 273–312. https://doi.org/https://doi.org/10.1016/S0364-5916(02)00037-8

Andrew, K.W., 1965. Empirical formulae for the calculations of some transformation temperatures. J. Iron Steel Inst. 203, 721–727.

ASTM Standard A1033 - 18, 2018. Standard Practice for Quantitative Measurement and Reporting of Hypoeutectoid Carbon and Low-Alloy Steel Phase Transformations. https://doi.org/10.1520/A1033-18.3.1.4

ASTM Standard E 562, 2011. Standard test method for determining volume fraction by systematic manual point count. https://doi.org/10.1520/E0562-11.2

ASTM Standard E1382-97, 2010. Standard test methods for determining average grains size using semiautomatic and automatic image analysis.

Babu, S.S., 2004. The mechanism of acicular ferrite in weld deposits. Curr. Opin. Solid State Mater. Sci. 8, 267–278. https://doi.org/10.1016/j.cossms.2004.10.001

Babu, S.S., Bhadeshia, H., 1992. Stress and the acicular ferrite transformation. Mater. Sci. Eng. A 156, 1–9.

Babu, S.S., Bhadeshia, H., 1990. Transition from bainite to acicular ferrite in reheated Fe–Cr–C weld deposits. Mater. Sci. Technol. 6, 1005–1020. https://doi.org/10.1179/026708390790189605

Babu, S.S., David, S.A., Vitek, J.M., Mundra, K., DebRoy, T., 1999. Model for inclusion formation in low alloy steel welds. Sci. Technol. Weld. Join. 4, 276–284. https://doi.org/10.1179/136217199101537879

Bai, Q., Ma, Y., Xing, X., Chen, Z., Kang, S., 2017. Prediction of the temperature distribution and microstructure in the HAZ of SA508Gr4 reactor pressure vessel steel. ISIJ Int. 57.

Beidokhti, B., Kokabi, A.H., Dolati, A., 2014. A comprehensive study on the microstructure of high strength low alloy pipeline welds. J. Alloys Compd. 597, 142–147. https://doi.org/10.1016/j.jallcom.2014.01.212

Beidokhti, B., Kokabi, A.H., Dolati, A., 2009a. Effect of titanium addition on the microstructure and inclusion formation in submerged arc welded HSLA pipeline steel. J. Mater. Process. Technol. 209, 4027–4035. https://doi.org/10.1016/j.jmatprotec.2008.09.021

Beidokhti, B., Kokabi, A.H., Dolati, A., 2009b. Influences of titanium and manganese on high strength low alloy SAW weld metal properties. Mater. Charact. 60, 225–233. https://doi.org/10.1016/j.matchar.2008.09.005

Bhadeshia, H., 2001. Bainite in steels, 2nd ed. IOM Communications Ltd, London. https://doi.org/10.1201/9781315096674-4

Bhadeshia, H., 1981. A rationalisation of shear transformations in steels. Acta Metall. 29, 1117–1130. https://doi.org/10.1016/0001-6160(81)90063-8

Bhadeshia, H., Keehan, E., Karlsson, L., Andrén, H.O., 2006. Coalesced bainite. Trans. Indian Inst. Met. 59, 689–694.

Bhatti, A.R., Saggese, M.E., Hawkins, D.N., Whiteman, J.A., Golding, M.S., 1984. Analysis of inclusions in submerged arc welds in microalloyed Steels. Weld. J. 63, 224–230.

Bhole, S.D., Nemade, J.B., Collins, L., Liu, c., 2006. Effect of nickel and molybdenum additions on weld metal toughness in a submerged arc welded HSLA line-pipe steel. J. Mater. Process. Technol. 173, 92–100. https://doi.org/10.1016/j.jmatprotec.2005.10.028

Bott, I.S., Rios, P.R., 1998. On the effectiveness of inclusions as nucleation sites in weld deposits. Scr. Mater. 38, 1269–1274. https://doi.org/10.1016/S1359-6462(98)00033-5

Byun, J.S., Shim, J.H., Cho, Y.W., 2003. Influence of Mn on microstructural evolution in Ti-killed C-Mn steel. Scr. Mater. 48, 449–454. https://doi.org/10.1016/S1359-6462(02)00437-2

Callister, W.D., Rethwisch, G.D., 1940. Material Sciences and Engineering, 8th ed.

Chen, Y.Z., Liu, F., Yang, G.C., Liu, N., Zhou, Y.H., 2007. δ/γ transformation in non-equilibrium solidified peritectic Fe-Ni alloy, in: Science China-Physics Mechanics & Astronomy. pp. 421–431.

Curry, D.A., Knott, J.F., 1976. The relationship between fracture toughness and microstructure in the cleavage fracture of mild steel. Met. Sci. 10, 1–6. https://doi.org/10.1179/030634576790431453

Dallam, C.B., Olson, D.L., 1989. Stress and grain size effects on weld metal ferrite formation. Weld. J. 68, 198.

Davis, C.L., King, J.E., 1996. Cleavage Initiation in the intercritically reheated coarse-grained Heat affected zone : Part I1 . Failure criteria and statistical effects. Metall. Mater. Trans. A 27, 3019–3029.

Davis, C.L., King, J.E., 1994. Cleavage initiation in the intercritically reheated coarse-grained heat-affected zone: Part I. Fractographic evidence. Metall. Mater. Trans. A 25, 563–573. https://doi.org/10.1007/BF02651598

De Andrés, C.G., Caballero, F.G., Capdevila, C., Álvarez, L.F., 2002. Application of dilatometric analysis to the study of solid-solid phase transformations in steels. Mater. Charact. 48, 101–111. https://doi.org/10.1016/S1044-5803(02)00259-0

De Andrés, C.G., Capdevila, C., Madariaga, I., Gutiérrez, I., 2013. Role of molybdenum in acicular ferrite formation under continuous cooling in medium carbon microalloyed forging steel. Scr. Mater. 45, 709–716.

Dolby, R.E., 1980. Factors controlling HAZ and weld metal toughness in C-Mn steels, in: GARRETT, MARRIOTT (Eds.), Engineering Applications of Fracture Analysis. pp. 117–134. https://doi.org/10.1016/b978-0-08-025437-1.50017-6

Dowling, J.M., Corbett, J.M., Kerr, H.W., 1986. Inclusion phases and the nucleation of acicular ferrite in submerged arc welds in high strength low alloy steels. Metall. Trans. A 17, 1611–1623. https://doi.org/10.1007/BF02650098

Dumoulin, P., Guttmann, M., Foucault, M., Palmier, M., Wayman, M., Biscondi, M., 1980. Role of molybdenum in phosphorus-induced temper embrittlement. Met. Sci. 14, 1–15. https://doi.org/10.1179/030634580790438163

Ebden, J.R., Weatherly, G.C., 1983. Weld metal fracture modes in a series of HSLA steel weldments. Can. Metall. Q. 22, 149–155. https://doi.org/10.1179/cmq.1983.22.2.149

Evans, Bailey, 1997. Metallurgy of basic weld metal. Elsevier.

Fairchild, Howden, Clark, 2000. Mechanism of brittle fracture in a microalloyed steel: Part II. Mechanistic modeling. Metall. Mater. Trans. A Phys. Metall. Mater. Sci. 31, 653–667. https://doi.org/10.1007/s11661-000-0008-3

Farrar, Zhang, 1995. Aspect ratios and morphology of acicular ferrite in C-Mn-Ni weld metals. Mater. Sci. Technol. 11, 759–764. https://doi.org/10.1179/mst.1995.11.8.759

Fattahi, M., Nabhani, N., Hosseini, M., Arabian, N., Rahimi, E., 2013. Effect of Ti-containing inclusions on the nucleation of acicular ferrite and mechanical properties of multipass weld metals. Micron 45, 107–114. https://doi.org/10.1016/j.micron.2012.11.004

Grange, R.A., Hribal, C.R., Porter, L.F., 1977. Hardness of tempered martensite in carbon and low-alloy steels. Met. Trans A 8 A, 1775–1785. https://doi.org/10.1007/BF02646882

Gubeljak, N., 2003. Unstable fracture behavior of weld metal at a high strength low alloy steel. Facta Univ. 3, 715–727.

Guillou, R., Guttmann, M., Dumoulin, P., 1981. Role of molybdenum in phosphorus-induced temper embrittlement of 12%Cr martensitic stainless steel. Met. Sci. 15, 63–72. https://doi.org/10.1179/030634581790426552

Hua, G., Li, C., Cheng, X., Zhao, X., Feng, Q., Li, Z., Li, D., Szpunar, J.A., 2018. First-principles study on influence of molybdenum on acicular ferrite formation on TiC particles in microallyed steels. Solid State Commun. 269, 102–107. https://doi.org/10.1016/j.ssc.2017.10.001

Kadoi, K., Nakata, Y., Inoue, H., Saruwatari, S., 2020. Relationship between solidification sequence and toughness of carbon steel weld metal. Mater. Charact. 165. https://doi.org/10.1016/j.matchar.2020.110402

Kang, B.Y., Kim, H.J., Hwang, S.K., 2000. Effect of Mn and Ni on the variation of the microstructure and mechanical properties of low-carbon weld metals. ISIJ Int. 40, 1237–1245. https://doi.org/10.2355/isijinternational.40.1237

Kang, Y., Han, K., Park, J.H., Lee, L., 2015. Variation in the chemical driving force for intragranular nucleation in the multi-pass weld metal of Ti-containing HSLA steel. Metall. Mater. Trans. A Phys. Metall. Mater. Sci. 46, 3581–3591. https://doi.org/10.1007/s11661-015-2958-5

Kang, Y., Jeong, S., Kang, J.H., Lee, C., 2016. Factors affecting the inclusion potency for acicular ferrite nucleation in high-strength steel welds. Metall. Mater. Trans. A Phys. Metall. Mater. Sci. 47, 2842–2854. https://doi.org/10.1007/s11661-016-3456-0

Kanjilal, P., Pal, T.K., Majumdar, S.K., 2006. Combined effect of flux and welding parameters on chemical composition and mechanical properties of submerged arc weld metal. J. Mater. Process. Technol. 171, 223–231. https://doi.org/10.1016/j.jmatprotec.2005.06.083

Kim, B.C., Lee, S., Kim, N.J., Lee, D.Y., 1991. Microstructure and local brittle zone phenomena in high-strength low-alloy steel welds. Metall. Trans. A 22, 139–149. https://doi.org/10.1007/BF03350956

Kim, K.H., Seo, J.S., Lee, C., Kim, H.J., 2011. Grain size of acicular ferrite in ferritic weld metal. Weld. World 55, 36–40. https://doi.org/10.1007/BF03321318

Kirkaldy, J.S., Baganis, E.A., 1978. Thermodynamic prediction of the Ae3 temperature of steels with additions of Mn, Si, Ni, Cr, Mo, Cu. Metall. Trans. A 9 A, 495–501. https://doi.org/10.1007/BF02646405

Kirkaldy, J.S., Venugopalan, D., 1984. Phase transformations in ferrous alloys, The American Institute of Mining, Metallurgical, and Petroleum Engineers, Incorporated.

Koseki, T., Ohkita, S., Yurioka, N., 1997. Thermodynamic estimation of inclusion characteristics in low alloy steel weld metals. Sci. Technol. Weld. Join. 2, 231–235. https://doi.org/10.1179/stw.1997.2.5.231

Koseki, T., Thewlis, G., 2005. Inclusion assisted microstructure control in C-Mn and low alloy steel welds. Mater. Sci. Technol. 21, 867–879. https://doi.org/10.1179/174328405X51703

Kunitake, T., Okada, Y., 1998. The estimation of bainite transformation temperatures in steels by the empirical formulas. Tetsu-To-Hagane/Journal Iron Steel Inst. Japan 84, 53–57.

Lambert-Perlade, A., Gourgues, A.F., Besson, J., Sturel, T., Pineau, A., 2004a. Mechanisms and modeling of cleavage fracture in simulated heat-affected zone microstructures of a high-strength low alloy steel. Metall. Mater. Trans. A Phys. Metall. Mater. Sci. 35, 1039–1053. https://doi.org/10.1007/s11661-004-1007-6

Lambert-Perlade, A., Gourgues, A.F., Pineau, A., 2004b. Austenite to bainite phase transformation in the heat-affected zone of a high strength low alloy steel. Acta Mater. 52, 2337–2348. https://doi.org/10.1016/j.actamat.2004.01.025

Lan, L., Kong, X., Qiu, C., Zhao, D., 2016. Influence of microstructural aspects on impact toughness of multi-pass submerged arc welded HSLA steel joints. Mater. Des. 90, 488–498. https://doi.org/10.1016/j.matdes.2015.10.158

Maruyama, N., Smith, G.D.W., Cerezo, A.C., 2003. Interaction of the solute niobium or molybdenum with grain boundaries in alpha-iron. Mater. Sci. Eng. A 353, 126–132. https://doi.org/10.1016/S0921-5093(02)00678-0

Mathers, J.A., 2018. Welding of HSLA steels [WWW Document]. Weld. Inst. URL https://www.twi-global.com/technical-knowledge/job-knowledge/welding-of-hsla-steels-098/

Mohseni, P., Solberg, J.K., Karlsen, M., Akselsen, O.M., Østby, e., 2012. Investigation of mechanism of cleavage fracture initiation in intercritically coarse grained heat affected zone of HSLA steel. Mater. Sci. Technol. 28, 1261–1268. https://doi.org/10.1179/1743284712Y.0000000056

Nako, H., Hatano, H., Okazaki, Y., Yamashita, K., Otsu, M., 2014. Crystal orientation relationships between acicular ferrite, oxide, and the austenite matrix. ISIJ Int. 54, 1690–1696. https://doi.org/10.2355/isijinternational.54.1690

Ohkita, s, Shigeru, Y., Sukihiko, Y., 1995. Recent development in controlling the microstructure and properties of low alloy steel weld metals. ISIJ Int. 35, 11701182.

Ohmori, Y., Ohtsubo, H., Jung, Y.C., Okaguchi, S., Ohtani, H., 1994. Morphology of bainite and widmanstätten ferrite. Metall. Mater. Trans. A 25, 1981–1989. https://doi.org/10.1007/BF02649046

Okaguchi, S., Ohtani, H., Ohmori, Y., 1991. Morphology of Widmanstatten and bainitic ferrites. Mater. Trans. https://doi.org/10.2320/matertrans1989.32.697

Okazaki, Y., Ishida, H., Suenaga, K., Hidaka, T., 2012. Influence of oxide inclusion compositions on microstructure and toughness of weld metal for high-strength steel. Weld. Int. 26, 593–600. https://doi.org/10.1080/09507116.2011.592687

Pak, J.H., Bhadeshia, H.K.D.H., Karlsson, L., Keehan, E., 2008. Coalesced bainite by isothermal transformation of reheated weld metal. Sci. Technol. Weld. Join. 13, 593–597. https://doi.org/10.1179/136217108X338926

Pandey, N.D., Bharti, A., Gupta, S.R., 1994. Effect of submerged arc welding parameters and fluxes on element transfer behaviour and weld-metal chemistry. J. Mater. Process. Tech. 40, 195–211. https://doi.org/10.1016/0924-0136(94)90486-3

Peet, M.J., Hasan, H.S., Bhadeshia, H.K.D.H., 2011. Prediction of thermal conductivity of steel. Int. J. Heat Mass Transf. 54, 2602–2608. https://doi.org/10.1016/j.ijheatmasstransfer.2011.01.025

Rees, G.I., Bhadeshia, H.K.D.H., 1994. Thermodynamics of acicular ferrite nucleation. Mater. Sci. Technol. 10, 353–358. https://doi.org/10.1179/mst.1994.10.5.353

Ren, D., Xiao, F., Tian, P., Wang, X., Liao, B., 2009. Effects of welding wire composition and welding process on the weld metal toughness of submerged arc welded pipeline steel. Int. J. Miner. Metall. Mater. 16, 65–70. https://doi.org/10.1016/S1674-4799(09)60011-X

Ricks, R.A., Howell, P.R., Barritte, G.S., 1982. The nature of acicular ferite in HSLA steel weld metals. Rev. Fr. Transfus. 17, 732–740. https://doi.org/10.1016/S0035-2977(71)80008-1

Rosenthal, J.L., 1946. The theory of moving sources of heat and its application to metal treatments. Trans. ASME.

Seo, K., Kim, K.H., Kim, H.J., Ryoo, H., Evans, G.M., Lee, C., 2019a. Microstructural and inclusion characteristics of C–Mn steel welds at a minimal level of titanium. Met. Mater. Int. https://doi.org/10.1007/s12540-019-00390-4

Seo, K., Kim, Y.M., Kim, H.J., Lee, C., 2015. Characterization of inclusions formed in Ti-containing steel weld metals. ISIJ Int. 55, 1730–1738. https://doi.org/10.2355/isijinternational.ISIJINT-2014-800

Seo, K., Ryoo, H., Kim, H.J., Lee, C., 2019b. Quantitative evaluation of nucleation potency of ti-containing inclusions for acicular ferrite. ISIJ Int. 59, 1105–1112. https://doi.org/10.2355/isijinternational.ISIJINT-2018-622

Shi, Y., Han, Z., 2008. Effect of weld thermal cycle on microstructure and fracture toughness of simulated heat-affected zone for a 800 MPa grade high strength low alloy steel. J. Mater. Process. Technol. 207, 30–39. https://doi.org/10.1016/j.jmatprotec.2007.12.049

Skobir, D., 2001. High-strength low-alloy (HSLA) steels:, in: Alloying: Understanding the Basics. ASM international, pp. 295–301.

Solutions Statistics, n.d. Sample size formula [WWW Document]. URL https://www.statisticssolutions.com/dissertation-resources/sample-size-calculation-and-sample-size-justification/sample-size-formula/#:~:text=For example%2C in regression analysis,minimum sample size of 30. (accessed 2.11.20).

Song, M., Xie, Y., Song, B., Xue, Z., Nie, N., Hu, C., Xu, R., 2019. The microstructure and property of the Heat affected zone in C-Mn Steel treated by rare earth. High Temp. Mater. Process. 38, 362–369. https://doi.org/doi:10.1515/htmp-2017-0175

Srinivasan, G.R., Wayman, C.M., 1968. The crystallography of the bainite transformation-I. Acta Metall. 16, 621–636. https://doi.org/10.1016/0001-6160(68)90136-3

Steven, W., Hayens, A., 1956. Temperature of formation of martensite and bainite in low alloy steels, coem effects of chemical composition. J. Iron Steel Inst. 183, 349–359.

Sugden, A.A.B., Bhadeshia, H.K.D.H., 1989. Lower acicular ferrite. Metall. Trans. A. https://doi.org/10.1007/BF02663212

Surian, E., De Rissone, M., De Vedia, L., 2005. Influence of molybdenum on ferritic high-strength SMAW all-weld-metal properties. Weld. J. (Miami, Fla) 84.

Takahashi, J., Ishikawa, K., Kawakami, K., Fujioka, M., Kubota, N., 2017. Atomic-scale study on segregation behavior at austenite grain boundaries in boron- and molybdenum-added steels, Acta Materialia. Elsevier B.V. https://doi.org/10.1016/j.actamat.2017.05.021

Thewlis, G., 2000. Weldability of X100 linepipe. Sci. Technol. Weld. Join. 5, 365–377. https://doi.org/10.1179/136217100101538434

Thewlis, G., Whiteman, J.A., Senogles, D.J., 1997. Dynamics of austenite to ferrite phase transformation in ferrous weld metals. Mater. Sci. Technol. 13, 257–274. https://doi.org/10.1179/mst.1997.13.3.257

Torkamani, H., Shahram, R., Garcea-Mateo, C., Rassizadehghani, J., 2017. The Influence of La and Ce Addition on Inclusion Modification in Cast Niobium Microalloyed Steels. Met. - Open Access Metall. J. 7, 377.

Trzaska, 2016. Calculation of critical temperatures by empirical formulae. Arch. Metall. Mater. 61, 981–986. https://doi.org/10.1515/amm-2016-0167

Tweed, J.H., Knott, J.F., 1987. Micromechanisms of failure in CMn weld metals. Acta Metall. 35, 1401–1414. https://doi.org/10.1016/0001-6160(87)90087-3

Vervynckt, S., Verbeken, K., Lopez, B., Jonas, J.J., 2012. Modern HSLA steels and role of non-recrystallisation temperature. Int. Mater. Rev. 57, 187–207. https://doi.org/10.1179/1743280411Y.0000000013

Vezzu, S., Scappin, M., Biatetto, G., Timelli, G., 2019. On the Effect of Slight Variations of Si, Mn, and Ti on inclusions properties, microstructure, and mechanical properties of YS460 C-Mn steel welds. Metallogr. Microstruct. Anal. https://doi.org/10.1007/s13632-019-00536-1

Viano, D.M., Ahmed, N.U., Schumann, G.O., 2000. Influence of heat input and travel speed on microstructure and mechanical properties of double tandem submerged arc high strength low alloy steel weldments. Sci. Technol. Weld. Join. 5, 26–34. https://doi.org/10.1179/stw.2000.5.1.26

Yang, L., Wang, W., Zhang, Z., Zhang, J., Meng, M., Shimming, H., Bai, Q., 2015. Effect of Mn and Ni on microstructure and impact toughness of submerged arc weld metals. Trans. Tianjin Univ. 21, 562–566. https://doi.org/10.1007/s12209-015-2480-2

You, W., Xu, W., Bai, B., Fang, H., 2006. Materialometrical approach of predicting the austenite formation temperatures. Mater. Sci. Eng. A 419, 276–282. https://doi.org/10.1016/j.msea.2005.12.031

You, Y., Shang, C., Chen, L., Subramanian, S., 2013. Investigation on the crystallography of the transformation products of reverted austenite in intercritically reheated coarse grained heat affected zone. Mater. Des. 43, 485–491. https://doi.org/10.1016/j.matdes.2012.07.015

Zhang, Z., 2021. The iron-iron carbide (Fe-Fe 3 C) phase diagram microstructures of iron α - ferrite Interstitial sites of FCC Interstitial sites of BCC.

Zhang, Z., Farrar, R.A., 1997. Influence of Mn and Ni on the microstructure and toughness of C-Mn-Ni weld metals. Weld. J. (Miami, Fla) 76, 183-s.

Appendix

A. Detailed thermal cycling data

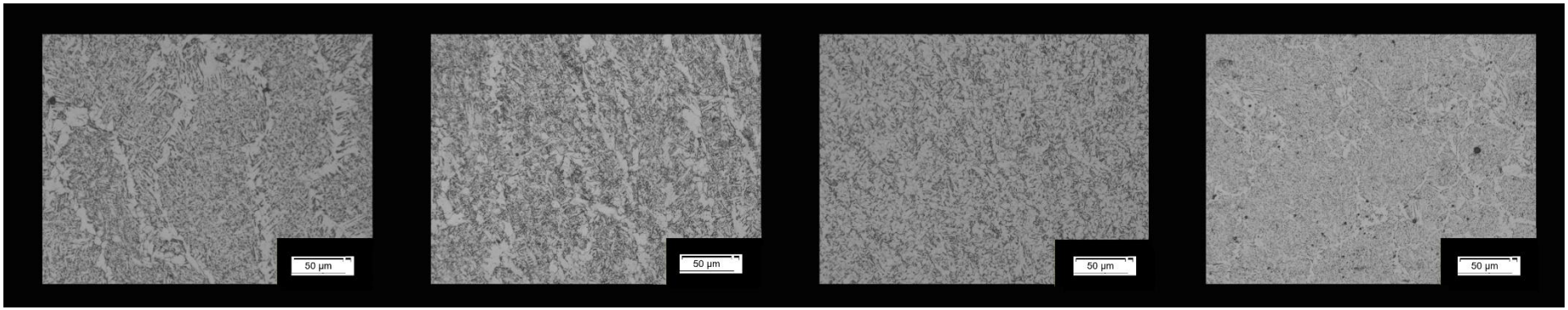

Figure 161: Optical micrographs of Weld 1 in the as-welded, intercritically reheated, grain-refinement, and grain-growth conditions. The micrographs were taken at 200× magnification.

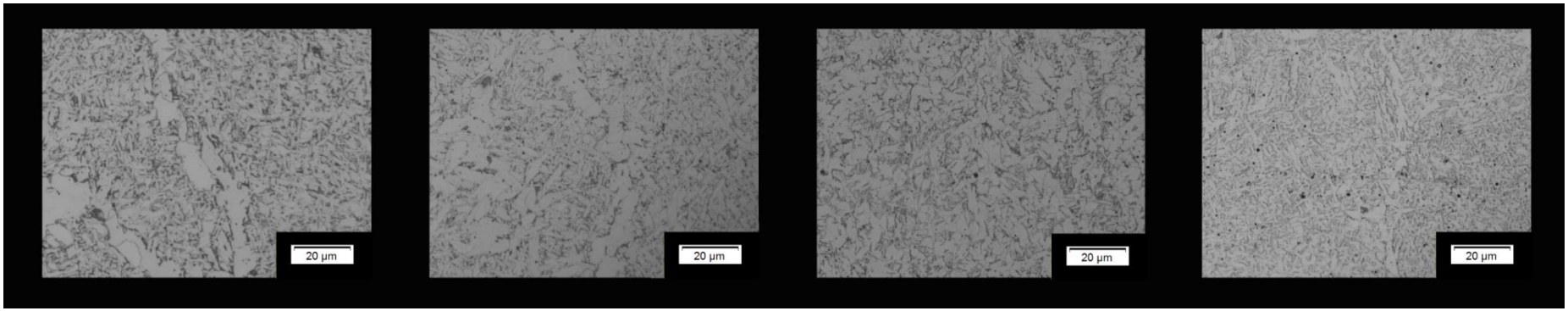

Figure 162: Optical micrographs of Weld 1 in the as-welded, intercritically reheated, grain-refinement, and grain-growth conditions. The micrographs were taken at 200× magnification.

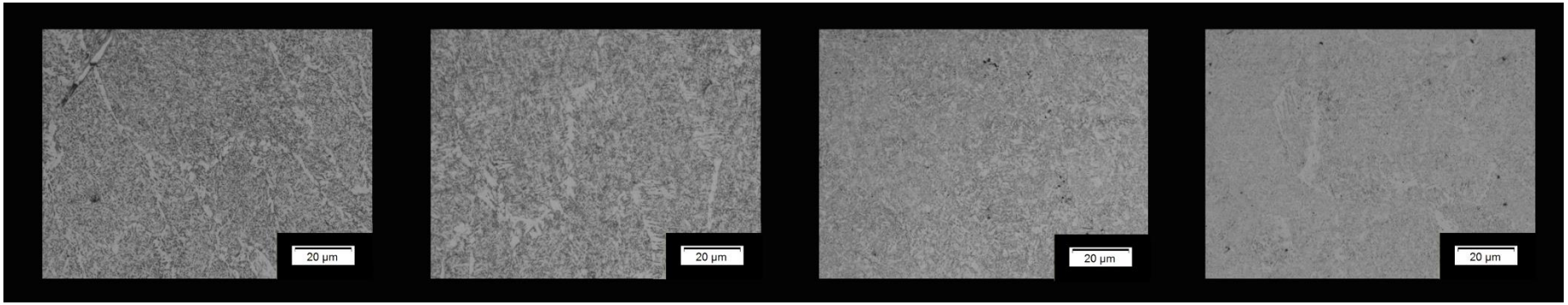

Figure 163: Optical micrographs of Weld 2 in the as-welded, intercritically reheated, grain-refinement, and grain-growth conditions. The micrographs were taken at 200×x magnification.

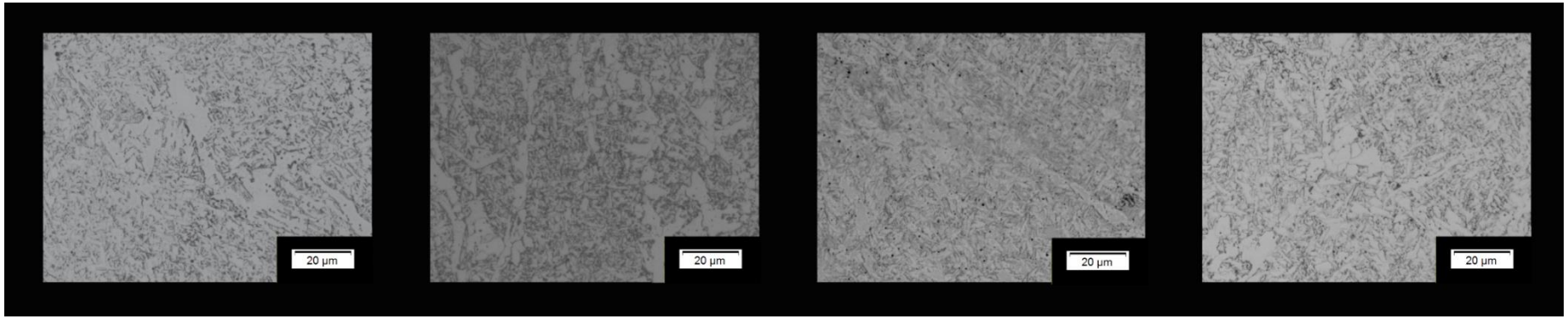

Figure 164: Optical micrographs of Weld 2 in the as-welded, intercritically reheated, grain-refinement, and grain-growth conditions. The micrographs were taken at 500× magnification.

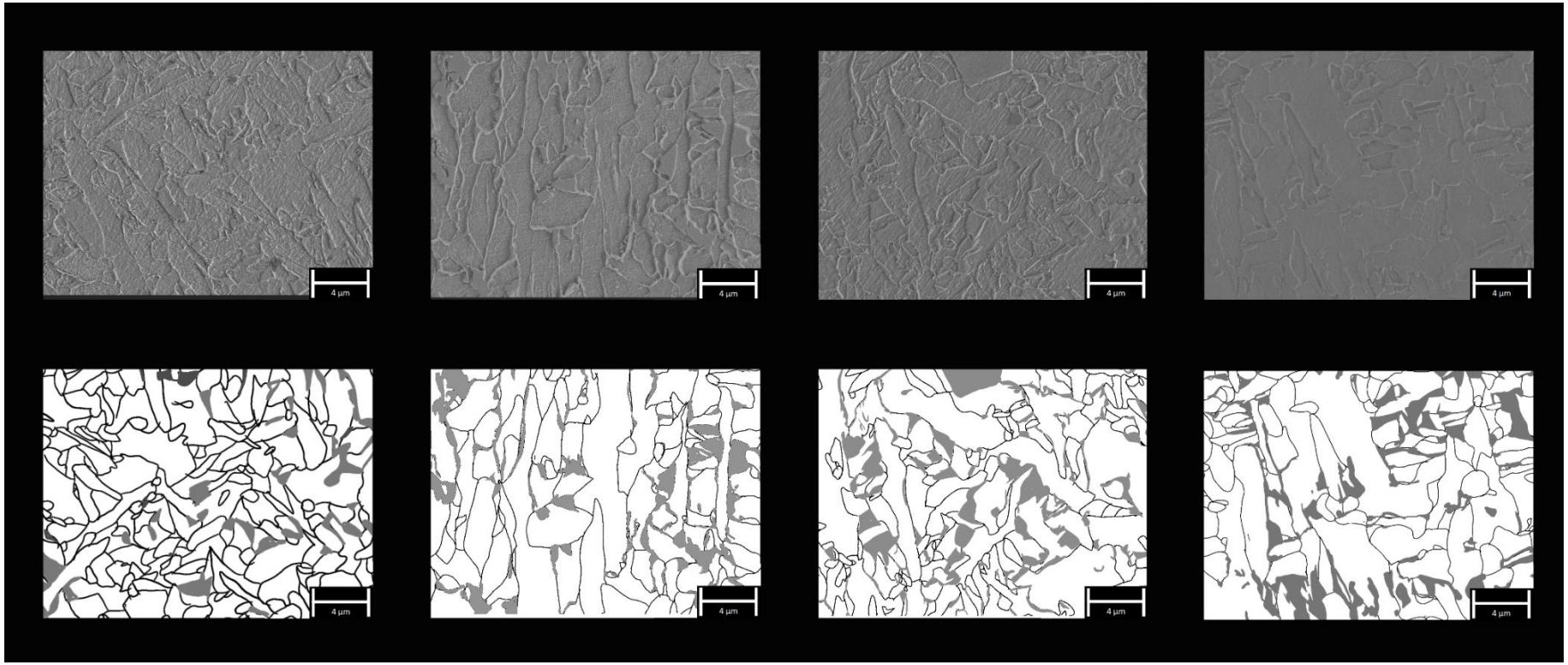

Figure 165: SEM micrographs of Weld 2 in the as-welded, intercritically reheated, grain-refinement, and grain-growth conditions. The micrographs are shown in the original and processed conditions.

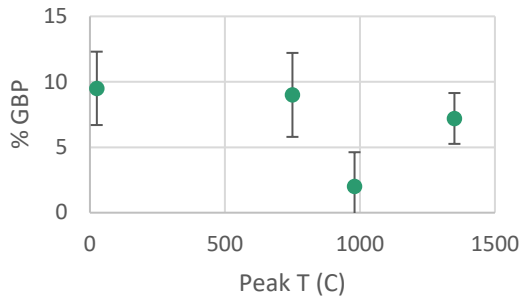

Figure 166: Scatter plot showing % GBP as a function of peak temperature reached during thermal cycling of Weld 2.

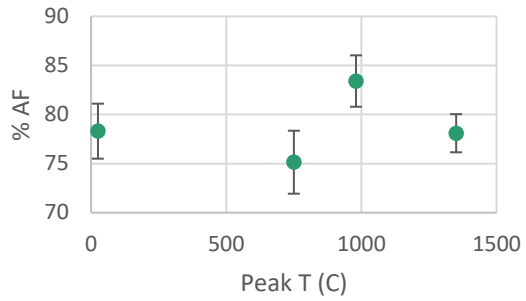

Figure 167: Scatter plot showing % AF as a function of peak temperature reached during thermal cycling Weld 2.

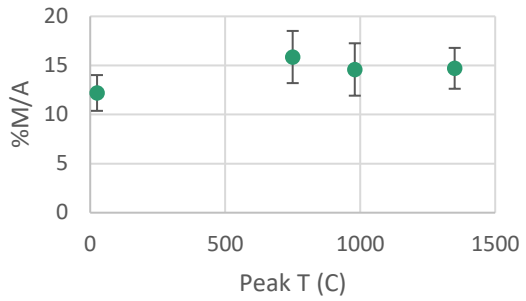

Figure 168: Scatter plot showing % M/A as a function of peak temperature reached during thermal cycling of Weld 2.

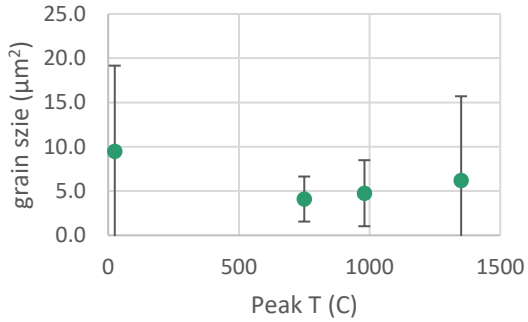

Figure 169: Scatter plot showing the number of ferrite-type grains per 100 µm^2 as a function of peak temperature reached during thermal cycling of Weld 2.

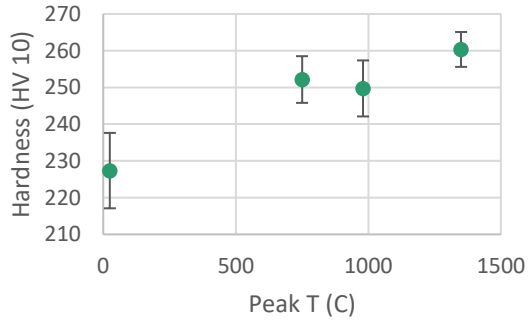

Figure 170: Scatter plot showing the change in impact energy as a function of peak temperature reached during thermal cycling of Weld 2.

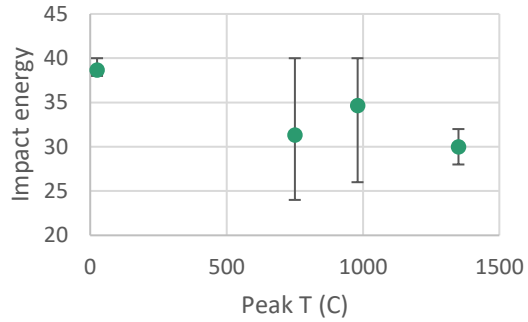

Figure 171: Scatter plot showing the change in impact energy as a function of peak temperature reached during thermal cycling of Weld 2.

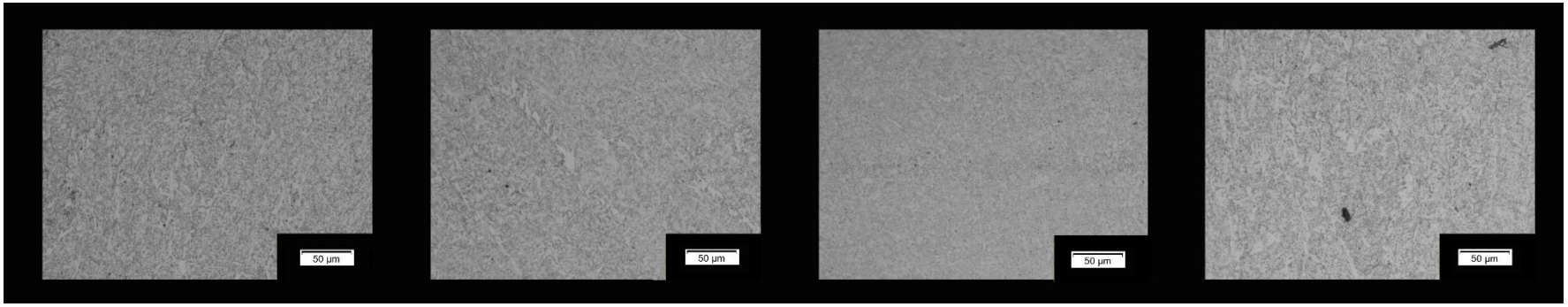

Figure 172: Optical micrographs of Weld 3 in the as-welded, intercritically reheated, grain-refinement, and grain-growth conditions. The micrographs were taken at 200× magnification.

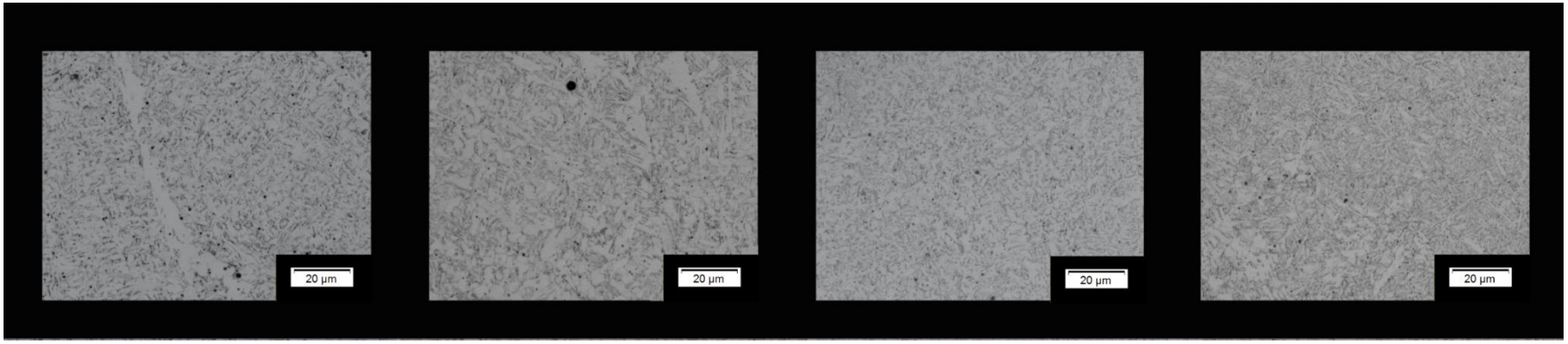

Figure 173: Optical micrographs of Weld 3 in the as-welded, intercritically reheated, grain-refinement, and grain-growth condition. The micrographs were taken at 500× magnification.

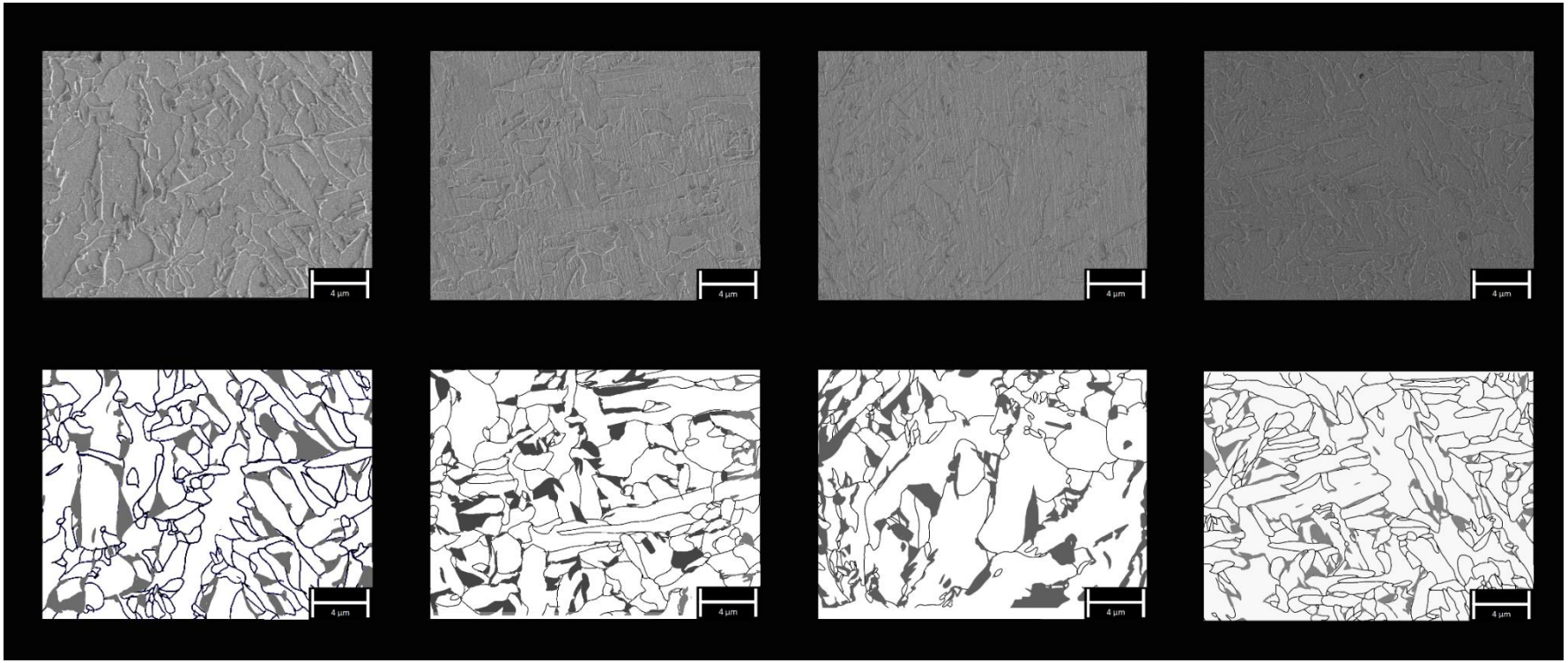

Figure 174: SEM micrographs of Weld 3 in the as-welded, intercritically reheated, grain-refinement, and grain-growth conditions. The micrographs are shown in the original and processed conditions.

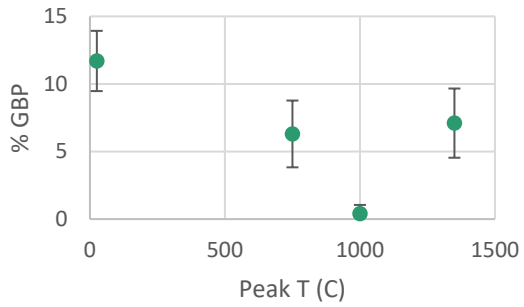

Figure 175: Scatter plot showing % GBP as a function of peak temperature reached during thermal cycling of Weld 3.

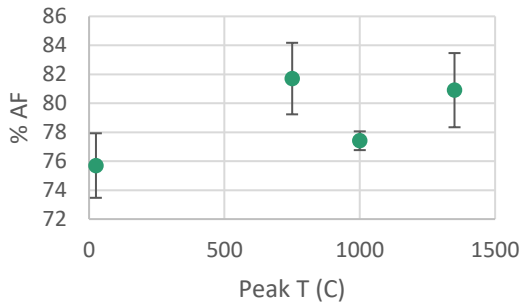

Figure 176: Scatter plot showing % AF as a function of peak temperature reached during thermal cycling of Weld 3.

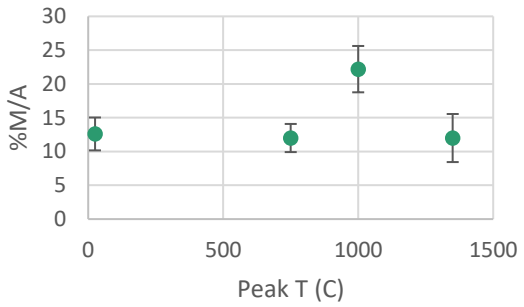

Figure 177: Scatter plot showing % M/A as a function of peak temperature reached during thermal cycling of Weld 3.

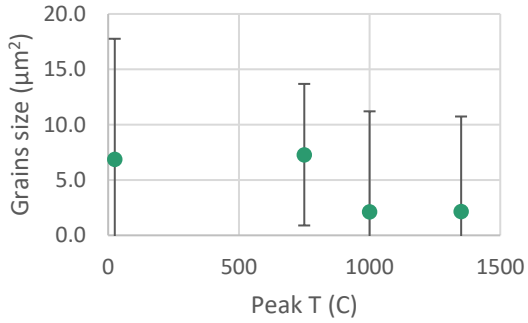

Figure 178: Scatter plot showing the number of ferrite-type grains per 100 µm² as a function of peak temperature reached during thermal cycling of Weld 3.

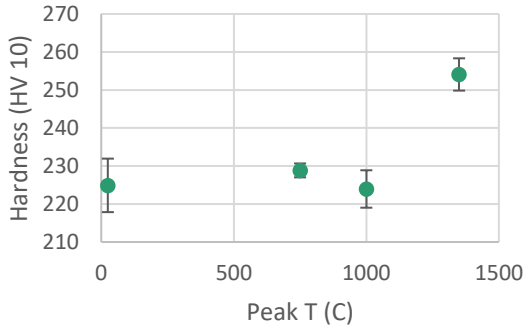

Figure 179: Scatter plot showing the change in hardness as a function of peak temperature reached during thermal cycling of Weld 3.

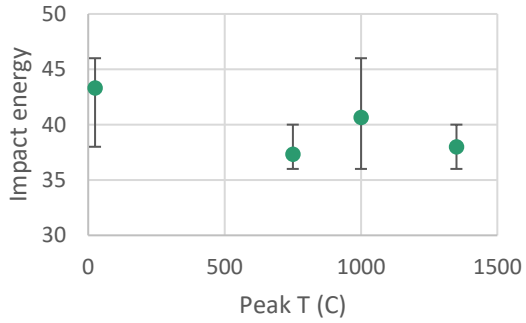

Figure 180: Scatter plot showing the change in impact energy as a function of peak temperature reached during thermal cycling of Weld 3.

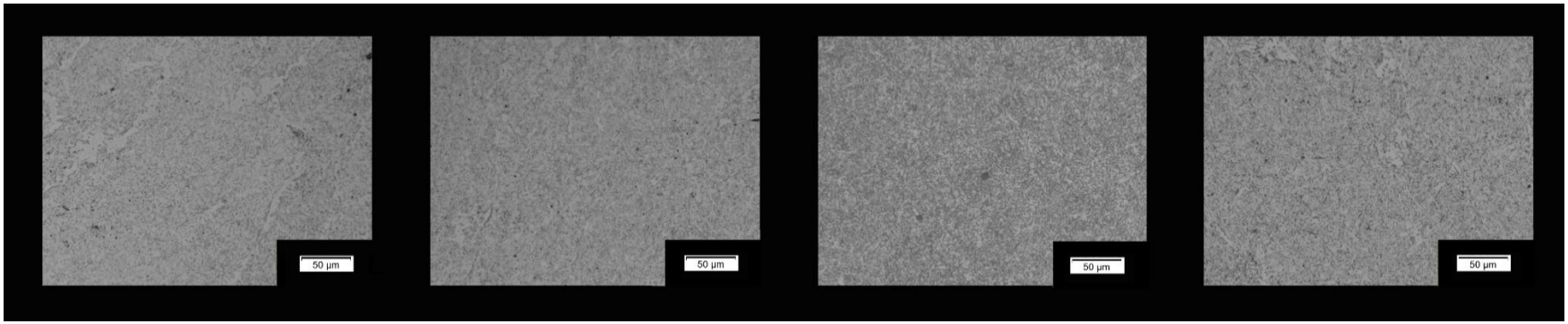

Figure 181: Optical micrographs of Weld 4 in the as-welded, intercritically reheated, grain-refinement, and grain-growth conditions. The micrographs were taken at 200× magnification.

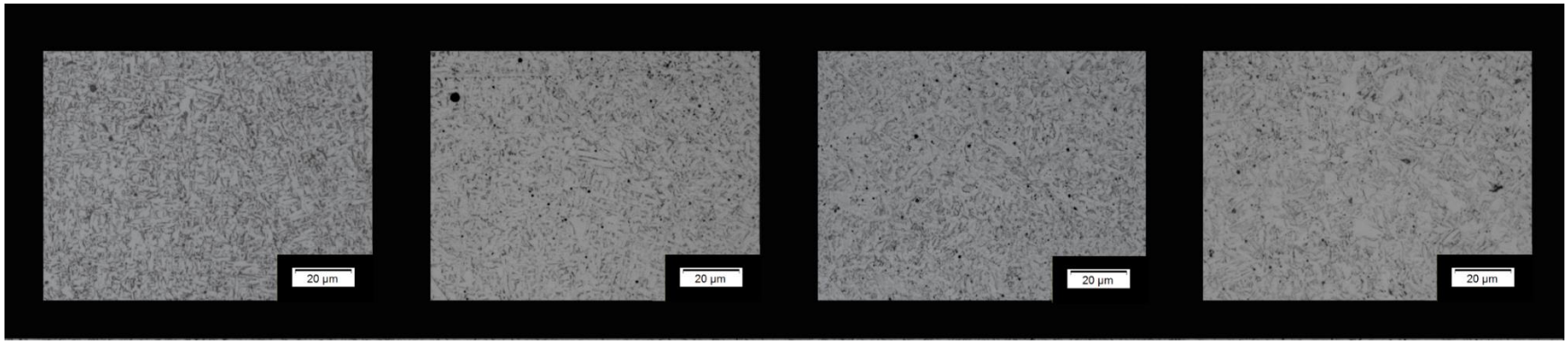

Figure 182: Optical micrographs of Weld 4 in the as-welded, intercritically reheated, grain-refinement, and grain-growth conditions. The micrographs were taken at 500× magnification.

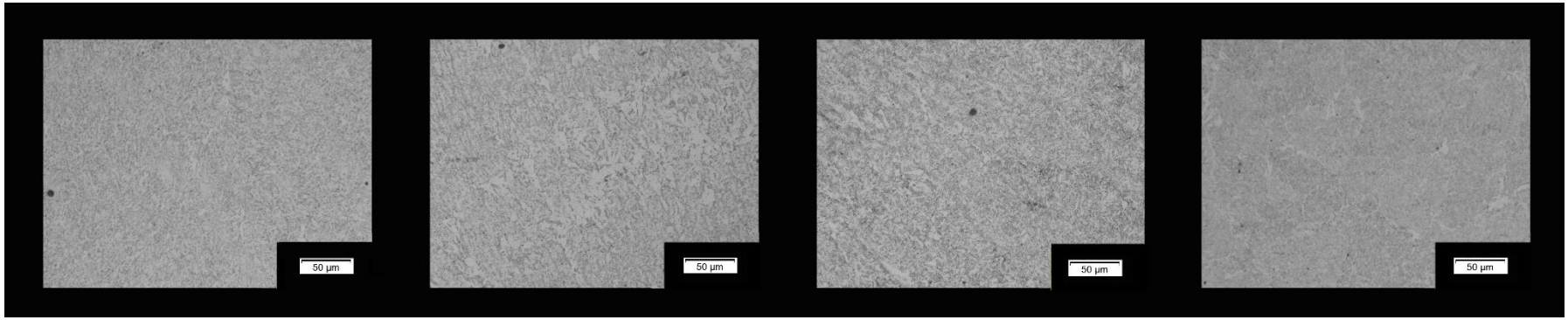

Figure 183: Optical micrographs of Weld 5 in the as-welded, intercritically reheated, grain-refinement, and grain-growth conditions. The micrographs were taken at 200× magnification.

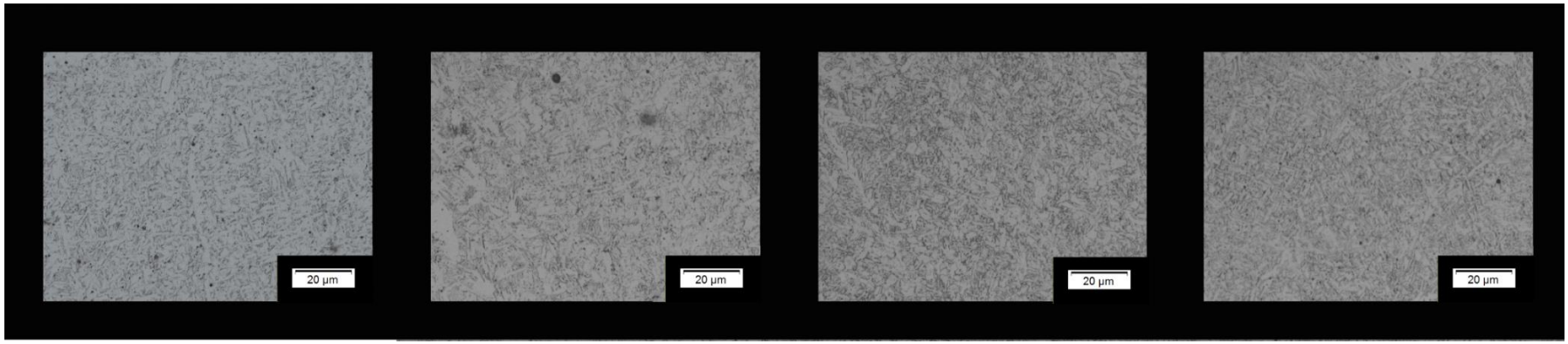

Figure 184: Optical micrographs of Weld 5 in the as welded, intercritically reheated, grain-refinement, and grain-growth conditions. The micrographs were taken at 500× magnification.

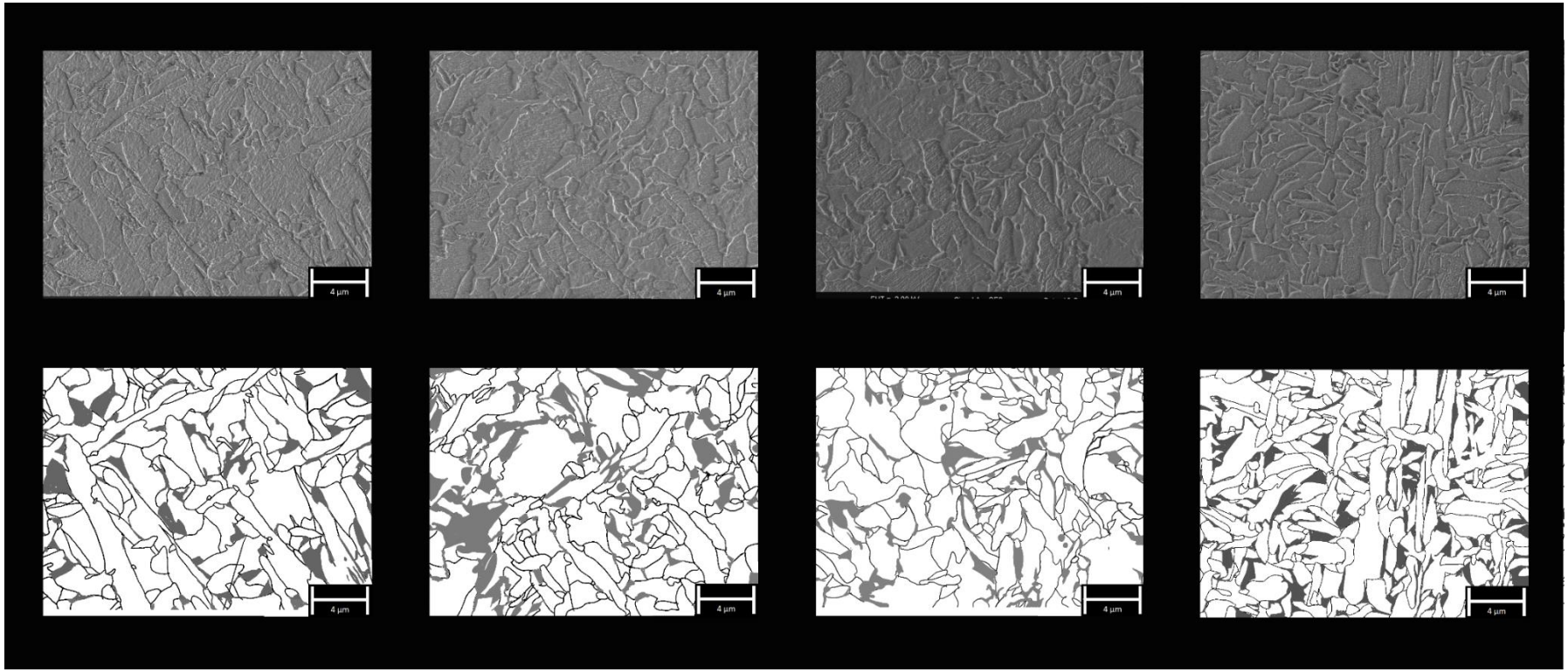

Figure 185: SEM micrographs of Weld 5 in the as welded, intercritically reheated, grain-refinement, and grain-growth conditions. The micrographs are shown in the original and processed conditions.

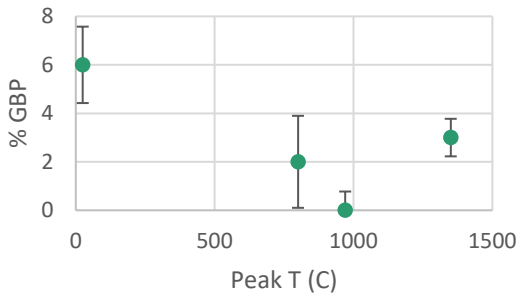

Figure 186: Scatter plot showing % GBP as a function of peak temperature reached during thermal cycling of Weld 5.

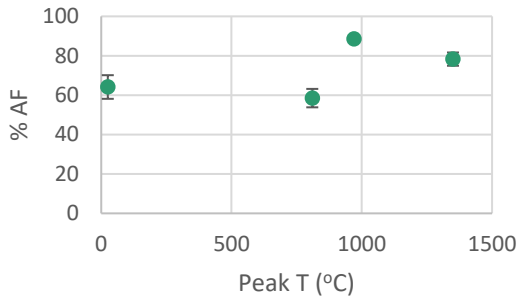

Figure 187: Scatter plot showing % AF as a function of peak temperature reached during thermal cycling of Weld 5.

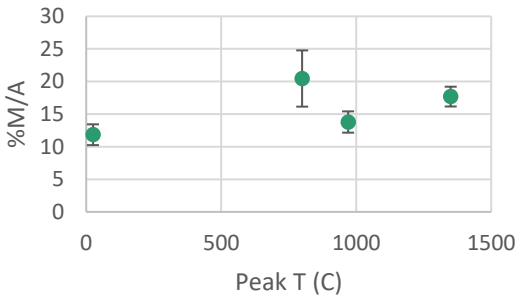

Figure 188: Scatter plot showing % M/A as a function of peak temperature reached during thermal cycling of Weld 5.

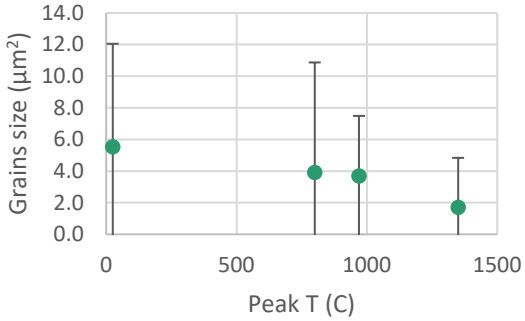

Figure 189: Scatter plot showing the number of ferrite-type grains per 100 µm² as a function of peak temperature reached during thermal cycling of Weld 5.

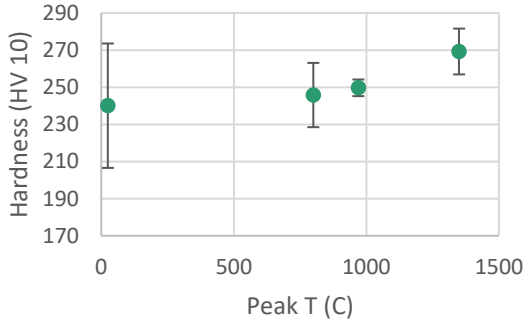

Figure 190: Scatter plot showing the change in hardness as a function of peak temperature reached during thermal cycling of Weld 5.

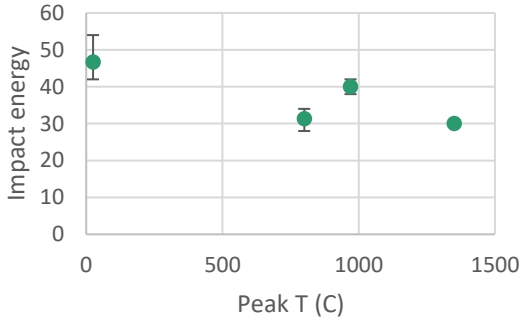

Figure 191: Scatter plot showing the change in impact energy as a function of peak temperature reached during thermal cycling of Weld 5.

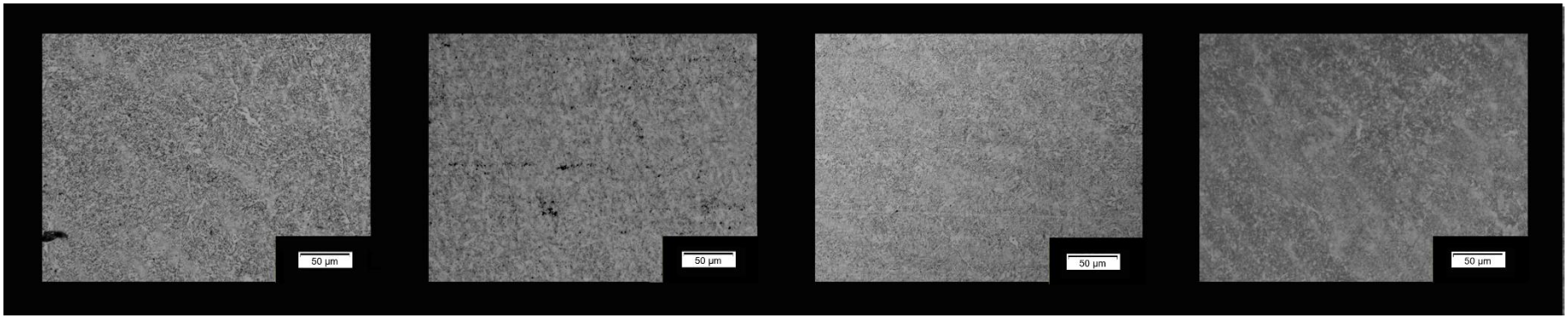

Figure 192: Optical micrographs of Weld 6 in the as-welded, intercritically reheated, grain-refinement, and grain-growth conditions. The micrographs were taken at 500× magnification.

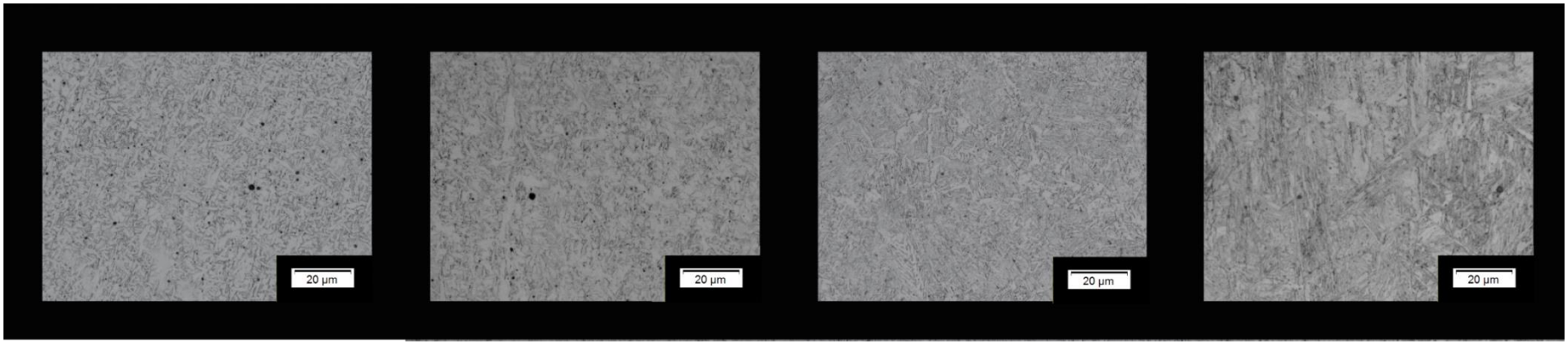

Figure 193: Optical micrographs of Weld 6 in the as-welded, intercritically reheated, grain-refinement, and grai- growth conditions. The micrographs were taken at 500× magnification.

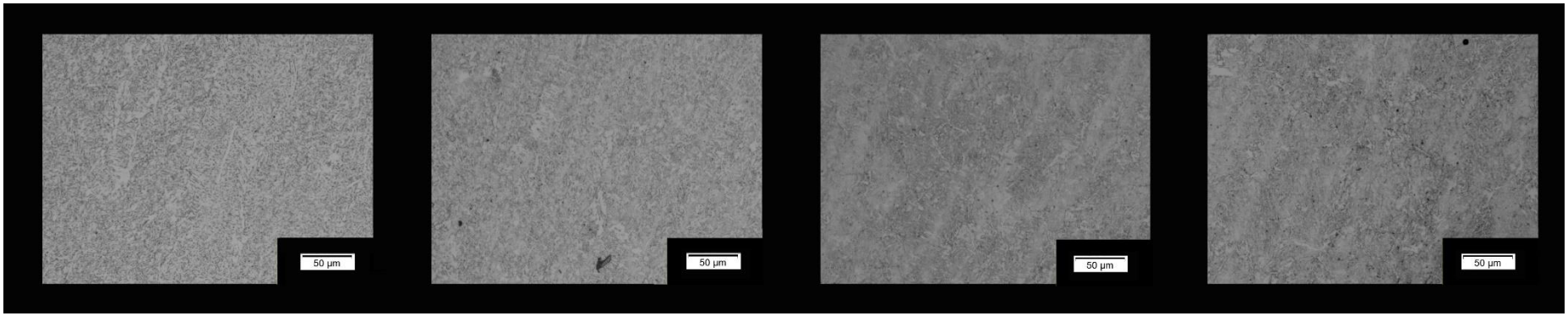

Figure 194: Optical micrographs of Weld 7 in the as-welded, intercritically reheated, grain-refinement, and grain-growth conditions. The micrographs were taken at 200× magnification.

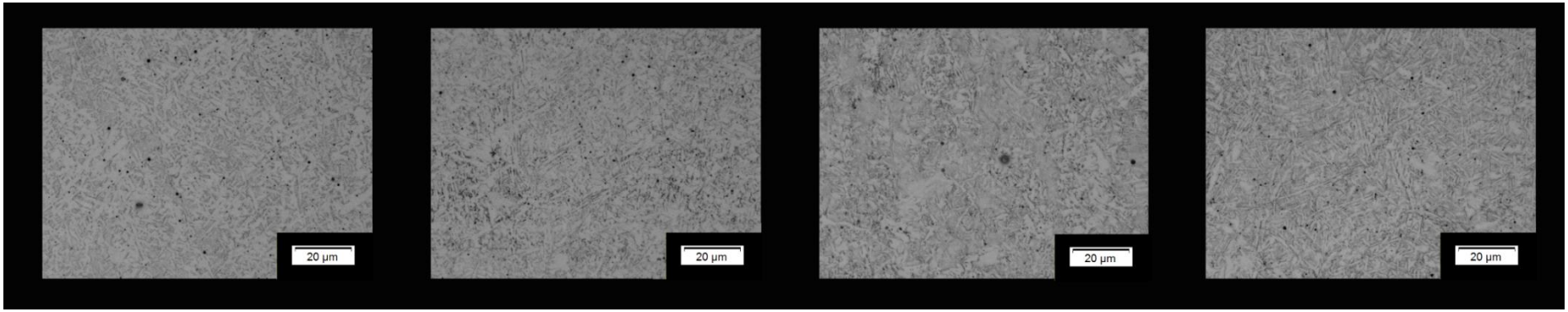

Figure 195: Optical micrographs of Weld 7 in the as-welded, intercritically reheated, grain-refinement, and grain-growth conditions. The micrographs were taken at 500× magnification.

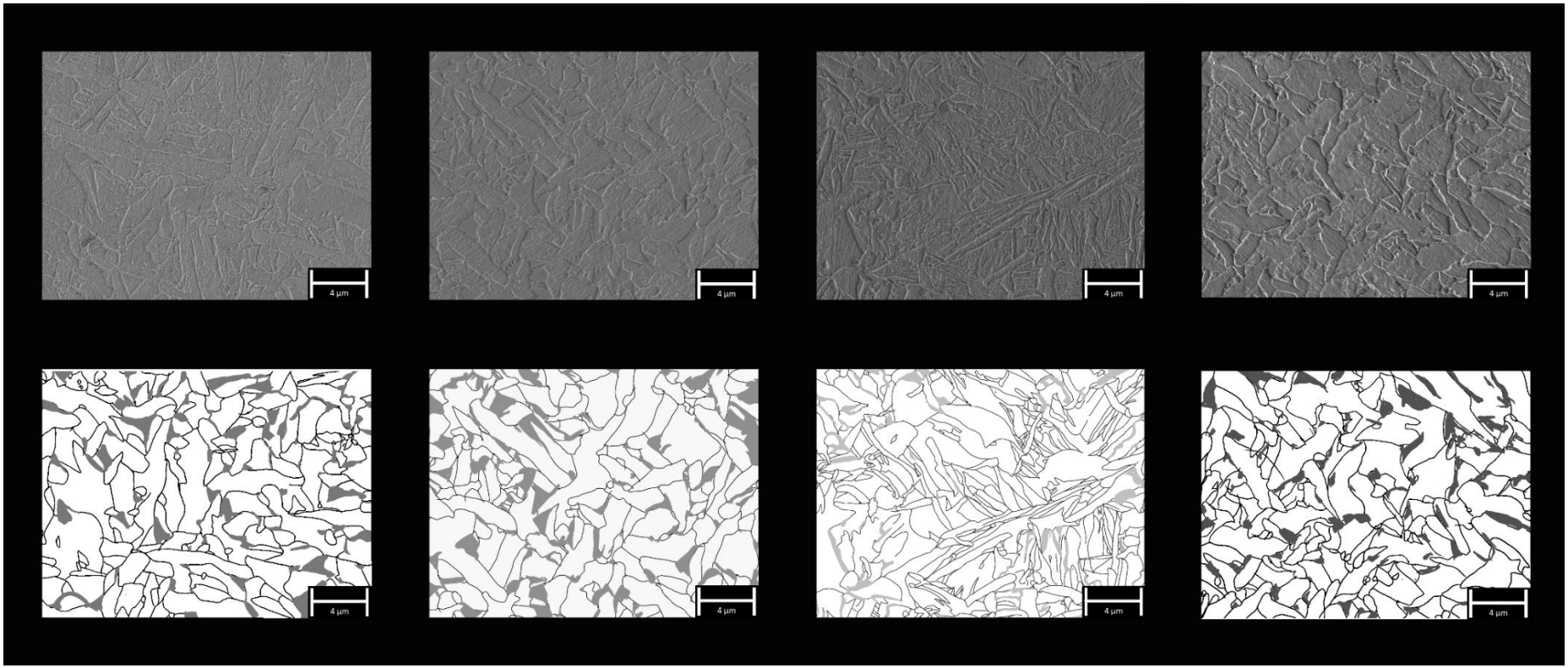

Figure 196: SEM micrographs of Weld 7 in the as-welded, intercritically reheated, grain-refinement, and grain-growth conditions. The micrographs are shown in the original and processed conditions.

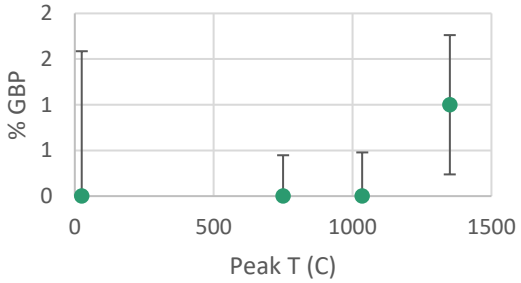

Figure 197: Scatter plot showing % GBP as a function of peak temperature reached during thermal cycling of Weld 7.

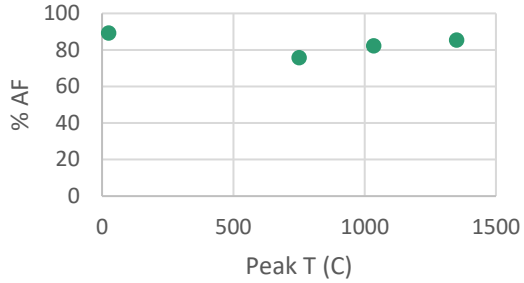

Figure 198: Scatter plot showing % AF as a function of peak temperature reached during thermal cycling of Weld 7.

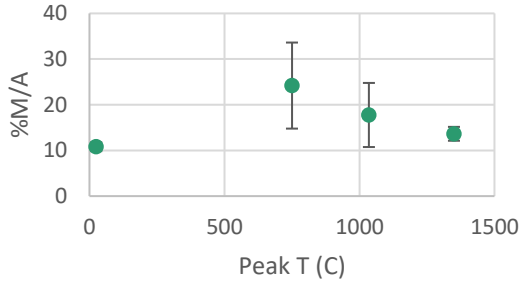

Figure 199: Scatter plot showing % M/A as a function of peak temperature reached during thermal cycling of Weld 7.

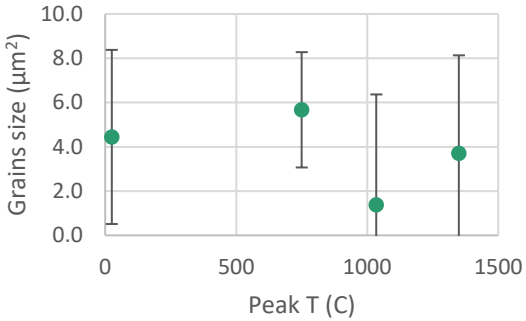

Figure 200: Scatter plot showing the number of ferrite-type grains per 100 µm^2 as a function of peak temperature reached during thermal cycling of Weld 7.

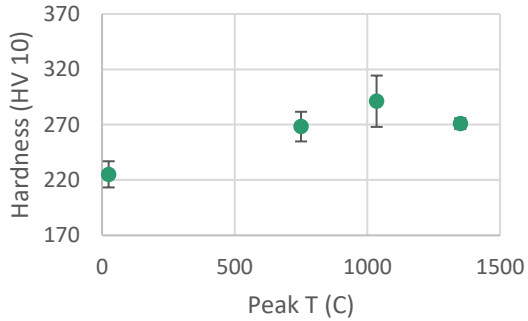

Figure 201: Scatter plot showing the change in hardness as a function of peak temperature reached during thermal cycling of Weld 7.

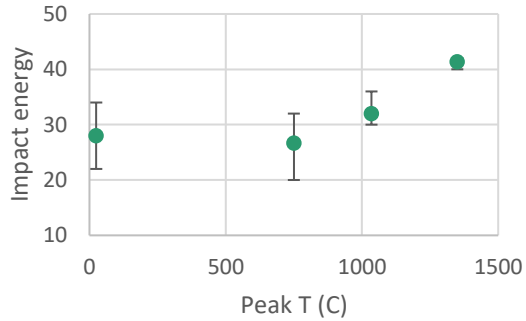

Figure 202: Scatter plot showing the change in impact properties as a function of peak temperature reached during thermal cycling of Weld 7.

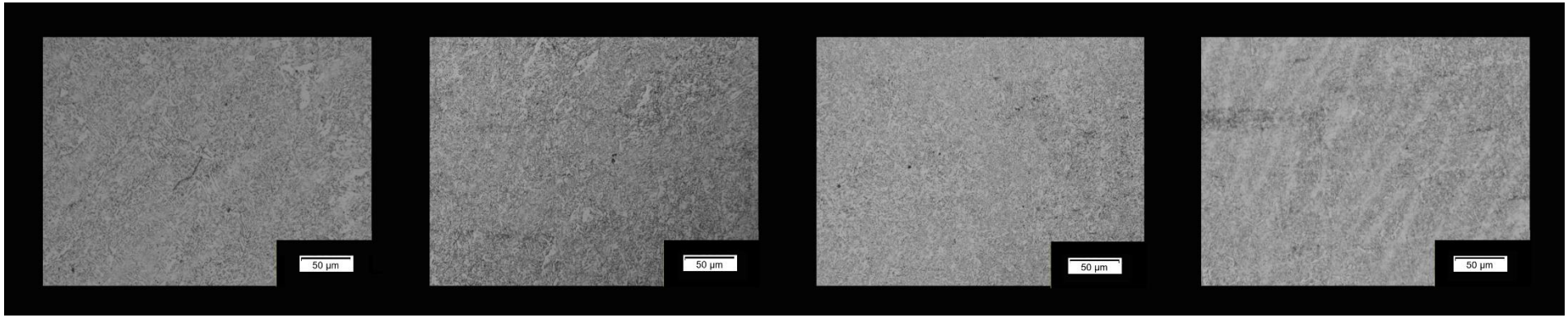

Figure 203: Optical micrographs of Weld 8 in the as-welded, intercritically reheated, grain-refinement, and grain-growth conditions. The micrographs were taken at 200× magnification.

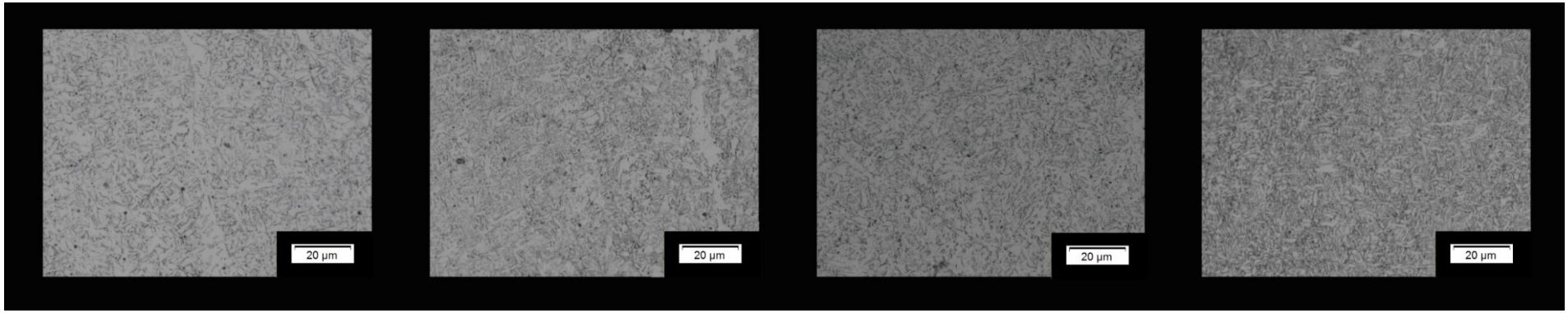

Figure 204: Optical micrographs of Weld 8 in the as-welded, intercritically reheated, grain-refinement, and grain-growth conditions. The micrographs were taken at 500× magnification.

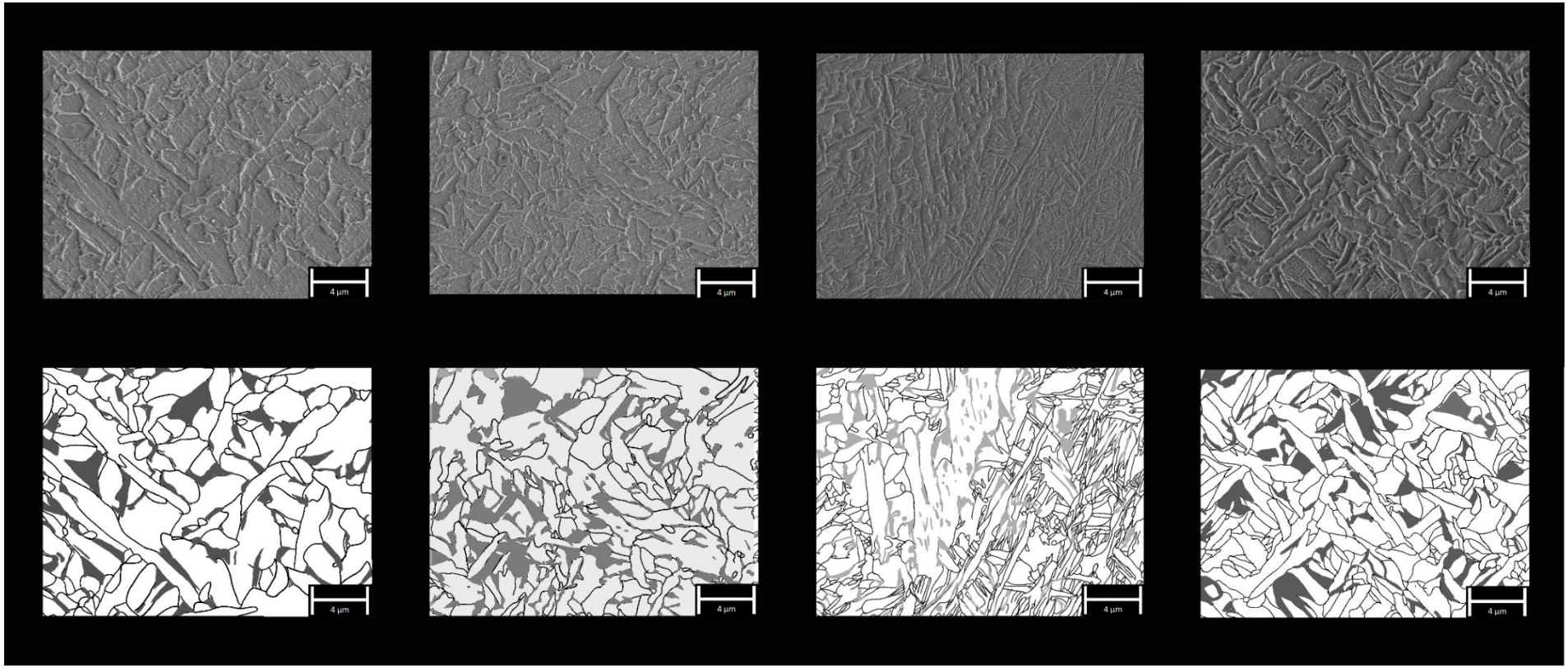

Figure 205: SEM micrographs of Weld 8 in the as-welded, intercritically reheated, grain-refinement, and grain-growth condition. The micrographs are shown in the original and processed conditions.

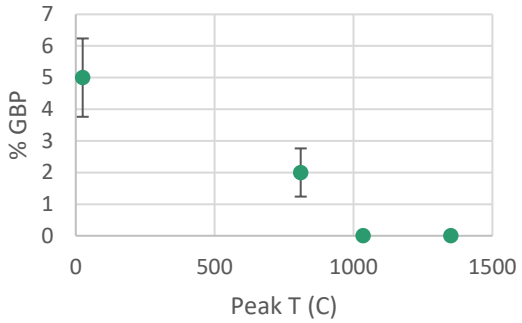

Figure 206: Scatter plot showing % GBP as a function of peak temperature reached during thermal cycling of Weld 8.

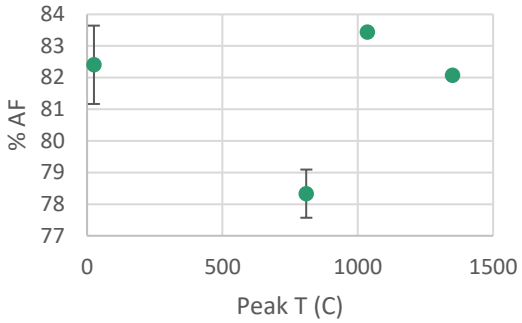

Figure 207: Scatter plot showing % AF as a function of peak temperature reached during thermal cycling of Weld 8.

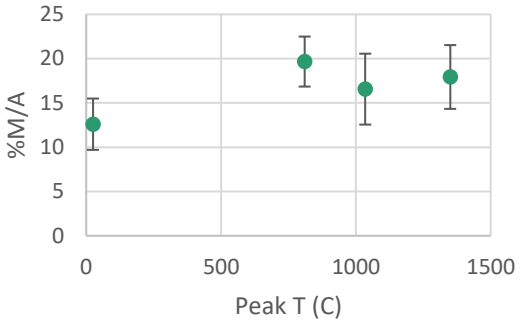

Figure 208: Scatter plot showing % M/A as a function of peak temperature reached during thermal cycling of Weld 8.

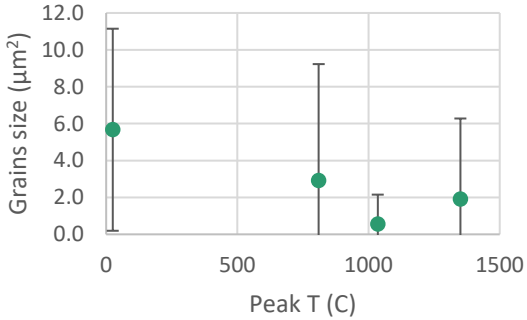

Figure 209: Scatter plot showing the grain size as a function of peak temperature reached during thermal cycling of Weld 8.

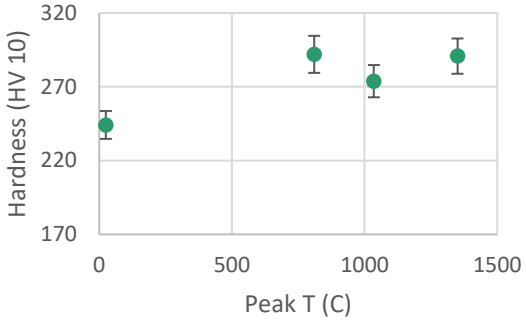

Figure 210: Scatter plot showing the change in hardness as a function of peak temperature reached during thermal cycling of Weld 8.

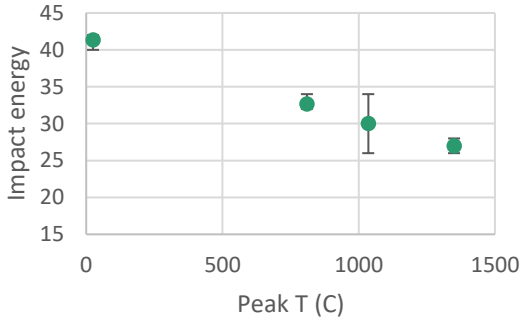

Figure 211: Scatter plot showing the change in hardness as a function of peak temperature reached during thermal cycling of Weld 8.

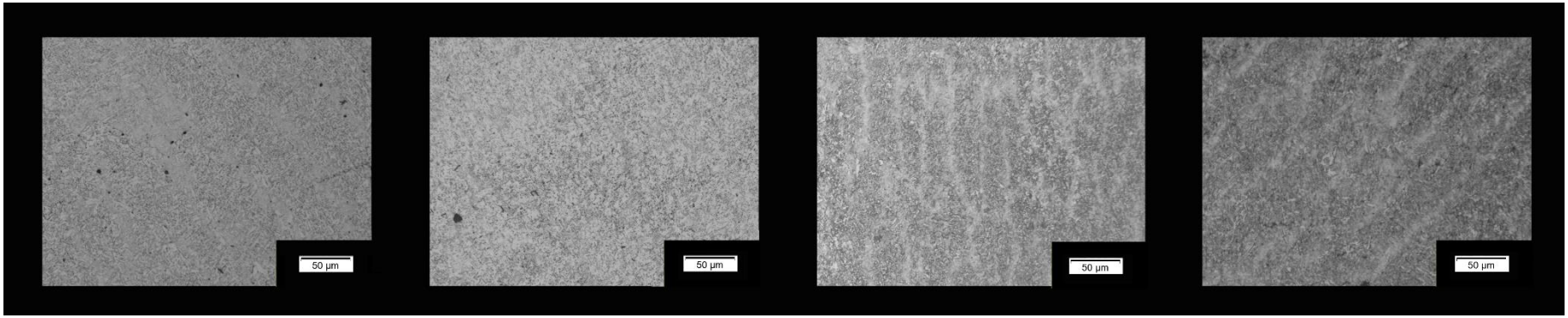

Figure 212: Optical micrographs of Weld 9 in the as-welded, intercritically reheated, grai- refinement, and grain-growth conditions. The micrographs were taken at 200× magnification.

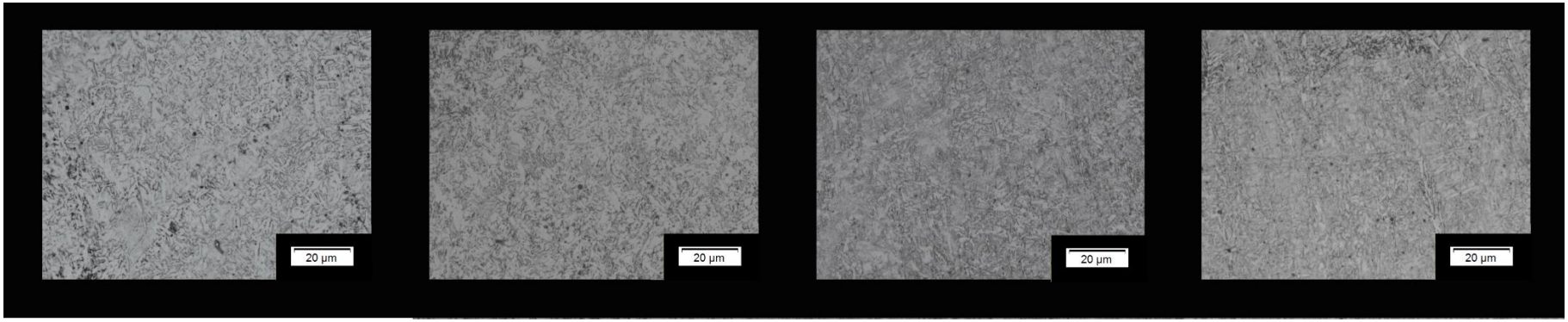

Figure 213: Optical micrographs of Weld 9 in the as-welded, intercritically reheated, grain-refinement, and grain-growth conditions. The micrographs were taken at 500× magnification.

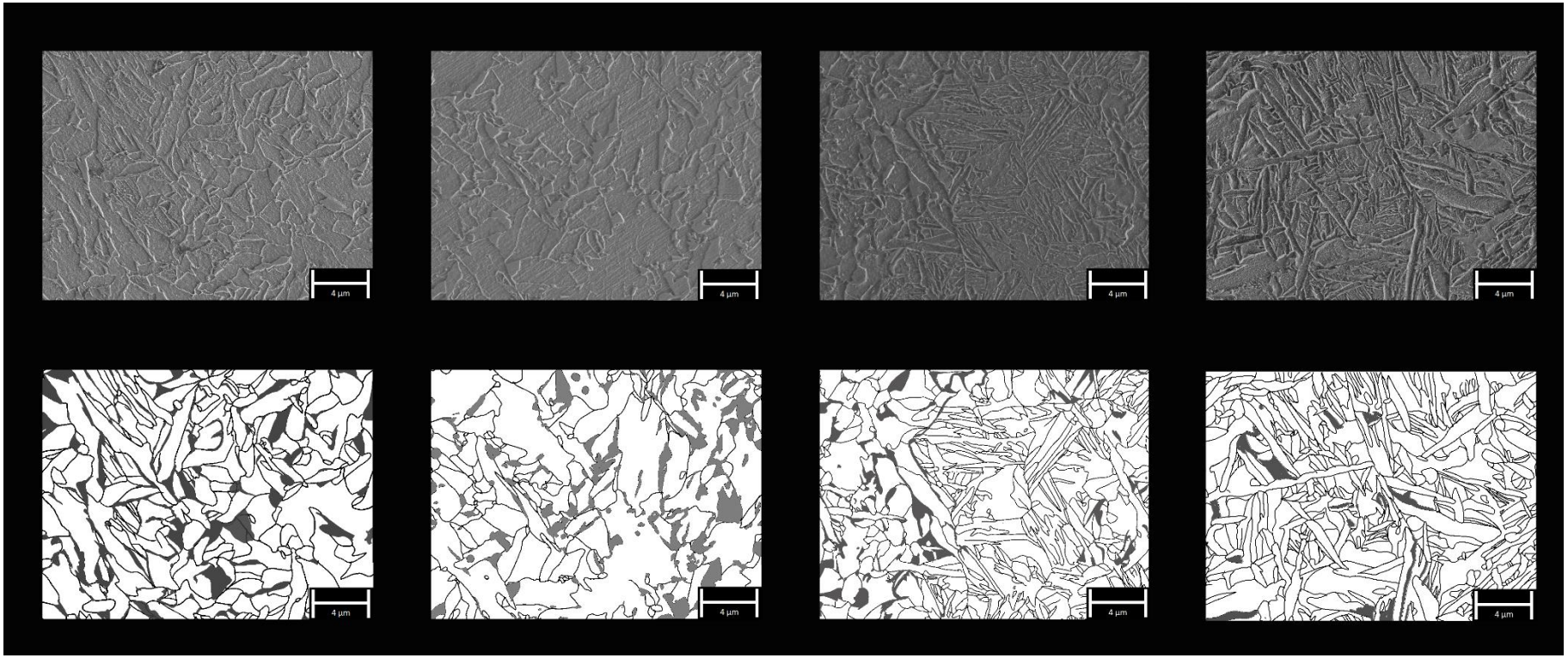

Figure 214: SEM micrographs of Weld 9 in the as-welded, intercritically reheated, grain-refinement, and grain-growth conditions. The micrographs are shown in the original and processed conditions.

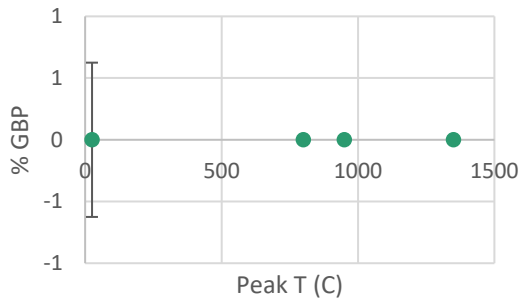

Figure 215: Scatter plot showing % GBP as a function of peak temperature reached during thermal cycling of Weld 9.

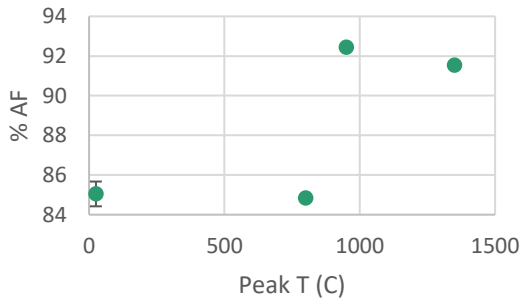

Figure 216: Scatter plot showing % AF as a function of peak temperature reached during thermal cycling of Weld 9.

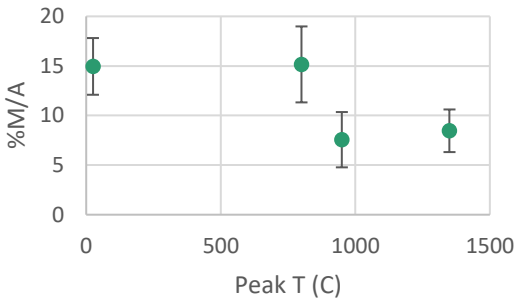

Figure 217: Scatter plot showing % M/A as a function of peak temperature reached during thermal cycling of Weld 9.

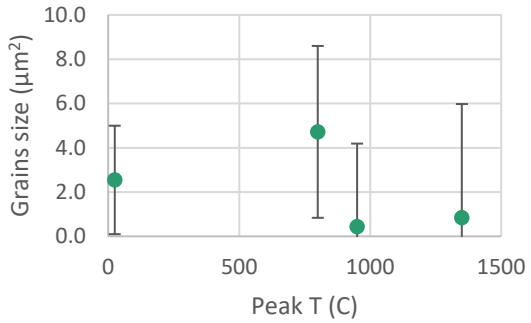

Figure 218: Scatter plot showing the number of ferrite-type grains per 100 µm as a function of peak temperature reached during thermal cycling of Weld 9.

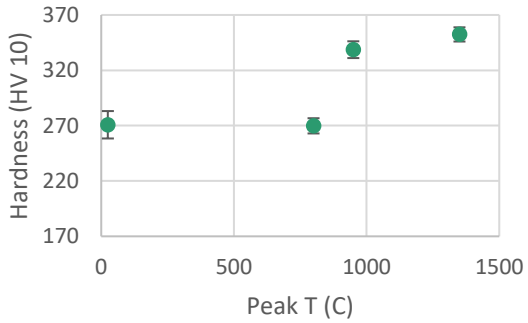

Figure 219: Scatter plot showing the change in hardness as a function of peak temperature reached during thermal cycling of Weld 9.

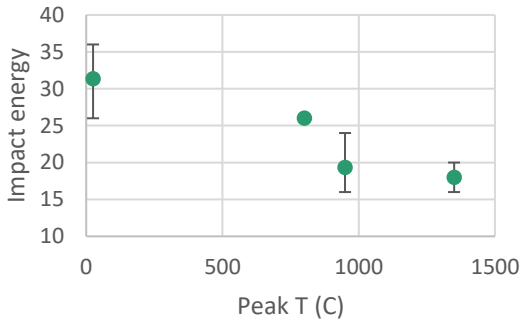

Figure 220: Scatter plot showing the change in impact energy as a function of peak temperature reached during thermal cycling of Weld 9.

B. Certificate (Lincolnweld 860 Flex/ Lincolnweld L-61 welding wire)

The Lincoln Electric Company
22801 St. Clair Avenue
Cleveland, Ohio 44117-1199

CERTIFICATE OF CONFORMANCE

LINCOLN ELECTRIC
THE WELDING EXPERTS

Product: **Lincolnweld® 860® Flux / Lincolnweld® L-61® Electrode**
Classification: **F6P5-EM12K-H8, F7A4-EM12K-H8 (Also meets the requirements of F7A2-EM12K-H8)**
Specification: **AWS A5.17:2019, ASME SFA-5.17**
Date **July 01, 2020**

This is to certify that the product named above is of the same classification(s) and design as the material used for the tests reported herein. The material was tested according to the specification(s) indicated and met all requirements. It was manufactured and supplied according to a Quality System Program that meets the requirements of ISO9001 among others as documented on The Lincoln Electric web page (*http://www.lincolnelectric.com/en-us/company/Pages/certifications.aspx*).

Operating Settings	**F6P5-EM12K-H8 Requirements**	**F7A4-EM12K-H8 Requirements**	**RESULTS**	
Required Size for Classification	5/32 inch	5/32 inch	5/32" (4.0 mm)	5/32" (4.0 mm)
Current Type/Polarity	AC or DC+ or DC-	AC or DC+ or DC-	DC+	DC+
Nominal Voltage, V	27 - 30	27 - 30	30	30
Nominal Current, A	475 - 575	475 - 575	475	475
Average Heat Input, kJ/cm (kJ/in)			2.0 (50.3)	2.0 (50.3)
Travel Speed, cm/min (in/min)	(15 - 17)	(15 - 17)	43 (17)	43 (17)
Contact Tip to Work Distance, mm (in)	(1 - 1.5)	(1 - 1.5)	38 (1.5)	38 (1.5)
Pass/Layers			21/10	21/10
Preheat Temperature, °C (°F)	(60 - 325)	(60 - 325)	25 (73)	25 (73)
Interpass Temperature, °C (°F)	(325 max.)	(325 max.)	135 (275)	135 (275)
Postweld Heat Treatment	1 hour @ 1150°F	As-welded	As-welded	1 hour @ 620°C (1150°F)
Mechanical Properties of Weld Metal				
Tensile Strength, MPa (ksi)	(60 - 80)	(70 - 95)	510 (74)	480 (69)
Yield Strength, 0.2% Offset, MPa (ksi)	(48 min.)	(58 min.)	420 (61)	360 (53)
Elongation %	22 min.	22 min.	30	35
Average Impact Energy Joules @ -46 °C (ft-lbs @ -50 °F)	(20 min.)			148 (109) 141,147,156 (104,108,115)
Average Impact Energy Joules @ -40 °C (ft-lbs @ -40 °F)		(20 min.)	145 (107) 140,147,148 (104,108,109)	
Average Hardness, HRB	Info. Only	Info. Only	84	79
Chemical Composition of Weld Metal (weight %)				
C	Info. Only	Info. Only	0.05	0.05
Mn	Info. Only	Info. Only	1.52	1.52
Si	Info. Only	Info. Only	0.35	0.36
S	Info. Only	Info. Only	0.009	0.010
P	Info. Only	Info. Only	0.018	0.018
Cu	Info. Only	Info. Only	0.06	0.06

Electrode composition (weight %)	**EM12K Requirements**	**Electrode Results**
C	0.05 - 0.15	0.12
Mn	0.80 - 1.25	0.99
Si	0.10 - 0.35	0.22
S	0.030 max.	0.008
P	0.030 max.	0.005
Cu (Total)	0.35 max.	0.07

The Lincoln Electric Company
22801 St. Clair Avenue
Cleveland, Ohio 44117-1199

CERTIFICATE OF CONFORMANCE

LINCOLN ELECTRIC
THE WELDING EXPERTS®

Product: **Lincolnweld® 860® Flux / Lincolnweld® L-61® Electrode**
Classification: **F6P5-EM12K-H8, F7A4-EM12K-H8 (Also meets the requirements of F7A2-EM12K-H8)**
Specification: **AWS A5.17:2019, ASME SFA-5.17**
Date **July 01, 2020**

Diffusible Hydrogen (per AWS A4.3)	F6P5-EM12K-H8 Requirements	F7A4-EM12K-H8 Requirements	RESULTS
Required Size for Classification			5/32" (4.0 mm)
Current Type/Polarity			DC+
Nominal Voltage, V			28
Nominal Current, A			525
Diffusible Hydrogen, mL/100g	8 max.	8 max.	2
Abs. Humidity (gr moisture/lb dry air)			77

1. This document meets the requirements of AWS A5.01M/A5.01 Schedule G. When a specific lot number is referenced it also meets the requirements of EN10204, type 2.2. It does not meet the requirements of type 3.1.
2. The size(s) of electrode tested is determined by the requirements for this classification. All other sizes manufactured will also meet these requirements.
3. Radiographic Inspection: Met requirements.
4. Strength values in SI units are reported to the nearest 10 MPa converted from actual data. Preheat and interpass temperature values in SI units are reported to the nearest 5 degrees.

July 01, 2020
Daniel Gaul, Certification Supervisor — Date

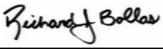

July 02, 2020
Rich Bollas, Certification Supervisor — Date

C. Proof of concept

Table 51: Chemical composition of parent metal and 4 welds deposited to test the proof of concept. Welds indicate that both Ni and Ti alloying occurs during SAW.

	Plain PM	Plain WM	Ni WM	Ti	NiTi WM
C	0.24	0.13	0.11	0.11	0.11
Mn	0.65	1.15	1.15	1.21	1.12
Si	0.23	0.41	0.4	0.41	0.38
P	0.15	0.024	0.027	0.03	0.025
S	0.016	0.019	0.021	0.021	0.021
Cr	0.07	0.08	0.07	0.08	0.07
Mo	0.003	0.01	0.01	0.005	0.01
Ni	0.02	0.04	3.03	0.04	3.09
Al	0.002	0.01	0.01	0.01	0.01
Cu	0.005	0.07	0.08	0.08	0.07
Nb	0.002	0.002	0.002	0.002	0.002
Ti	0.001	0.015	0.015	0.035	0.026
V	0.001	0.004	0.005	0.005	0.005
Sn	0.006	0.007	0.007	0.008	0.007
Sb	0.001	0.001	0.001	0.001	0.001
B	0.001	0.001	0.001	0.001	0.001

Table 52: Chemical composition of 3 welds deposited as proof of concept for welding. Results show that both Ni and Mo are successfully alloyed.

	A	B	C
C	0.092	0.086	0.091
Mn	1.37	1.35	1.31
S	0.018	0.018	0.018
P	0.013	0.014	0.014
Si	0.27	0.26	0.26
Cr	0.09	0.03	0.1
Mo	0	0.21	0.215
Ni	1.72	0.03	1.88
Cu	0.09	0.09	0.09
Al	0.009	0.012	0.015
V	0.006	0	0.006
Nb	0	0.009	0.008
B	0	0	0
Ti	0.041	0.042	0.055
Fe	Matrix	Matrix	Matrix